

**Oxidation-Induced Phase Transformations and Lifetime Limits of
Chromia-Forming Nickel-Base Alloy 625**

Von der Fakultät für Georessourcen und Materialtechnik
der Rheinisch-Westfälischen Technischen Hochschule Aachen

zur Erlangung des akademischen Grades eines
Doktors der Naturwissenschaften

genehmigte Dissertation

vorgelegt von **Diploma of Master**

Anton Chyrkin

aus Kiew

Berichter: Univ.-Prof. Jochen M. Schneider, Ph.D.
Univ.-Prof. Dr.-Ing. Lorenz Singheiser

Tag der mündlichen Prüfung: 05. Dezember 2011

Diese Dissertation ist auf den Internetseiten der Hochschulbibliothek online verfügbar

Kurzfassung

Die Kriechbeständigkeit der kommerziellen Nickelbasislegierung INCONEL 625 bei hohen Temperaturen beruht auf Mischkristallverfestigung in Kombination mit Ausscheidungshärtung durch die intermetallische Phase δ -Ni₃Nb und Karbide vom Typ (Ni,Mo,Si)₆C. In oxidierenden Atmosphären bildet dieser Werkstoff auf dessen Oberfläche eine kontinuierliche, langsam wachsende Chromoxidschicht, die das Material gegen schnellen Oxidationsangriff schützt. Das Chromoxidwachstum führt zu einer Chromverarmung in einer Zone unterhalb der Oxidschicht. Umfangreiche mikrostrukturelle Charakterisierung oxidiert Proben ergab, dass sich in der chromverarmten Zone ein ausscheidungsfreier Bereich unterhalb der oxidischen Deckschicht bildet, obwohl Chrom kein wesentlicher Bestandteil in beiden Ausscheidungsphasen ist. Außerdem ergaben die Mikrostrukturuntersuchungen, dass sich unmittelbar an der Metall/Oxid-Grenzfläche ein dünner Saum aus niobreichen Ausscheidungen der intermetallischen Phase δ -Ni₃Nb bildet.

Durch thermodynamische und kinetische Modellierung der Verarmungsvorgänge mittels der kommerziellen software Thermo-Calc/DICTRA konnte gezeigt werden, dass die innere Phasenan- und Phasenabreicherung während der Oxidation (englische Abkürzung SPE) durch sogenannte Aufwärtsdiffusion („uphill-diffusion“) des δ -Ni₃Nb stabilisierenden Elementes Niob im Chromaktivitätsgradienten bedingt ist. SPE ist daher eine Konsequenz der oxidationsbedingten Chromverarmung unter der Oxidschicht. Laut der durchgeführten thermodynamischen Berechnungen sinkt die chemische Aktivität von Niob in INCONEL 625 mit abnehmendem Chromgehalt. Durch den andauernden Chromverbrauch in der Legierungsmatrix zur Bildung der Oxidschicht an der Oberfläche stellt sich die niedrigste Niobaktivität an der Metall/Oxid-Grenzfläche ein, d.h. an der Stelle mit der geringsten Chromkonzentration. Dieser Aktivitätsgradient ist die Triebkraft für die Aufwärtsdiffusion von Niob in Richtung der Metall/Oxid-Grenzfläche entgegen dessen eigenem Konzentrationsgradienten.

Die Untersuchungen ergaben, dass in der chromverarmten Zone in INCONEL 625 ebenfalls eine Auflösung des M₆C-Karbids auftritt, obwohl Chrom kein Hauptbestandteil des (Ni,Mo,Si)₆C-Karbid ist. Laut thermodynamischen Berechnungen beruht die Karbidauflösung in INCONEL 625 auf einer Erhöhung der Kohlenstoffaktivität bei abnehmender Chromkonzentration. Dies führt zu einer Rückdiffusion von Kohlenstoff, d.h. Kohlenstoff diffundiert von der Metall/Oxid-Grenzfläche, die am stärkstem an Chrom verarmt ist, in Richtung der Probenmitte. Dies bewirkt eine Auflösung des M₆C in der chromverarmten Zone.

Es konnte gezeigt werden, dass der SPE-Effekt in dünnen Folienproben (typischerweise 0.1 mm) von INCONEL 625 viel weniger ausgeprägt ist als in dicken Blechproben. Diese Abhängigkeit der Probendicke ist auf unterschiedliche Reservoirs des oxidbildenden Elementes, sowie des δ -Phase stabilisierenden Elementes Niob zurückzuführen. Die dünnen Folienproben werden schneller an Chrom verarmt als die dicken Proben. Dies führt zu flacheren Chromkonzentrationsprofilen, d.h. zu einer geringeren Triebkraft für die Aufwärtsdiffusion von Niob in Richtung der Metall/Oxid-Grenzfläche. In dünneren Proben ist daher der SPE-Effekt wesentlich schwächer und es tritt nach längeren Auslagerungszeiten eine vollständige Auflösung von M₆C in der Probenmitte auf.

Somit wird der SPE-Effekt in sehr dünnwandigen Komponenten, d.h. in sehr dünnen Folien oder in Metallschäumen, aus INCONEL 625 nicht beobachtet. Die Anreicherung der δ -Phase an der Metall/Oxid-Grenzfläche tritt während der Oxidation von Metallschäumen mit einem Partikeldurchmesser von 20-60 μm nicht auf und kann bei der Modellierung der oxidationsbedingten Lebensdauergrenzen solcher Komponenten aus INCONEL 625 vernachlässigt werden.

Mittels einer FEM-Berechnung der Chromverarmung an der Metall/Oxid-Grenzfläche wurde gezeigt, dass die oxidationsbedingte Lebensdauergrenze in einem sphärischen Schaumpartikel eine parabolische Zeitabhängigkeit vom Radius der Schaumpartikel aufweist. Die berechneten Lebensdauerwerte sind in guter Übereinstimmung mit den experimentell ermittelten Werten.

Auf Basis der ermittelten Oxidationsvorgänge wurde eine neue, allgemeine, analytische Beschreibung der oxidationsbedingten Lebensdauer für dünnwandige Komponente (Folien, Dräte, Metallschäume) hergeleitet. Das neue Modell stellt eine bequeme und einfache Gleichung dar, die eine Lebensdauervorhersage ohne Einsatz von zeitaufwendigen Rechenverfahren ermöglicht. Die neue Lebensdauerformel zeigt zum einen eine hervorragende Übereinstimmung mit den Ergebnissen bisheriger, jedoch zeitaufwendiger Lebensdauermodelle, zum anderen eine gute Übereinstimmung mit den experimentellen Lebensdauerwerten von Metallschäumen aus INCONEL625.

Abstract

For its high creep resistance the commercial nickel-base alloy 625 relies on solid solution strengthening in combination with precipitation hardening by formation of $\delta\text{-Ni}_3\text{Nb}$ and $(\text{Ni},\text{Mo},\text{Si})_6\text{C}$ precipitates during high-temperature service. In oxidizing environments the alloy forms a slow growing, continuous chromia layer on the material surface which protects the alloy against rapid oxidation attack. The growth of the chromia base oxide scale results during exposure at 900 – 1000°C in oxidation-induced chromium depletion in the subsurface zone of the alloy. Microstructural analyses of the cross-sectioned specimens revealed that this process results in formation of a wide subsurface zone in which the mentioned strengthening phases are dissolved, in spite of the fact that both phases do not contain substantial amounts of the scale-forming element chromium. The cross-sectional analyses revealed that, in parallel to the formation of a precipitate depleted zone, a thin, continuous layer of niobium-rich intermetallic precipitates formed in the immediate vicinity of the scale/alloy interface.

The Subsurface Phase Enrichment (abbreviated as SPE) was shown to be the result of an uphill-diffusion of niobium, i.e. the element stabilizing the strengthening precipitates $\delta\text{-Ni}_3\text{Nb}$, in the chromium activity gradient and is thus a natural consequence of the oxidation-induced chromium depletion beneath the chromia scale. The thermodynamic calculations carried out using the Thermo-Calc/DICTRA software packages revealed that in alloy 625 the chemical activity of niobium decreases with decreasing chromium content. As chromium is being continuously removed from the alloy as the result of the chromia scale growth, the zone of lowest Nb-activity is formed in the location with the lowest chromium concentration, i.e. the scale/alloy interface. This creates a driving force for Nb to diffuse towards the scale/alloy interface against its own concentration gradient, which is known in literature as uphill-diffusion phenomenon.

Also the M_6C carbide is found to dissolve in the subsurface zone during high-temperature oxidation of alloy 625 although chromium is only a minor constituent in this $(\text{Ni}_3\text{Mo}_3)\text{C}$ base carbide. The thermodynamic calculations revealed the carbide dissolution to find its cause in the increasing carbon activity with decreasing chromium content which forced carbon to diffuse back from the subscale zone towards the bulk alloy resulting in carbide dissolution beneath the chromia scale.

SPE is experimentally found to be substantially less pronounced in thin foils than in thick specimens of alloy 625. It could be shown that this effect is related to the smaller reservoirs of the scale-forming element chromium as well as that of the $\delta\text{-Ni}_3\text{Nb}$ phase stabilizing element niobium in the thin specimens. As the thinner specimens (thickness in the range of 0.1 mm) become more rapidly depleted in chromium resulting in flatter chromium depletion profiles, a smaller driving force for uphill-diffusion of Nb towards the scale/alloy interface leads to a substantially less pronounced δ -phase enrichment/depletion than in specimens of a few mm thickness. Decreasing specimen thickness suppresses the enrichment/depletion process of the $\delta\text{-Ni}_3\text{Nb}$ phase and results in complete dissolution of the M_6C carbide after longer exposure times.

SPE is not observed during oxidation of extremely thin-walled specimens, e.g. extremely thin foils or metal foam particles fabricated from alloy 625. During high-temperature oxidation of metal foams consisting of e.g. 20-60 μm diameter particles, the $\delta\text{-Ni}_3\text{Nb}$ phase enrichment at the scale/alloy interface does not occur and can thus be virtually ignored when modelling the oxidation-induced lifetime limits of alloy 625 metal foams.

The lifetime prediction based on the finite-difference calculation of the chromium depletion at the metal/oxide interface of a spherical metal foam particle showed a parabolic dependence of the time to breakaway from the foam particle radius. The predicted lifetimes were found to be in good agreement with the experimental results.

A new analytical lifetime model to predict times to breakaway of thin-walled components (foils, wires, metal foams, etc.) was developed as an extension of the available lifetime models. The lifetime model derived is a simple mathematical expression which is able to substitute conventional robust equations thus making the lifetime prediction less time consuming and more efficient. The simplified lifetime treatment shows excellent agreement with the conventional lifetime models and is also in good agreement with the experimental breakaway results for alloy 625 metal foams.

Table of Contents

1. Introduction	1
2. Literature review	3
2.1 Fundamentals of oxidation	3
2.1.1 Thermodynamics	3
2.1.2 Oxidation kinetics	6
2.1.3 High-temperature oxidation of NiCr-base alloys	9
2.2 Breakaway oxidation due to oxidation-induced depletion	12
2.2.1 General remarks	12
2.2.1 Analytical lifetime models	16
2.2.3 Numerical approaches in oxidation modeling	21
2.3 Phase transformations induced by high-temperature oxidation processes	24
2.3.1 General remarks	24
2.3.2 Dissolution of precipitate phases	26
2.3.3 Subsurface phase transformation in single-phase materials	29
2.3.4 Formation of a new phase driven by oxidation	31
2.4 Summary of the literature review	33
3. Aims of the present study	34
4. Experimental	35
4.1 Materials	35
4.1.1 INCONEL 625 metal foams	35
4.1.2 Microstructure of metal foams	36
4.2 Specimen preparation	38
4.2.1 Sheet specimens	38
4.2.2 Foam specimens	39
4.3 Oxidation tests	39
4.3.1 Cyclic oxidation tests	40
4.3.2 Discontinuous oxidation tests	40
4.3.3 Thermogravimetry (TG)	40
4.4 Characterization of oxidized specimens	41
4.4.1 Optical metallography and electron microscopy	41
4.4.2 X-ray diffraction analysis	41
4.4.3 GDOES analysis	41
5. Modeling background	43
5.1 Equilibrium calculations	43
5.2 Diffusion calculations	44
5.3 Diffusion in alloys with dispersed precipitates	46
6. Subscale phase transformation processes in alloy 625	49
6.1 Phase equilibria in alloy 625 at 900 and 1000°C	49

6.2 Oxidation behavior at 900°C.....	53
6.3 Modeling depletion/enrichment processes at 900°C	57
6.4 Depletion/enrichment processes at 1000°C	64
6.5 Mechanism of M₆C dissolution	71
6.6 Uphill-diffusion of niobium in the Ni-Cr-Mo-Nb system	75
6.7 Possible effect of subscale phase changes on oxide scale growth	79
6.8 Summary of subscale phase transformations	83
7. Effect of specimen thickness on phase transformations in alloy 625	85
7.1 General remarks.....	85
7.2 Effect of specimen thickness on depletion/enrichment processes of δ-phase.....	86
7.3 Dissolution of M₆C carbide during oxidation of thin alloy 625 foils	94
7.4 Summary of the specimen thickness effect	96
8. Oxidation behavior of Ni-base metal foams at 700-900 °C.....	97
8.1 General remarks.....	97
8.2 Oxidation behavior of INCONEL 625 foams in air	97
8.2.1 Data representation.....	97
8.2.2 Oxidation behavior of metal foams at 700°C.....	100
8.2.3 Oxidation behavior of metal foams at 800°C.....	101
8.2.4 Oxidation behavior of metal foams at 900°C.....	105
8.3 Chromium depletion in alloy 625 foam particles	109
8.3.1 EDX spectra	109
8.3.2 Chromium depletion profiles in foam particles.....	111
8.4 Oxidation kinetics of alloy 625 sheets	115
8.5 Oxidation behavior of alloy 625 foams in Ar – 4%H₂ – 20% H₂O	118
8.6 Finite-difference lifetime model for metal foams	122
8.7 Summary of oxidation behavior of INCONEL 625 metal foams.....	125
9. Lifetime prediction for alloys with large k_p/D ratio	126
9.1 General remarks.....	126
9.2 Analytical lifetime model for alloys with large k_p/D ratio	126
9.3 Oxidation-induced lifetime limits of alloy 625 at 900°C	135
9.4 Summary of lifetime modeling	140
10. Conclusions.....	141
11. References	144

1. Introduction

As the increasing energy demand becomes one of the most challenging problems of the modern world, the power generating industry aims to develop new strategies to increase energy efficiency. Primarily, this implies increasing operating temperatures of the power generating units, which requires application of metallic materials with better mechanical properties and higher oxidation/corrosion resistance.

Most technically used high-temperature alloy systems are multicomponent and multiphase materials. They contain precipitates, frequently for increasing the high temperature mechanical properties. The heat-resistant alloys developed for application at high temperatures in oxidizing environments rely for their oxidation resistance on the formation of dense, well-adherent, protective surface scales. Most commonly used commercial high-temperature alloys, e.g. Ni-base superalloys, high chromium steels, FeCrAl-base alloys and (Ni/Co)CrAlY coatings, form protective chromia or alumina scales. The formation of the oxide scale results in a progressive depletion of the selectively oxidizing element (chromium or aluminium) from the alloy which leads to compositional and microstructural changes in the alloy beneath the oxide scale [1].

The oxidation-induced subscale depletion of the scale-forming element may have two important consequences for the alloy microstructure and hence the alloy: (i) phase dissolution/precipitation due to compositional changes in the subsurface zone; (ii) breakaway oxidation of thin-walled components, i.e. accelerated growths of iron- and/or nickel-rich oxides after a critical depletion of the scale-forming element. Modeling both phenomena and thus predicting lifetime limits of the components as a result of chemical breakdown and/or deterioration of mechanical properties are critically important for evaluating the performance of the materials and their suitability for a certain high-temperature application.

The vast majority of high-temperature alloys contain as strengthening precipitates various phases which contain significant amounts of the scale-forming element, for example Cr-rich carbides in austenitic steels [2] and Ni-base superalloys [3] or Al-rich β -Ni(Co)Al-phase in NiCoCrAlY coatings [4, 5]. The formation of the precipitate free zone as a result of selective removal of the scale-forming element during high-temperature oxidation has been extensively studied by a number of researches.

However, a number of alloy systems exist in which the strengthening precipitates in the alloy matrix do not contain substantial amounts of the scale-forming alloying element (Cr or Al respectively). Examples of such alloy systems are the chromia-forming nickel base alloys of the type INCONEL 625 or INCONEL 718 [6, 7] which contain as main strengthening phase δ -Ni₃Nb, i.e. a compound which does not contain substantial amounts of the scale-forming element chromium. A similar situation prevails in case of high chromium ferritic steels such as alloy 441 or Crofer 22H [8-10] in which the strengthening is imparted by the formation of Laves-phase of the type Fe₂(Nb,W). Also some commercially available alloys of the FeCrAl type may be considered as an example of such an alloy system: due to a minor carbon addition the alloys may contain precipitates of chromium rich carbide, i.e a phase which does not contain the scale-forming element aluminium [11].

Since in all these alloy systems the precipitate phases contain hardly any or only minor amounts of the respective scale-forming element, the subscale depletion processes must fundamentally differ from the conventional depletion/dissolution processes described above for alloy/coating systems in which the precipitates contain substantial amounts of the scale-forming element (chromium or aluminium, respectively).

The present study aims to describe and elucidate the mechanisms of the subscale phase transformations occurring in alloy systems, which contain precipitate phases containing no or minor amount of the scale-forming alloying element. The alloy system selected for the investigation is the commercially available, Ni-base chromia-forming alloy INCONEL® 625. The studies aim at a description of the subscale phase transformation processes driven by high-temperature oxidation, their influence on the occurrence of breakaway oxidation in alloy 625 and development of a lifetime prediction model for thin-walled components (thin foils and metal foams) manufactured from this material.

2. Literature review

2.1 Fundamentals of oxidation

2.1.1 Thermodynamics

Most metallic materials interact with the corrosive environment to form metal oxides [12]:



Whether this process is likely to occur, is defined by the change of the Gibbs free energy according to the second law of thermodynamics:

$$\Delta G_{M_xO_y} = \Delta H_{M_xO_y} - T\Delta S_{M_xO_y} \quad (2.2)$$

where G is the Gibbs free energy, H and S the enthalpy and the entropy of the metal-oxygen system, and T the absolute temperature. As most high-temperature exposures take place at constant temperature and pressure, the change in the isobaric-isothermal potential ΔG is an appropriate criterion for a prediction whether an oxidation process may occur at a given temperature:

$\Delta G_{M_xO_y} < 0$ – formation of the oxide

$\Delta G_{M_xO_y} = 0$ – metal and oxide coexist in equilibrium

$\Delta G_{M_xO_y} > 0$ – oxide decomposition

For chemical reaction (2.1) the free energy change ΔG can be expressed as:

$$\Delta G_{M_xO_y} = \Delta G_{M_xO_y}^o + RT \ln \left(\frac{a_{M_xO_y}}{a_M^x \cdot a_{O_2}^{y/2}} \right) \quad (2.3)$$

where $\Delta G_{M_xO_y}^o$ is the free energy of the system when all species are in the standard state, R is the ideal gas constant and a denotes the activities of the reacting species. The thermodynamic

activity a_i is a quantitative measure of the deviation from the standard state for a given species and is defined as [13]:

$$a_i = \frac{p_i}{p_i^o} \quad (2.4)$$

where p_i is the vapor pressure of the species over the solution phase (liquid or solid) and p_i^o is the partial vapor pressure of the species in the standard state, i.e. the partial vapor pressure of the species over the pure element at total pressure equal to 1 bar. For pure elements the chemical activity is equal to unity.

When the metal-oxygen system is equilibrated, the free energy $\Delta G_{M_xO_y}$ equals zero and Equation (2.3) reduces to

$$\Delta G_{M_xO_y}^o = -RT \ln \left(\frac{a_{M_xO_y}}{a_M^x \cdot a_{O_2}^{y/2}} \right). \quad (2.5)$$

Further, the activities of the pure solids (M and M_xO_y) can be taken as unity and the oxygen activity can, by definition, be substituted by the oxygen partial pressure $p_{O_2}^*$ at which the metal and the oxide coexist

$$\Delta G_{M_xO_y}^o = \frac{y}{2} RT \ln(p_{O_2}^*), \quad (2.6)$$

or

$$p_{O_2}^* = \exp \left(\frac{2}{y} \cdot \frac{\Delta G_{M_xO_y}^o}{RT} \right). \quad (2.7)$$

The oxygen partial pressure $p_{O_2}^*$ defined by Equation (2.7) is called the dissociation pressure of the oxide. If the oxygen partial pressure of the environments is higher than $p_{O_2}^*$, the oxide M_xO_y will decompose. Should p_{O_2} be lower than $p_{O_2}^*$, the metal surface will remain unoxidized; the corresponding oxide will decompose to form metal and oxygen.

The thermodynamic stability of oxides can be assessed using the Ellingham/Richardson diagram (Figure 2.1) in which the standard free energies for the formation of oxides and the respective dissociation pressures are plotted as a function of temperature.

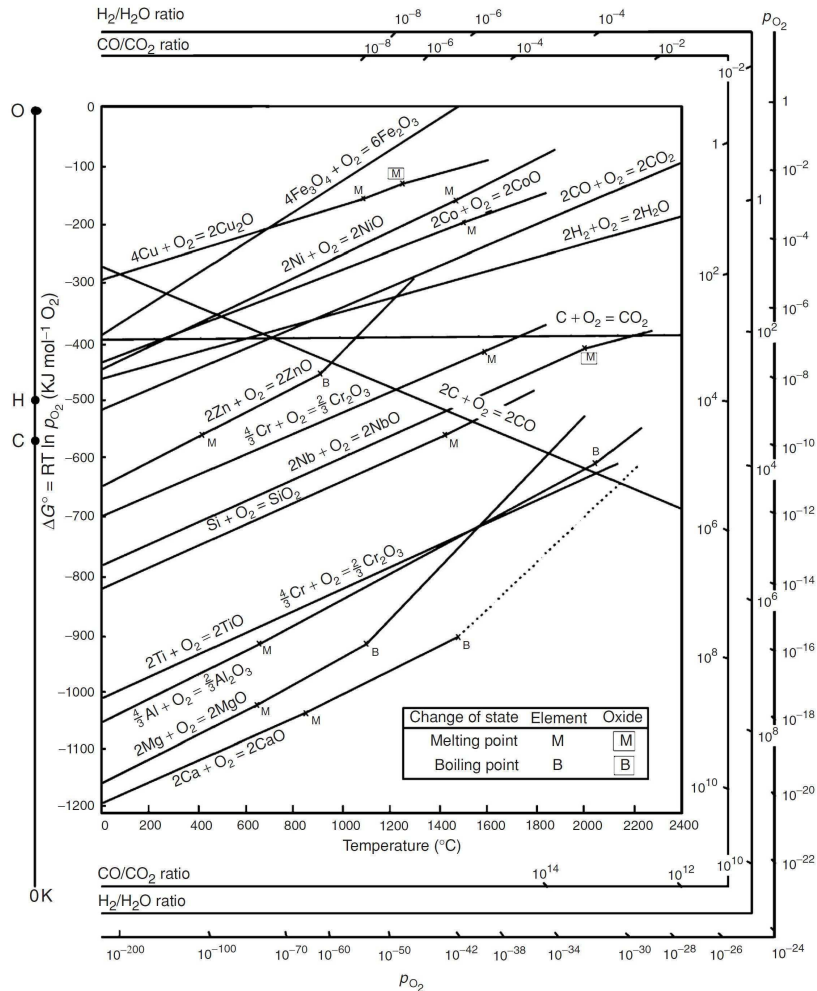


Figure 2.1: Standard free energies of formation of selected oxides as a function of temperature (Ellingham/ Richardson diagram) [13]. Also shown are corresponding equilibrium H₂/H₂O- and CO/CO₂-ratios

This plot allows the quantitative comparison of the thermodynamic stabilities of different oxides: the lower the dissociation pressure of the oxide, the more chemically stable the latter is.

As apparent from the Ellingham/Richardson diagram, the dissociation pressures increase with increasing temperature which means that oxides become thermodynamically less stable at higher temperatures. Thus, increasing the temperature while keeping constant partial pressure of oxygen of the environment can suppress the oxidation process. This is schematically shown

in Figure 2.2. The lines in Figure 2.2 show stability ranges of pure metals M (below the respective line) and their respective oxides (above the respective line).

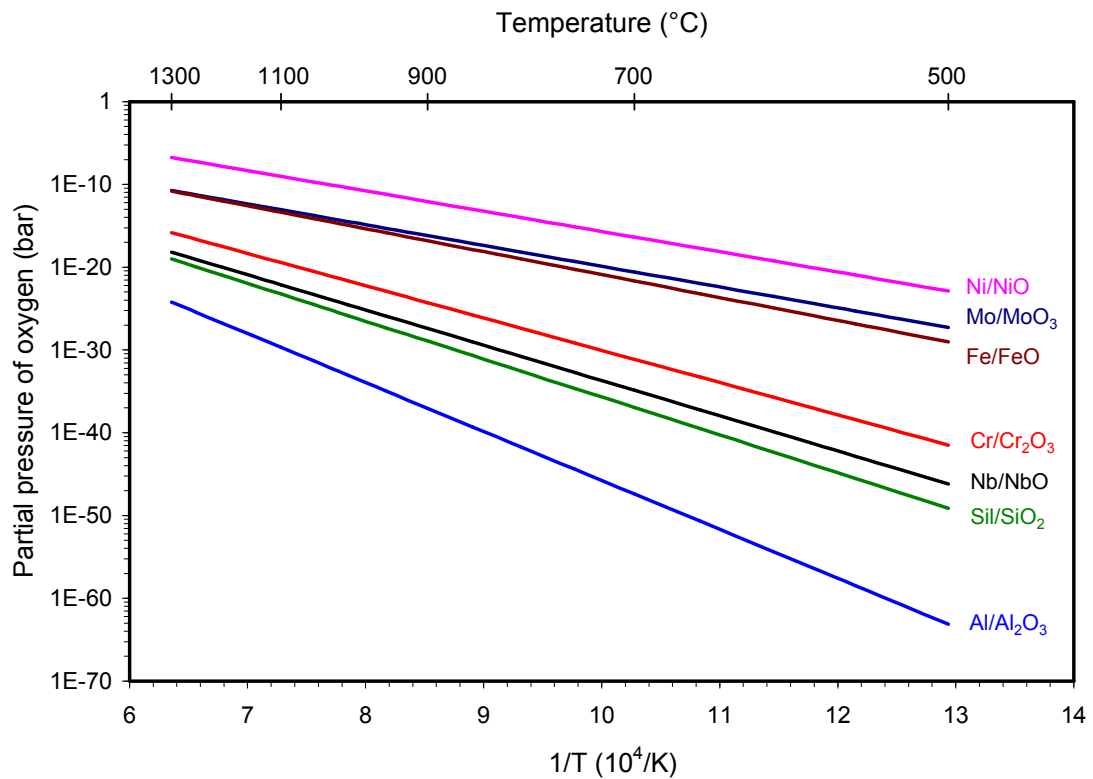


Figure 2.2: Dissociation pressures for several oxides as function of temperature for unit metal activities. Thermodynamic data are taken from [14-16]

2.1.2 Oxidation kinetics

Although thermodynamic considerations are crucial for understanding which oxidation products are likely to form, they are not sufficient for complete understanding and description of the oxidation process. If a metal surface is exposed to an oxidative environment, it starts readily to adsorb oxygen molecules from the gas phase. The molecules dissociate on the metal surface, accept electrons from the metal and react with it to form an extremely thin oxide layer. The reacting species, the metal and the oxidant, are thus separated from each other by the reaction products and further reaction is affected by solid state diffusion through the oxide scale.

Diffusion transport of species in solids occurs via imperfections or defects in the crystal structure [12]. Oxides are ionic crystals. They can have either stoichiometric or nonstoichiometric compositions. Stoichiometric ionic crystals are rare. From the viewpoint of conductivity, nonstoichiometric ionic compounds are semiconductors characterized by negative or positive Hall Effect and thus different types of defects in the lattice. Electrical charge can be transferred by electrons (n-type semiconductors) or electron holes (p-type semiconductors).

The n-type defects arise as a result of either metal excess (metal interstitials) or oxygen deficit (oxygen vacancies) in the oxide lattice. The excess positive charge of an interstitial metal ion has to be compensated by additional electrons in the conduction band. In the same way the effective positive charge of the oxygen vacancies are balanced by extra electrons thus imparting the oxide n-type conductivity. Conversely, p-type oxides are characterized by metal vacancies or oxygen interstitials, of which the negative charge is compensated by electron holes.

The mechanism of oxide scale growth is strongly dependent on the structure and mobility of the lattice defects in the oxide. For instance, the transport of oxygen through the oxide scale can be regarded as a flux of oxygen interstitials from the gas/oxide toward the oxide/metal interface as well as a flux of oxygen vacancies in the opposite direction. The transport of metal occurs as an outward flux of metal interstitials or as an inward flux of metal vacancies. If oxygen ions are the mobile species, they diffuse through the oxide scale to form the new oxide at the oxide/metal interface. In the case of metal ions diffusing outwards the oxide formation occurs at the oxide/gas interface.

The basic theoretical treatment of diffusion controlled growth of oxide scales on metals was developed by Carl Wagner [17]. This theory requires several assumptions: (i) the lattice diffusion in the oxide scale is the rate-controlling step of the oxidation process; (ii) thermodynamic equilibrium holds at both interfaces; (iii) the oxide scales are compact and free of pores [17]. Thus, an oxygen activity gradient across the oxide scale is established, i.e. the oxygen partial pressure at the scale surface is defined by the ambient atmosphere while it equals the dissociation pressure of the oxide at the scale metal interface (Figure 2.3).

According to the diffusion law, the flux of metal species B is proportional to the gradient of the chemical potential $\Delta\mu_B$ across the oxide scale of thickness X_{BO} [16]

$$j_B = -D_B \frac{\Delta\mu_B}{X_{BO}}. \quad (2.8)$$

The scaling rate is proportional to the ion flux flowing through the scale

$$\frac{dX_{BO}}{dt} = j_B \cdot V_{BO} \quad (2.9)$$

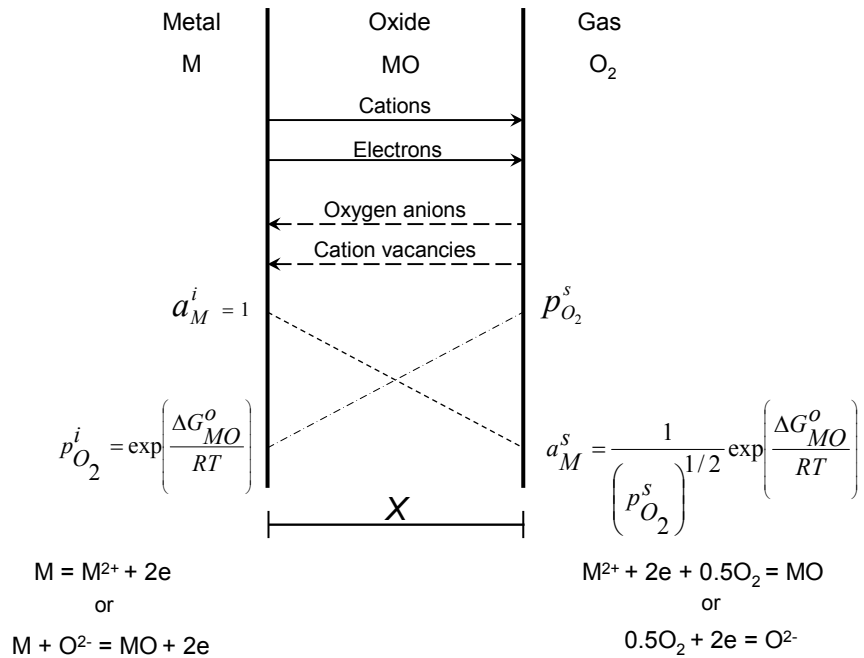


Figure 2.3: Wagner's model of oxidation [13]

where V_{BO} is the molar volume of oxide BO. Combination of Equations (2.8) and (2.9) with subsequent integration yields the parabolic dependence of the scale thickening.

$$X_{BO}^2 = 2k_p t + C \quad (2.10)$$

For $C = 0$ the value of k_p is given by the product

$$k_p = D_B V_{BO} \Delta\mu_B. \quad (2.11)$$

The parabolic oxidation rate predicted by Wagner is often observed experimentally in high-temperature oxidation processes. However, this theory is, as mentioned above, based on numerous assumptions which are often not completely fulfilled. The overall oxidation kinetics can be affected by various independent phenomena, e.g. enhanced metal consumption due to oxide spallation with consequent healing of the scale [18] or reactive evaporation of the scale-forming oxide [19]. Another significant simplification in Wagner's theory is that it considers only lattice diffusion in the oxide and does not take into account short-circuit diffusion along grain boundaries. For oxides with a negligibly low number of lattice defects, e.g. Al_2O_3 , the diffusion of oxygen along grain boundaries is frequently found to be the rate-controlling process and may result in subparabolic oxidation kinetics [20].

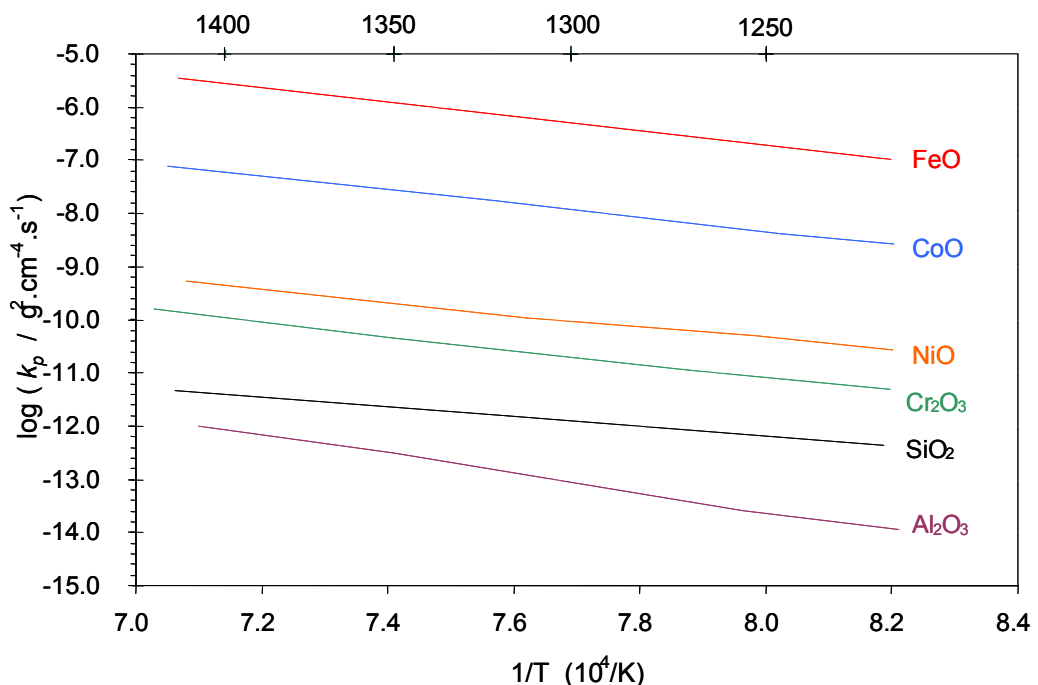


Figure 2.4: Parabolic oxidation rate constant for several pure metals as function of reciprocal temperature

2.1.3 High-temperature oxidation of NiCr-base alloys

NiCr-base high-temperature alloys have been used in numerous practical applications for over 80 years. These alloys were more systematically developed than any others. The vast majority

of NiCr-base alloys rely for protection against oxidation attack on chromia-base scales which form on the surface during high-temperature service as a result of selective oxidation of the main alloying element chromium.

Most commercially available Ni-base alloys are variations of the binary nickel-chromium alloy Nichrome 80 : 20, i.e. Ni–20Cr (in wt%). Additions of cobalt, molybdenum, tungsten are usually used for solution strengthening. The alloy also becomes strengthened by precipitates of chromium-rich carbides and/or intermetallic precipitate phases of the type γ' - Ni_3M ($\text{M} = \text{Al}, \text{Ti}, \text{Nb}, \text{Ta}$).

The oxidation resistance of the NiCr-base alloys has been extensively studied and reviewed in several papers [21, 22]. The isothermal section of the Ni–Cr–O system is shown in Figure 2.5. In contrast to the Fe–Cr–O system [23], the nickel-base system shows substantially less mutual solubility of the oxide phases. The high-temperature oxidation of diluted Ni-Cr alloys is controlled by growth of a NiO scale layer. A two-layer scale develops, the inner fine-grained layer containing small particles of the spinel NiCr_2O_4 in a NiO matrix. Depending on temperature, internal precipitation of Cr_2O_3 may also be observed [22].

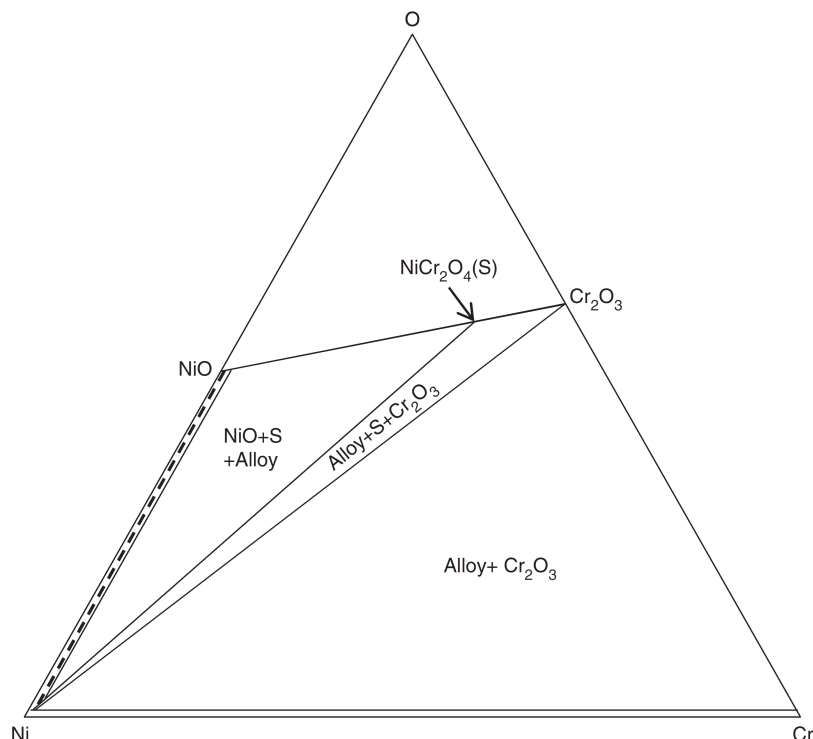


Figure 2.5: Isothermal section of the Ni–Cr–O diagram at 1000°C [23]

The addition of small amounts (1-2 wt %) of chromium increases the oxidation rate of nickel [21] (Figure 2.6) which is generally thought to be related to a dopant effect (Wagner-Hauffe mechanism). Dissolution of Cr ions in the p-type NiO increases the concentration of the mobile cation vacancies, although the solubility of Cr^{+3} in nickel monoxide is relatively limited.

Above a certain critical chromium content continuous Cr_2O_3 scales develop on the surface, and the oxidation rate constant k_p drops dramatically (Figure 2.6). The formation and maintenance of a continuous external chromia scale requires that two criteria are satisfied. First, the concentration of the scale-forming element Cr must exceed the value $N_{\text{Cr}}^{(1)}$ necessary for outward diffusion to prevent internal oxidation [24]. For the Ni-Cr system this criterion is

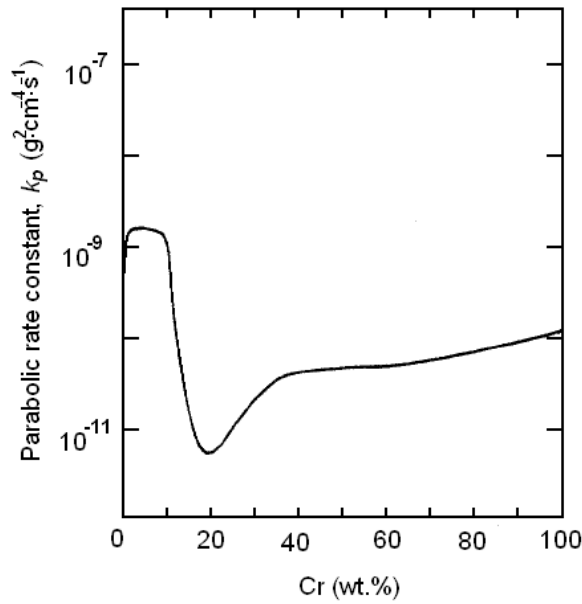


Figure 2.6: Variation of the parabolic rate constant with alloy composition for Ni-Cr alloys at 1000°C in oxygen at 1 bar [22]

$$N_{\text{Cr}}^{(1)} > \left[\frac{\pi g^*}{3} N_o^{(S)} \frac{D_o V_{\text{all}}}{D_{\text{Cr}} V_{\text{ox}}} \right]. \quad (2.12)$$

Here $N_O^{(s)}$ is the oxygen solubility in the alloy, D_O is the diffusivity of oxygen in the alloy, D_{Cr} is the alloy interdiffusion coefficient, and V_{all} and V_{ox} are the molar volumes of the alloy and oxide, respectively. The factor g^* is generally approximated as 0.3 [25].

The second criterion for the sustainable growth of the oxide scale is that the solute flux towards the scale/alloy interface is sufficient to maintain the external scale once it is formed [26]

$$N_{Cr}^{(2)} > \frac{V_{all}}{32\nu} \left(\frac{\pi k_p}{D_{Cr}} \right)^{1/2} \quad (2.13)$$

where k_p is the parabolic rate constant for growth of the external scale expressed in m^2s^{-1} . Essuman et al. [27] estimated the critical value $N_{Cr}^{(1)}$ for the Ni-Cr system at 1050°C to be approximately 13 at% whereas only 3 at% is needed to sustain the external growth of chromia according to Equation (2.13). The observed transition to the formation of an external chromia scales occurs between 15 and 20 wt% Cr but the Cr_2O_3 layer does not develop immediately after start of the exposure. When the alloy surface is brought in contact with an oxidizing environment both NiO and Cr_2O_3 nucleate on the surface. Nickel oxide grows more rapidly than chromia. Thus the subsurface zone becomes depleted in nickel which promotes the exclusive formation of Cr_2O_3 after longer times [16].

2.2 Breakaway oxidation due to oxidation-induced depletion

2.2.1 General remarks

The vast majority of heat-resistant (mostly Fe- or Ni-base) alloys developed for application at high temperatures in oxidizing environments rely for their oxidation resistance on the formation of a dense, well-adherent, protective chromium or aluminium oxide scale on the alloy surface. The formation of the oxide layer is associated with a continuous depletion of the scale-forming element (Cr and Al, respectively) from the alloy which may, after long service times, eventually result in breakdown of the protective oxide scale.

When a protective scale of slow growing oxide (Cr_2O_3 or Al_2O_3) can no longer be maintained, other alloy components, e.g. the base element, iron or nickel, start to oxidize. This phenomenon of breakdown or breakaway oxidation becomes inevitable when the interfacial concentration of the scale-forming element C^i decreases to a value lower than the minimum value required to sustain or to re-form (C_B) the selective growth of the desired scale (chromia or alumina). Although there is no satisfactory way of predicting the value of C_B , it can be measured experimentally. The problem is then to predict the capacity limits of the alloy to supply the selectively oxidizing element to the interface.

Assuming the specimen to be an infinitely large sheet so that edge effects can be neglected, the problem is one of diffusion in a single dimension, normal to the oxidizing surfaces. The resulting Cr/Al-depletion profiles derived by Wagner are shown in Figure 2.7. The analytical expression for the time dependent concentration profiles of the scale-forming element in the depleted subscale zone are given by

$$\frac{(C(x,t) - C^i)}{(C^0 - C^i)} = \left[\frac{\operatorname{erf}\left(\frac{x}{(4Dt)^{1/2}}\right) - \operatorname{erf}\left(\frac{k_C}{2D}\right)^{1/2}}{\operatorname{erf}\left(\frac{k_C}{2D}\right)^{1/2}} \right]. \quad (2.14)$$

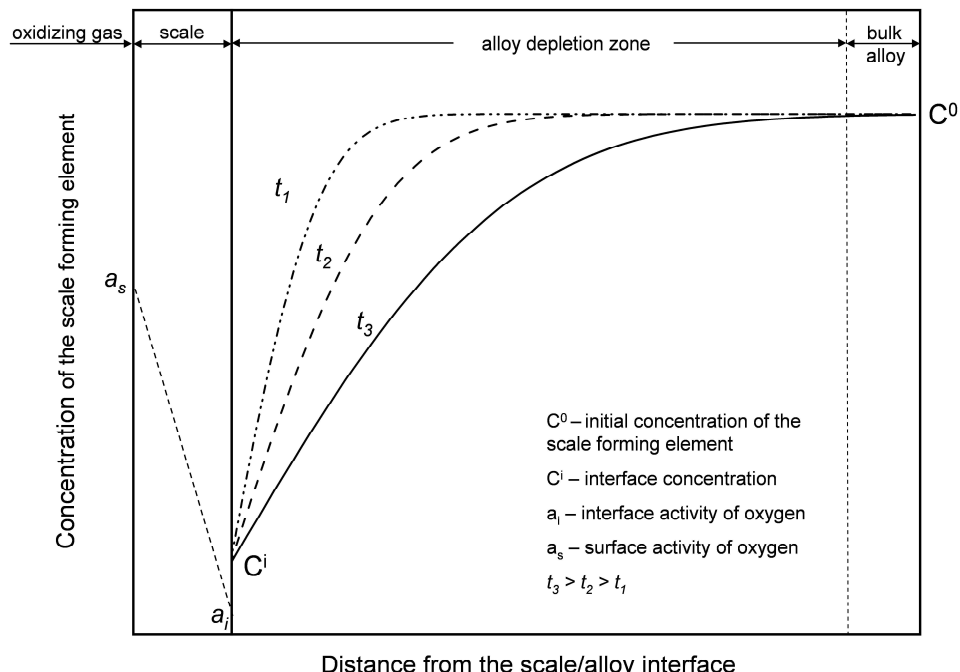


Figure 2.7: Schematic diffusion profiles in an infinitely thick specimen when a scale-forming element is selectively oxidized [28, 29]

Here C^i is the interface concentration of the scale-forming element, C^0 is the initial concentration of that element in the alloy, D (in $\text{m}^2\cdot\text{s}^{-1}$) the element diffusion coefficient in the alloy, x the distance from the scale/alloy interface, t the oxidation time and k_c is the alloy recession rate constant (in $\text{m}^2\cdot\text{s}^{-1}$) defined by

$$\zeta^2 = 2k_c \cdot t . \quad (2.15)$$

The alloy recession constant k_c is related to the parabolic oxidation rate constant k_p expressed in terms of oxide layer thickness (Equation 2.10) by the Pilling – Bedworth ratio ϕ , i.e. the ratio of the molar volume of the metal oxide to the molar volume of the corresponding metal consumed to form the oxide

$$k_c = \frac{1}{\phi^2} \cdot k_p . \quad (2.16)$$

From Wagner's oxidation theory [26] it can be derived that, if a parabolic time dependence of the scale thickening prevails, the concentration of the scale-forming element at the oxide/alloy interface C^i is time independent and can be expressed as

$$C^i = C^0 - \frac{100M_{el}}{M_{alloy}} \frac{1}{2\phi} \left(\frac{\pi \cdot k_p}{D} \right)^{1/2} \quad (2.17)$$

Here M_{alloy} is the average atomic weight of the alloy and M_{el} is the atomic weight of the scale-forming element, k_p is expressed in m^2s^{-1} .

When the diffusion distance of Cr (or Al) is similar or larger than the specimen/component dimensions after prolonged oxidation, the constant Cr (or Al) interface concentration can no longer be maintained [28] because the Cr (or Al) reservoir can no longer sustain the Cr (or Al) flux towards the oxide/metal interface required for the parabolic growth of the protective chromia/alumina scale.

Therefore, after a certain oxidation time, the Cr (or Al) interface concentration C^i starts to decrease (Figure 2.8) as the oxidation process continues until it finally drops below the critical value C_B which is required to maintain the protective Cr_2O_3 (or Al_2O_3) layer.

Upon the time at which the Cr (or Al) interface concentration reaches the value C_B , breakaway oxidation occurs. A generalized problem can be formulated as follows: the time to breakaway, i.e. the time at which the interface concentration of the scale-forming element falls below the experimentally established critical value C_B , has to be defined as a function of

- 1) Concentration of the scale-forming element (C^0)
- 2) Effect of alloy chemistry on C_B
- 3) Temperature dependent kinetic parameters (k_p and D)
- 4) Specimen geometry (sheet thickness, rod diameter, particle size, etc.).

Two “extreme” cases for depletion of a flat, thin specimen may be described:

- a) $k_p/D \gg 1$ – diffusion of the scale-forming element is relatively slow which results in a concentration gradient across the specimen and substantial depletion at the scale/alloy interface (Figure 2.8a) right from the beginning of oxidation. The interface concentration will remain time independent until the concentration profile reaches the middle of the specimen.
- b) $k_p/D \ll 1$ – diffusion of the scale-forming element is so rapid that almost no concentration gradient establishes within the specimen, i.e. the concentration profiles are essentially flat (see Figure 2.8b). The interface concentration starts to decrease immediately after the onset of oxidation.

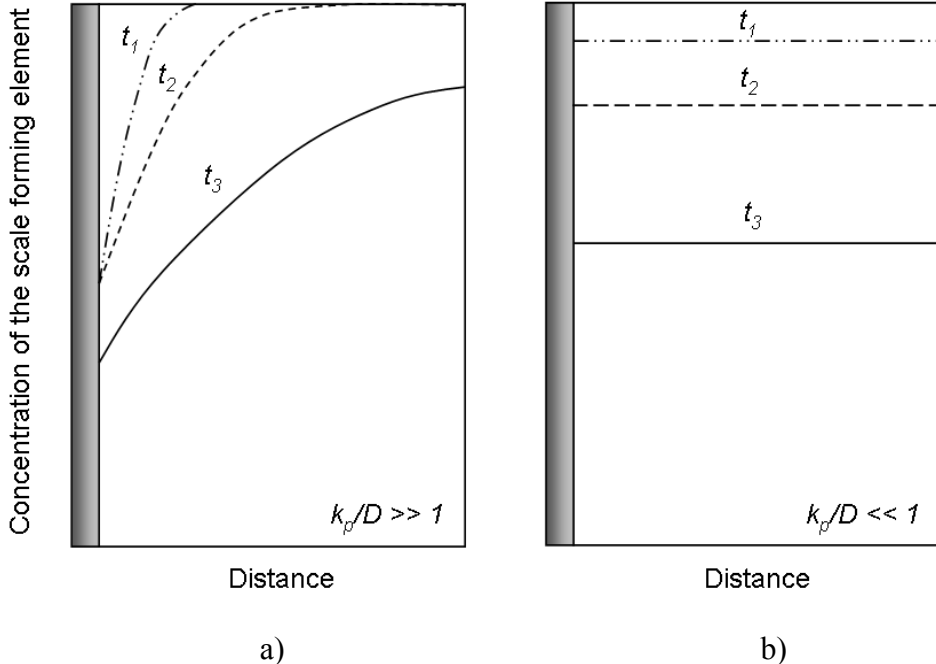


Figure 2.8: Schematic representation of concentration profiles of the scale-forming element in a thin-walled specimen for two borderline cases: (a) diffusion of the selectively oxidizing element in the alloy is slow ($k_p/D \gg 1$) and (b) diffusion is fast ($k_p/D \ll 1$)

2.2.1 Analytical lifetime models

First, the situation where scale growth is very slow and/or alloy diffusion rapid ($k_p/D \ll 1$) is considered (see Figure 2.8b). This has experimentally been shown to be the case for chromia-forming ferritic steels at $T \geq 800^\circ\text{C}$ [30, 31] and especially alumina-forming FeCrAl alloys at $T \geq 900^\circ\text{C}$ [32, 33]. This problem has been treated by Quadakkers and Bongartz [33] assuming that the scale/alloy interface movement as a result of oxide scale growth can be neglected. Especially for the alumina-forming materials the oxidation kinetics is not strictly parabolic [34] but obey a power law time dependence of the oxide thickening

$$\frac{\Delta W}{A} = k \cdot t^n \quad (2.18)$$

where $\frac{\Delta W}{A}$ is the area specific weight gain, k the oxidation rate constant, t the oxidation time, n is generally found to be near to 0.33, i.e. near cubic kinetics. The model is based on

equating the rate of metal solute, i.e. Al, consumption by oxidation with the available solute reservoir in the substrate. In case of a FeCrAl sheet the corresponding amount of aluminium withdrawn from each side of the slab is

$$\frac{\Delta W_{Al}}{A} = 1.124 \cdot k \cdot t^n \quad (2.19)$$

where the dimensionless numerical factor is the Al/O mass ratio in Al_2O_3 . If the alloy sheet thickness is d , the reduction in alloy aluminium content is ΔC_{Al} (in $\text{mg}\cdot\text{cm}^{-2}$).

$$\Delta C_{Al} = \frac{C_{Al}^0 - C_{Al}}{100} \cdot \rho \cdot \frac{d}{2} \cdot A = 1.124 \cdot k \cdot t^n \cdot A \quad (2.20)$$

where ρ is the alloy density in $\text{mg}\cdot\text{cm}^{-3}$. If the critical value for breakaway is C_B , the time t_B needed to reach this concentration is thus

$$t_B = \left[4.4 \cdot 10^{-3} (C_{Al}^0 - C_B) \frac{\rho \cdot d}{k} \right]^{\frac{1}{n}} \quad (2.21)$$

Quadakkers and Bennett [32] examined sheets of several alumina-forming FeCrAl alloys oxidized at 1200°C. The Al-concentration profiles were shown to be essentially flat. Using a C_B value of 1.3 wt% for breakaway oxidation of the oxide dispersion strengthened alloy MA956, the lifetimes were predicted as a function of sheet thickness using Equation (2.21), as shown in Figure 2.9 (the line labelled “no spalling”). The experimental lifetimes are in good agreement with the calculated values, as could be expected of a simple mass balance. At greater sheet thicknesses, i.e. longer lifetime, the experimental times to breakaway are shorter than predicted by Equation (2.21). This was attributed to scale spallation occurring during intermediate specimen cooling. After each spallation, alumina grew again, according to the same kinetics until the next scale spalling occurred.

Assuming that equal amounts of aluminium are lost in each spallation event,

$$\frac{\Delta W_{Al}^*}{A} = 1.124 \cdot k \cdot (t^*)^n \quad (2.22)$$

where t^* is the time between spallation events and ΔW_{Al}^* the corresponding aluminium loss (occurring after reaching a critical scale thickness x^*), then the time to breakaway for a flat specimen is given by

$$t_B = 4.4 \cdot 10^{-3} \frac{(C_{Al}^0 - C_B) \cdot \rho \cdot d}{k^{\frac{1}{n}}} \cdot (\Delta W_{Al}^*)^{\frac{1}{n}-1} \quad (2.23)$$

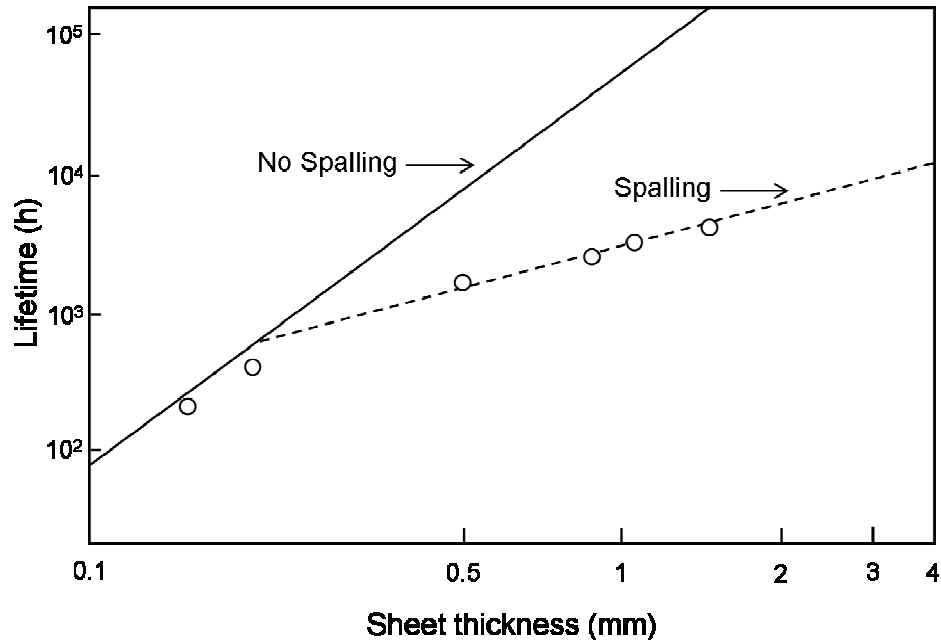


Figure 2.9: Lifetime limits for breakdown of alumina scales on sheet of the FeCrAl alloy MA956. Straight lines predicted from Equations (2.21) and (2.23), and points show experimentally observed data [33]

The dashed line in Figure 2.9 shows lifetimes calculated using Equation 2.23 on the basis of the experimentally observed critical oxide layer thickness for spalling to occur ($x^* = 10 \mu\text{m}$). As can bee seen from Figure 2.9, this simple mass balance prediction shows good agreement with the experimentally determined lifetimes.

The mass balance model was validated not only for alumina-forming FeCrAl alloys [32] at temperatures above approximately 900°C but also for chromia-forming ferritic steels above approximately 800°C [30, 31]. For the latter material Equation (2.21) should be slightly changed to account for chromia instead of alumina formation

$$t_B = \left[2.3 \cdot 10^{-3} (C_{Cr}^0 - C_B) \frac{\rho \cdot d}{k} \right]^{\frac{1}{n}} \quad (2.24)$$

Modified expressions were derived to account for other, e.g. cylindrical or spherical, geometries [35]. The applicability of this model is limited to ferritic materials, especially alumina formers at high temperatures, which fulfill the requirement that the ratio of k_p/D is quite small (Figure 2.8). Maréchal et al. [36] showed that at temperatures lower than 900°C aluminium concentration profiles in FeCrAl alloys cannot be considered completely flat and Wagner's formula should be used [29]. Furthermore, the above approach is not suitable for describing the oxidation of austenitic steels and Ni-base alloys because of the slow Cr (or Al) diffusion in these materials, i.e. the value of k_p/D is relatively large (see Figure 2.8).

The concentration profile inside the alloy beneath the protective oxide scale (Figure 2.8) can be found by solving the general diffusion equation

$$\frac{\partial C}{\partial t} = D \frac{\partial^2 C}{\partial x^2} \quad (2.25)$$

where C is the local concentration of the selectively oxidizing element and x is the space coordinate along the axis perpendicular to the specimen surface. Since the oxidation rate is small, the displacement of the oxide/alloy interface can in most cases be ignored [29]. According to Equation (2.17), the interface concentration of the selectively oxidizing element C^i is constant and defined by the ratio k_p/D . Once the diffusion front reaches the centre of the specimen, the interface concentration starts to decrease due to insufficient flux of the scale-forming element B . The time upon which the interface concentration drops below the critical value C_B is the time to breakaway.

The general solution for Equation (2.25) is quoted by Crank [37] with a parabolic time dependent flux of B at the oxide/alloy interface as a boundary condition

$$\frac{C - C^i}{C^0 - C^i} = \frac{4}{\pi} \sum_{n=0}^{\infty} \frac{(-1)^n}{2n+1} \exp\left(-\frac{D(2n+1)^2 \pi^2 t}{4L^2}\right) \cos \frac{(2n+1)\pi \cdot x}{2L} \quad (2.26)$$

where $2L$ is the sheet thickness. Solving the equation for thermal conductivity for an infinite slab of thickness $2L$, Carslaw and Jaeger [38] showed that the diffusion front reaches the middle of the slab when

$$\frac{Dt}{L^2} \approx 0.05 \quad (2.27)$$

Equation (2.27) can be useful as a rough estimation of lifetime. However, it systematically underestimates the lifetime of a sheet specimen because, depending on oxidation conditions, the time span between the interface concentration C^i starts to decrease and reaches the value C_B can be quite substantial. The subsequent decrease of C^i with time has been treated by Whittle [39]. Whittles' solution was later revised and amended by Cowen and Webster [40] into the form

$$C(x, t) = C^0 - \frac{100M_{el}}{M_{alloy}} \frac{1}{2\phi} \left(\frac{\pi \cdot k_p}{D} \right)^{1/2} \sum_{n=0}^{\infty} \left(erfc \left[\frac{2nL + x}{(4Dt)^{1/2}} \right] + erfc \left[\frac{2(n+1)L - x}{(4Dt)^{1/2}} \right] \right) \quad (2.28)$$

Evans and Donaldson [41] showed that oxidation-induced diffusion of chromium out of a thin sheet of austenitic steel can be described with reasonable accuracy by Equation (2.28) (Figure 2.10).

Strutt and Vecchio [42] used the model to predict the width of the precipitate free zone (σ -phase) in austenitic steel of a type 347 during oxidation in the temperature range 650 to 816°C. Recently Whittles' model was successfully used by Bauer et al. [43] to predict the time to breakaway of thin foils made of the austenitic steel 1.4848, during isothermal exposure in air at 1013°C.

The model derived by Whittle and Cowen can be regarded as a good approximation for lifetime calculations on reasonably thin flat specimens. For very thin foils the oxidation-induced alloy recession can amount to 20-30% of the specimen thickness, thus distorting essentially the calculated lifetimes.

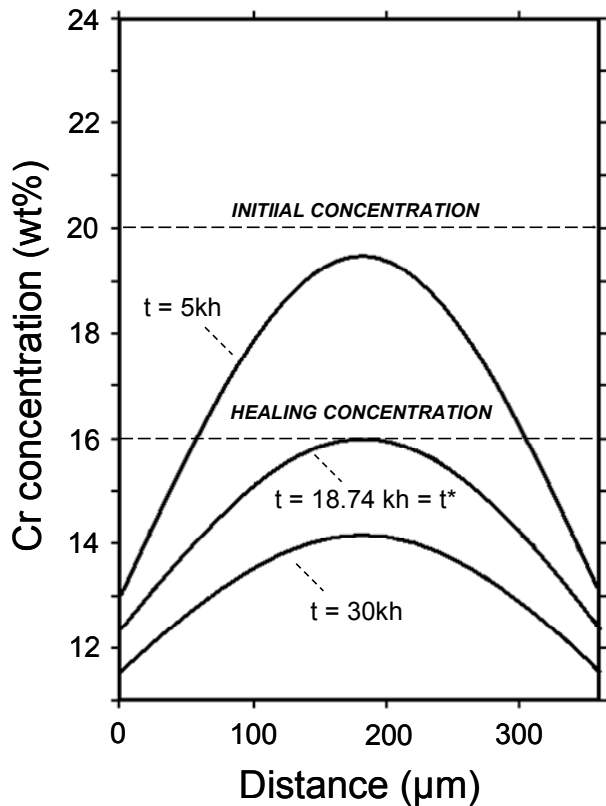


Figure 2.10: Computed chromium-depletion profiles in 20Cr–25Ni–Nb-stabilized austenitic steel for various exposure times at 1173 K from Ref. [44]. The critical condition for breakaway arises after 18 740h

2.2.3 Numerical approaches in oxidation modeling

Most analytical oxidation models [24, 28, 45] were developed for single-phase binary alloys. However, most commercial alloys of practical importance are designed as multicomponent and multiphase materials to exhibit adequate oxidation resistance at high temperatures along with good mechanical properties. Advances in computation techniques allowed the development of novel numeric models for describing high-temperature oxidation of multicomponent/phase alloys. The finite-element method was first applied by Whittle et al. [1] to binary Fe-Cr alloys as well as Ni-Cr alloys [46]. Solving the diffusion equation with appropriate boundary conditions, i.e. simulating selective oxidation of one of the alloy constituents, the authors were able to compute chromium depletion profiles for parabolic, cubic, and logarithmic oxidation kinetics (Figure 2.11).

The calculated concentration profiles of Cr show that the Cr concentration at the alloy/oxide interface remains constant in case of a parabolic oxidation rate whereas it increases with increasing oxidation time for subparabolic rate laws, i.e. cubic or logarithmic. Vice versa, the interface concentration of Cr has to decrease, as the oxidation proceeds, if the oxidation kinetics is more rapid than parabolic, e.g. as a result of oxide spallation [18] or reactive evaporation of chromia [47] which can be taken into account as an additional linear term in Equation 2.10.

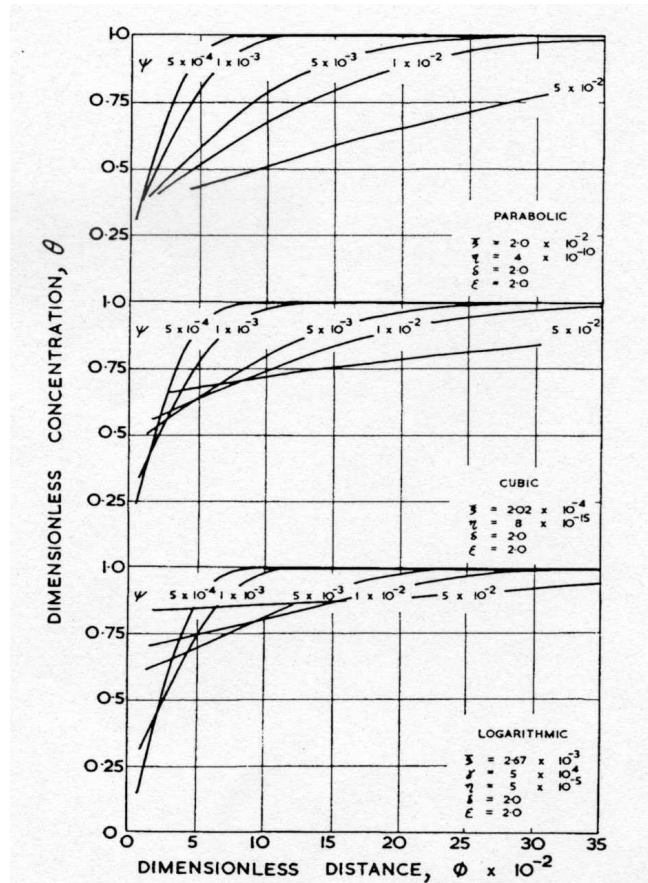


Figure 2.11: Dimensionless concentration of the scale-forming element, θ , in a binary alloy as a function of dimensionless distance from the original alloy/oxide interface, ϕ , at various times of oxidation according to parabolic, cubic, and logarithmic oxidation rate laws [1]

The finite-difference oxidation model was extended to a ternary single-phase γ -Ni-Cr-Al alloy by Nesbitt [48-51] and to Fe-Ni-Cr alloys by Danielewski [52-54]. The FEM-based oxidation/depletion models recently developed for 2-dimensional diffusion by Pragnel et al. [55, 56] and Hansson et al. [57] showed that the specimen edges become more depleted in

aluminium/chromium during high-temperature oxidation than the flat alloy/oxide interface, as could be expected due to geometry effects.

The finite-difference technique has the additional advantage that it allows a simultaneous calculation of phase equilibria in the alloys during oxidation, e.g. dissolution of β -NiAl phase in a CoCrAlY alloy [58] and carburization of Cr-rich nickel-base alloys [59-61]. The models are based on a numerical calculation of the element concentration profiles in multicomponent alloys with simultaneous computation of phase compositions according to the available phase diagrams. Turpin et al. [62, 63] used DICTRA [64], a commercial finite-difference software package, to simulate carburization processes in stainless steels. DICTRA was also used for calculation of interdiffusion processes between alloys of different compositions [65-67], e.g. oxidation resistant coatings on Ni-base superalloys.

Nijdam et al. [68] developed a coupled kinetic-thermodynamic model for describing oxidation of a γ -Ni-Cr-Al alloy taking into account transient oxidation stages expressed by means of linear and cubic kinetics before the parabolic stage, governed by solid-state diffusion, is established. Further, Nijdam and Sloof [69] adapted the model to a multiphase alloy thus being able to compute concentration profiles and mole fractions of β -NiAl phase in a two phase alloy with high Al content. The model considers three general cases: (i) the oxidation of a single-phase alloy, (ii) the oxidation of a two-phase alloy with precipitate dissolution and (iii) the oxidation of a single-phase alloy undergoing an oxidation-induced phase transformation.

The model accurately predicted the averaged Al and Cr profiles and the width of the Al-depleted single phase zone beneath the oxide scale in Ni-Cr-Al alloys during oxidation at 1100°C. Furthermore, it was found experimentally that the addition of other elements such as Co, Ta and Re can significantly affect the Al concentration at the alloy/scale interface. Thus, the time until occurrence of protective scale breakdown can be extended by alloying NiCrAl-base coatings with other elements.

The finite-difference computation technique is a powerful tool for modeling diffusion processes in commercial high-temperature alloys. The calculation of compositional changes driven by the protective oxidation of these alloys is nowadays possible for complex multicomponent and multiphase systems. By calculating chromium (or aluminium) depletion

in the subsurface zone it is possible to predict the lifetime limits of thin components and thus estimate the deterioration of mechanical properties as a result of precipitate phase dissolution caused by the oxidation process. Thus, the FEM-based modeling describing the oxidation/depletion/interdiffusion processes in high-temperature alloys has a strong potential for reducing the amount of experimental studies and for finding new ways and strategies in the development of oxidation-resistant materials.

2.3 Phase transformations induced by high-temperature oxidation processes

2.3.1 General remarks

The formation of protective, slow growing, and adherent chromia (or alumina) scales is logically associated with the selective oxidation of the alloy constituent Cr (or Al) and eventually will thus result in oxidation-induced compositional changes in the subsurface zone of the alloy. Depending on the alloy system, the subscale phase transformations may either involve the formation of a new phase or the dissolution of an existing one. Possible modes of subsurface degradation, as summarized by Young and Gleeson [70], include internal precipitate formation, void formation, phase transformation, and phase dissolution (Figure 2.12).

These phenomena may have a detrimental effect on the alloy performance due to:

- Degradation of toughness and ductility of the alloy;
- Cracking and/or deformation caused by internal stresses;
- Reduced oxidation resistance.

The subscale phase transformations (phase formation or dissolution) are an important consequence of selective oxidation of the scale-forming element. In both cases the compositional changes in the subsurface zone of the alloy result in a change of the original alloy microstructure. For instance, the intermetallic compound β -NiAl is upon oxidation selectively depleted in the subscale region in aluminium which is consumed to form an Al_2O_3 scale. This results eventually in the subsurface formation of γ' - Ni_3Al and, after longer times, even γ -Ni.

The formation of a new phase beneath the oxide scale can have a detrimental effect on the scale adherence and lead to its spallation, e.g. during thermal cycling. Modeling the oxidation-induced phase transformation to calculate the time at which a new phase forms is thus an important requirement for reliable lifetime prediction [71].

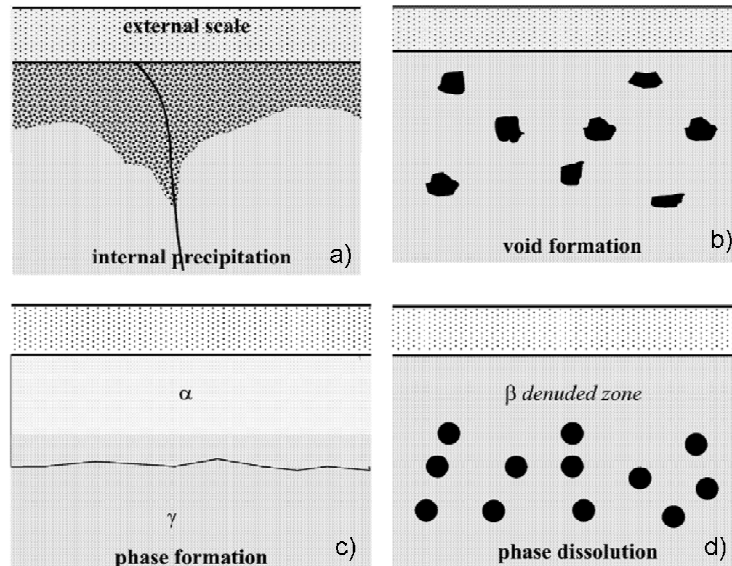


Figure 2.12: Schematic representation of possible modes of subsurface degradation as a result of oxidation: a) internal precipitation, b) void formation, c) phase formation, d) phase dissolution [70]

Phase dissolution is found to occur in alloys in which the alloy matrix has relatively high oxidation resistance [72]. For instance, many nickel-base superalloys consist of a γ -FCC nickel rich matrix and uniformly distributed γ' -Ni₃Al precipitates. These alloys rely for their high creep resistance at high temperatures on the presence of minority precipitate phases such as γ' . The dissolution of γ' -Ni₃Al in the subscale region occurs as a result of formation of an Al₂O₃-rich scale [73] occurring in some types of γ/γ' alloys, e.g. CMSX-4 [74, 75]. In that case the γ' -Ni₃Al phase acts as an Al reservoir for the continued growth of the alumina scale. The same effect is found in chromium-rich carbide precipitates in iron- and nickel/cobalt-base alloys [76-79] whereby the carbide phase acts a reservoir for the external growth of chromia scale.

Strutt and Vecchio [42] described sequential phase formation and dissolution during the high-temperature oxidation of a type 347 stainless steel. However, the driving force of the phase transformation in this case was not oxidation but an aging of the steel. Cr-rich sigma phase precipitates appeared in the steel after approximately 200-400 h exposure in the temperature

range 650 to 816°C. The formed sigma phase started to dissolve subsequently beneath the Cr₂O₃-rich scale due to continuing oxidation, i.e. progressing chromium depletion. The authors concluded that the sigma phase formation did not substantially affect the oxidation behavior of the alloy because the total chromium content of 18 wt% in the 347 stainless steel is relatively high. Therefore the alloy could withstand minor, localized depletion due to sigma phase formation. If the chromium content of an alloy is borderline from the viewpoint of oxidation resistance, the additional chromium subsurface depletion due to minor precipitates, which tie-up chromium, may be detrimental.

2.3.2 Dissolution of precipitate phases

In the case of oxidation-induced phase dissolution a two-phase alloy consisting of an oxidation resistant matrix phase and uniformly distributed precipitates is considered. The precipitate phase, rich in the more oxygen active, less noble solute element acts as a reservoir for the continued selective oxidation of the more reactive element to form the oxide scale of the solute-metal. This situation is schematically represented in Figure 2.13, where N_B^0 is the initial mole fraction of the solute element B, N_B^α the solubility limit in the matrix, N_B^i the concentration of B at the scale/alloy interface [70].

Dissolution of the precipitate phase is assumed to be sufficiently fast so that local matrix-precipitate equilibrium prevails. If diffusion of B through the precipitate denuded subscale zone is also fast enough to sustain external scaling, the interface concentration N_B^i will be approximately constant [28].

Carter et al. [80] used diffusion analysis to describe the depletion profile of B in the precipitate free zone whereby interface recession due to scale formation was taken into account. Equating the flux of B within the alloy with that in the oxide scale results in the expression

$$N_B^0 - N_B^i = \frac{u}{\gamma \exp(\gamma^2)} + \pi^{1/2} u \cdot \text{erf}(\gamma) \quad (2.29)$$

where u and γ are related to the alloy recession rate constant, k_c , and depth of precipitate dissolution, X_d :

$$u = \left(\frac{k_c}{4D} \right)^{1/2} \quad (2.30)$$

$$\gamma = \left(\frac{X_d}{4Dt} \right)^{1/2} \quad (2.31)$$

Equation (2.29) was applied to the kinetics of widening of the precipitate free zone during oxidation of Ni-Si alloys consisting of a γ -FCC matrix and β -Ni₃Si precipitates as well as Co-Si alloys containing α -Co₂Si silicides. The model successfully predicted the depth of the Si depleted zone. The applicability of the diffusion model depends on the validity of the assumption that the precipitate dissolution process is sufficiently fast that it does not affect the solute element supply.

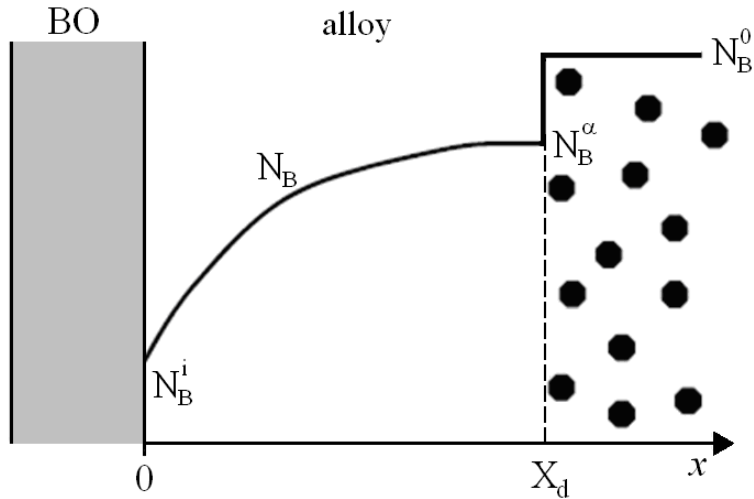


Figure 2.13: Analytical solution for diffusion profile of the scale-forming element B in the subsurface region of a binary, two-phase alloy A–B forming external oxide scale BO [70] assuming precipitate formation to be sufficiently fast

This diffusion model was also applied by Durham et al. [77] to describe the dissolution process of Cr-base carbide precipitates upon oxidation of Fe–15Cr–0.5C base model alloys. The software Thermo-Calc [81] was used to predict how alloying additions would affect the alloy microstructure, i.e. phase constitution, precipitate compositions and weight fractions. The base alloy Fe–15Cr–0.5C was austenitic at the test temperature of 850°C. Adding 1.0 wt% silicon to the iron-base alloy changes its phase constitution to $\alpha + M_7C_3$. By using nickel

as an austenite stabilizer, a silicon containing iron-base alloy was manufactured to study the chemical effect of silicon on the oxidation process apart from the structural changes, i.e. formation of the austenitic matrix. Another model alloy without silicon was produced by adding molybdenum as the ferrite stabilizer to investigate the effect of changing the alloy matrix from FCC to BCC. Finally, the molybdenum-bearing alloy was austenitized by adding nickel in order to verify whether the molybdenum had any effect on the oxidation behavior apart from stabilizing a BCC matrix.

Two scaling types were observed during oxidation of the model alloys at 850°C: either a protective chromium-rich oxide scale was formed accompanied by subsurface carbide dissolution (Figure 2.14), or a fast growing iron-rich oxide scale engulfing the carbide precipitates. The ferritic model alloys always formed protective chromia scales, whereas the austenitic materials formed non-protective, rapidly growing iron-base oxide scales except in the case of the silicon containing austenite.



Figure 2.14: Dissolution of chromium carbides in the subsurface zone of hot-forged model alloy Fe-15Cr-0.5C after 336h of oxidation in pure oxygen at 850°C [77]

Chromium depletion profiles measured by EPMA were fitted using Equation (2.29). The width of the precipitate free zone was measured metallographically. The values of D_{Cr} obtained were found to be in good agreement with the literature data. The effect of silicon on the oxidation behavior was shown to be related to its ability to form a very thin silica layer between the chromia scale and the adjacent alloy, which was previously shown to reduce the oxidation rates of ferritic Fe-Cr alloys [82, 83] and austenitic Fe-Cr-Ni steels [41, 43, 84, 85].

2.3.3 Subsurface phase transformation in single-phase materials

The high-temperature oxidation of MoSi_2 provides a good example of an oxidation-induced phase transformation in the subscale zone of a single-phase material. MoSi_2 exhibits excellent oxidation resistance at high temperature because of the formation of a thin protective silica layer. Two possible oxidation reactions exist for MoSi_2 [86]



and



The first reaction (2.32) describes formation of a mixed scale consisting of SiO_2 and MoO_3 whereas reaction (2.33) is a sum equation of external SiO_2 scale growth in parallel with subscale formation of Mo_5Si_3 as a result of Si depletion. Numerous studies [87-90] showed that at temperatures above 1000°C the second reaction prevails. The lower silicide Mo_5Si_3 is formed between the MoSi_2 base material and the protective external scale as a result of Si depletion caused by the growth of a protective silica layer. The same considerations apply for oxidation of WSi_2 (Figure 2.15).

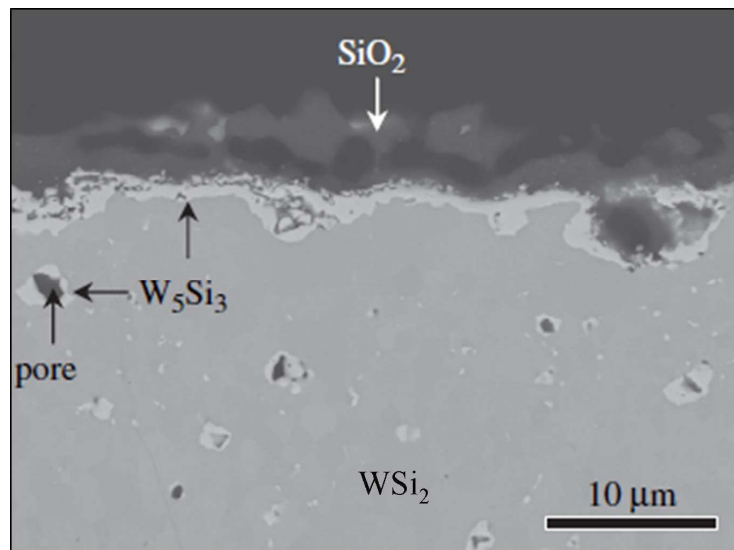


Figure 2.15: Formation of W_5Si_3 layer beneath the silica scale after 3h oxidation of WSi_2 at 1200°C in air [91]

Rapid and easy diffusion of silicon in both silicides, MoSi_2 and Mo_5Si_3 , at high temperatures governs the oxidation mechanism. Oxygen permeates through the silica layer and reacts with

the silicide to form $\text{SiO}_{2(s)}$. The silicon is continuously supplied to the scale/alloy interface from the bulk of material which results in silicon depletion in the subscale zone. Once the subsurface composition is changed, the phase transformation occurs in accordance with the Mo-Si phase diagram (Figure 2.16).

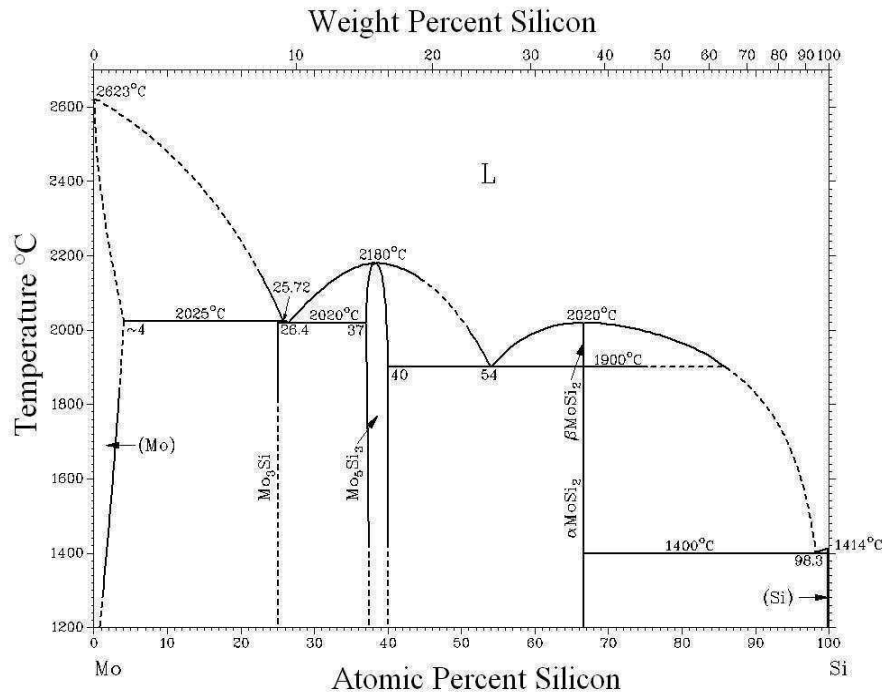


Figure 2.16: Mo-Si binary phase diagram [94]

Similar phase transformations in silicides occur as a result of silicon evaporation in vacuum [92] and in molybdenum-silicon diffusion couples [93]. If a MoSi_2 specimen is heated in vacuum, a weight loss is observed due to silicon evaporation. A thin Mo_5Si_3 layer is formed at the silicide surface. In vacuum MoSi_2 tends to decompose according to the following phase transformations $\text{MoSi}_2 \rightarrow \text{Mo}_5\text{Si}_3 + \text{Si} \rightarrow \text{Mo}_3\text{Si} + \text{Si} \rightarrow \text{Mo} + \text{Si}$. According to the binary phase diagram, the Mo-Si system moves towards a solid solution of Si in α -Mo with decreasing silicon content (Figure 2.16). These phase transformations are also observed after heat treatment of a MoSi_2 coating on metallic molybdenum at 1400°C [92]. As summarized by Fitzer [92], possible phase transformations in MoSi_2 driven by oxidation, silicon evaporation or siliconizing are shown in Figure 2.17.

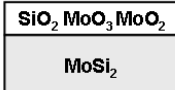
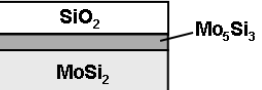
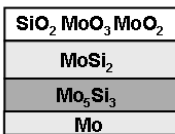
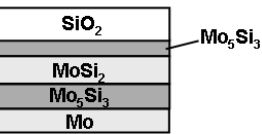
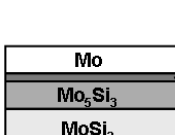
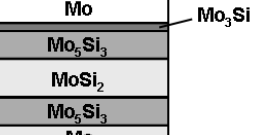
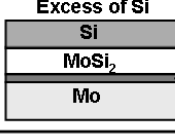
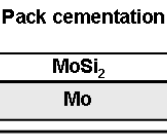
Oxidation of thick specimen	Total oxidation  Selective oxidation 
Oxidation of semi-infinitely thick specimen	Total oxidation  Selective oxidation 
Silicon evaporation from silicides	Thick specimen  
Siliconizing	Excess of Si  Pack cementation 

Figure 2.17: Schematic representation of possible phase transformations in MoSi_2 caused by Si depletion/enrichment during oxidation, silicon evaporation or siliconizing [92]

2.3.4 Formation of a new phase driven by oxidation

The oxidation-induced formation of a new phase in the subscale layer can also be observed during oxidation of the intermetallic phase $\gamma\text{-TiAl}$. The phase formation involves aluminium depletion in the sub-oxide zone due to the formation of an Al_2O_3 scale. However, in contrast to MoSi_2 , the formation of an intermetallic phase with lower Al content due to compositional changes in the subscale zone, as would be expected from the binary Ti-Al phase diagram, is not exactly the effect which is observed during high-temperature oxidation of $\gamma\text{-TiAl}$.

Copland et al. [95] showed that upon oxidation $\gamma\text{-TiAl}$ forms a subscale layer of Z- $\text{Ti}_{50}\text{Al}_{30}\text{O}_{20}$ at 1000°C if a protective alumina scale is formed during the initial stages of oxidation. The Z phase was first identified beneath the alumina scale during oxidation of $\gamma\text{-TiAl}$ in air at 900°C by Zheng et al. [96]. Figure 2.18 shows a cross-sectional secondary electron image of a Ti-52Al (at%) alloy after 50h oxidation in pure oxygen at 1000°C [95]. The specimen surface was ground to a 600-grit finish prior to oxidation to promote the initial formation of an Al_2O_3 -rich scale. Analysis of the diffusion path for this oxidized alloy revealed that the subscale formation of the Z phase requires very little titanium diffusion and essentially equal amounts of oxygen enrichment and aluminium depletion [70]

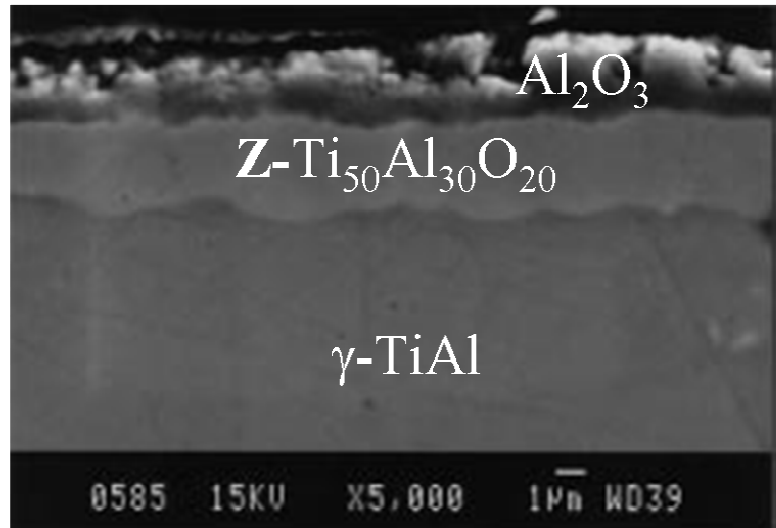
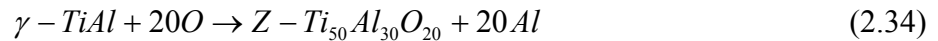


Figure 2.18: Secondary electron image of a cross-sectioned γ -TiAl alloy abraded to a 600-grit surface finish and then oxidized in pure oxygen at 1000°C for 50h [95]

The aluminium released in this reaction diffuses toward the scale/alloy interface to form more alumina scale. The Z phase was shown to form at the Z/γ -TiAl interface which implies a high oxygen permeability in the phase. With continued oxidation, the Z phase layer transforms at the Z/γ -TiAl boundary into a mixture of α_2 - Ti_3Al and Z. The reason for degradation of the Z/γ -TiAl interface is the continuous aluminium depletion from the Z/γ -TiAl interface which simultaneously results in the breakdown of the protective Al_2O_3 scale with the subsequent formation of a non-protective, mixed TiO_2/Al_2O_3 oxide scale. However, the subscale formation of Z phase in γ -TiAl-based alloys during high-temperature oxidation is not itself a cause of non-protective oxidation. On the contrary, the Z phase formation beneath the alumina scale supports the formation of a protective alumina scale. Addition of silver was shown to stabilize the Z phase [97] which therefore promoted formation of a long-term, stable, protective Al_2O_3 scale.

2.4 Summary of the literature review

Numerous studies showed that high-temperature oxidation of alloys may result in compositional changes beneath the oxide scale which may cause phase transformations (dissolution of the strengthening precipitate phases and/or precipitation of new phases) in the subscale zone and breakaway oxidation due to critical Cr (or Al) depletion after longer exposure times. Both depletion and phase transformation phenomena may have a detrimental effect on material performance.

A number of analytical models describing compositional changes in the subscale zone induced by oxidation are available in literature. The analytical solutions were further adapted to thin-walled specimens/components to describe depletion kinetics of the scale-forming element thus enabling reasonably reliable lifetime prediction. However, the applicability of the analytical models is limited to binary alloys and mostly parabolic scaling kinetics.

Numerical finite-difference approaches extended the applicability range of previously developed oxidation/depletion models to multicomponent alloys. Additionally, the finite-difference models allow to describe multiphase systems, i.e. take into account oxidation-induced phase transformations in the subsurface region as well as a deviation from ideal parabolic kinetics.

Theoretical approaches in studying oxidation phenomena offer a very significant contribution to the interpretation of new experimental results, i.e. understanding and describing the evolution of microstructure and properties of high-temperature materials in oxidizing environments.

3. Aims of the present study

As shown in the previous chapter, most of available analytical modeling approaches to describe high-temperature oxidation consider a simplified case of a binary single-phase alloy. Multicomponent and multiphase systems are therefore modeled using numerical calculations techniques, e.g. finite difference method. Over past 30 years, virtually all studies on effect of oxidation on the alloy subscale microstructure considered precipitate phases rich in the scale-forming element (Cr or Al) as a result of compositional changes driven by oxide scale growth. In the present investigation attention is drawn to the alloy systems in which strengthening precipitate phases contain only minor amounts of the scale-forming element e.g. Ni-base alloys 625 and 718 or Nb-containing ferritic steels like Crofer 22 H.

For instance, alloy INCONEL[®] 625 is a widely used high-temperature material. This alloy contains as main strengthening phase $\delta\text{-Ni}_3\text{Nb}$, i.e. a compound which does not contain substantial amounts of the scale-forming element Cr. Unlike chromium carbide strengthened nickel base alloys (e.g. alloy 617, alloy X) [3] or austenitic steels [2] alloy 625 should not in fact exhibit oxidation-induced dissolution of the strengthening precipitate phase in the subscale zone, as described in section 2.3.2, because chromium is not the main constituent of the $\delta\text{-Ni}_3\text{Nb}$ precipitates.

The present study is meant to provide a comprehensive analysis of phase transformation phenomena occurring in the subsurface zone of alloy 625 during high-temperature oxidation in different atmospheres (with high and low oxygen partial pressure). The main aim of the investigation is to understand the effect of oxidation-induced chromium depletion on the microstructure of alloy 625, i.e. enrichment/depletion of the alloying elements, dissolution and precipitation of the strengthening phases accounting for their effect on the oxidation process.

Another important aspect of the chromium depletion process studied was to investigate the breakaway oxidation of thin-walled materials fabricated from INCONEL 625, especially development of a lifetime model which allows prediction of times to breakaway for INCONEL 625 metal foams as function of microstructure and temperature.

4. Experimental

4.1 Materials

The commercial chromia-forming alloy INCONEL® 625 is a nickel-base alloy strengthened by (Ni,Mo)₆C-type carbides and intermetallic δ-Ni₃Nb precipitates. In the present investigation oxidation testing was carried out using compact sheet specimens of alloy 625 produced by Huntington Alloy Products to study the subscale phase transformation driven by oxidation and acquire necessary kinetic data (oxidation rates and diffusion coefficients) for the use as input parameter in predictive lifetime modeling. In parallel, highly porous metal foams were produced from alloy 625 and subjected to oxidation in air and low-pO₂ environments to observe breakaway oxidation in thin-walled components. The compositions of the studied alloy specimens and metals foams are given in Table 4.1.

Table 4.1: *Chemical composition of INCONEL 625 alloy in wt% measured by ICP-OES*

Composition	Ni	Cr	Mo	Fe	Nb	Al	Cu	Mn	Si	C
Sheet specimens	Bal.	21.58	8.39	3.6	3.51	0.30	-	0.11	0.25	0.02
Metal foam	Bal.	21.8	8.1	4.5	3.33	0.001	0.1	0.17	0.45	0.03

4.1.1 INCONEL 625 metal foams

The INCONEL 625 foams were produced using the SRFS-process developed by Mohr et. al [98]. This procedure (Figure 4.1) provides a method to produce foams from metal powder as raw material, being a simple and cost-efficient manufacturing process, comparable with that of common ceramic processing routes. The main advantage of this technique is that the foaming step is performed at room temperature so that no extensive process control is required [98].

Metal powder is mixed with an aqueous solution of phosphoric acid into a slurry. The acid reacts with the metal powder particles whereas hydrogen evolves as a reaction product thereby foaming the slip. Additionally, metal phosphates are formed which act as binding agents thus consolidating the structure. After drying, the green body is sufficiently stable to be processed into the desired shape. The powder particles must be connected to each other, and the metal phosphates have to be reduced to pure metal. Otherwise the inorganic particles would not be sintered, and the foam structure would break down after heat treatment. The

green body is therefore sintered in a reducing atmosphere in a non-continuous batch process. After cooling the foam can be processed and machined by milling, grinding, welding, etc.

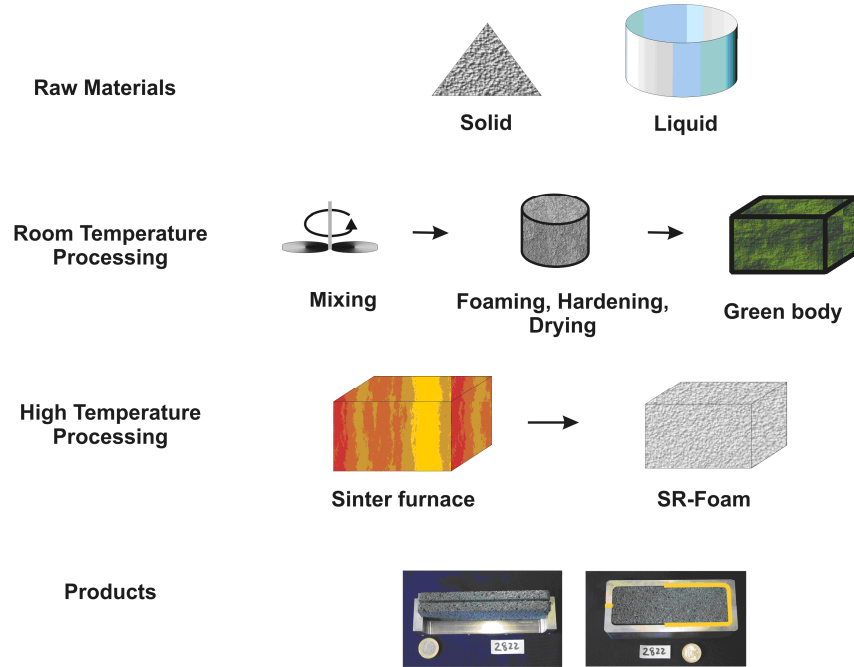


Figure 4.1: Schematic representation of various steps in the Slip-Reaction-Foam-Sinter-process [98]

4.1.2 Microstructure of metal foams

The structural characteristics of the metal foams are summarized in Table 4.2. The calculation of porosities and mean particle radii (\bar{r}) was carried out using optical micrographs of the as-received metal foams.

The quantitative particle size analysis performed on the optical images revealed essential scatter in particle size; mean values taken as a basis for the lifetime modeling are calculated as the maxima in the distribution of particle size (Figure 4.2) and are summarized in Table 4.2.

Table 4.2: Structural characteristics (density, porosity and mean particle radius) of the metal foams studied

Batch designation	Density ($\text{g}\cdot\text{cm}^{-3}$)	Porosity (vol. %)	\bar{r} (μm)
LKW	2.10	56	6
MLD	1.24	73	11
MLE	1.36	78	12
MKK	1.68	86	20
KUS	1.73	85	32
KUP	1.32	73	30
MMJ	1.03	87	12
MMH	1.63	83	18
MMK	1.43	86	16
MMM	1.90	85	31

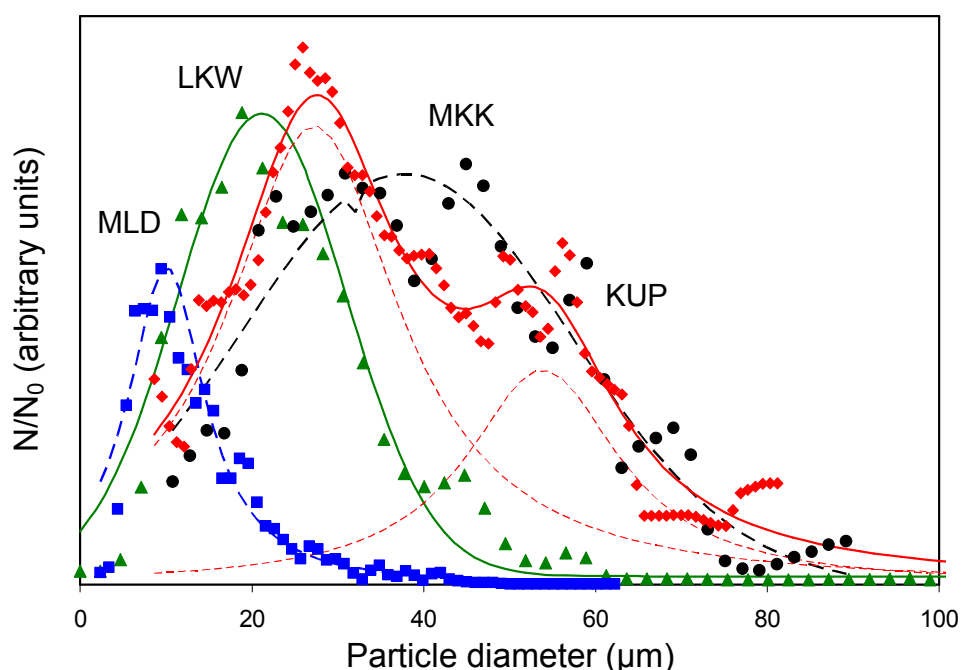


Figure 4.2: Particle size distribution in different batches of INCONEL 625 metal foams fabricated by the SRFS-process

The microstructure of the foams with various particle size distributions is shown in Figure 4.3. According to the optical micrographs, only two coarse-grained foams (batch designations KUS and KUP) had a 3D network microstructure. The other foams consisted of particle agglomerates which are poorly linked in space.

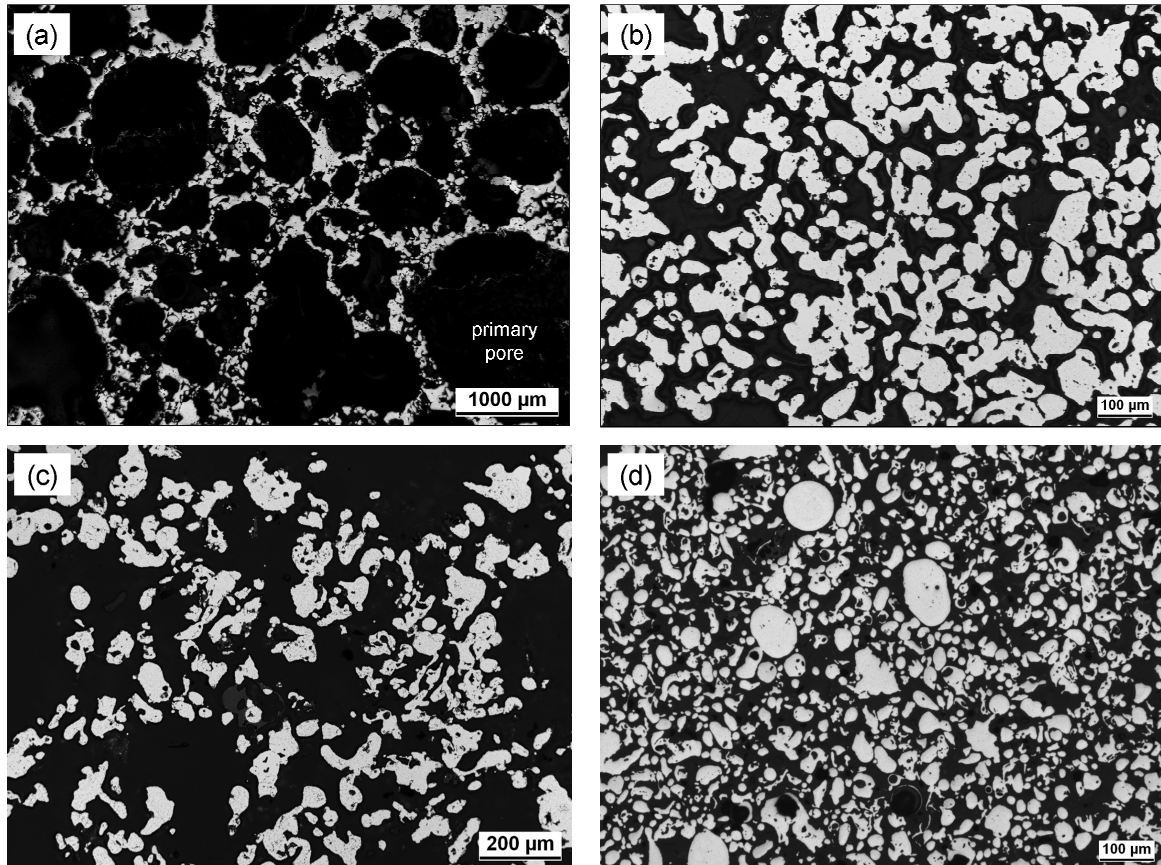


Figure 4.3: Metallographic cross-sections of the INCONEL 625 metal foams: (a) – KUS (mean particle radius $\bar{r} = 32.3 \pm 5.2 \mu\text{m}$); (b) – MKK ($\bar{r} = 20.3 \pm 4.8 \mu\text{m}$); (c) – MMK ($\bar{r} = 16.2 \pm 4.2 \mu\text{m}$); (d) – LKW ($\bar{r} = 6.1 \pm 1.8 \mu\text{m}$)

4.2 Specimen preparation

4.2.1 Sheet specimens

Specimens measuring $20 \times 10 \text{ mm}$ or $10 \times 10 \text{ mm}$ were cut from a forged alloy 625 bar produced by Huntington Alloy Corp (chemical composition is given in Table 4.1) and ground

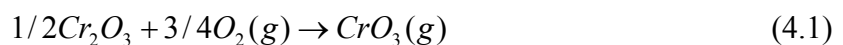
down to 1200 grit surface finish using SiC grinding paper. In order to ensure homogeneous access of the oxidizing gas to the specimen surfaces, the specimens were hung on a platinum wire during exposure in a high-temperature furnace. A 2 mm diameter hole close to the specimen length edge was drilled for that purpose. Sheet specimens of different thickness varying from 0.1 to 1 mm were used to take into account a possible specimen thickness effect on oxide growth rate [99] and to adjust different reservoirs of the scale-forming element Cr [100]. All specimens were degreased using ethanol in an ultrasonic cleaner prior to oxidation.

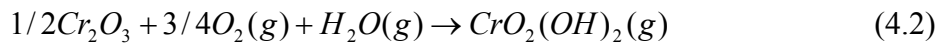
4.2.2 Foam specimens

Selected INCONEL 625 foams with different granularity (Table 4.2) were chosen for the cyclic oxidation testing. Cubic coupons measuring $10 \times 10 \times 10$ mm were sectioned from the foam bodies, ultrasonically cleaned in water, rinsed in ethanol and then dried in air prior to oxidation testing.

4.3 Oxidation tests

The oxidation tests were carried out in two atmospheres: air and an environment with a low equilibrium oxygen partial pressure (Ar-4%H₂-2%H₂O). The air experiments on the metal foams were carried out to induce breakaway oxidation after long exposure times which would correspond to the service lifetime limits of the material. The low pO₂ exposures were necessary for two independent reasons. First, this atmosphere suppresses formation of nickel-rich oxides thus promoting formation of near single-phase chromia layers. Oxidation tests in the atmosphere, in which NiO is thermodynamically unstable, allow to estimate the relative significance of the chromia growth and the formation of breakaway type, Ni-rich oxides for the lifetime of the foam. This atmosphere has the additional advantage that the oxidation results are, unlike in air oxidation, not affected by the formation of volatile Cr-oxide and/or Cr-oxyhydroxides. As shown in [19], volatile Cr-species in air can form according to the reactions





Volatile Cr-species, such as $CrO_3(g)$ and/or $CrO_2(OH)_2(g)$ being formed at high temperature thus deplete the oxide scale and the subscale zone in chromium. This has a consequence that Cr consumption cannot be determined with high accuracy from gravimetric or metallographic results. As seen from e.g. [101], the formation of the volatile species is only significant in high-p_{O₂} gases and therefore can be avoided in Ar-4%H₂-2%H₂O.

4.3.1 Cyclic oxidation tests

The foam specimens were subjected to cyclic oxidation testing in the temperature range of 700-1000°C in laboratory air, each cycle consisting of 120 min heating at the respective temperature and 15 min cooling. The foam coupons were placed in alumina crucibles and were moved in a vertical furnace which was heated to the test temperature. During the cooling step the specimens were removed from the furnace and cooled by pressurized air. The specimens were weighed and visually examined for spalling/damage every 36 h.

4.3.2 Discontinuous oxidation tests

Discontinuous, long-term oxidation tests were carried out at 700-1000°C in laboratory air and in Ar-4% H₂-20% H₂O for metal foams and in Ar-4% H₂-2% H₂O for sheet specimens up to 1000h exposure. Mass change measurements were carried out after cooling down to room temperature every 100 (metal foams) or 250 (sheet specimens) hours. The samples were visually examined for spalling/breakaway oxidation.

4.3.3 Thermogravimetry (TG)

The short-term isothermal oxidation tests with in-situ monitoring of the weight change kinetics were carried out in synthetic air (mixture of nitrogen with 20 vol.% oxygen) and Ar-4% H₂-2% H₂O using a thermo-balance (SETARAM® TG 92). The heating rate was 90°C per minute, the flow rate of the gas was 2 l/h, and the cooling rate was approximately 10°C per minute. The isothermal exposure time in all TG-tests was 72h.

4.4 Characterization of oxidized specimens

4.4.1 Optical metallography and electron microscopy

The oxidized foam specimens were mounted in an epoxy resin, ground with SiC sand-paper from 240 to 1200 mesh and polished down to 1 μm surface finish. The oxidized sheet specimens were electrochemically coated with nickel prior to mounting into the resin. To impart electrical conductivity to the oxidized specimens, a thin gold coating was applied by sputtering. The nickel coating was applied for obtaining better contrast between the oxide scale and the mounting material during microscopic observations. The metallographic cross-sections were characterized by optical metallography. Porosity and granularity of the metal foams was estimated by quantitative microstructural analysis of the metallographic cross-sections using the Olympus Image Analysis software [102]. For SEM (Scanning electron microscopy) studies, the cross-sections were coated with Pt. The specimens were investigated using a LEO 440 SEM appliance equipped with an Inca EDX (Energy dispersive X-ray analysis) System. For the WDX (Wavelength dispersive X-ray analysis) the Zeiss Supra 50 instrument coupled with Inca WDX was used.

4.4.2 X-ray diffraction analysis

The phase compositions of the oxide scales and the subscale zone of the oxidized sheet specimens were determined using the D4 ENDEAVOR XRD set-up from BRUKER AXS. The XRD patterns were obtained using a copper cathode as a radiation source (K_{α} , wavelength 1.5419 \AA). The scanning step was 0.02°; the scanning time was 8 s.

4.4.3 GDOES analysis

Glow Discharge Optical Emission Spectroscopy (GDOES) was used for detailed characterization of the oxide scales. The GDOES analyzer was equipped with a standard 4-mm glow discharge source (Jobin Yvon), a polychromator, and a monochromator optical spectrometer. The matching box allows continuous monitoring of the d.c. bias voltage. To obtain a suitable shape of the sputter crater, the analysis conditions were chosen to be 700 Pa

and 60 W. The measured depth profiles were quantified using a procedure similar to that described in reference [103, 104].

5. Modeling background

5.1 Equilibrium calculations

Phase equilibria in multicomponent and multiphase systems are calculated by minimizing the Gibbs energy of the system. The molar Gibbs energy of a solution phase α can be described as

$$G_m^\alpha = G^{\alpha,\text{ref}} + G^{\alpha,\text{id}} + G^{\alpha,\text{ex}} \quad (5.1)$$

The sum consists of a term referring to the pure elements in the standard state $G^{\alpha,\text{ref}} = \sum_{i=1} x_i^\alpha G_i^{a,0}$, a term to account for ideal mixing $G^{\alpha,\text{id}} = RT \sum_{i=1} x_i^\alpha \ln(x_i^\alpha)$, and a term to describe the non-ideal mixing $G^{\alpha,\text{ex}}$ due to interactions between the solute atoms. The Gibbs excess energy for multicomponent systems is usually modeled using a polynomial extension which contains molar fractions of alloy constituents and phenomenological coefficients. For instance, Muggianu's method [105] for a ternary system yields

$$G^{\text{ex}} = x_1 x_2 \sum_{i=0}^{n(1,2)} G_i^{12} (x_1 - x_2)^i + x_1 x_3 \sum_{i=0}^{n(1,3)} G_i^{13} (x_1 - x_3)^i + x_2 x_3 \sum_{i=0}^{n(2,3)} G_i^{23} (x_2 - x_3)^i \quad (5.2)$$

Here x_i is the molar fraction and G_i^{jk} are the interaction parameters. The latter ones along with the Gibbs energies of the pure components are formulated as polynomial functions of temperature and stored in data bases. The thermodynamic data are assessed according to experimentally available data, e.g. enthalpies, heat capacities, transformation temperatures, and activities. This technique of data assessment, known as CALPHAD (Calculation of Phase Diagrams) method, has been extensively used in thermodynamic calculations [106]. In the present study calculations of equilibria in nickel-base alloys were carried out using the thermodynamic databases TTNI7. The commercial software package Thermo-Calc [81] was used to calculate the equilibrium state of a multicomponent system by minimizing its Gibbs energy. The software computes for a given alloy composition phase fractions and compositions of stable phases as well as transformation temperatures and other thermodynamic quantities, e.g. chemical potentials and activities.

5.2 Diffusion calculations

The rate of phase transformations in solids is often controlled by diffusion processes. To build up an accurate model for describing processes of high-temperature oxidation involving multicomponent and multiphase alloys, kinetic factors have to be taken into account. To address this challenging problem, the commercial software package DICTRA (**D**iffusion **C**ontrolled phase **T**RAnsformation) [64] was developed in the 1990s. The program is coupled with the Thermo-Calc software, which provides the necessary thermodynamic data for calculation of interdiffusion coefficients and phase equilibria. Additionally, it contains kinetic data for atomic mobility of the elements in multicomponent solutions. The kinetic data needed to calculate the multicomponent diffusion coefficients are stored in the form of mobilities of the elements i :

$$M_i = \frac{M_i^0}{RT} \exp\left(\frac{-Q_i}{RT}\right) \quad (5.3)$$

where M_i^0 is the frequency factor, Q_i the activation enthalpy, R the gas constant and T the absolute temperature. The flux of a component k in a direction z for an isothermal, isobaric single-phase binary alloy is given by Fick's first law

$$J_k = -D_k \frac{\partial C_k}{\partial z}. \quad (5.4)$$

Here D_k is the phenomenological diffusion coefficient; C_k is the concentration of component k and z is the distance. The original diffusion law defines the concentration gradient as a driving force for diffusion. Nowadays it is generally argued that the gradient of the chemical potential/activity is the true driving force. However, concentration gradients are still considered as a valid approximation for many materials because they are more convenient to handle. Additionally, it was found that in multicomponent systems the diffusion of a component depends not only on its own chemical potential gradient but can also be affected by the chemical potential gradient of any other alloy constituent. Therefore a multicomponent extension of Fick's first law was proposed by Onsager [107], who established a linear relationship between a flux and a thermodynamic driving force in the system

$$J_k = - \sum_{i=e}^n L_{ki} \frac{\partial \mu_i}{\partial z} \quad (5.5)$$

Here μ_i is the composition dependent chemical potential of an element i , L_{kj} is a phenomenological coefficient which is associated with the mobilities M_i of the individual species

$$L_{ki} = - \sum_{i=e}^n (\delta_{ik} - C_k V_i) \cdot C_i y_{va} M_i \quad (5.6)$$

where δ_{ik} is the Kronecker delta, i.e. $\delta_{ik} = 1$ when $j = k$ and $\delta_{ik} = 0$ otherwise. C_k and C_i are the concentrations of alloy constituent k and i , V_i is the partial molar volume of element i , and y_{va} is the fraction of vacant lattice sites in the sublattice. For reasons of practical convenience Equation (5.5) is re-arranged in terms of the concentration gradients

$$J_k = - \sum_{j=1}^n D_{kj} \frac{\partial C_j}{\partial z} \quad (5.7)$$

with

$$D_{kj} = - \sum_{i=e}^n L_{ki} \frac{\partial \mu_i}{\partial C_j} \quad (5.8)$$

Together with Fick's second law, i.e. continuity equation

$$\frac{\partial c_k}{\partial t} = - \frac{\partial J_k}{\partial z} \quad (5.9)$$

this gives a system of coupled partial differential equations which can be solved numerically to determine the flux of each component [108]. The software generates values of the concentration dependent interdiffusion coefficients using Equation (5.8) and the kinetic atomic mobility data stored in the mobility databases together with the thermodynamic factor $\frac{\partial \mu_i}{\partial C_j}$ calculated by Thermo-Calc. The DICTRA software then solves the diffusion equations

in the region in which the matrix phase is present. Several grid-points are set in the region in which diffusion processes are simulated. The software solves the diffusion equations on each

grid-point in the vicinity of the respective grid-point. The calculations are performed repeatedly on each grid-point for each time-step until the set exposure time t is reached. The calculation algorithm is summarized in Figure 5.1. The calculation yields molar/weight fractions and/or concentration profiles after different times. The kinetic data used in the present investigation were taken from the MOBNI1 (nickel-base alloys) database.

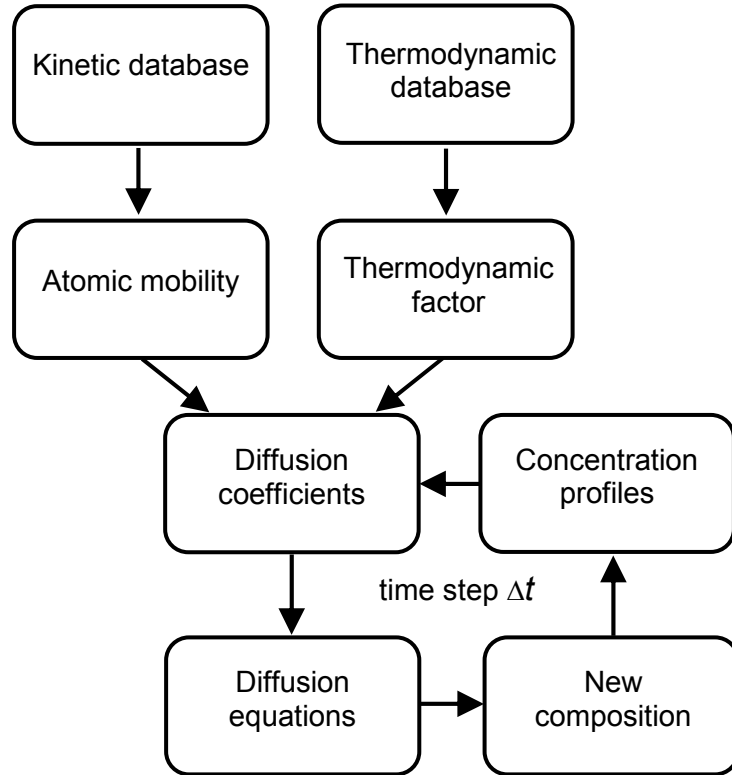


Figure 5.1: Algorithm of the diffusion calculation in DICTRA [64]

5.3 Diffusion in alloys with dispersed precipitates

Most commercial alloys are multiphase materials which may contain several precipitate phases in their microstructure. A model for diffusion in multiphase dispersed systems was developed by Engström *et al.* [109] and implemented in DICTRA. A simplified representation of diffusion in a system with precipitate phases is shown in Figure 5.2.

The precipitate phase is present in form of dispersed particles in a continuous matrix phase in which a gradient in composition exists. This model is based on the assumption that thermodynamic equilibrium prevails locally in each grid-point and that diffusion inside the precipitate phase can be neglected. Diffusion is assumed to occur only in the matrix phase. The dispersed phase particles act as a point sink or source for solute atoms. The amount of the dispersed phase and its composition is calculated assuming local thermodynamic equilibrium at a number of grid-points set in the simulation region.

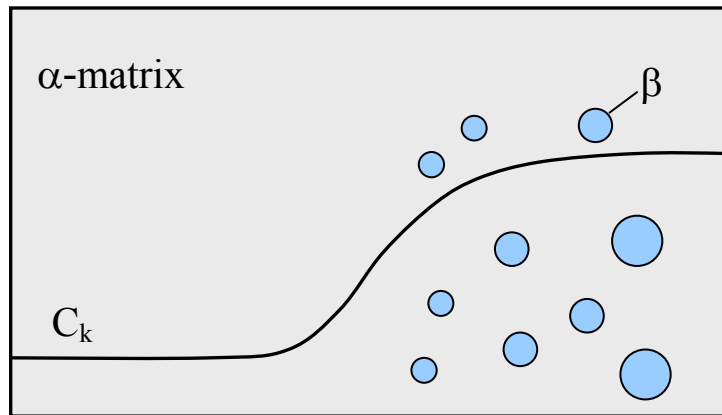


Figure 5.2: Schematic representation of diffusion in alloy containing dispersed precipitates phases immersed in a single-phase matrix phase [110]

To take into account the increase of the diffusion path through the precipitates, the diffusivity of each component is multiplied by a labyrinth factor. For instance, Engström *et al.* [110] found that a labyrinth factor of v^2 , where v is the volume fraction of the matrix phase, was a reasonable approximation even for systems with high fractions of precipitates. For a time step t the diffusion equations for the matrix phase are solved as described in the previous section. After each time step, equilibrium in each grid point is calculated using Thermo-Calc data, and the new phase compositions are obtained. The matrix composition changes and the software can solve the diffusion equations for this new matrix composition. The calculation procedure (see Figure 5.3) is re-iterated until the set exposure time is reached. Thus the DICTRA software allows prediction of the composition and the amount of each phase present in the alloy varying with time along the space coordinate.

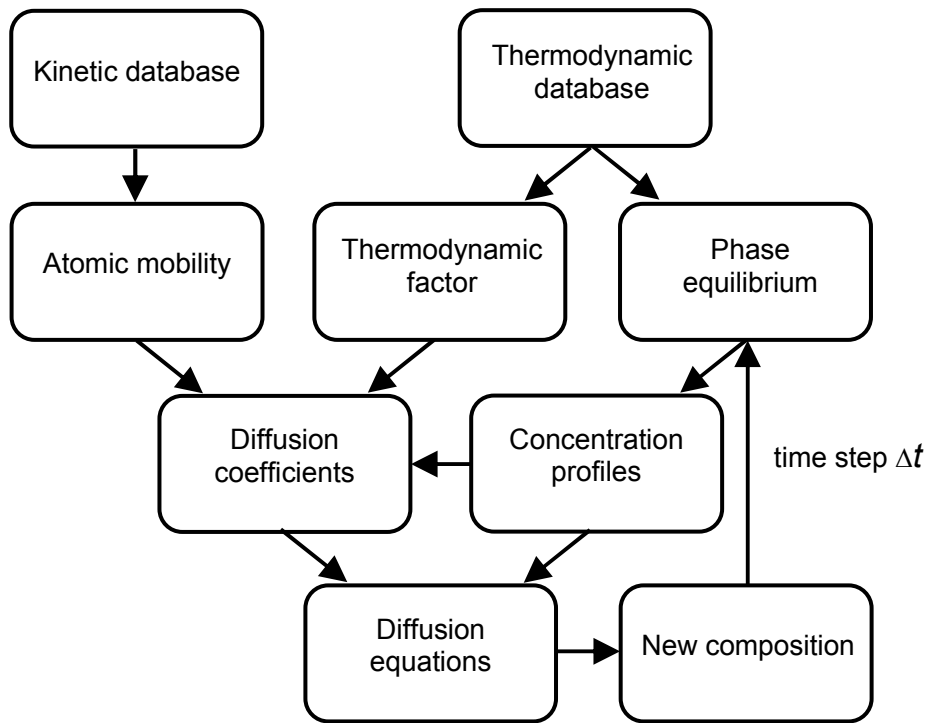


Figure 5.3: Algorithm of the diffusion calculation in DICTRA, assuming a dispersed precipitate phase in equilibrium with the alloy matrix

6. Subscale phase transformation processes in alloy 625

6.1 Phase equilibria in alloy 625 at 900 and 1000°C

Figure 6.1 shows the microstructures of alloy 625 after exposure for 1000 hours at 1000 and 900°C. At the latter exposure temperature the alloy formed two types of precipitates whereas only one precipitate phase was present at 1000°C. According to the EDX point analyses of the 900°C specimen (Figure 6.2), one precipitate type is rich in nickel and niobium, the other is rich in nickel, molybdenum and silicon.

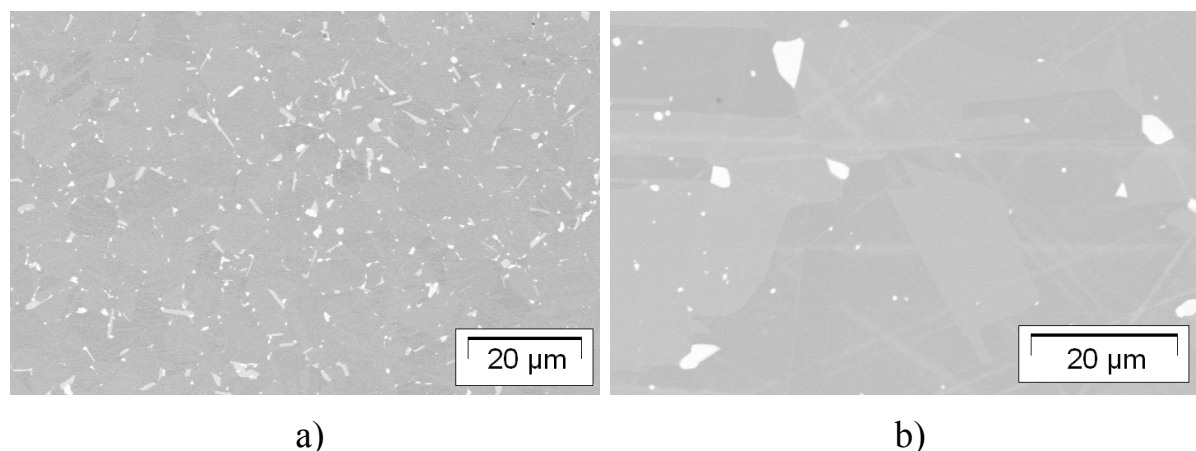


Figure 6.1: SEM images of the alloy 625 microstructure after 1000 h exposure at 900°C (a) and 1000°C (b)

The EDX analysis for the 1000°C specimen revealed only a single precipitate type which was rich in nickel, molybdenum and silicon. Additionally, the WDX mappings showed these precipitates to contain carbon. Simulation of the phase equilibria using Thermo-Calc [81] for the alloy 625 composition given in Table 4.1 yields the following stable phases at 1000°C: Ni-rich γ -FCC and Mo-rich carbide M_6C whereby M is mainly Mo and Ni. The latter is in agreement with the experimental finding; however, an important difference between experiment and calculation was found, i.e. the Thermo-Calc calculation substantially underestimated the amount of silicon dissolved in the carbide phase (Figure 6.2b).

The Ni-Mo(W) rich M_6C carbides [111] were described previously for numerous Mo and/or W-rich austenitic steels [112, 113] and nickel-base alloys [114-116], including alloy 625. In the studied temperature range of 800-1100°C most authors emphasize the stabilizing effect of silicon on the M_6C carbide at 800°C, Si-concentrations as high as 12 at% in the carbide phase were found e.g. by EPMA and TEM studies [115].

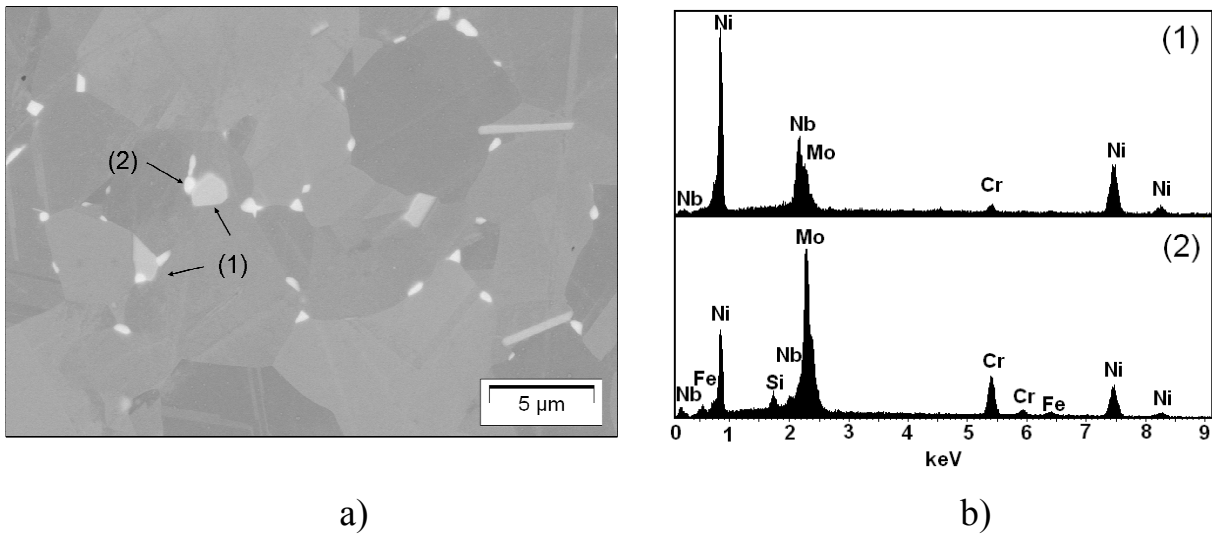


Figure 6.2: SEM/BSE image of precipitate phases in alloy 625 after 100h exposure at 900°C and EDX spectra (accelerating voltage 15 kV) of points marked in Figure (a)

At 900°C the Thermo-Calc result revealed presence of the Nb-rich δ -Ni₃Nb phase parallel with M₆C (Figure 6.3 and Table 6.1). By EDX spectroscopy a composition very close to Ni₃Nb was identified with niobium being partially substituted by molybdenum and chromium, i.e. 2.0 and 0.9 at% respectively, compared to 3.7 and 3.9 at% given by Thermo-Calc. The experimentally determined nickel content in the δ -phase was close to 75 at%, in agreement with the phase stoichiometry. Weak reflexes, which were attributed to the δ -phase, were found in the XRD pattern of the 900°C specimens confirming the presence of the δ -Ni₃Nb phase in the alloy at the respective temperature. Additional XRD reflexes were too weak to allow unequivocal identification of the additional phase(s) present in the microstructure.

The second phase present, next to the δ -phase after 900°C exposure is rich in molybdenum and nickel (Figure 6.2b). Additionally, it contains a small amount of chromium and minor amounts of niobium and silicon. Comparison of the measured data with the Thermo-Calc calculation suggests the precipitate to be chromium and silicon containing M₆C, as found at 1000°C. This type of precipitate was, next to δ -Ni₃Nb, previously observed in alloy 625 in the temperature range 800-900°C by several authors [7, 117, 118]. In the EDX spectra the concentrations of the metallic constituents of the Ni/Mo-rich precipitates were quite similar to those found at 1000°C, however, no presence of carbon could unequivocally be identified by WDX analysis. As carbon solubility in typical nickel base alloys generally decreases with

decreasing temperature, slightly larger amounts of the M₆C phase would be expected to form at 900 than at 1000°C.

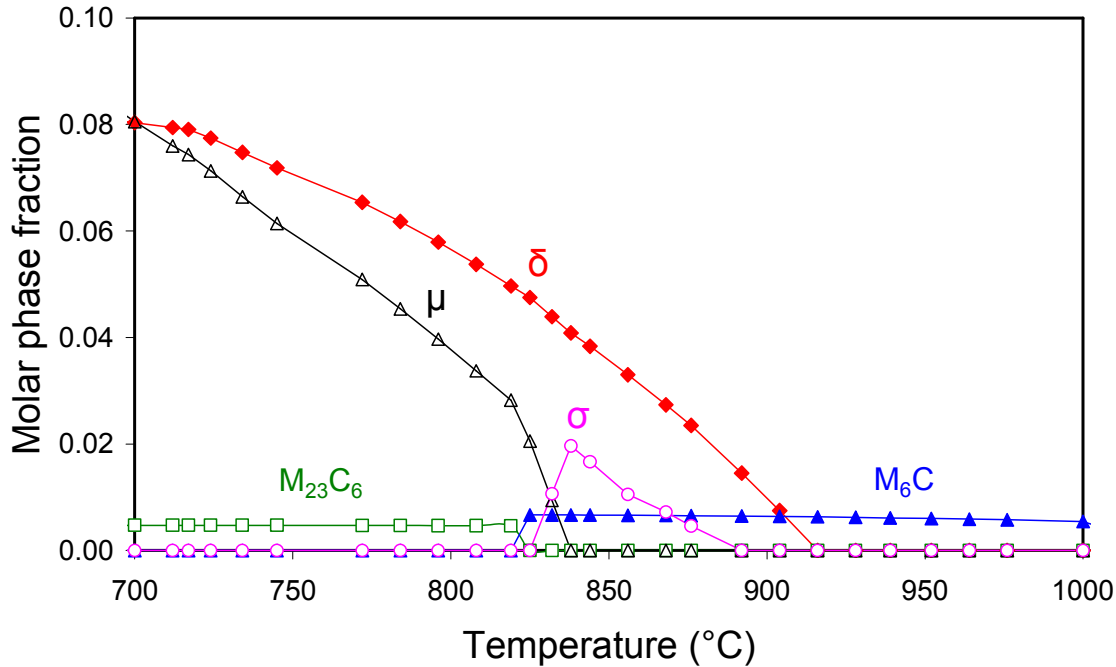


Figure 6.3: Temperature dependence of phase composition in alloy 625 calculated in Thermo-Calc using the TTNI7 database

This would agree with the Thermo-Calc calculations (Figure 6.3), predicting that M₆C carbide transforms into M₂₃C₆ at temperatures beneath approximately 820°C confirming results in reference [7] showing M₂₃C₆ carbide to be present after heat treatment at 720°C. However, because the own WDX analyses did not allow detecting presence of carbon in the Ni/Mo-rich compound at 900°C, in the following modeling sections (e.g. section 6.3), calculations of the subscale phase transformations for specimens during 900°C oxidation were carried out distinguishing between an alloy with and without presence of M₆C in the alloy microstructure.

The X-ray diffraction analysis carried out on the abraded alloy surface after 1000h heat treatment at 900°C revealed only weak reflexes which could be attributed to the orthorhombic phase δ-Ni₃Nb (Figure 6.4). The XRD pattern was not conclusive for unequivocal identification of other phases at 900°C apparently due to their very small amounts in the alloy microstructure at this temperature.

Table 6.1: Calculated compositions of stable phases in alloy 625 using Thermo-Calc in wt%

Phase	Ni	Cr	Mo	Nb	Fe	Si	C
1000°C							
FCC	62.48	21.48	8.8	3.48	3.51	0.25	5×10^{-3}
M ₆ C	26.3	16.56	48.5	5.11	0.84	1.2×10^{-2}	2.68
900°C							
FCC	62.46	21.7	8.76	3.29	3.54	0.25	1.8×10^{-3}
M ₆ C	25.78	15.82	49.55	5.2	0.98	0.01	2.67
Delta	64.66	0.6	2.96	31.62	0.16	0	0
850°C							
FCC	61.85	23.01	8.94	2.27	3.66	0.26	1×10^{-3}
M ₆ C	25.82	15.59	50.4	4.3	1.10	0.01	2.67
Delta	64.71	0.5	2.93	31.66	0.14	0	0
Sigma	28.83	34.3	33.62	0	3.23	3×10^{-3}	0
800°C							
FCC	62.48	23.76	7.87	1.75	3.83	0.28	6×10^{-4}
M ₂₃ C ₆	7.24	67.4	19.79	4×10^{-5}	0.43	0	5.11
Delta	64.87	0.43	2.86	31.73	0.11	0.28	0
Mu-phase	28.3	22.95	47.6	0.13	0.98	4×10^{-3}	0

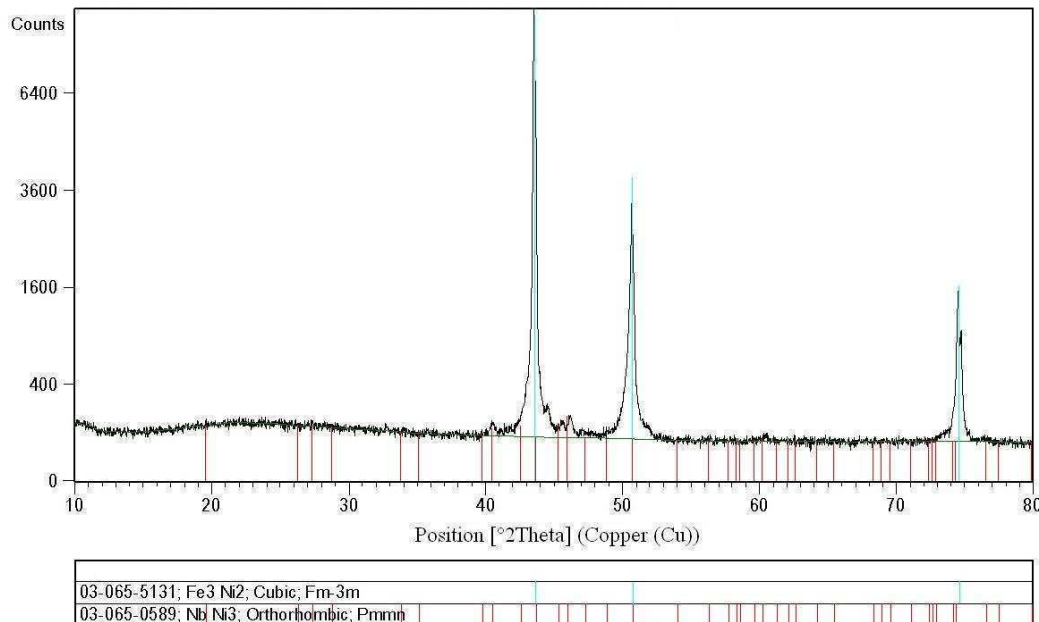


Figure 6.4: XRD pattern of alloy 625 specimen after 1000h exposure at 900°C. The oxidation affected layer was abraded to reach the original alloy microstructure, not affected by oxidation

6.2 Oxidation behavior at 900°C

Figure 6.5 shows weight change data during discontinuous oxidation at 900°C in air and Ar–4%H₂–2%H₂O. The formed surface oxide scale nearly exclusively consists of chromia (Figure 6.6) and obeys a near parabolic time dependence of the oxide thickening.

The scaling rate of the thinner specimens (0.3 mm) was slightly higher than that of the thicker ones and the specimens exposed in Ar–4%H₂–2%H₂O formed smoother and thicker scales compared to those grown during exposure in air. Both observations are in agreement with previous results related to oxidation of NiCr-base alloys [27, 99]. Minor amounts of internal aluminium oxide precipitates are formed which were mainly present at the alloy grain boundaries (Figure 6.6).

Figure 6.6 clearly reveals after 900°C exposure in both test gases a subscale zone in which the initially present precipitates are dissolved. After 1000h exposure this zone has a width of approximately 60 µm.

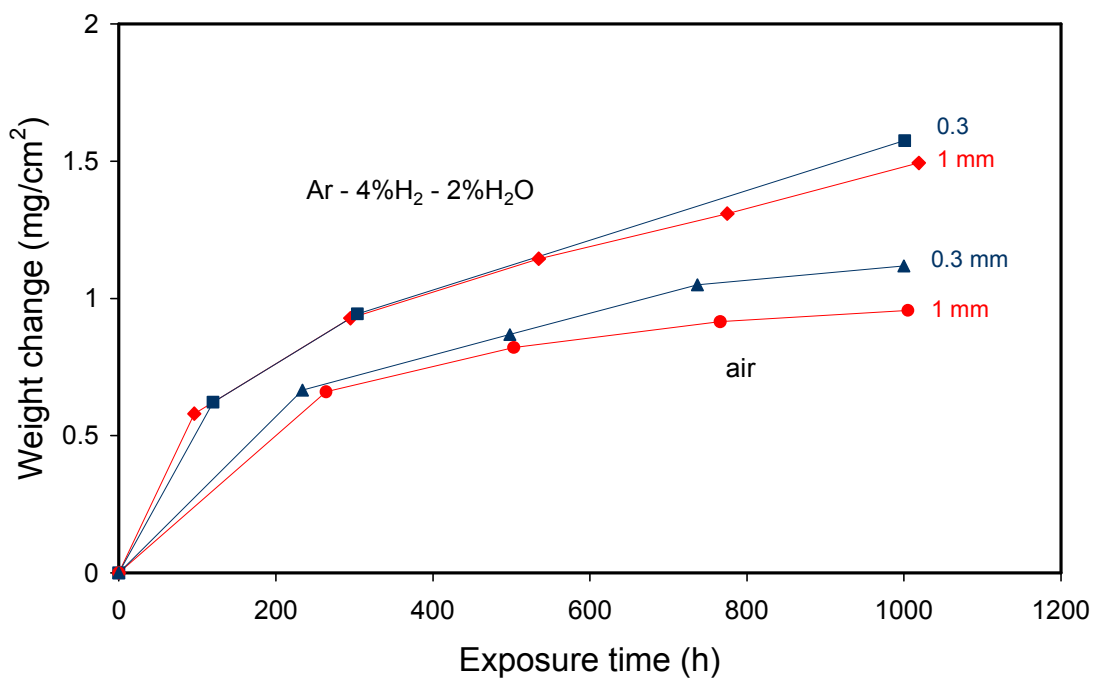


Figure 6.5: Weight change curves of alloy 625 (specimen thickness 1 and 0.3 mm respectively) during discontinuous oxidation at 900°C in air and Ar–4%H₂–2%H₂O

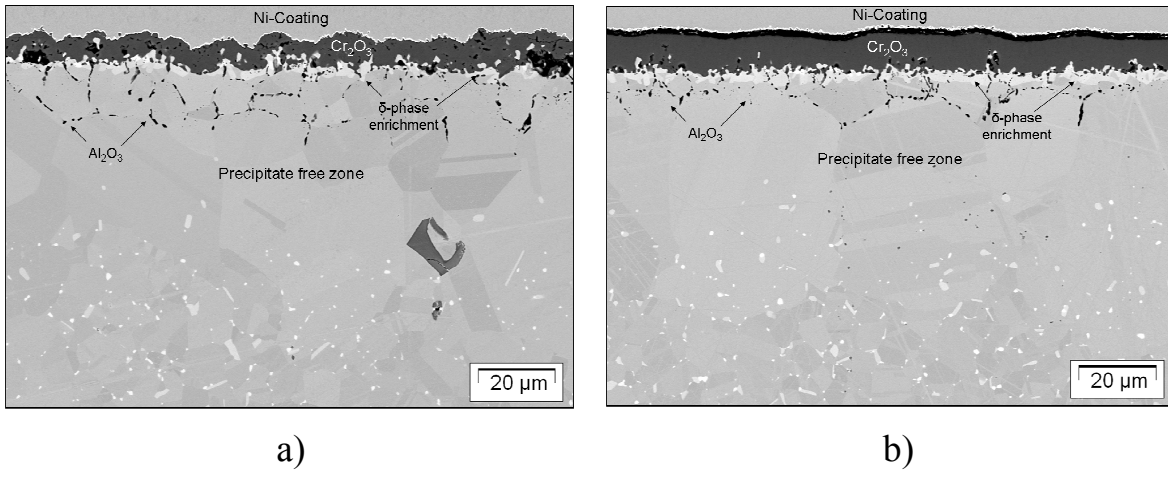


Figure 6.6: SEM images showing cross-sections of 1 mm thick alloy 625 specimens after 1000h exposure at 900°C in air (a) and Ar–4%H₂–2%H₂O (b)

The alumina precipitates at the alloy grain boundaries in the immediate vicinity of the oxide/alloy interface seem to stabilize the original alloy grain size underneath the oxide scale by hampering recrystallization of the originally small grains into larger ones which are found in the precipitate free zone. In spite of the dissolution of the Mo- and/or Nb- rich phases in this zone, an enrichment of the latter precipitates seems to occur in the immediate vicinity of the alloy/oxide interface. The EDX analyses in Figure 6.7 and comparison with the results in the previous section clearly show presence of δ-phase at the scale/alloy interface.

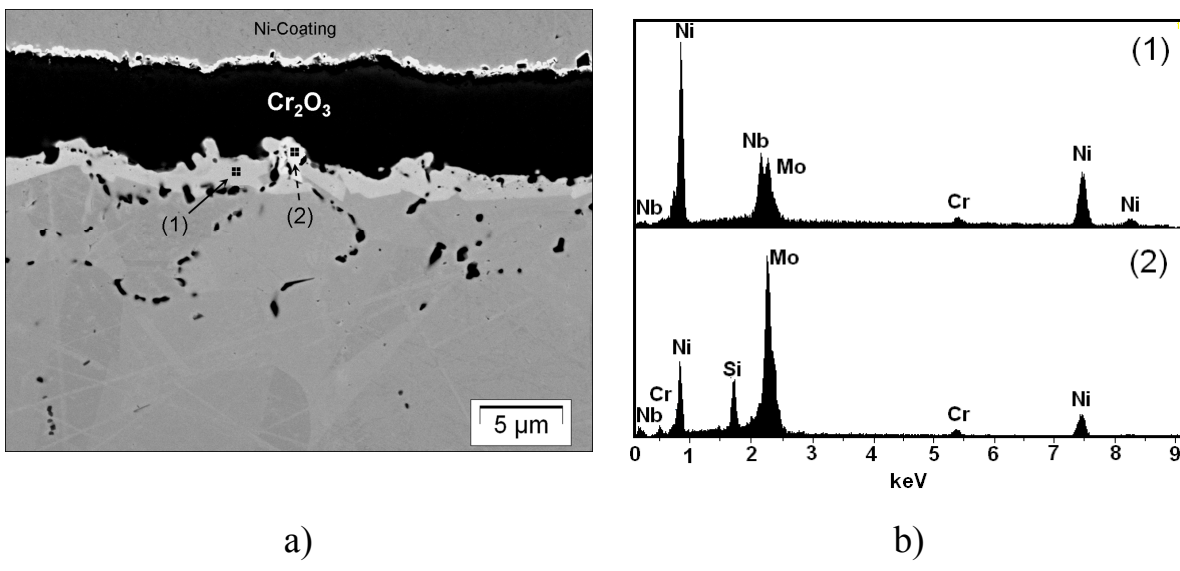


Figure 6.7: Formation of intermediate compounds near the scale/alloy interface after 300h exposure in Ar–4%H₂–2%H₂O at 900°C. EDX spectra (b) discussed in the text were measured on spots indicated by arrows; (1) – Nb-rich phase, (2) – Mo-rich phase

The GDOES profiles of the specimen after 1000h exposure in Ar–4%H₂–2%H₂O in Figure 6.8 show a zone with a width of approximately 60 μm in which niobium is depleted compared

to its initial concentration in the alloy, however, in parallel, strong niobium enrichment prevails in the immediate vicinity of the alloy/oxide interface.

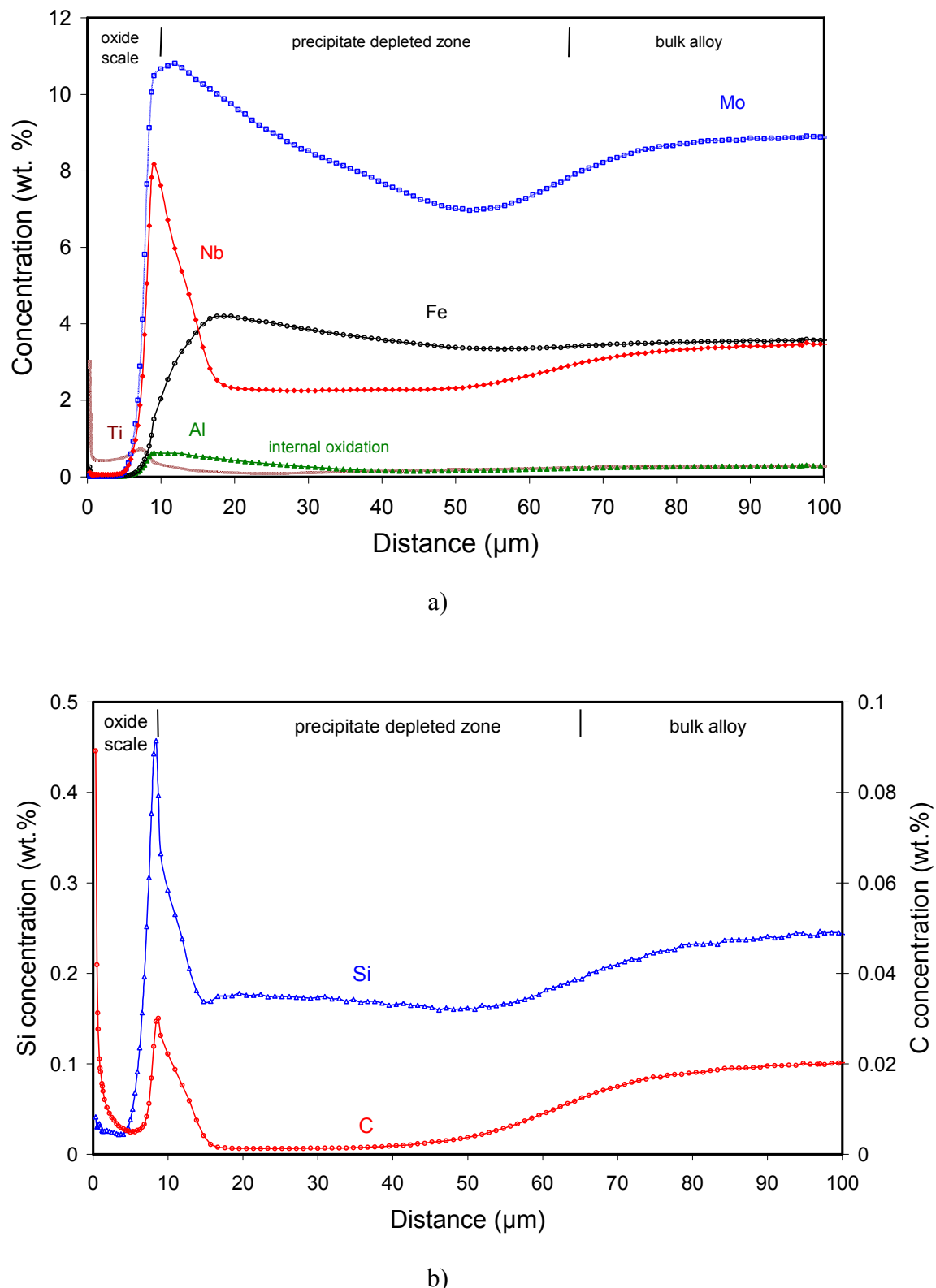


Figure 6.8: GDOES depth profiles of alloying elements in 1 mm thick alloy 625 specimen after 1000h oxidation in Ar-4%H₂-2%H₂O at 900°C

The EDX line scans from the bulk alloy towards the scale/metal interface in Figure 6.9 show clearly that subscale depletion also occurs for chromium to a similar depth as found for niobium. For molybdenum a similar but less pronounced depletion/enrichment profile occurs as for niobium. Also carbon and silicon tend to become enriched in the vicinity of the alloy oxide interface.

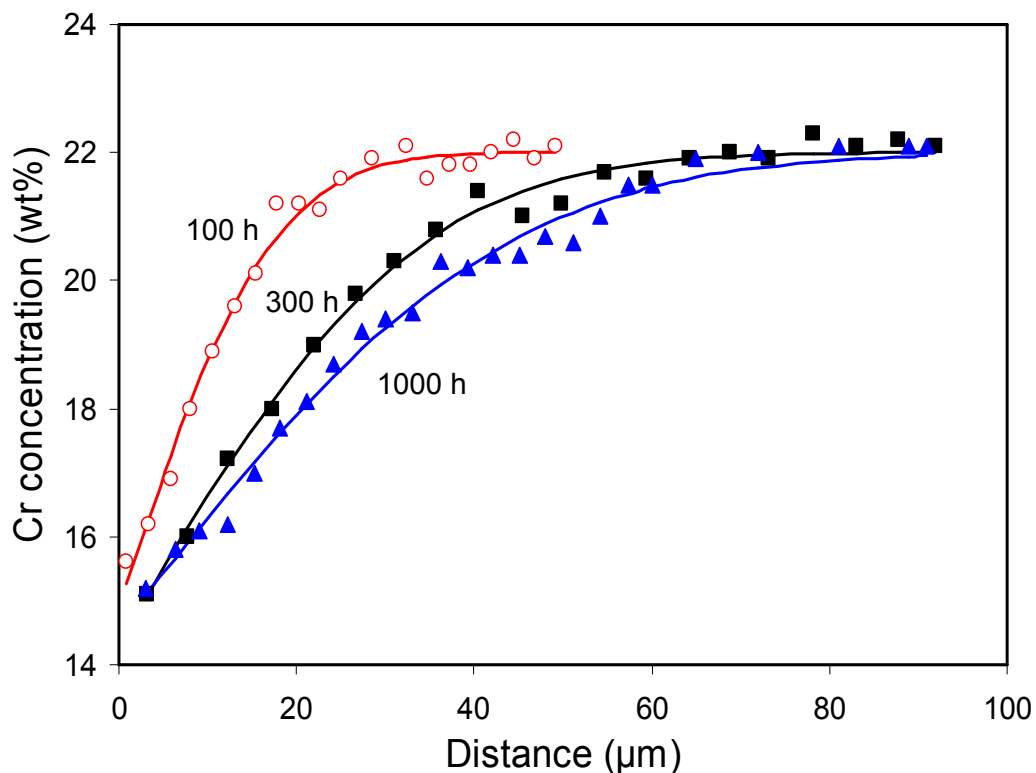


Figure 6.9: Chromium concentration profiles in alloy 625 after oxidation in air at 900°C measured by EDX spectroscopy (dots) compared with calculated values (lines) using classical Wagner's theory for single-phase binary alloy (Equation 2.14) [29]. The curves were calculated using $k_p = 8 \times 10^{-18} \text{ m}^2 \text{s}^{-1}$ and $D_{Cr} = 2.5 \times 10^{-16} \text{ m}^2 \text{s}^{-1}$

The formation of the $\delta\text{-Ni}_3\text{Nb}$ precipitates beneath the chromia scale was confirmed by the XRD analysis carried out on the oxidized specimen surface. Apart from the strong reflexes of chromia and the $\gamma\text{-FCC}$ nickel-rich matrix phase, well discernable $\delta\text{-Ni}_3\text{Nb}$ reflexes could be unequivocally identified in the XRD pattern in Figure 6.10.

A similar Subsurface Phase Enrichment (abbreviated in the present study as SPE) has been observed by other authors in a number of Ni-base alloys; however, as far as known to the

author, no explanation for this effect has been presented. Moddeman et. al [119] observed niobium enrichment beneath the oxide scale in a Nb-containing superalloy INCONEL 718 after a short term heat treatment at 1000°C using XPS/AES depth profiling. Based on the XPS chemical shift of the 3d-line of Nb, the authors came to the conclusion that unoxidized Ni₃Nb particles existed in the oxide layer. A niobium enrichment at the oxide/alloy interface resulting in the precipitation of the Ni₃Nb phase in INCONEL 718 after 48 h oxidation in air at 900°C was also found by Delaunay et al. [120]. The EDX mappings in reference [121] suggest a similar effect to occur in case of INCONEL 625 after 1000h of cyclic oxidation in air at 900 and 1000°C, however, no details on the microstructural features were given by the authors.

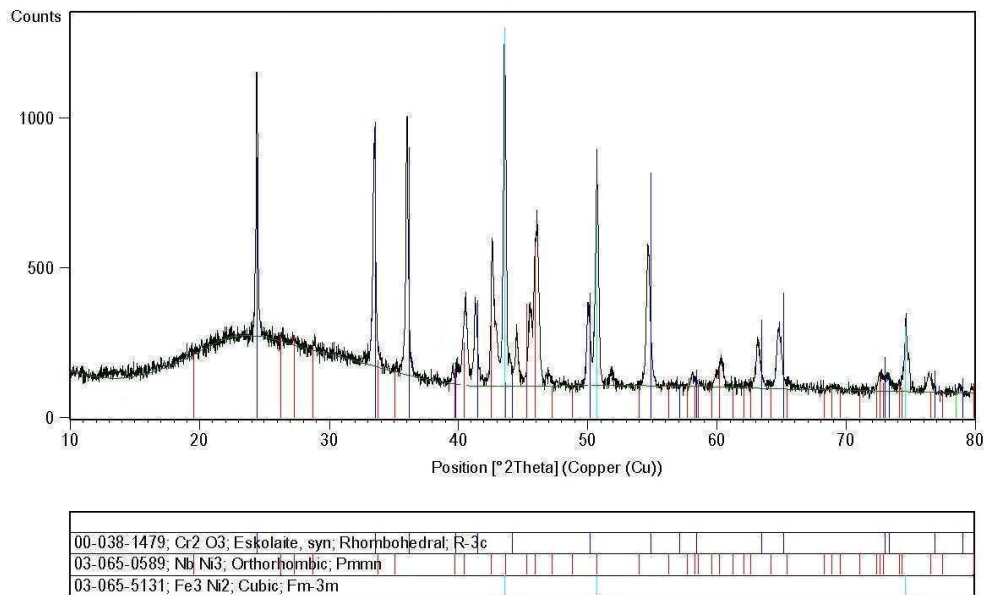


Figure 6.10: XRD pattern of oxidized 1mm tick alloy 625 specimen after 1000h exposure at 900°C in air

6.3 Modeling depletion/enrichment processes at 900°C

The most striking effect in the above described subscale phase changes in the alloy is the formation of a precipitate depleted zone with a width of approximately 60 µm in parallel with a strong enrichment of δ-phase in the immediate vicinity of the scale/alloy interface.

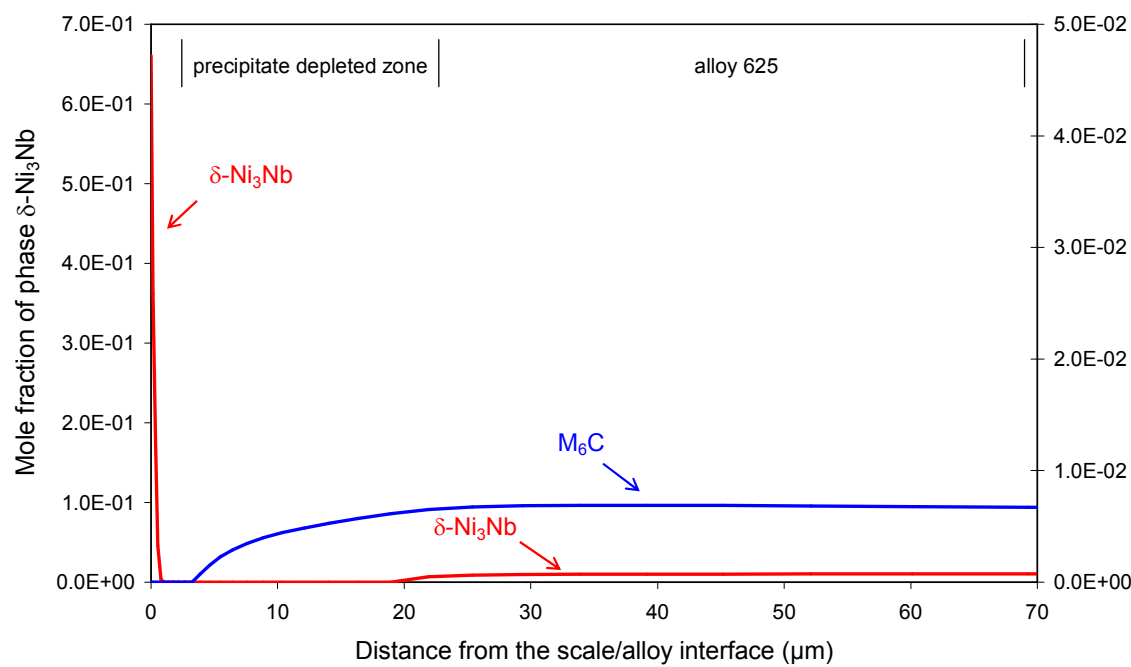
Considering the composition of the δ -phase, it is apparent that the main requirement which must be fulfilled to form precipitates of this phase near the scale/alloy interface is a strong driving force for niobium to diffuse from the bulk alloy towards the scale/alloy interface. Apparently, the establishment of such a driving force must be indirectly caused by the subscale depletion of chromium because this element is the only significant metallic constituent in the surface oxide scale.

To establish, whether the formation of niobium rich δ -phase is indeed only a result of the oxidation-induced subscale chromium depletion, a test with the finite-difference software DICTRA [64] was carried out. An “imaginary diffusion couple” was used as input whereby one part of the couple was alloy 625 and the other part was vacuum. Then the boundary conditions were set in such a way that a preset chromium flux occurs from the alloy in direction of the vacuum. The chromium flux, simulating the chromium loss as a result of surface oxide formation, was derived from the measured parabolic oxidation rate for the chromia growth to be

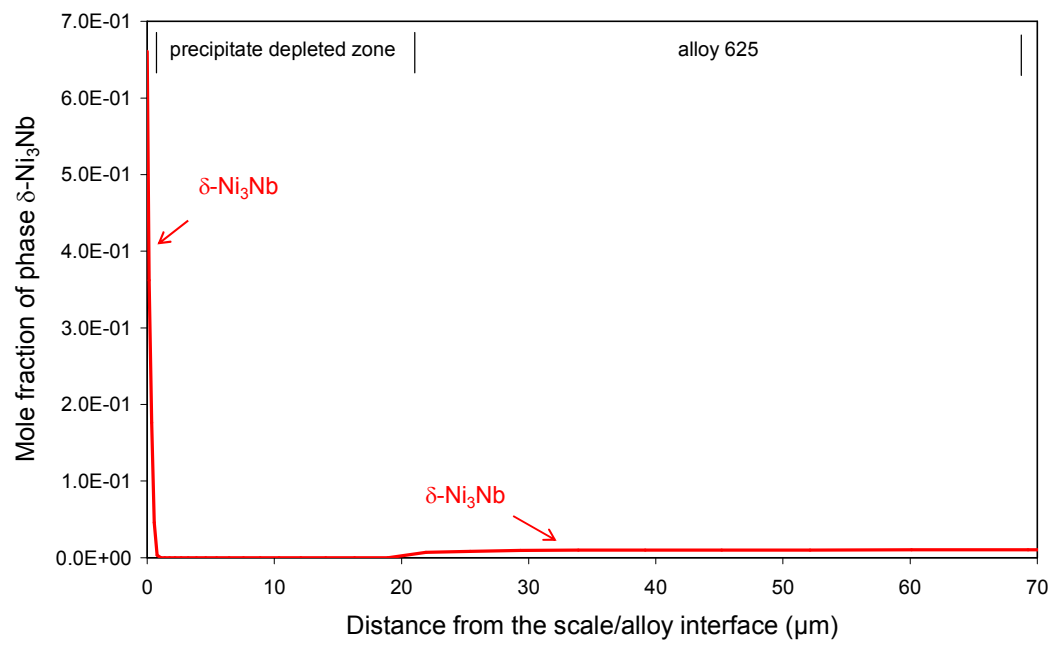
$$J = \frac{(2k_p)^{1/2}}{\bar{V}_{Cr_2O_3}} t^{-1/2} \quad (6.1)$$

in which J is the flux of chromium in $\text{mol}\cdot\text{cm}^{-2}\cdot\text{s}^{-1}$, k_p the parabolic oxidation rate constant in $\text{cm}^2\cdot\text{s}^{-1}$ (see e.g. Equation (2.10)), $\bar{V}_{Cr_2O_3}$ the molar volume of chromium oxide in $\text{cm}^3\cdot\text{mole}^{-1}$, and t the time in s.

The calculated phase distribution in the subsurface depletion layer after an oxidation time of 100 hours is shown in Figure 6.11. For the reason mentioned in the previous section, the calculation was carried out with and without accounting for presence of the M_6C phase in the alloy microstructure. The result shows formation of a precipitate free zone, whereby, for the case that M_6C formation is taken into account, the depth of δ -phase depletion is larger than that of M_6C . In parallel, a strong enrichment of δ -phase occurs in the immediate vicinity of the scale/alloy interface in agreement with the experimental observations described in the previous section. This δ -phase enrichment occurs independent of the fact whether M_6C is accounted for or not.



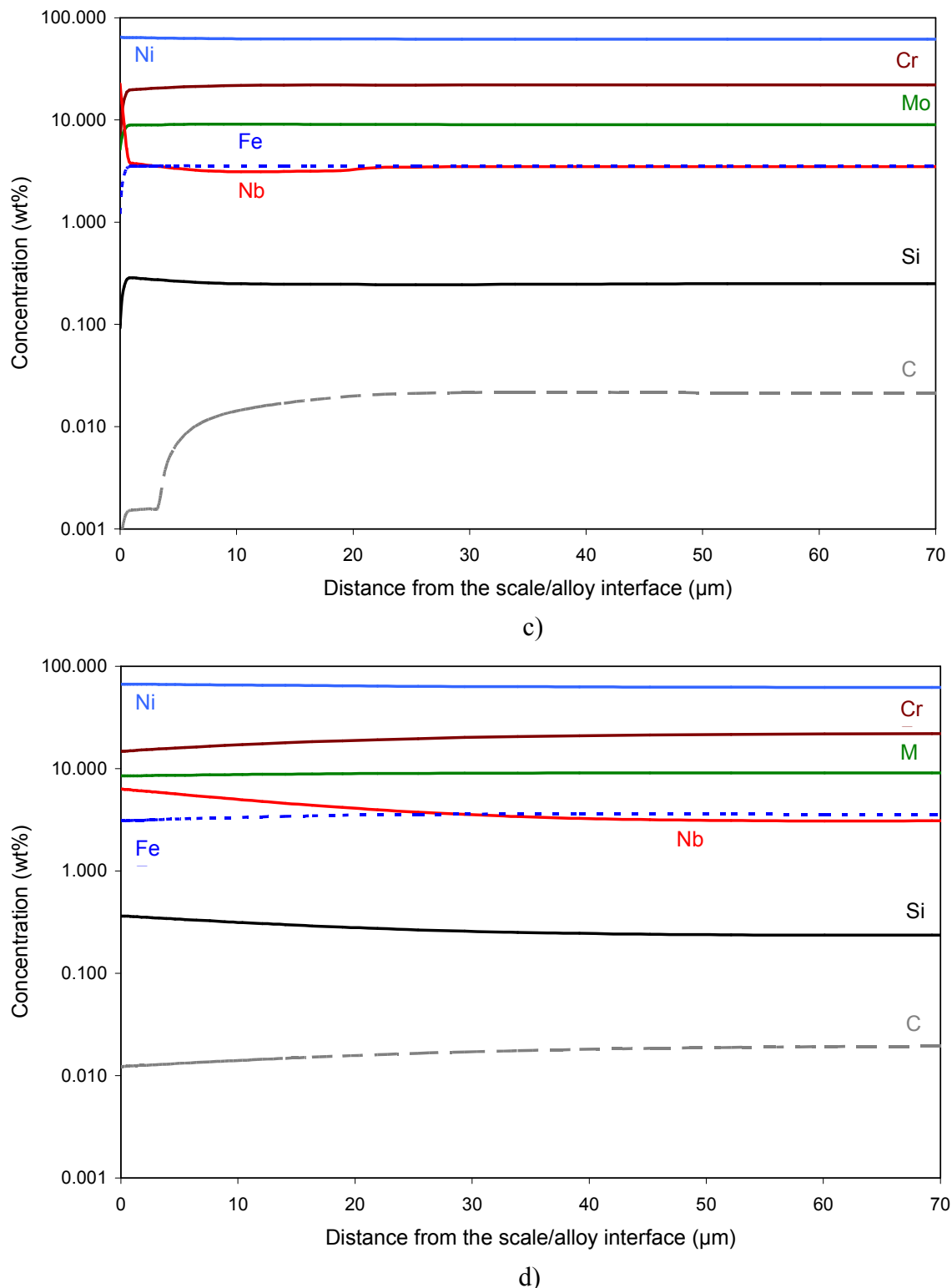
a)



b)

Figure 6.11: Phase distribution in surface-near region of alloy 625 specimen after 100h oxidation at 900°C calculated in DICTRA using oxidation rate from Figure 6.5; (a) taking formation of $M_6\text{C}$ into account, (b) ignoring $M_6\text{C}$ formation. Corresponding concentration profiles of alloying elements calculated taking into account phase formation (c) and ignoring it (d). As input parameter was taken parabolic rate constant $k_p = 9 \times 10^{-18} \text{ m}^2 \text{s}^{-1}$

continued Figure 6.11



A major drawback of the DICTRA modeling is that the programme assumes diffusion only to occur in the γ -nickel base alloy matrix, not in the δ - and/or M_6C -phase. This has as result that after longer exposure time, i.e. when the calculated amount of the δ -phase at the scale/alloy interface becomes very substantial, the amount of γ -phase in which diffusion occurs is so strongly reduced, that diffusion eventually nearly ceases which is, of course, not in agreement with reality. This means that the DICTRA software does not allow an accurate prediction of the subscale concentration profiles after very long term exposures. The calculated results in Figure 6.11, however, clearly reveal that the experimentally observed enrichment of δ -phase in the immediate vicinity of the scale/alloy interface occurs as a natural result of the oxidation-induced chromium depletion.

At first sight the calculated results in Figure 6.11 may seem surprising, because an obvious question is why chromium depletion leads to formation of a wide δ -phase depleted zone although this precipitate present in the initial alloy microstructure does not contain chromium as the main metallic constituent. A second question which arises is why Nb enrichment in the immediate vicinity of the oxide/alloy interface occurs solely as a result of oxidation-induced chromium depletion?

If chromium is depleted, the concentration of the other elements (mainly Ni, Nb, Mo) in the depletion zone should increase because the sum of all elements naturally will remain 100%. The GDOES profile of niobium (Figure 6.8) exhibits a sharp increase of the Nb concentration (more than 8 wt %) at the oxide/metal interface which obviously cannot be explained by mere chromium depletion. Even if the total chromium content in alloy 625 (approx. 22 wt %) would imaginarily be removed from the alloy, the Nb concentration would only rise to approximately 4.5 wt %. Since the concentration of niobium underneath the chromia scale is doubled compared to the initial Nb concentration in the alloy, diffusion of the element from the bulk alloy obviously occurred. The formation of the niobium rich δ -phase in the vicinity of the oxide/alloy interface would thus require niobium diffusion from a region of low towards a region of high concentration, i.e. a niobium flux against its concentration gradient.

Such a so-called uphill diffusion [122] would only be expected if the chemical potential of niobium in the bulk alloy would be higher than that near the oxide/alloy interface. From

diffusion theory [123], the flux J_k of species k can be explicitly defined as a function of the chemical potential gradient

$$J_k = -\frac{1}{\bar{V}_m} \cdot M_k x_k \frac{\partial \mu_k}{\partial z} \quad (6.2)$$

Here M_k is the mobility of species k , \bar{V}_m the molar volume, x_k the molar fraction of species k , μ_k the chemical potential, and z the spatial coordinate (in case of oxidation, distance from the oxide/alloy interface). If μ_{Nb} increases along the chromium depletion profile from the scale/alloy interface in direction of the bulk alloy (Figure 6.9), and thus the niobium flux will be negative, Nb will diffuse in the opposite direction down the activity gradient, i.e. towards the oxide/alloy interface. In other words, if μ_{Nb} would decrease with decreasing chromium content, niobium would be expected to diffuse towards the most chromium depleted site, i.e. the scale/alloy interface.

To check this possibility, Figure 6.12 shows the effect of chromium content in the base composition of alloy 625 on the chemical potential of the various alloying elements, using the database TTNI7 adapted to the Thermo-Calc software. The data clearly shows a strong influence of alloy chromium content on the chemical activity of niobium whereby decreasing chromium content decreases the niobium activity. A similar effect prevails for silicon but not for carbon.

This observation allows explaining the experimentally observed main oxidation-induced depletion/enrichment processes in the subsurface zone in the alloy. The chromium depletion due to oxide scale formation and growth results in a strong decrease of the niobium activity. If the chromium concentration falls below 18 wt %, the activity of niobium has decreased to such a low level that the δ -phase is no longer stable. This explains the formation of the observed δ -phase depleted subscale zone (Figure 6.7)

However, due to the established chromium-depletion-induced niobium activity gradient, diffusion of niobium occurs from the inner part of the chromium depletion zone towards the surface. This leads to such a strong niobium enrichment that in the area of the lowest chromium activity, i.e. in the immediate vicinity of the oxide/alloy interface, δ -phase

formation becomes favored. This precipitate formation will deplete niobium from the surrounding alloy matrix thereby further decreasing the niobium activity resulting in a sustaining of the driving force for diffusion of niobium towards the surface. These processes can at least qualitatively explain the experimental observations, i.e. an enrichment of the niobium rich δ -phase at the scale/alloy interface and beneath that a zone of approximately 60 μm (after 1000h exposure at 900°C) in which the δ -phase is strongly depleted.

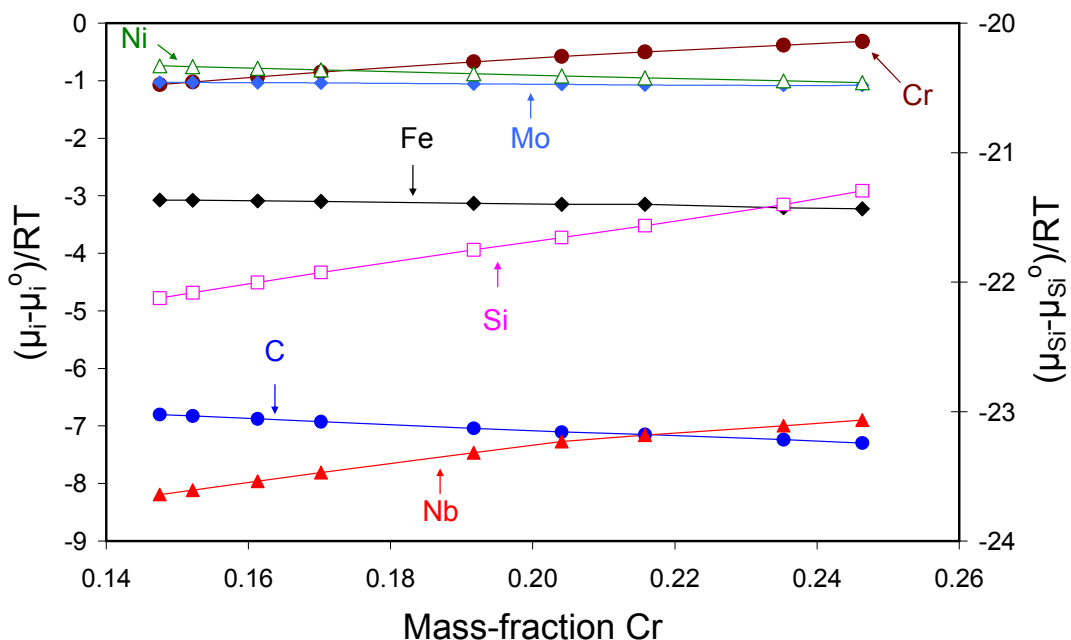


Figure 6.12: Chemical potentials of elements constituting alloy 625 at 900°C as a function of chromium content calculated in Thermo-Calc using the TTNI7 database

If formation of M_6C is taken into account (Figure 6.11b) also this precipitate tends to dissolve in the chromium depleted zone. However, the dissolution mechanism fundamentally differs from that for δ -phase. Weak enrichment of carbon underneath the oxide scale found in the GDOES profile (Figure 6.8) cannot be explained by means of chemical potentials since μ_{C} increases appreciably with decreasing chromium concentration (Figure 6.12).

Looking at the GDOES profiles one may notice that the area confined by the niobium peak underneath the oxide scale is commensurable with that confined by the Nb profile and the line drawn at the initial niobium concentration in the alloy (3.5 wt%). In other words, the amount of depleted niobium from the precipitate free zone is approximately equal to the amount of niobium enriched beneath the oxide scale. In case of carbon, the depleted zone in Figure 6.8b

looks much broader than the area confined under the carbon peak. Thus, carbon seems to diffuse backwards from the oxide/alloy interface into the bulk alloy thus forming the carbide depleted zone, as will be more extensively explained in the next section. Nevertheless, the slight carbon enrichment at the oxide/alloy interface may have a “mechanical” explanation: small carbide particles were captured as small inclusions (see Figure 6.7) by the growing δ - Ni_3Nb layer.

6.4 Depletion/enrichment processes at 1000°C

Figure 6.13 shows the weight change data for alloy 625 during oxidation at 1000°C in air and in Ar–4%H₂–2%H₂O. The oxidation process is similar to that described in the previous sections for 900°C with the exception that substantial oxide spallation occurs at 1000°C for the 1.0 mm thick specimen oxidized in air. This phenomenon was reproducible and has been previously found for alloy 625 oxidized under slightly different experimental conditions [124]. Also, the better adherence of chromia scales formed in Ar-H₂-H₂O based gases compared to that of air formed scales is in agreement with previous observations [125].

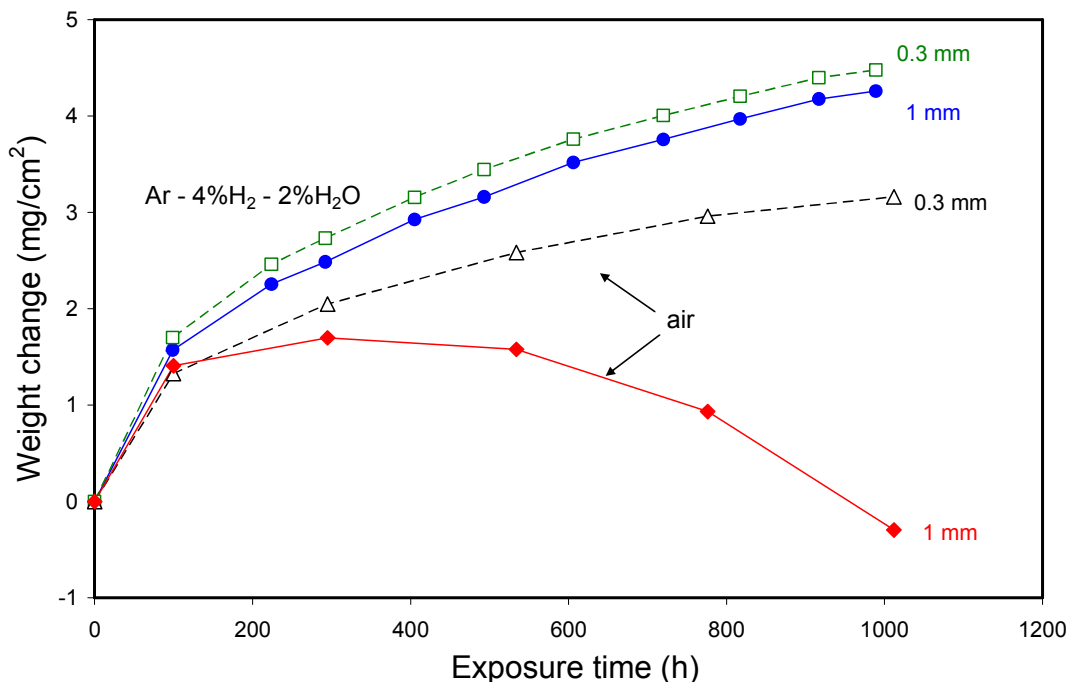


Figure 6.13: Weight change curves for alloy 625 specimens of different thicknesses (0.3 and 1 mm) during oxidation at 1000°C in air and in Ar–4%H₂–2%H₂O

During oxidation at 1000°C the oxide scale formation is qualitatively similar to that at 900°C, i.e. the surface scale consists virtually exclusively of chromia and only minor internal oxidation of aluminium is found (Figure 6.14). Although the thinner specimen of alloy 625 (0.3 mm) showed no significant mass loss in the weight change curve (Figure 6.13), cracks parallel to the scale/alloy interface are present in the outer part of the chromia layer (Figure 6.14a) whereas well discernable cracks are found in the scale formed on the thick specimen (Figure 6.14b). Conversely, the oxide scale grown in Ar–4%H₂–2%H₂O is thick and smooth (Figure 6.14c) and shows no signs of spallation after 1000h exposure at 1000°C. Therefore, data determined for the specimens exposed in this environment were used for the further modeling calculations.

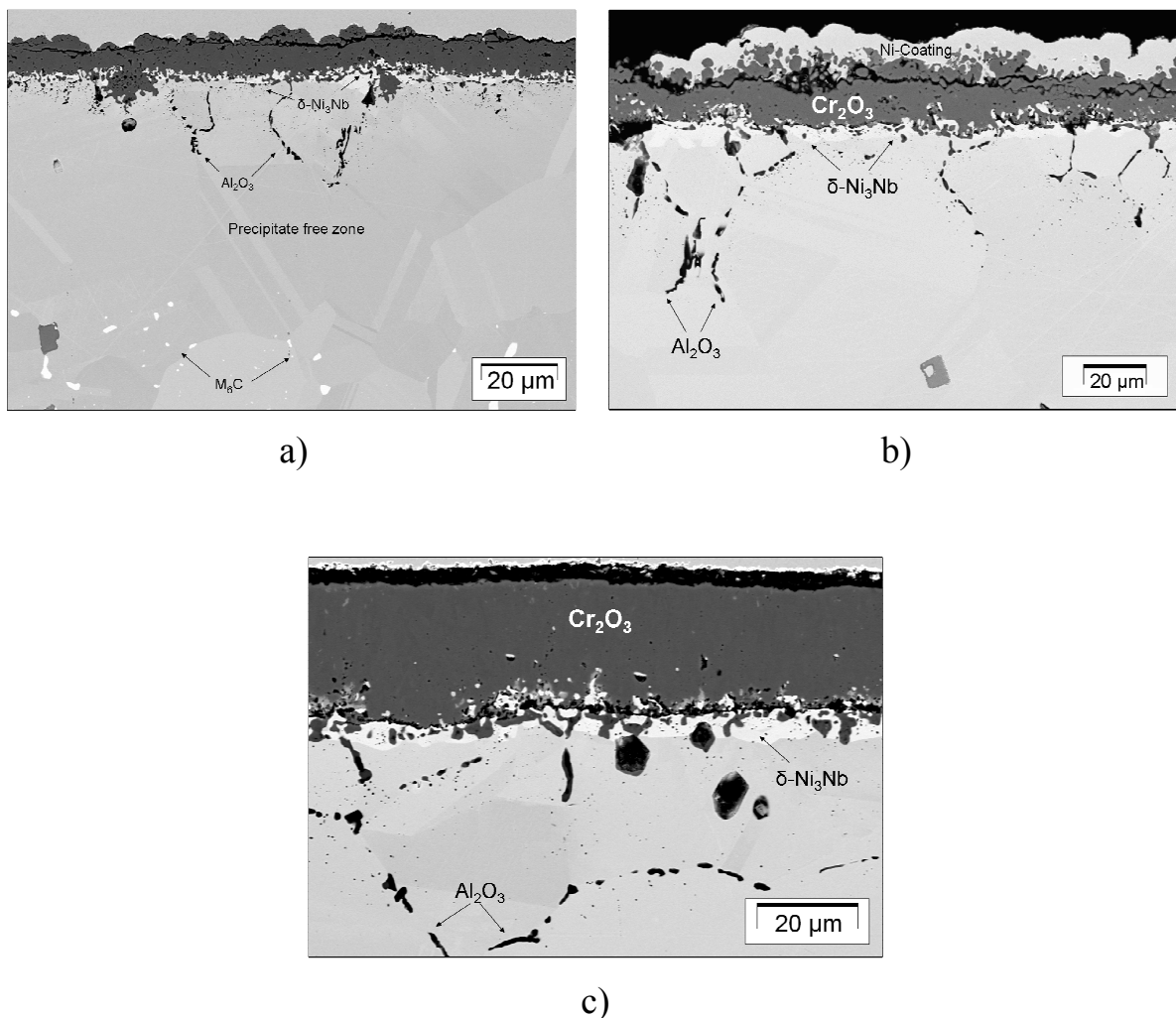


Figure 6.14: SEM images showing cross-sections of alloy 625 after 1000h oxidation at 1000°C in air of (a) 0.3 mm and (b) 1 mm specimens. Figure (c) shows cross-section of specimen (thickness 1 mm) after 1000h oxidation in Ar–4%H₂–2%H₂O

After exposure in both test environments, a precipitate depleted subscale zone is formed similar to that observed after 900°C exposure. The width of this zone (approximately 65 µm after 1000h in Ar–4%H₂–2%H₂O) is larger than at 900°C (considering M₆C carbide) which is not surprising, considering the increasing oxidation rate and chromium diffusion coefficient in the alloy with increasing temperature. A further factor which affects the differences in width of the precipitate depletion zone at the two test temperatures is that, unlike at 900°C, no δ-phase is present in the original alloy microstructure after 1000°C exposure (Figure 6.1).

The most important observation is that also after the 1000°C exposure a precipitate enriched zone is formed in the immediate vicinity of the oxide/alloy interface (Figure 6.14). After 1000h the thickness of this layer is approximately 3 µm in width. Careful analysis by EDX and WDX revealed that the phase forming this layer is not the M₆C phase present in the as-received alloy microstructure. The X-ray element mapping in Figure 6.15 shows the phase to be rich in niobium; it contains only a small amount of molybdenum. Quantitative analysis revealed the phase to be δ-phase with a an approximate composition of 74 at% nickel, 13% niobium, 2.5% chromium, 9% molybdenum, and 1% iron, i.e. a similar composition as that found after the 900°C exposures.

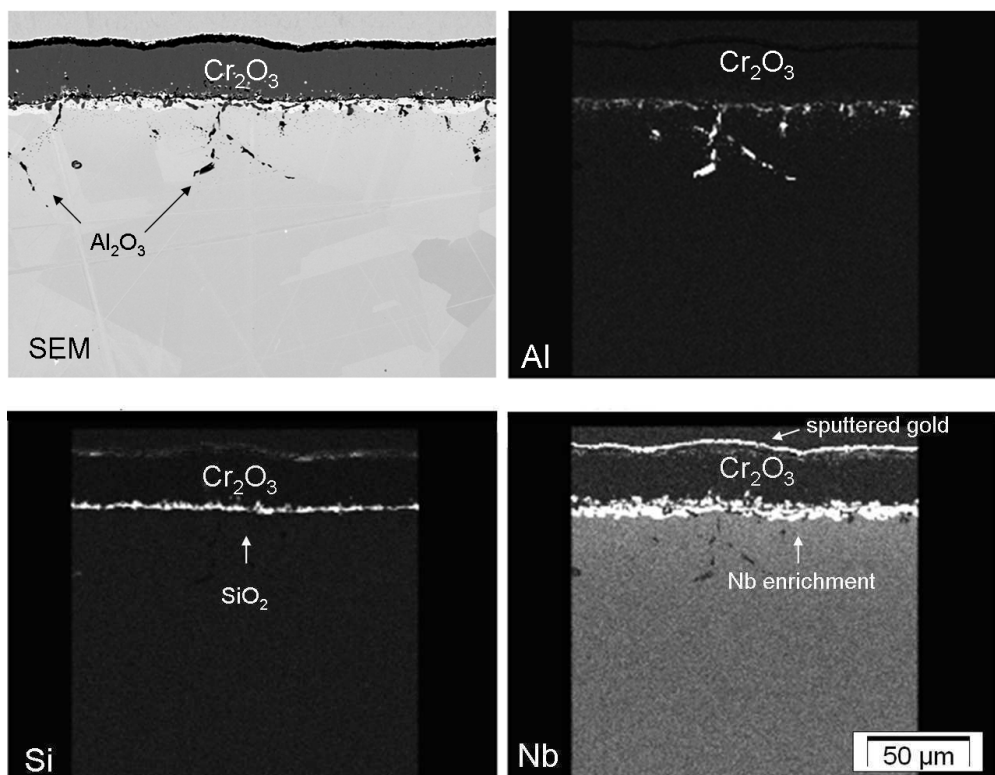
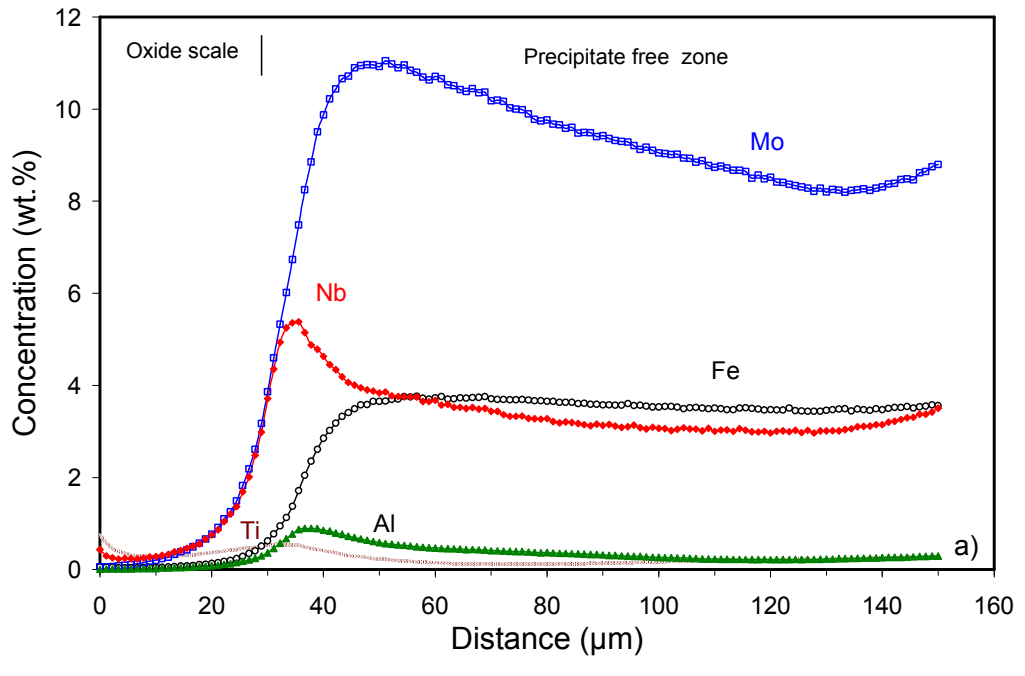
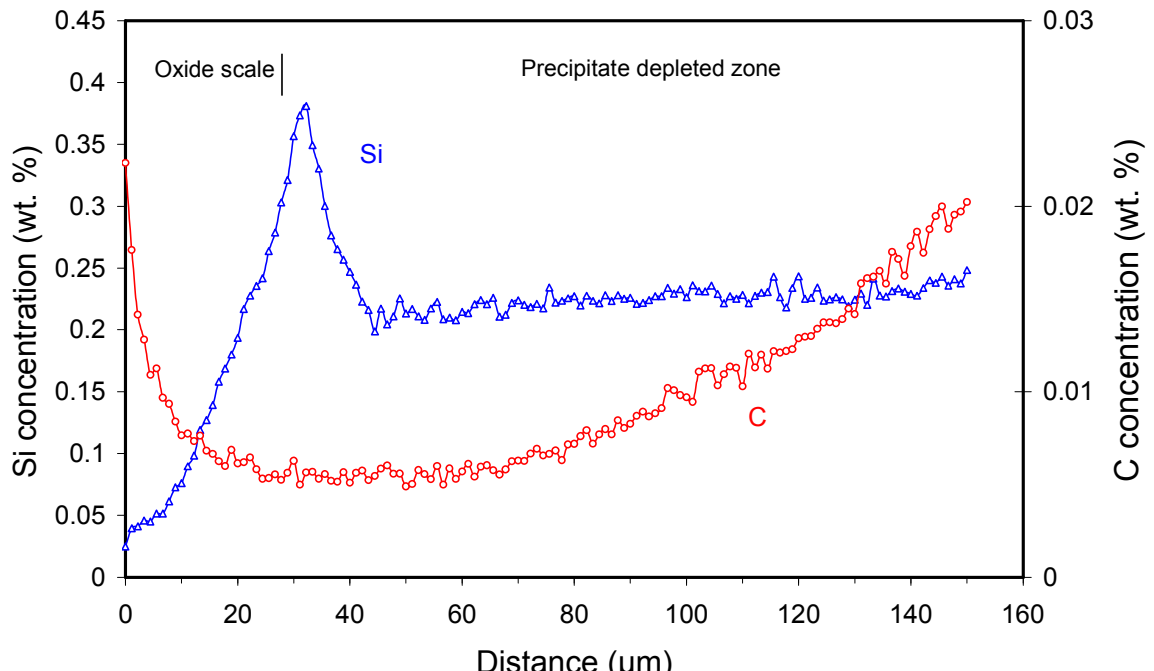


Figure 6.15: SEM cross-section and element mappings in 1 mm thick alloy 625 specimen after 1000h oxidation in Ar–4%H₂–2%H₂O at 1000°C



a)



b)

Figure 6.16: GDOES depth profiles of alloying elements in 1 mm thick alloy 625 specimen after 1000h oxidation in Ar–4%H₂–2%H₂O at 1000°C

The formation of this compound may at first sight be surprising because it is not present in the microstructure of the as-received alloy at 1000°C. However, as illustrated by the data in Figures 6.11 and 6.12, its formation is a logical consequence of the mechanism described above for the 900°C exposure. Niobium enrichment in the subscale is clearly confirmed by the GDOES profiles (Figure 6.16) of a specimen after 1000h exposure in Ar–4%H₂–2%H₂O at 1000°C. Different from the finding at 900°C (Figure 6.8b), the carbon profile in Figure 6.16b exhibits no enrichment beneath the oxide scale.

The GDOES profiles confirm the hypothesis that carbon diffuses backwards from the scale/alloy interface as a result of the oxidation-induced chromium depletion. No δ-phase is present in the alloy at the start of the oxidation process and it takes a certain time until the phase starts to form in the subscale area. Therefore the possibility of a M₆C particle becoming embedded by the growing δ-phase layer is less likely than at 900°C. Carbon has sufficient time to “escape” the subscale zone forming a carbide free region and this process is thermodynamically favorable because the carbon activity in the bulk alloy (where the chromium content is still high) is lower than that in the chromium depleted zone beneath the oxide scale (Figure 6.15).

The chromium concentration profiles measured by EDX analysis in the 0.3 mm specimens after oxidation in air at 1000°C (Figure 6.17) reveal a steeper concentration gradient for Cr than that at 900°C (see Figure 6.9). The Cr interface concentration at 1000°C is approximately 10 wt% compared to 15 wt% at 900°C. Hence the driving force for niobium to diffuse from the bulk alloy towards the scale/alloy interface should be higher at 1000°C than at 900°C. The chromium concentration profile measured after 1000h exposure cannot be fitted by Wagner’s equation because the diffusion distance of Cr calculated using Equation (2.27) and $D_{Cr} = 7.2 \times 10^{-16} \text{ m}^2\text{s}^{-1}$ is approximately 225 μm after 1000h (70μm after 100h, and 125μm after 300h) which is more than the specimen half-thickness $L = 150 \mu\text{m}$ for the 0.3 mm specimens.

Considering the above described δ-phase enrichment/depletion mechanism, the oxidation-induced depletion of chromium in the subsurface zone at 1000°C results, like at 900°C, in a decrease of the niobium activity (Figure 6.18). As the lowest chromium and thus also niobium activity prevails near the scale/alloy interface, niobium will diffuse from the inner part of the depletion zone towards the surface.

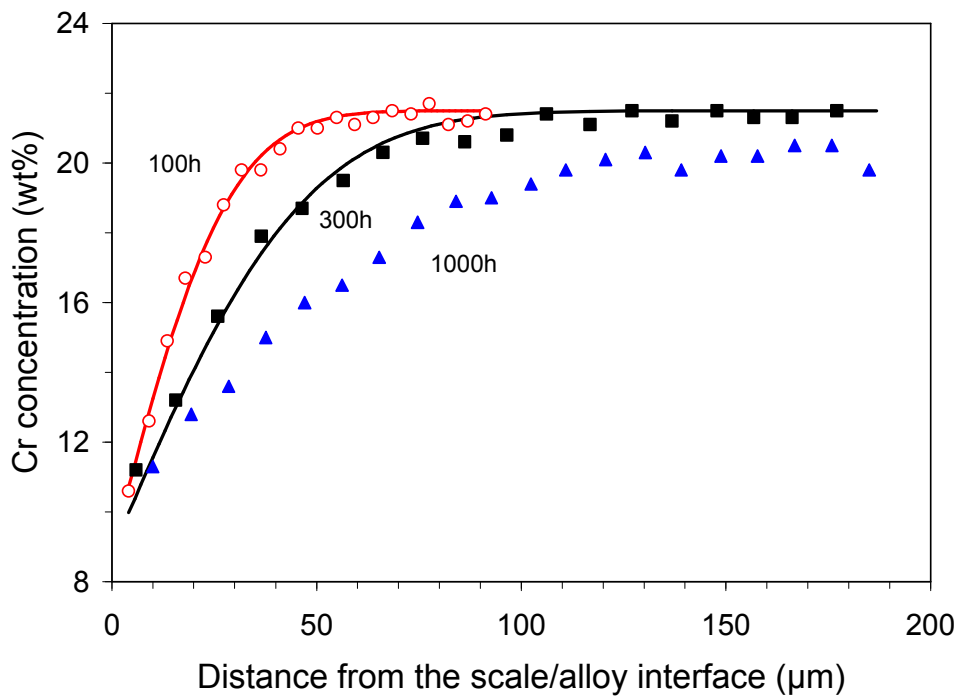


Figure 6.17: Chromium concentration profiles in alloy 625 after oxidation in air at 1000°C measured by EDX spectroscopy (symbols) compared with calculated values (lines) using classical Wagner's theory for a single-phase binary alloy (Equation 2.14) [29]. The curves were calculated using $k_p = 4 \times 10^{-17} \text{ m}^2 \text{s}^{-1}$ and $D_{Cr} = 7.2 \times 10^{-16} \text{ m}^2 \text{s}^{-1}$

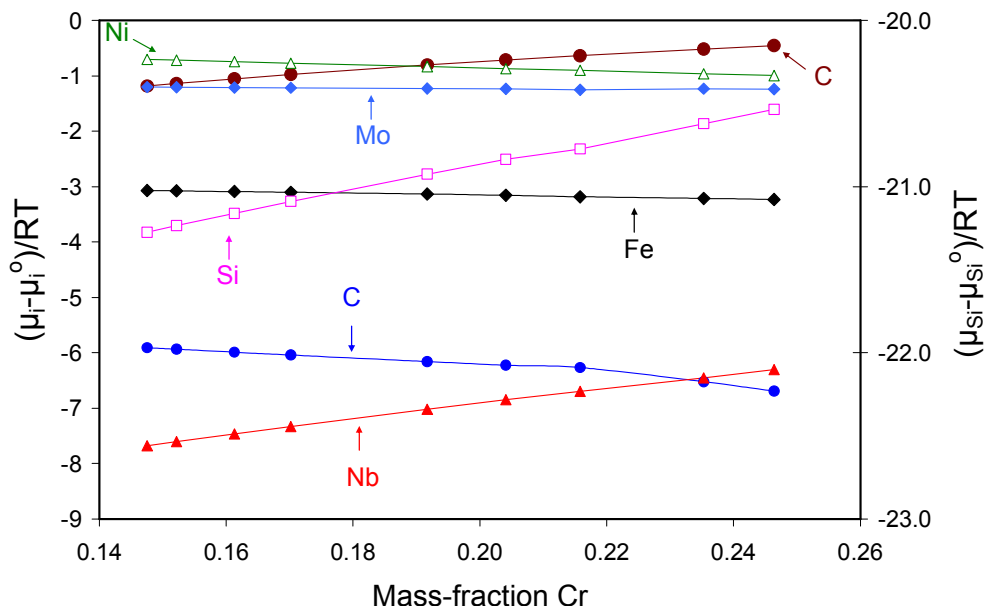


Figure 6.18: Chemical potentials of elements constituting alloy 625 at 1000°C as a function of chromium content calculated in Thermo-Calc using the TTNI7 database

The Thermo-Calc calculation reveals that for the chromium and molybdenum concentrations prevailing in the alloy matrix adjacent to the alloy/oxide interface, a niobium content of 5.1 wt% is required for δ -phase to become stable. It will therefore take a certain time until niobium is sufficiently enriched in the subscale area to allow $\delta\text{-Ni}_3\text{Nb}$ formation. Since the oxide/alloy interface remains precipitate free for a certain time, the obstacle encountered in the depletion simulations at 900°C, i.e. diffusion in the interface zone being “blocked” after the near continuous intermetallic subscale layer is formed, does not prevail at 1000°C. The oxidation modeling in DICTRA in Figure 6.19 confirmed that δ -phase should be present in the immediate vicinity of the scale/alloy interface in alloy 625 after 1000h oxidation at 1000°C. The calculated thickness of the precipitate layer is approximately 2.5 μm , in reasonable agreement with the experimental findings (Figure 6.14).

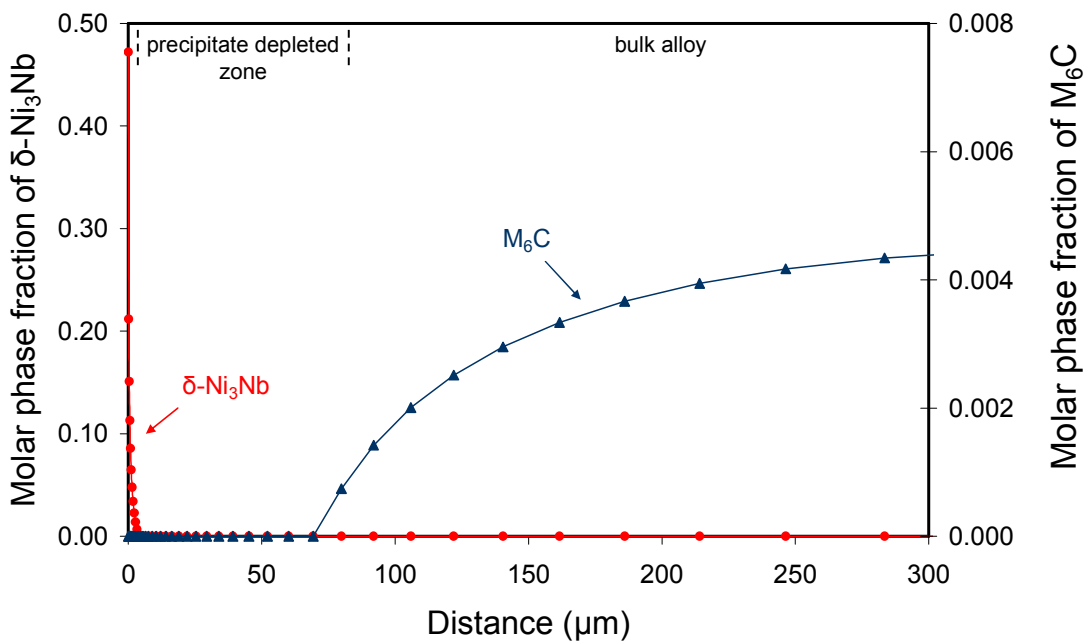


Figure 6.19: DICTRA calculation showing distribution of $\delta\text{-Ni}_3\text{Nb}$ and $M_6\text{C}$ phases in alloy 625 as function of depth in 1 mm thick specimen after 1000h oxidation in $\text{Ar}-4\%\text{H}_2-2\%\text{H}_2\text{O}$ at 1000°C

In spite of the differences in initial alloy microstructures at the two test temperatures 900 and 1000°C, the enrichment/depletion of δ -phase in the subscale zone of alloy 625 at 1000°C has qualitatively the same nature as that at 900°C. Since the thermodynamic calculations of chemical potentials of elements in the alloy at 1000°C did qualitatively not substantially differ from those at 900°C, the uphill-diffusion as well as the eventual $\delta\text{-Ni}_3\text{Nb}$ phase formation beneath the oxide scale, is expected to occur at 1000°C. This was confirmed experimentally

and predicted on the basis of calculations using Thermo-Calc and DICTRA. The driving force for the uphill-diffusion of niobium in direction of the scale/alloy interface is the decrease of its activity in the subscale zone as a result of the oxidation-induced chromium depletion, the activity being the lowest in the area of most pronounced Cr depletion, i.e. the immediate vicinity of the oxide/alloy interface.

6.5 Mechanism of M₆C dissolution

An observation which remains to be explained is the dissolution of the M₆C carbide up to a depth of approximately 65 µm after 1000h at 1000°C (Figures 6.14a and 6.19). A possible reason would be that correlations between Mo activity and Nb concentration exist. The described depletion/enrichment of Nb in the subsurface zone could then be the reason for the dissolution of the M₆C phase. However, a DICTRA calculation ignoring presence and formation of the δ-Ni₃Nb phase, and thus presence of a Nb concentration profile, revealed development of a similar depletion profile of the M₆C phase as shown in Figure 6.14a.

A further calculation was therefore carried out for a model alloy composition which contained the same amounts of Mo and the other alloying elements present in alloy 625, however without Nb addition and with a low carbon content of 0.011 wt%. This low content was selected because at this carbon concentration Thermo-Calc/DICTRA revealed the model alloy at 1000°C to be single phase, i.e. without formation of M₆C precipitates. Assuming chromium depletion kinetics as used for the calculation in Figure 6.19, the calculation revealed diffusion of carbon to occur from the chromium depleted zone towards the alloy mid-section plane including formation of the M₆C carbide in the specimen centre, as illustrated in Figure 6.20.

This result shows that the oxidation-induced chromium depletion causes carbon to diffuse back from the subscale zone towards the specimen centre, irrespective of the fact whether the initially present carbon is in solution or partially tied up in form of carbide. The formation of the M₆C depleted subscale layer in the real alloy 625 (Figure 6.14a) is thus related to a back diffusion of carbon from the chromium depleted zone in direction of the bulk alloy. The driving force for this effect is the increase of the carbon chemical potential with decreasing chromium concentration (Figures 6.12 and 6.18).

At first sight there seems to be a certain degree of contradiction in this statement because one might expect that the amount of Ni- and Mo-rich M₆C carbide in the subsurface zone should increase if the carbon activity increases along the chromium gradient. Additionally, back diffusion of carbon in direction of the centre of the alloy should only proceed until its chemical potential becomes equal to that in the bulk of the specimen at which the M₆C phase is stable in the original alloy microstructure. Back diffusion of carbon would thus not be expected to occur to such an extent that the carbide in the subsurface zone should become unstable.

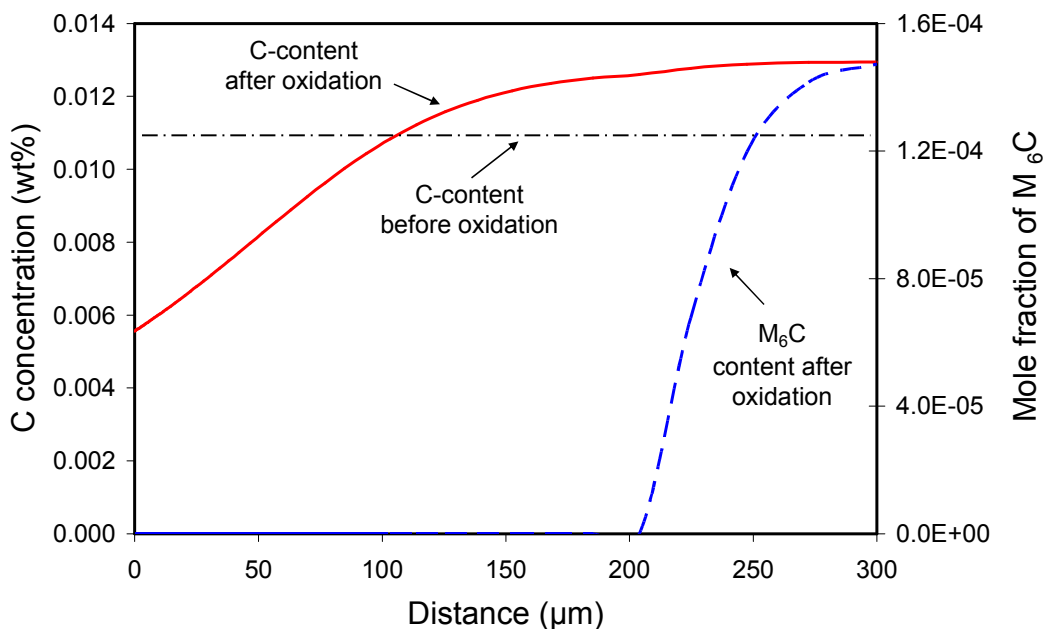


Figure 6.20: DICTRA simulation of carbon diffusion in 0.6 mm thick specimen of model alloy corresponding to alloy 625 composition, however, without Nb addition after 1000h oxidation at 1000°C (using oxidation data from Figure 6.13). The initial carbon content was set at a level of 0.011% to obtain an initial alloy microstructure in which no M₆C is present

To clarify this apparent contradiction, Table 6.2 compares the phase equilibria at 1000°C in the original alloy 625 composition (including the Cr content of 22 percent) and an imaginary alloy with a Cr content of only 10% (as measured to prevail at the oxide/alloy interface after 1000h exposure at 1000°C, see e.g. Figure 6.17). In this imaginary alloy the concentrations of all the other alloying elements present in alloy 625 were increased proportionally, to obtain as sum of all elements 100%. This composition would thus be representative for the alloy composition with reduced chromium content at the scale/alloy interface, ignoring diffusion of any other alloying elements.

The data in Table 6.2 illustrate that the M₆C carbide is at 1000°C stable in the original alloy 625 as well as in the imaginary low-Cr alloy. In the latter alloy the carbon activity in equilibrium with the M₆C carbide equals 3.5×10^{-3} whereas it equals 1.8×10^{-3} in the original alloy. So, the low Cr content of 10% does in itself not have as result the carbide dissolution, but the carbon activity in equilibrium with the carbide phase is higher than that in the original alloy. Consequently, carbon will have to diffuse from the low-Cr zone in direction of the centre of the specimen. It is this process which then destabilizes the carbide.

The calculated C activity required to stabilize the M₆C in the imaginary alloy with 10 wt% Cr appears to be 3.3×10^{-3} . The back diffusion of carbon will proceed until its activity in equilibrium with the low Cr content of 10 wt%, equals that in the bulk alloy (1.8×10^{-3}). It is obvious that, if this situation is reached, the carbide in the Cr-depleted zone is no longer stable.

Table 6.2: Equilibria calculated using Thermo-Calc (1000°C) for original alloy 625 composition and for imaginary alloy with reduced Cr content of 10% corresponding to Cr interface concentration after 1000h oxidation. In the latter material the concentrations of all other alloying elements were correspondingly increased to obtain as sum of all concentrations of the alloying elements 100%

		Original alloy	Chromium depleted alloy	
Mole fraction of M ₆ C		5.1×10^{-3}	6.7×10^{-3}	
Element	wt%	activity	wt%	activity
Ni	61.7	4.0×10^{-1}	71.2	5.6×10^{-1}
Cr	22.0	5.5×10^{-1}	10.0	1.8×10^{-1}
Mo	9.0	2.9×10^{-1}	10.4	3.1×10^{-1}
Nb	3.5	1.3×10^{-3}	4.0	2.3×10^{-4}
Fe	3.5	4.2×10^{-2}	4.0	4.9×10^{-2}
Si	0.25	1.0×10^{-9}	0.29	3.9×10^{-10}
C	0.02	1.8×10^{-3}	0.023	3.5×10^{-3}

This description explains the driving force for the back diffusion of carbon. The carbide stability and dissolution is further influenced by the effect of Cr content on the activity of the

other alloying elements and the resulting diffusion processes. Since the molybdenum and nickel activity do not change substantially along the chromium concentration gradient (Figure 6.18), the influence of Nb on the stability of the M_6C phase has to be estimated. For this purpose the amount of M_6C phase at 1000°C was calculated by Thermo-Calc for two model systems, i.e. Ni-Cr-Mo-C and Ni-Cr-Mo-Nb-C. Figure 6.21 shows that the amount of M_6C carbide decreases with decreasing Nb concentration, i.e. niobium apparently stabilizes the carbide. Chromium also tends to stabilize M_6C which is the second factor influencing carbide dissolution in the subsurface region as a result of back diffusion of carbon.

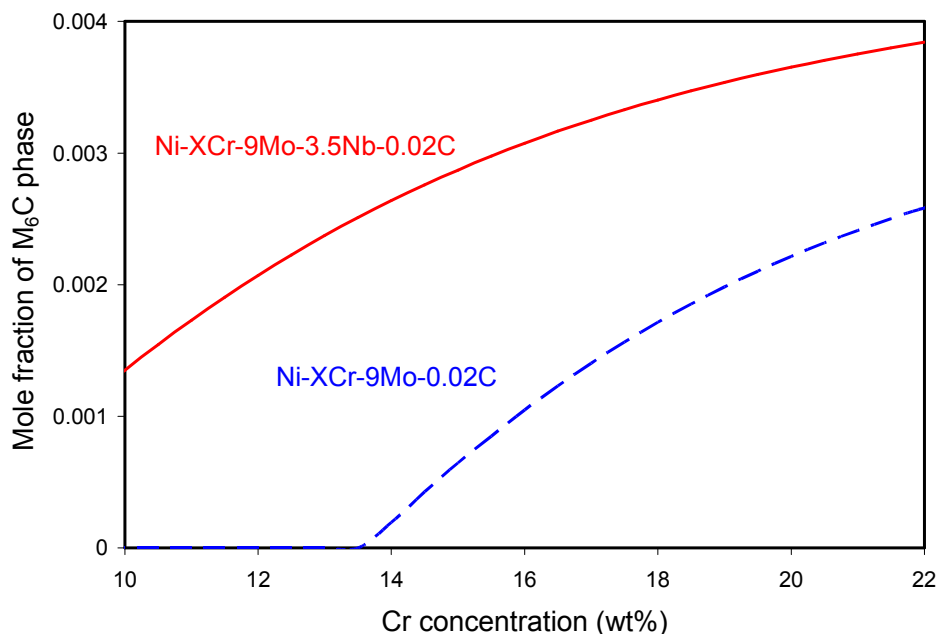


Figure 6.21: Amount of M_6C phase as function of Cr and Nb content at 1000°C, calculated using Thermo-Calc, assuming model Ni-Cr-Mo-C and Ni-Cr-Mo-Nb-C alloys. Concentrations of the alloying elements are given in the graph

As discussed in the previous sections and illustrated in Figures 6.8 and 6.16, the Nb concentration in the Cr depletion zone decreases during the oxidation process due to Nb diffusion towards the scale/alloy interface. This decrease in Nb concentration is, according to Figure 6.21, a further effect promoting dissolution of the carbide phase.

Thus, chromium depletion in the subscale zone induces (i) uphill-diffusion of niobium which results in formation of the δ - Ni_3Nb layer underneath the chromia scale, (ii) back diffusion of

carbon as a result of a C activity increase, and (iii) dissolution of M_6C carbide as a consequence of (i) and (ii).

6.6 Uphill-diffusion of niobium in the Ni-Cr-Mo-Nb system

In the previous sections it is claimed that the enrichment/depletion of δ -phase in the subscale zone of alloy 625 during high-temperature oxidation involves uphill-diffusion of at least one of the alloy constituents, i.e. niobium. As shown by the thermodynamic calculations using Thermo-Calc (Figures 6.12 and 6.18), the niobium activity decreases with decreasing Cr content. Thus, a driving force exists for niobium to diffuse from the bulk alloy towards the oxide/alloy interface, i.e. the most chromium depleted location in the alloy. In other words, niobium tends to diffuse down the chromium gradient. High-temperature oxidation involving chromia surface scale formation is not the only way for a concentration gradient to arise in the alloy. Considering a diffusion couple made of two Nb-containing nickel-base alloys with different chromium contents, one would expect, if the above considerations are correct, uphill-diffusion of niobium to occur from the high-Cr part of the diffusion couple to the low-Cr one.

To prove the nature of this effect and to determine the driving force for niobium diffusion in a concentration gradient of chromium, an “imaginary” diffusion couple was considered. The interdiffusion calculations were carried out using DICTRA. The high-Cr part is alloy 625 containing 22% Cr and 3.5% Nb whereas the low-Cr part was an imaginary nickel-base alloy containing 10% Cr and 8% Nb. Additionally, the low-Cr alloy contained, as alloy 625, 9% Mo to prevent strong diffusion of molybdenum into the model alloy, which might appreciably affect the calculation results. The temperatures and the holding times were the same as for the oxidation tests, i.e. annealing at 900 and 1000°C up to 1000h.

Assuming “normal” diffusion behavior, one would expect niobium to diffuse from the low-Cr/high-Nb part of the diffusion couple to the high-Cr/low-Nb one. However, the calculated concentration profile for Nb after 1000h annealing at 900°C reveals the opposite. Niobium diffuses towards the low-Cr/high-Nb part of the diffusion couple where its concentration is more than twice as high as in alloy 625 (Figure 6.22).

After 1000h annealing niobium is enriched, its concentration being increased by almost 2%, at the interface on the low-Cr side whereas the high-Cr part shows a 75 μm wide niobium depletion zone. Thus, the chromium concentration gradient across the diffusion couple results in uphill-diffusion of niobium from alloy 625 towards the low-Cr part of the diffusion couple. The chromium depleted alloy in contact with alloy 625 can be regarded as an approximation for the oxidation-induced chromium depleted subscale zone. Compared to the oxidation simulation, the interdiffusion calculations have an advantage of continuous diffusion across the diffusion couple.

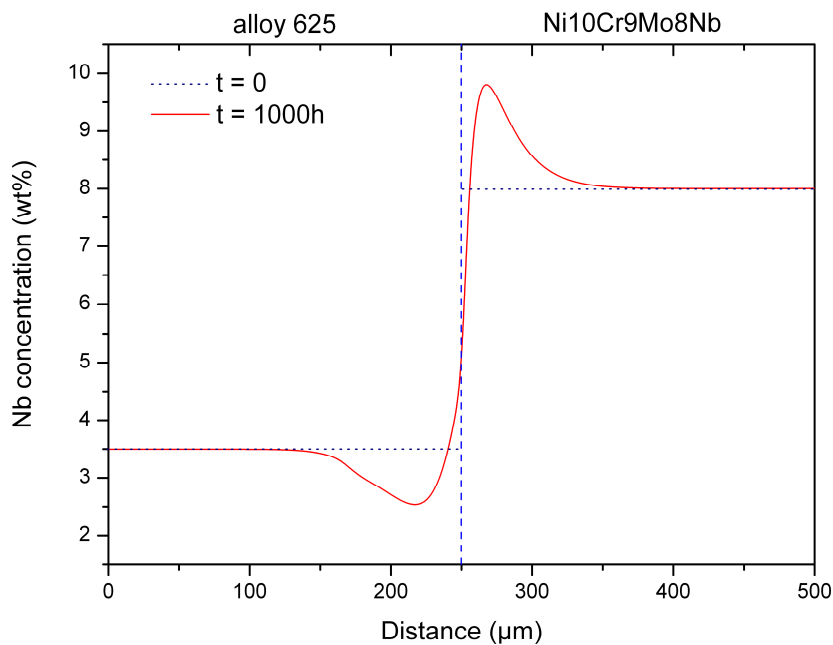


Figure 6.22: Calculated concentration profile of Nb in diffusion couple of alloy 625 and the model alloy Ni10Cr9Mo8Nb after 1000h annealing at 900°C

The formation of $\delta\text{-Ni}_3\text{Nb}$ phase at the interface between model alloy and alloy 625 does not result in blocking of diffusion through the boundary because its amount only reaches 14%. The low-Cr alloy allows further diffusion of niobium into the alloy whereby a closed system prevails for the oxidation simulations in DICTRA. Being confined by the oxide/scale interface, Nb is strongly enriched to form a dense layer of the $\delta\text{-Ni}_3\text{Nb}$ phase on the alloy side. However, the phase formation beneath the oxide scale reduces the diffusion transport through the oxide scale/alloy interface because DICTRA assumes diffusion only to occur in the $\gamma\text{-FCC}$ matrix phase. This problem is avoided in the interdiffusion calculations which allow certain estimations of phase transformations driven by uphill-diffusion of Nb in the

concentration gradient of chromium (Figure 6.23) without the limitation of forming a continuous δ -phase layer. On the low-Cr side the molar fraction of the $\delta\text{-Ni}_3\text{Nb}$ phase increases up to 14% compared to the original amount of 2% whereas the high-Cr part, i.e. alloy 625, reveals formation of a $\delta\text{-Ni}_3\text{Nb}$ depleted zone. The width of the precipitate free zone is in reasonable agreement with the experimentally observed values of 60-65 μm in the oxidation tests.

Further DICTRA calculations were carried out for the studied diffusion couple at 950°C. At this temperature no $\delta\text{-Ni}_3\text{Nb}$ phase exists in both parts of the diffusion couple, i.e. the model alloy Ni10Cr9Mo8Nb and alloy 625 (see Figure 6.3). The calculated niobium profile after 1000h annealing at 950°C shows essentially the same features as that after annealing at 900°C, i.e. niobium is inclined to diffuse from the high-Cr part of the diffusion couple toward the low-Cr part down the chromium gradient. However, the Nb enrichment peak on the low-Cr side is lower and broader than that in the 900°C profile, which is caused by the higher temperature and thus faster diffusion of niobium and the other elements.

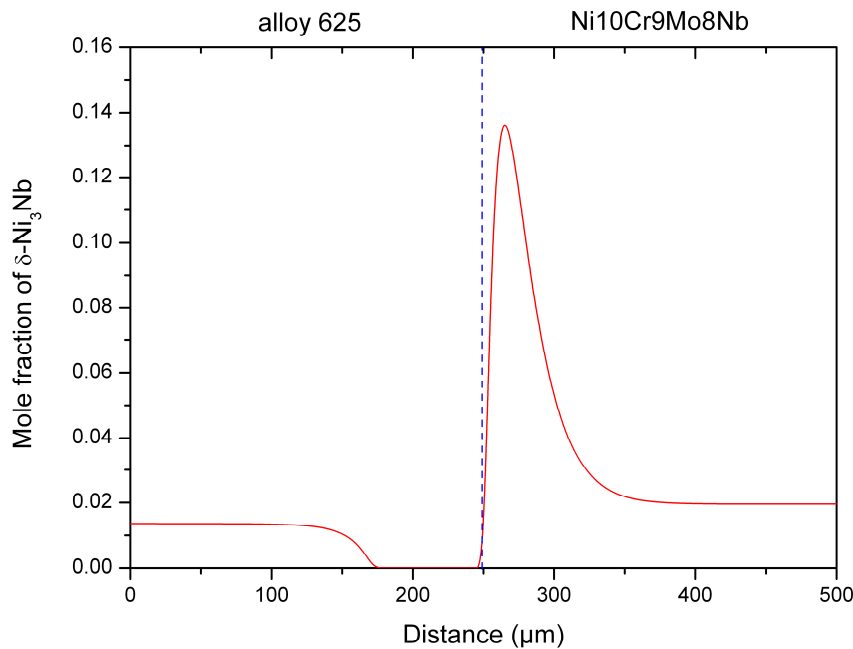


Figure 6.23: Calculated molar fraction of $\delta\text{-Ni}_3\text{Nb}$ phase across the alloy 625 / Ni10Cr9Mo8Nb diffusion couple after 1000h annealing at 900°C

The effect of temperature on interdiffusion between the model Ni15Cr9Mo8Nb alloy and alloy 625 is even more pronounced at 1000°C. In contrast to the oxidation modeling (Figure

6.19), the interdiffusion calculation in DICTRA revealed no δ -phase enrichment on the low-Cr side due to fast and unhampered diffusion of niobium into the low-Cr part of the diffusion couple. As explained above, niobium is strongly enriched at the scale/alloy interface in case of alloy 625 oxidation because it is confined in space by the scale/alloy interface. After a certain time this Nb enrichment results in the precipitation of the δ -Ni₃Nb phase in the immediate vicinity of the scale/alloy interface (see section 6.4) in contrast to the case described in the diffusion couple in which the Nb-enrichment is “evened out” because of unhampered diffusion across the diffusion couple.

That is why the second interdiffusion calculation was intentionally carried out at an intermediate temperature of 950°C. Although both alloys in the diffusion couple are single-phase at this temperature, the uphill-diffusion of niobium results in formation of δ -Ni₃Nb at the interface between the alloys on the low-Cr side (Figure 6.25). This result has the same nature as the precipitation of δ -Ni₃Nb at the scale/alloy interface after the long-term oxidation tests (Figure 6.14). In the 950°C calculation the δ -phase is found to form during annealing of the diffusion couple, although it is not present in the original microstructure of both studied alloys at the respective temperature.

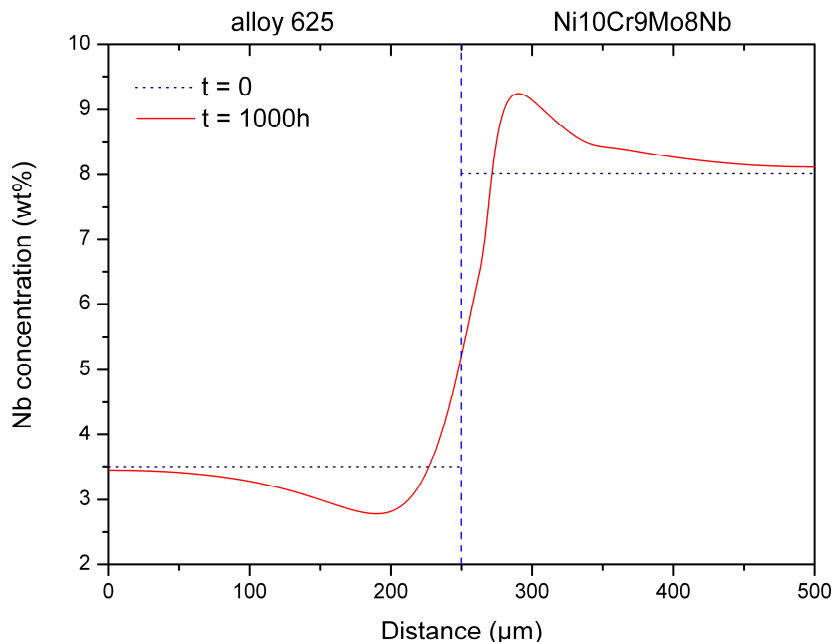


Figure 6.24: Calculated concentration profile of Nb in diffusion couple between alloy 625 and model alloy Ni10Cr9Mo8Nb after 1000h annealing at 950°C

The interdiffusion calculations using the finite-difference software DICTRA coupled with Thermo-Calc confirmed the phase transformations during high-temperature oxidation of alloy 625 to be a consequence of uphill-diffusion of niobium in the concentration gradient of chromium. In the case of high-temperature oxidation, the chromium gradient is established due to continuous consumption of the selectively oxidizing element Cr by the scaling process. The chromium gradient can also arise between two alloys in a diffusion couple with different chromium contents. The interdiffusion modeling revealed occurrence of both effects which were observed in the oxidation studies: (i) niobium tends to diffuse from the Cr-rich part of the alloy towards the low-Cr one, (ii) precipitation of the niobium rich phase $\delta\text{-Ni}_3\text{Nb}$ occurs on the low-Cr side of the interface in the diffusion couple.

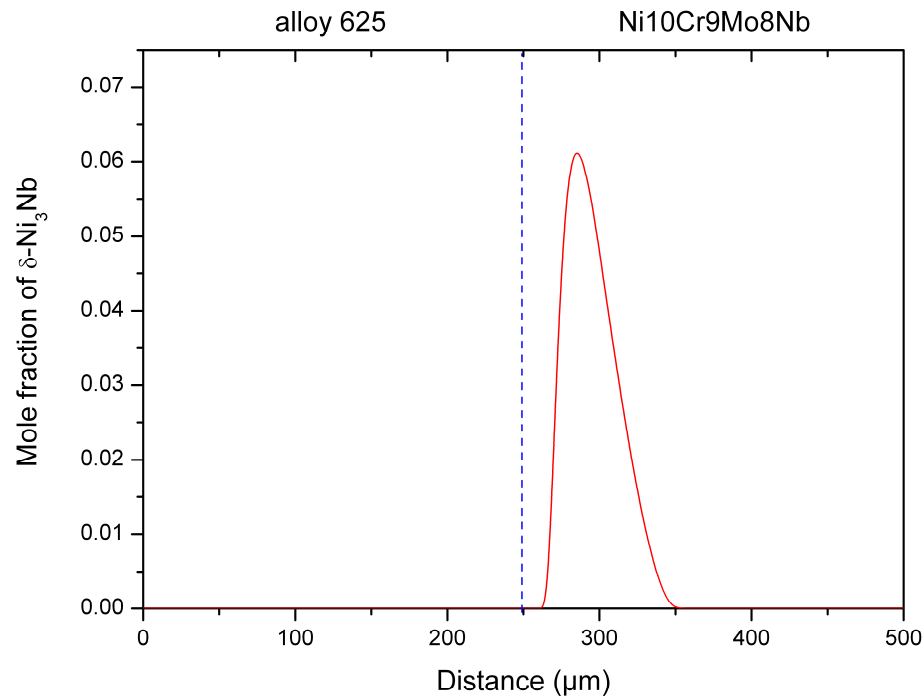


Figure 6.25: Calculated molar fraction of $\delta\text{-Ni}_3\text{Nb}$ phase across diffusion couple of alloy 625 and model alloy Ni10Cr9Mo8Nb after 1000h annealing at 950°C

6.7 Possible effect of subscale phase changes on oxide scale growth

As mentioned in section 6.3, the oxidation-induced subscale depletion processes in a single phase NiCr base alloy can with reasonable accuracy be described by classical Wagner's oxidation theory [29]. From this theory it can be derived that in case of a binary alloy with a

chromium content like in alloy 625, i.e. 22%, a near constant chromium concentration would establish at the scale/alloy interface (Equation (2.17)) if a parabolic time dependence of the scale thickening rate prevails, and if interface recession is ignored.

This chromium interface concentration is mainly governed by the ratio between the oxidation rate constant k_p and the chromium alloy interdiffusion coefficient D [28], i.e. the interface concentration will decrease with increasing ratio k_p/D [28]. The chromium flux related to the scale growth at a given exposure time will be correlated with the slope of the chromium concentration, more accurately the chromium activity, profile at the scale/alloy interface at that given oxidation time (see section 2.2.1).

Formation of an intermetallic phase such as $\delta\text{-Ni}_3\text{Nb}$ in direct contact with the oxide scale, as observed in case of alloy 625, is expected to affect the oxidation process compared to that of a binary, single-phase NiCr alloy. If a completely dense layer of δ -phase would form, the chromium activity gradient immediately beneath the oxide scale and thus the chromium flux towards the alloy/scale interface may differ from that in a binary NiCr alloy. Also the diffusion coefficient of chromium in the intermetallic phase is likely to be different from that in a binary NiCr matrix. Unfortunately, quantitative data of these parameters is, as far as known to the author, not available so that a quantitative estimation of the δ -phase formation on the chromium interdiffusion coefficient seems to be mere speculation.

A further factor which may affect the oxide scale formation, especially after long exposure times, is the gradual incorporation of the δ -phase into the chromia layer due to the inwardly moving alloy/oxide interface (Figure 6.7). During short term exposure a near-ideal double layer system is formed consisting of chromia and δ -phase (see e.g. Figure 6.7). Apparently, the niobium in the δ -phase does not oxidize beneath the chromia scale. When considering equilibrium of the oxides with the respective pure metals, NbO is found to possess a lower dissociation pressure (4.0×10^{-28} bar at 900°C) than Cr_2O_3 (5.3×10^{-25} bar) (see e.g. Figure 2.2). Assuming these values, the niobium would be expected to internally oxidize beneath the external chromia layer. However, because no internal Nb oxidation is observed, the niobium activity in the alloy and in the δ -phase is apparently quite small, i.e. much smaller than one would expect assuming activities being proportional to the respective mole fractions.

From the Thermo-Calc calculations it appears that in a binary Ni-22%Cr alloy at 900°C the chromium activity equals 0.33. In alloy 625, taking δ - and M₆C-phase into account, the activity equals 0.6. In the chromium depleted alloy matrix as prevailing near the scale/alloy interface (approximately 15 wt % chromium at 900°C; (see Figure 6.9), the activity drops to 0.32. The niobium activities in the original and the Cr-depleted alloy 625 are 8×10^{-4} and 2×10^{-4} , respectively. Considering the composition of the subscale layer (δ -phase in equilibrium with the alloy matrix) at the scale/alloy interface measured by EDX after 300 hours exposure (Figure 6.7), Thermo-Calc, using the thermodynamic data from TTNI7, reveals for the chromium and niobium activities values of 0.43 and 3.3×10^{-4} respectively. This reveals dissociation pressures for NbO and Cr₂O₃ in equilibrium with the γ -FCC matrix and the δ -Ni₃Nb phase to be 3.7×10^{-21} and 1.6×10^{-24} bar respectively (Figure 6.26).

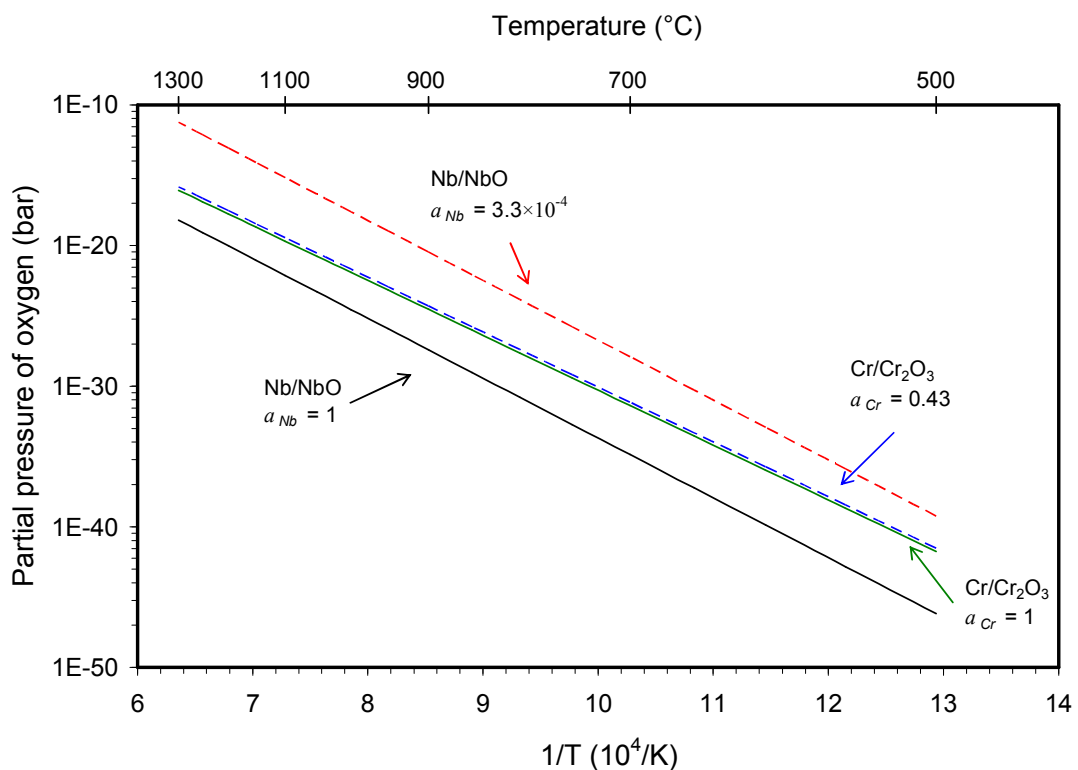


Figure 6.26: Dissociation pressures of NbO and Cr₂O₃ as function of temperature for standart state (unit metal activities) and in equilibrium with alloy 625 (activities calculated in Thermo-Calc for subscale composition measured by EDX)

This explains why up to the maximum exposure times of 1000h no (internal) oxidation of niobium in the alloy and/or in the δ -phase layer occurs. However, upon further thickening of the oxide layer, accompanied by the inward movement of the alloy/oxide interface, individual

particles of δ -phase become gradually embedded into the growing chromia scale, as previously observed Trindade et. al [126] in a Si enriched alloy 625 after 90h exposure in air at 1000°C.

After prolonged exposure and scale growth, these embedded particles (Figure 6.14c) become gradually located in scale areas at which the oxygen partial pressure is higher than that prevailing at the alloy/scale interface, i.e. sufficiently high to oxidize the niobium present in the intermetallic phase. It is difficult to estimate whether this oxidation process affects the chromia growth in a positive or a negative way. If Nb would be dissolved in chromia, the effect of this doping on the scale growth would depend on the valencies of the respective dopants and the major point defects in the chromia scale.

It has frequently been stated that at high oxygen partial pressure chromia is a p-type conductor with cation vacancies being the major point defects; at low oxygen partial pressure it is claimed to be an n-type conductor, the major point defects being chromium interstitials [12, 127]. In the latter case, doping with higher valency cations would decrease, in the first mentioned case increase the chromia growth [12, 127]. For the case of niobium doping, the valency may vary between 2 and 5 depending on the oxygen partial pressure, thus on the location in the chromia scale. Prediction of the effect of niobium doping on chromia growth is thus subject to severe uncertainties.

Oxidation of embedded particles of δ -phase in the chromia scale may affect the scale also in another way. Presence of small, oxidized particles of δ -phase can be seen in the scale cross-section in Figure 6.14. The oxidation of substantial amounts of δ -phase particles occurring after longer oxidation times may result in a volume change which may lead to microcracking of the chromia layer and is expected to result in an increased overall oxidation rate. Long term exposures (up to 3000h) of alloy 625 in the temperature range 900 – 1000°C under slightly different experimental conditions as used in the present study indicated morphological changes of the oxide scale occurring after approximately 3000 hours (Figure 6.27) which might relate to this mechanism [124].

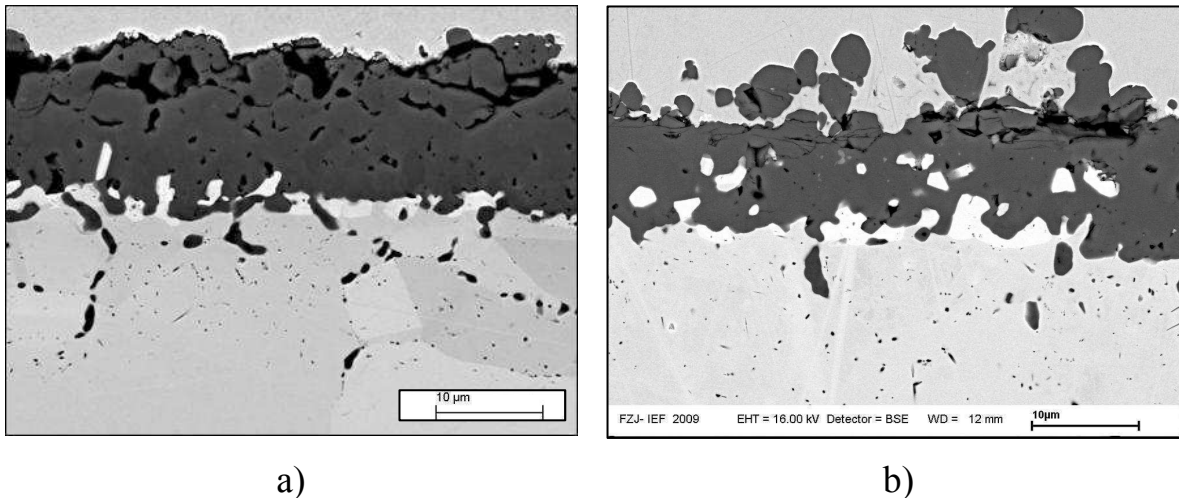


Figure 6.27: SEM images showing cross-sections of 1 mm thick alloy 625 specimens after 300 (a) and 1000h (b) exposure at 1000°C in air + 6%H₂O [124]

6.8 Summary of subscale phase transformations

At 1000°C the main precipitate phase in alloy 625 is silicon containing (Ni,Mo)₆C whereas with decreasing temperature δ-Ni₃Nb becomes the main precipitate. Although both phases contain only minor amounts of chromium, consumption of this element from the alloy as a result of chromia surface scale formation during high-temperature oxidation results in formation of a precipitate depleted zone in the subsurface layer. In spite of the fact that the thermodynamic database included in Thermo-Calc does not in all details correctly describe the actually prevailing phase equilibria in alloy 625, e.g. in respect to silicon solubility in the M₆C phase, the oxidation-induced subscale depletion and enrichment processes could be correctly described using the DICTRA/Thermo-Calc software.

The effect of chromium content on niobium activity causes uphill-diffusion of niobium in the chromium depleted zone towards the area of lowest chromium concentration, i.e. the scale/alloy interface. As a result, formation of a zone in which the δ-phase is dissolved occurs in parallel with formation of a virtually pure δ-phase layer in the immediate vicinity of the scale/alloy interface. This δ-phase layer even forms at oxidation temperatures as high as 1000°C, i.e. a temperature at which the δ-phase is thermodynamically not stable in equilibrium with the original alloy matrix not affected by chromium depletion.

Internal precipitation of alumina was found at grain boundaries beneath the chromia scale. However, no internal oxidation of niobium was observed, although the decomposition pressure of NbO is lower than that of Cr₂O₃, because of the low niobium activity in alloy 625, especially in the chromium-depleted subsurface zone.

After prolonged exposures, individual particles of δ-phase are gradually embedded into the growing chromia scale and become located in scale areas at which the oxygen partial pressure is higher than that prevailing at the metal/oxide interface. At sufficiently high oxygen partial pressure the δ-phase particles may oxidize to form Nb-rich oxides and thus lead to internal stresses in the oxide scale. The formation of fast-growing and voluminous Nb-rich oxides can result in severe spallation of the oxide after longer exposure times and may be thus detrimental for the alloy performance.

Modeling phase equilibria and diffusion processes revealed that the formation of the subsurface depletion zone is mainly caused by the influence of chromium concentration on the niobium and carbon activity in the alloy matrix. The latter effect results in carbon diffusion from the chromium depleted zone towards the specimen centre independent of the fact whether carbon in the initial alloy prevails in solid solution or whether it is partly tied up in form of carbide.

7. Effect of specimen thickness on phase transformations in alloy 625

7.1 General remarks

Numerous studies showed that the oxidation rate of alumina- and chromia-forming alloys is substantially affected by the specimen/coating thickness. In case of FeCr- [99] and FeCrAl-base [128] alloys and MCrAlY ($M = Ni/Co$) coatings [100] this effect is related to differences in the reservoir of oxygen active elements (e.g. Y or Zr) in thin and thick specimens/coatings.

The alumina growth rate is frequently found to increase with increasing specimen thickness due to the larger reservoir of yttrium or zirconium in thick specimens [128, 129]. In chromia-forming ferritic steels and Ni-base alloys an opposite effect is frequently observed. The specimen thickness dependence of growth rate of chromia scales is considered to be caused by compressive growth stresses in the oxide which can relax by plastic deformation of the substrate in thin specimens but are maintained to a great extent in thick specimens [130].

Subsurface phase transformations driven by oxidation-induced compositional changes beneath the oxide scale may also be affected by the specimen thickness. The δ -Ni₃Nb phase dissolution/enrichment effect described in the previous chapter involves mass transport of some alloying elements, e.g. niobium and/or molybdenum, from the bulk alloy to the scale/alloy interface. In thin foil specimens of alloy 625 (with a thickness in range 100-140 μm) the reservoir of the δ -Ni₃Nb phase stabilizing element Nb is obviously lower than in 1 mm sheets. This implies that the niobium supply from the bulk alloy to the scale/alloy surface in case of the thin specimens is essentially limited which might affect the occurrence of the δ -phase enrichment as a result of high-temperature oxidation.

7.2 Effect of specimen thickness on depletion/enrichment processes of δ -phase

As illustrated in Figure 7.1, high-temperature oxidation of a thin alloy 625 foil specimen is, similar as in case of thick sheet specimens, accompanied by the depletion/enrichment phase transformation processes described in the previous chapter:

- Precipitation of the δ -Ni₃Nb phase occurs at the scale/alloy interface although it is not present in the original alloy microstructure at 1000°C;
- Dissolution of M₆C (M=Ni, Mo) carbide as a result of back diffusion of carbon in the Cr concentration gradient toward the specimen centre.

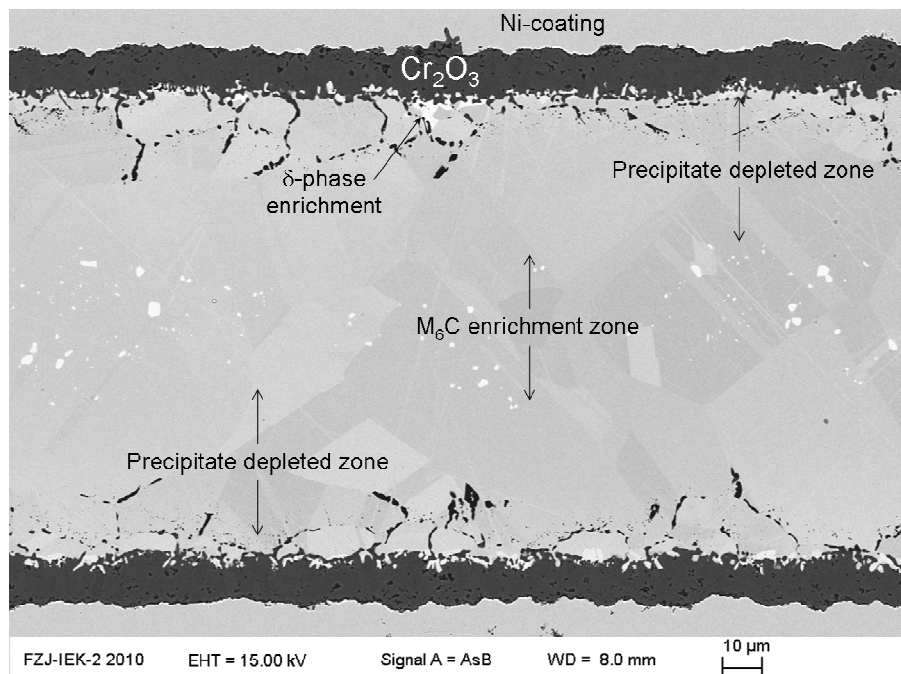


Figure 7.1: SEM image of cross-sectioned 140 μm thick alloy 625 foil after 300h oxidation in air at 1000°C

The concentration profiles of chromium in the 140 μm thick specimen of alloy 625 measured by EDX (Figure 7.2) after oxidation in air at 1000°C have several features which are different from those in the 0.3 mm thick specimens (section 6.4): (i) the Cr concentration profile has reached the mid-section plane of the specimen within the 300h exposure; (ii) the chromium concentration throughout the entire specimen decreases as the oxidation proceeds; (iii) the chromium concentration gradient in the immediate vicinity of the oxide scale decreases more pronounced with increasing oxidation time.

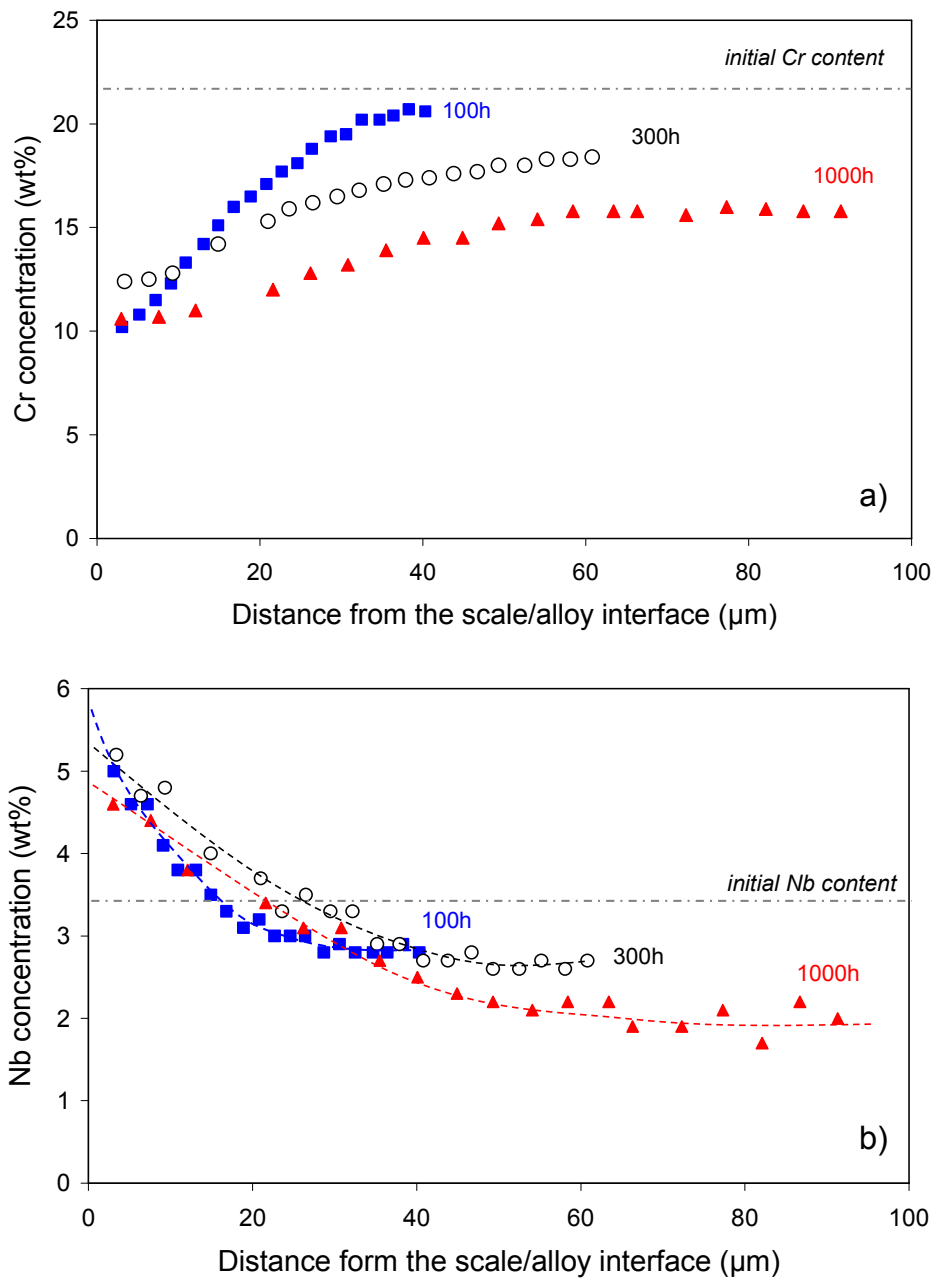


Figure 7.2: Concentration profiles of chromium (a) and niobium (b) in thin alloy 625 foils after oxidation in air at 1000°C measured by EDX spectroscopy. Thickness of δ -phase layer at scale/alloy interface is approximately 1-3 μm

The concentration profiles of niobium in Figure 7.2b are consistent with the uphill-diffusion model described in section 6.3, i.e. niobium diffusion from the bulk alloy towards the scale/alloy interface is driven by the gradient of the Nb chemical activity established along the chromium depletion profile. The bulk alloy is continuously depleted in Nb whereas the subsurface zone is enriched, which results in precipitation of the δ - Ni_3Nb phase (Figure 7.3).

As apparent from Figure 7.2b, the niobium gradient in the subscale zone also decreases with increasing oxidation time as a result of a decreasing driving force for the uphill-diffusion of Nb due to the establishment of flatter concentration profiles of Cr (Figure 7.2a).

Although the phase transformation processes occurring during high-temperature oxidation of the thin foils of alloy 625 exhibit similar features as previously described for thick sheets (chapter 6), significantly less $\delta\text{-Ni}_3\text{Nb}$ precipitates (in absolute amounts) were found to have formed at the scale/alloy interface during oxidation of the thin foils (Figure 7.3). The $\delta\text{-Ni}_3\text{Nb}$ precipitates are sporadically dispersed along the scale/alloy interface and do not form a continuous layer of the δ -phase. In contrast, the 1mm thin specimen forms during 1000h oxidation at 1000°C a thick continuous $\delta\text{-Ni}_3\text{Nb}$ layer (Figure 6.14).

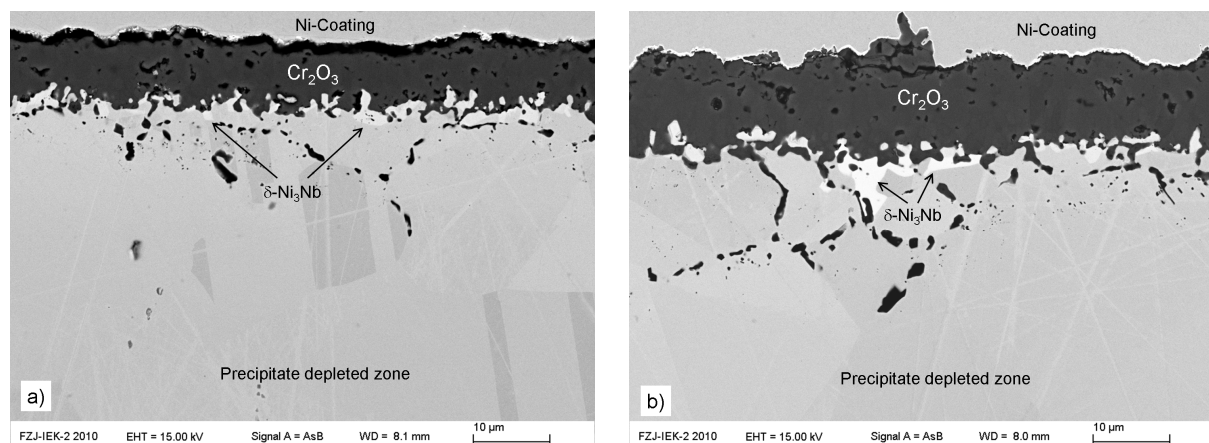


Figure 7.3: SEM images of cross-sectioned alloy 625 foils after 100h (a) and 300 (b) hours of oxidation in laboratory air at 1000°C

Figure 7.4 compares two cross-sectioned alloy 625 specimens with a thickness of 0.14 and 0.30 mm respectively after 1000h oxidation at 1000°C in air. As shown in Figure 7.4c, the chromia scales on the 0.3 mm thick specimen exhibit well distinguishable cracks after 1000h of exposure which results in higher oxygen permeability through the oxide layer resulting in local internal oxidation of chromium after longer exposure times (Figures 7.4a and 7.4c).

The X-ray mappings of the element Nb show clearly that the precipitation of the $\delta\text{-Ni}_3\text{Nb}$ phase beneath the chromia scale of the 0.3 mm specimen (Figure 7.4d) is far more pronounced than in the subsurface zone of the thinner specimen (Figure 7.4b).

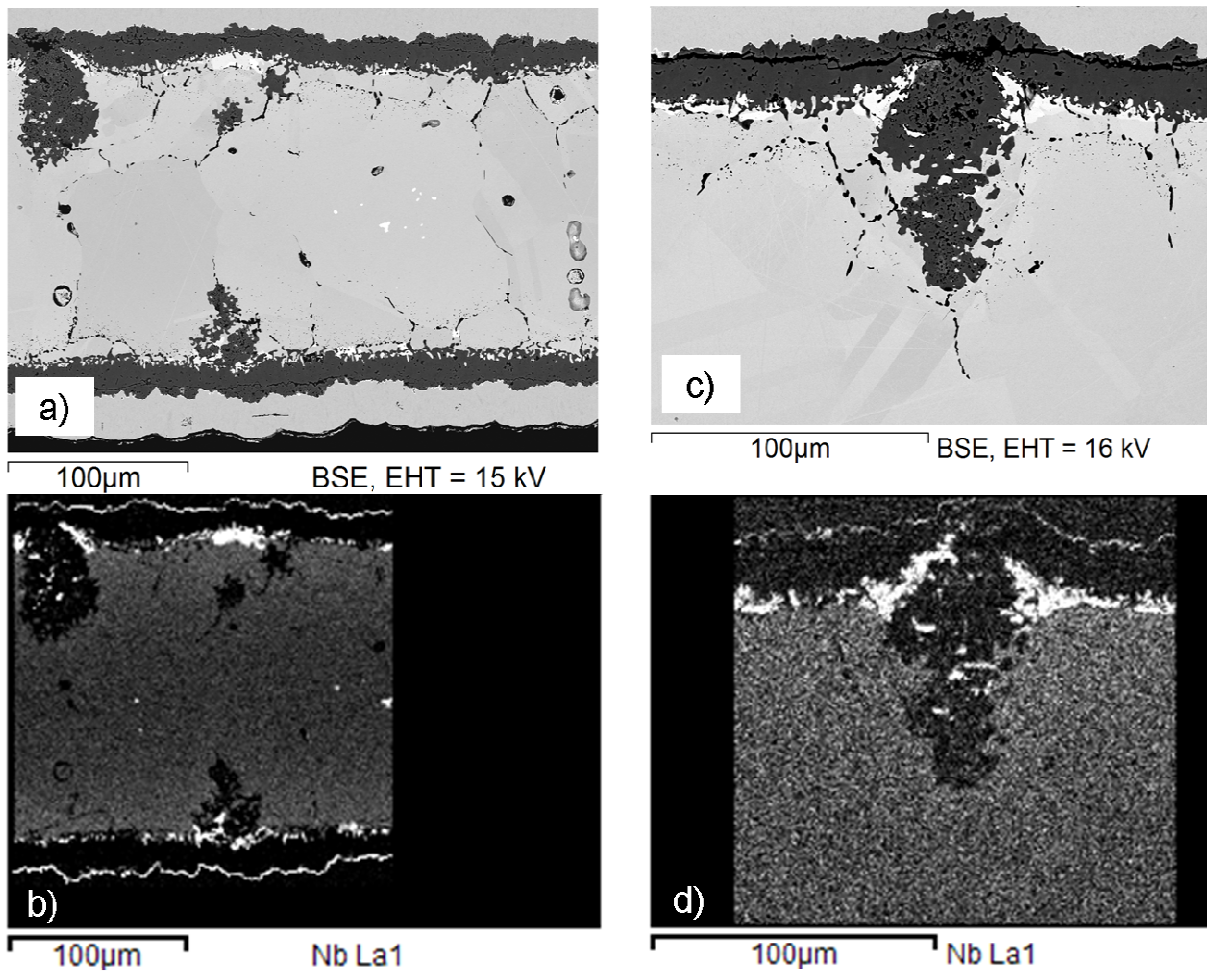


Figure 7.4: SEM/BSE images and EDX mappings for Nb of cross-sectioned 0.14 (a and b) and 0.3 mm (c and d) thick alloy 625 specimens after 1000h oxidation in air at 1000°C

The SPE phenomenon is less pronounced in the thinner foil specimen (0.14 mm) than in the thicker specimen because of the smaller Nb-reservoir. The absolute amount of Nb in the thin specimen (0.14 mm) is approximately 50% of that in the thick one. Therefore the thin specimen has twice less niobium for the precipitation at the scale/alloy interface whereas the thicker specimen is able to sustain a higher niobium flux toward the scale/alloy interface during longer oxidation time. To illustrate the effect of specimen thickness on SPE, a number of DICTRA simulations were carried out (Figure 7.5).

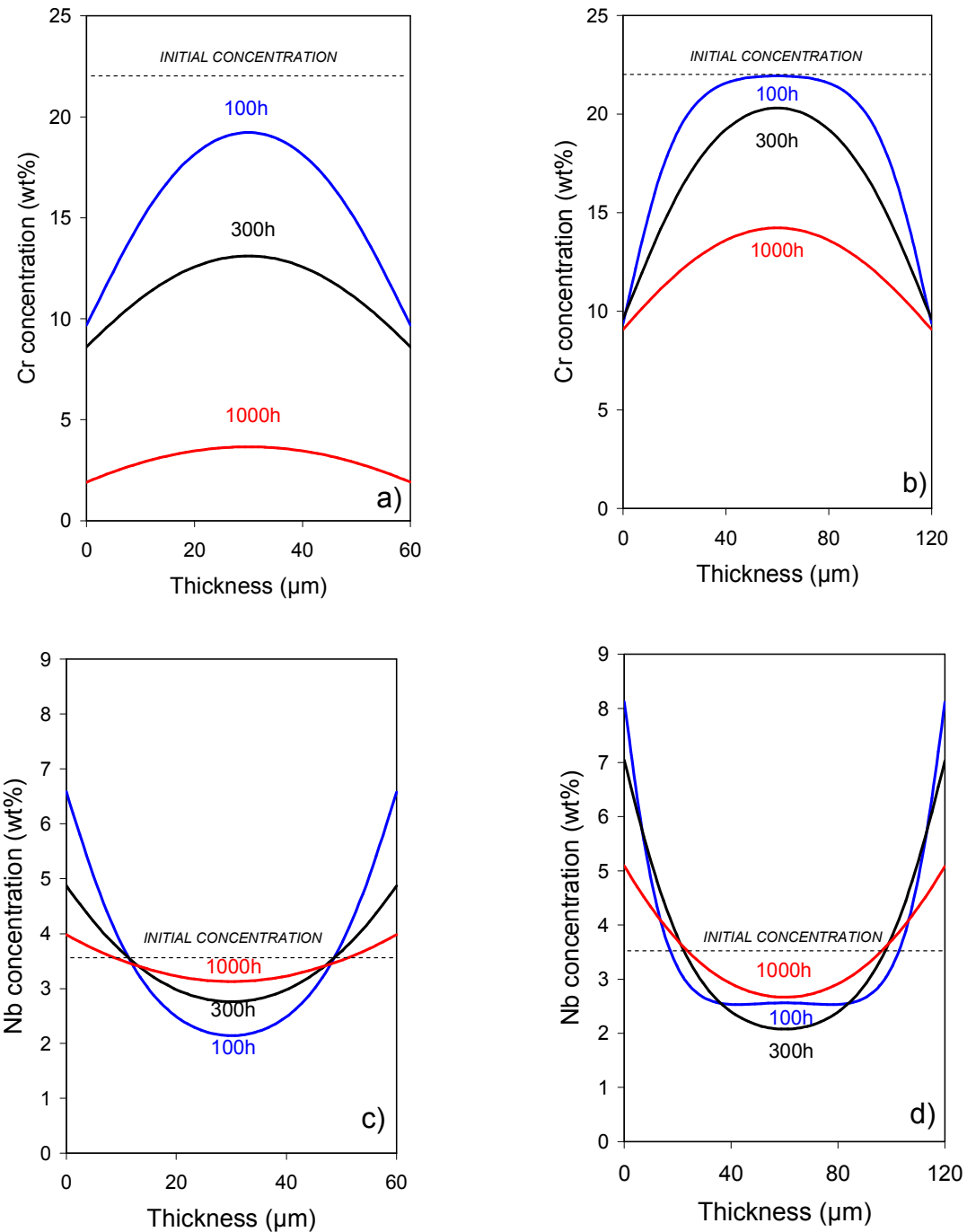


Figure 7.5: Concentration profiles of Cr (a, b) and Nb(c, d) after oxidation up to the maximum exposure time of 1000h at 1000°C calculated for two (60 and 120 μm thick) foils of alloy 625 using DICTRA software and oxidation kinetics from Figure 6.13

The oxidation simulations described in section 6.3 were carried out for two foils of different thickness, i.e. 60 and 120 μm thick, applying the appropriate boundary condition, i.e. a time dependent chromium flux, to both interfaces. The oxidation temperature was set 1000°C. The concentration profiles of chromium and niobium were calculated for three exposure times:

100, 300 and 1000h. The formation of the δ -Ni₃Nb phase was ignored in these calculations to avoid a possible distortion of the element profile due to formation of a continuous δ -phase layer at the scale/alloy interfaces.

The calculated interface concentration of Cr in the 60 μm thick foil specimen after 1000h oxidation is approximately 2 wt% (Figure 7.5a) which is in no way realistic. Breakaway oxidation is expected to occur if the Cr interface concentration would drop below 8-9 wt% [27]. However, oxidation in a low pO₂ environment can be considered to avoid this obstacle because the atmosphere and, first of all, the oxygen partial pressure seem to have no fundamental effect on SPE. Additionally, the calculation shows that the 120 μm thick specimen is less depleted in chromium than the thin one (Figure 7.5a) as would be expected from the Cr-reservoir considerations.

The calculated niobium concentration profiles are qualitatively consistent with the experimental data measured by EDX (Figure 7.2b). The calculations thus clearly confirm the driving force for the observed δ -phase formation (see e.g. Fig. 7.3); although δ -phase formation was not taken into account, clearly Nb uphill-diffusion occurs in direction of the scale/alloy interface. According to Fig. 7.5, the interface concentration of Nb initially increases but then starts to decrease with increasing oxidation time as the chromium concentration gradient decreases (Figures 7.2a and 7.5a). The interface concentration of niobium in the 120 μm thick specimen, e.g. after 1000h (Figure 7.5d), is approximately 1-2 wt% higher than that in the 60 μm thick specimen (Figure 7.5c) due to the larger Nb reservoir in the thicker specimen. It should be noted that the experimentally measured niobium concentration in the vicinity of the scale/alloy interface only slightly exceeds 5 wt%, which is caused by the precipitation of the niobium rich δ -Ni₃Nb phase at the scale/alloy interface. The δ -phase ties up part of the niobium in the δ -Ni₃Nb phase thus decreasing its concentration in the γ -matrix phase.

The WDX line-scans shown in Figure 7.6 summarize the effect of SPE after 1000h oxidation in air at 1000°C in a 140 μm thick foil specimen:

- Chromium depletion as a result of chromia scale growth
- Niobium enrichment at the scale/alloy interface due to uphill-diffusion of Nb

- Molybdenum enrichment at the scale/alloy interface as a result of both interface recession and weak uphill-diffusion of Mo towards the oxide/alloy interface.

The latter effect was experimentally observed on thick specimens, e.g. GDOES profiles shown in Figure 6.16. The molybdenum enrichment in the thin foils is found to be substantially more pronounced after 100h oxidation than after longer exposure times (see Figure 7.7).

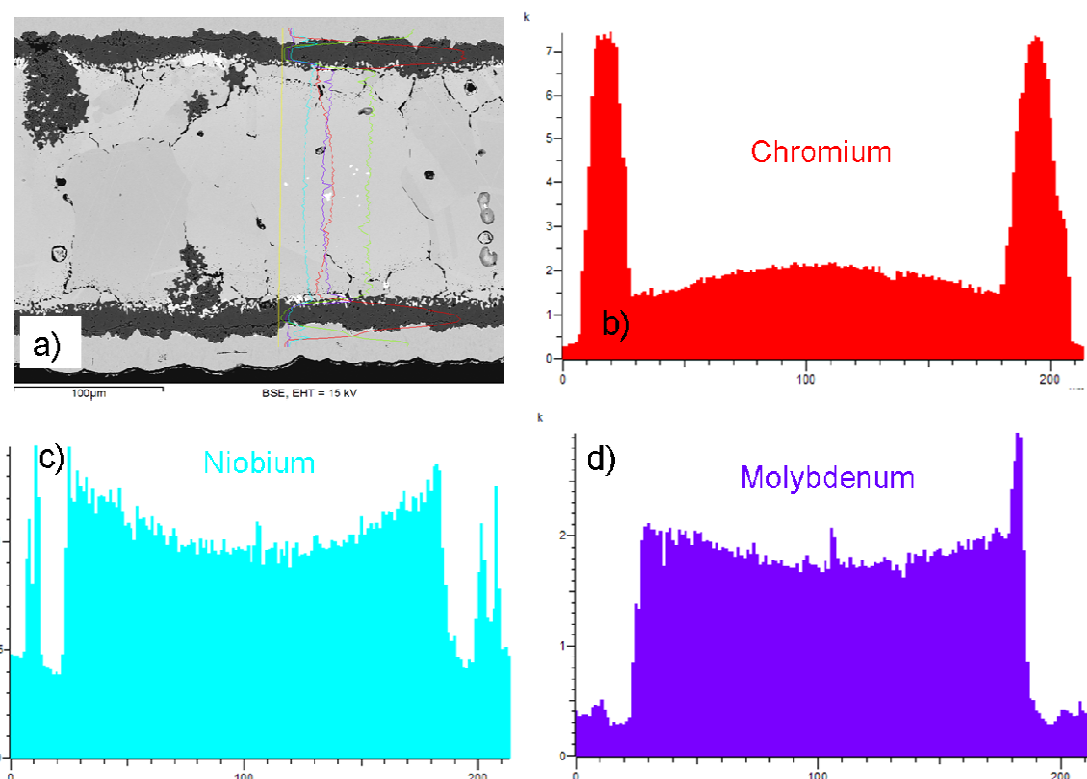


Figure 7.6: WDX line scan showing concentration profiles of Cr(b), Nb(c) and Mo(d) in cross-sectioned 0.14 mm thick foil of alloy 625 after 1000h oxidation in air at 1000°C

This can be explained by the calculated profiles in Figure 7.5. The Cr-depletion profile beneath the oxide scale in a thin specimen is after 100h substantially steeper than those after 300 and 1000h (Figure 7.2a). Consequently, the apparent Mo-“enrichment” at the scale/alloy interface (Figure 7.7) is more pronounced at shorter oxidation times than at longer ones. As the apparent “enrichment” decreases with decreasing oxidation time, this observation has thus to be attributed mostly to the “100% effect” which arises as a result of the interface recession caused by chromium consumption in the subsurface zone of the alloy to form the chromia scale.

It is apparent from the experimental data that the enrichment/depletion process of the δ - Ni_3Nb phase in alloy 625 during high-temperature oxidation is less pronounced in thin specimens than in thick ones because of the smaller Nb-reservoir in thin specimens. It can thus be concluded that a decreasing specimen thickness suppresses occurrence of SPE. The latter statement can be proven by checking whether the δ -phase enrichment/depletion occurs during oxidation of a metal foam specimen which consists of extremely small, sintered metallic particles (chapter 4).

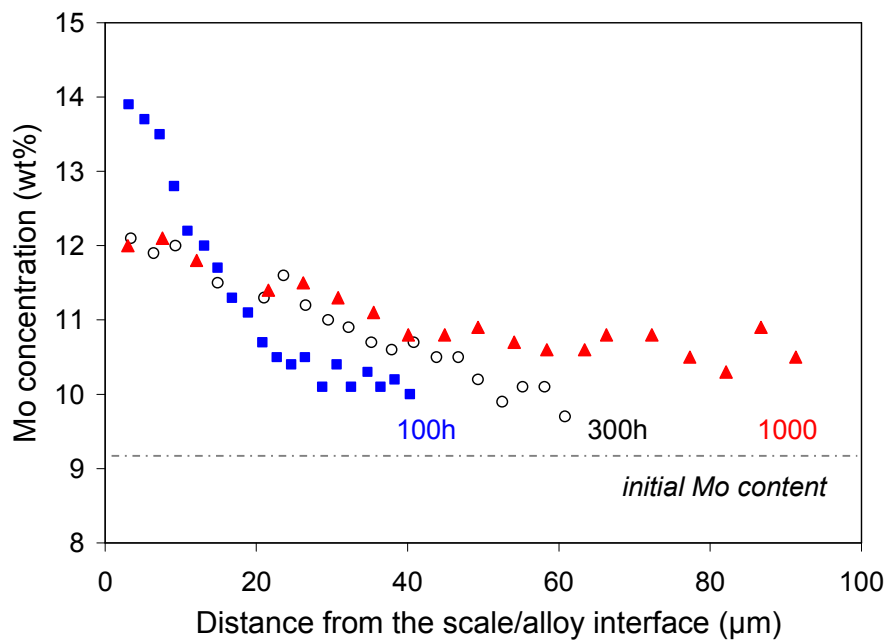


Figure 7.7: Concentration profiles of molybdenum in thin alloy 625 foils after oxidation in air at 1000°C measured by EDX spectroscopy.

A foam specimen of the batch with a mean particle radius of approximately 30 μm was oxidized in air for 100h at 900°C. At this temperature the δ - Ni_3Nb phase is present in the alloy microstructure and exhibits enrichment/depletion behavior in the subscale zone during oxidation of the foil and sheet specimens (see Figure 7.8 and section 6.2).

In contrast to the thick sheet specimens, no significant enrichment of the δ -phase at the scale/alloy interface is found in cross-sectioned foam particles, some of which are shown in Figure 7.8a. A few dispersed δ - Ni_3Nb precipitates are found beneath the chromia scale in Figure 7.8a but cannot be interpreted as the result of significant oxidation-induced uphill-

diffusion of niobium when compared with the sheet specimen shown in Figure 7.8b. The scale/alloy interface in the foam particles is virtually free of precipitates (Figure 7.8a) whereas the δ -Ni₃Nb precipitates form almost a continuous layer of approximately 1 μm thickness beneath the chromia scale in the sheet specimen (Figure 7.8b) already after only 100h of oxidation.

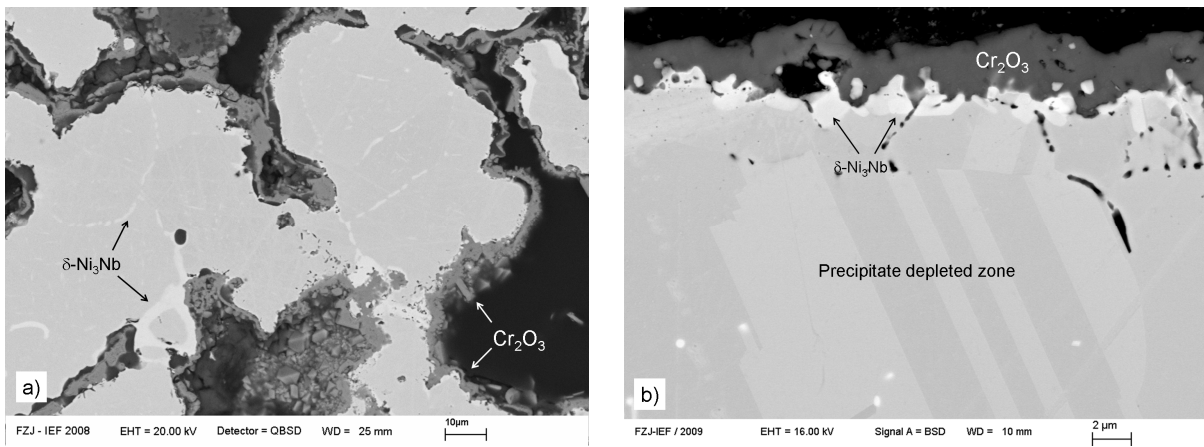


Figure 7.8: SEM images of cross-sectioned metal foam specimen KUP (a) and 1.0 mm thick sheet of alloy 625 (b) after 100 hours of oxidation in air at 900°C

This finding is of great importance for lifetime modeling carried out for metal foams in the next chapter. The SPE effect observed in thick sheet specimens should hardly occur in small metal foam particles and therefore should not affect substantially the breakaway oxidation occurring after a critical depletion of chromium in the foam particles. The lifetime of a spherical foam particle can thus be defined as the time at which the interface chromium concentration drops below the critical level C_B whereby the depletion process is not affected by SPE.

7.3 Dissolution of M₆C carbide during oxidation of thin alloy 625 foils

The M₆C carbide was shown to dissolve in the subscale zone during high-temperature oxidation of alloy 625 sheets as a result of back diffusion of carbon (section 6.5). The corresponding Thermo-Calc calculations revealed that the carbon activity is higher in the chromium depleted zone, i.e. in the subscale zone beneath the chromia scale, than in the bulk

alloy. The 140 μm thick foil shown in Fig. 7.1 exhibits after 300h oxidation at 1000°C a M_6C enrichment zone, approximately 40 μm in width, in the centre of the specimen.

Figure 7.9a shows the distribution of the M_6C phase in the 120 μm thick specimen after oxidation at 1000°C calculated using DICTRA simulations (see Figure 7.5). The width of the M_6C enrichment zone decreases as the oxidation proceeds while the mole fraction of the phase increases in the centre of the specimen. According to Figure 7.4, only a few coarse precipitates of M_6C carbide are seen in the middle of the foil after 1000h oxidation. This apparent contradiction with the DICTRA calculation can be related to the thickness/reservoir effect. If the calculation is carried out for a twice thinner specimen, i.e. 60 μm thick foil, the amount of the M_6C phase after 1000h (area confined by the M_6C profile in Figure 7.9a) is smaller than that in the 120 μm thick specimen (Figure 7.9b).

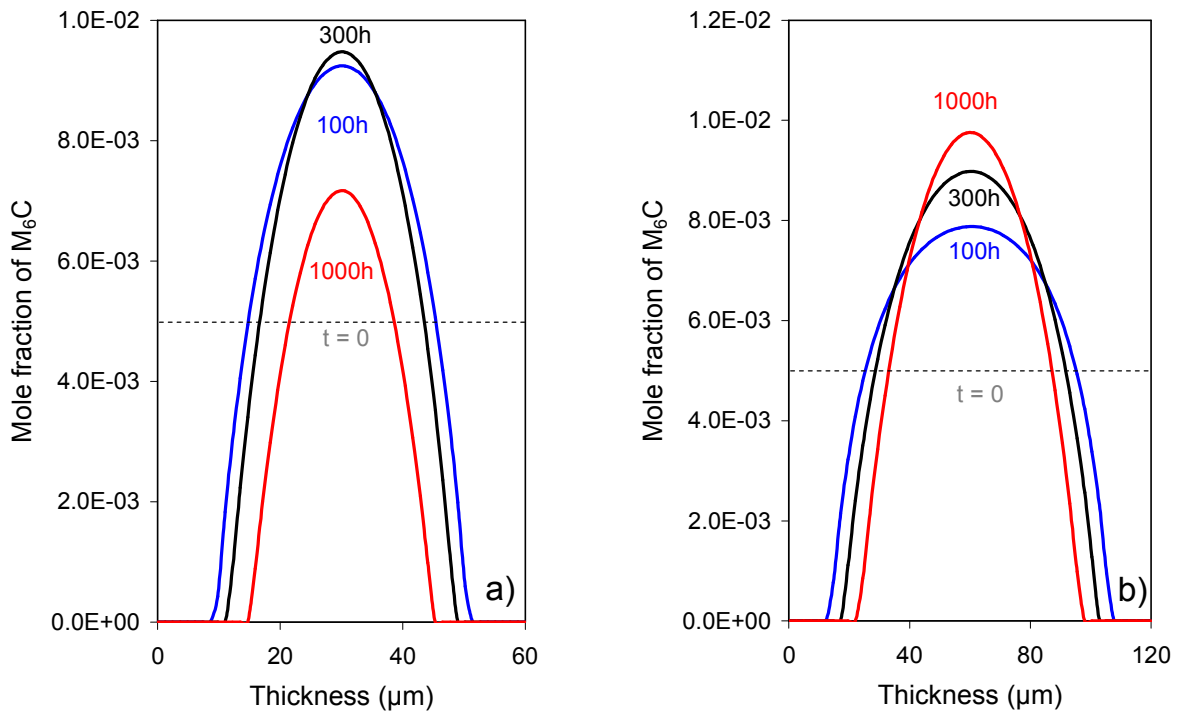


Figure 7.9: Mole fraction of phase M_6C after oxidation up to the maximum exposure time of 1000h at 1000°C calculated for two (60 and 120 μm thick) foils of alloy 625 using DICTRA software and oxidation kinetics from Figure 6.13

The amount of the M_6C phase enriched in the middle of the 60 μm thick foil decreases after prolonged oxidation as a result of strong chromium depletion of the thin specimen (see e.g. Figure 5a). The dissolution of the M_6C phase in the middle of the foil is the result of two

competing processes: (i) continuous chromium depletion as a result of oxidation and (ii) uphill-diffusion of niobium, i.e. another element stabilizing the M_6C phase (Figures 7.6 and 6.20). The smaller Cr- and Nb reservoirs in the thin foils thus result in dissolution of the M_6C carbide after longer exposure times due to a critical Cr- and/or Nb depletion.

7.4 Summary of the specimen thickness effect

The phase transformations in alloy 625 resulting from the oxidation-induced chromium depletion, i.e. depletion/enrichment of the Nb rich $\delta\text{-Ni}_3\text{Nb}$ phase and dissolution of the M_6C carbide in the oxidation affected zone, are substantially affected by the specimen thickness.

The thin specimens are characterized by smaller Cr- and Nb-reservoirs which results in more rapid depletion of chromium and less pronounced enrichment of niobium at the scale/alloy interface.

Decreasing specimen thickness suppresses the enrichment/depletion process of the $\delta\text{-Ni}_3\text{Nb}$ phase and results in complete dissolution of the M_6C carbide after longer exposure times. Therefore these effects are not observed during oxidation of extremely thin-walled specimens, e.g. metal foams fabricated from alloy 625.

The $\delta\text{-Ni}_3\text{Nb}$ phase enrichment at the scale/alloy interface does not occur during high-temperature oxidation of metal foams and can thus be virtually ignored when modeling the oxidation-induced lifetime of INCONEL 625 metal foams.

8. Oxidation behavior of Ni-base metal foams at 700-900 °C

8.1 General remarks

Metal foams are potentially suitable for various high-temperature applications in which low-density components with relatively high mechanical properties are required. Examples of such applications are materials for walls of combustion chambers (or furnaces), high-temperature catalysts supports, heat-exchangers and filters [131-133]. The high-temperature oxidation behavior of metal foams is therefore of substantial technological as well as scientific interest. However, only a very limited number of publications are available which deal with the oxidation behavior of porous metallic components [134, 135].

This chapter presents the investigation of the oxide growth kinetics and the compositional changes beneath the oxide scale during the high-temperature exposure in air at 700-900°C of INCONEL 625 foams (see Table 4.2) which were produced by the Slip-Reaction-Foam-Sinter-(SRFS)-process (for details of the manufacturing process see section 4.1.1). The modeling was employed using the DICTRA software thereby establishing a quantitative relationship between the foam structure and the oxidation limited lifetime under the given oxidation conditions.

8.2 Oxidation behavior of INCONEL 625 foams in air

8.2.1 Data representation

In order to determine the effect of particle size on the oxidation-limited lifetime, oxidation experiments were carried out on a range of foam specimens with different granularity. The microstructure of the as-received foams with various particle size distributions is shown in Fig. 4.2. According to the optical micrographs, only two coarse-grained foams (KUS) and (KUP) had a 3D network microstructure, which resulted in high lifetime values as well as long term mechanical stability of the foam specimens. The rest of the foams consist of particle agglomerates which are poorly linked in space. The quantitative particle size analysis performed on the optical images revealed substantial scatter in particle size; mean values taken as a basis for the lifetime modeling are summarized in Table 8.1.

Table 8.1: Structural characteristics (density, porosity and mean particle radius) of the metal foams studied

Batch designation	Density (g·cm ⁻³)	Porosity (vol. %)	\bar{r} (μm)
LKW	2.10	56	6
MLD	1.24	73	11
MLE	1.36	78	12
MKK	1.68	86	20
KUS	1.73	85	32
KUP	1.32	73	30
MMJ	1.03	87	12
MMH	1.63	83	18
MMK	1.43	86	16
MMM	1.90	85	31

The weight change data for the foams during cyclic oxidation in laboratory air can not be interpreted in an unambiguous way. The specific surface area of the metallic foams can not be defined accurately, i.e. it is too small to be determined by adsorption experiments and it can not be accurately estimated from geometrical considerations due to deviations from the ideal spherical shape of particles and due to their non-uniform size distribution. Therefore the gravimetric data expressed as area specific mass change in mg·cm⁻² vs. time does not yield meaningful information on the time dependence of oxide scale formation and growth. One suitable way to present the weight change data is normalization by the initial sample mass. Such a data treatment allows determining important oxidation parameters, e.g. activation energy, but it is applicable only within one single foam batch with a given particle size distribution. In order to compare oxidation curves of structurally different metallic foams, unified data-sets were considered, irrespective of the geometrical factor. A suitable way to present the oxidation data is to consider weight change during the early stages of oxidation (up to 100h) when the sample geometry (i.e. powder sphere size) does not yet affect the oxidation behavior appreciably. If the thickness of an oxide layer grown on a spherical particle is negligible compared to the particle radius, the oxidation rate will be very similar to that observed on a flat sample of the same material. A spherical particle of a metallic alloy of radius r_0 is considered to react over its entire surface with oxygen. Assuming parabolic oxidation

kinetics, the oxide/metal interface displacement (x_{all}) as a result of chromium consumption can be related to the oxide scale thickness at time t :

$$x_{all} = \frac{1}{\phi} x_{ox} = \frac{1}{\phi} \sqrt{2k_p t} \quad (8.1)$$

Here k_p is the parabolic oxidation rate constant in $\text{m}^2 \cdot \text{s}^{-1}$, ϕ the Pilling – Bedworth ratio, i.e. the ratio of the molar volume of metal oxide formed to the molar volume of the corresponding metal consumed, x_{ox} the oxide thickness and t the oxidation time. The relative shrinkage of the particle surface for $x_{all} \ll r_0$, which is the case during the early stages of oxidation, can be expressed as

$$\frac{\Delta S}{S_0} = \frac{S_0 - S_t}{S_0} = \frac{r_0^2 - (r_0 - x_{all})^2}{r_0^2} \cong \frac{2x_{all}}{r_0} = \frac{1}{\phi} \frac{\sqrt{8k_p t}}{r_0} \quad (8.2)$$

where S_0 and S_t denote the surface area at time 0 and t , respectively. For chromium oxide growing on a Ni-base alloy $\phi = 2.10$ [41]. Using Equation (8.2) for a particle of arbitrary radius of 30 μm and the parabolic rate constant calculated from the weight gain data in Figure 6.5 (see section 6.2), which for alloy 625 is $9 \times 10^{-18} \text{ m}^2 \cdot \text{s}^{-1}$ at 900°C (the experimentally measured value of k_p is in reasonable agreement with the literature data, i.e. $2.0 \times 10^{-17} \text{ m}^2 \cdot \text{s}^{-1}$ at 900°C [136]), it is apparent that the time at which the particle surface is going to shrink by 5% is approximately 128h. According to the metallographic cross-sections of the foams oxidized for 108h at 900°C (see section 8.2.4), no considerable indications for occurrence of breakaway oxidation are found up to this exposure time. Most alloy particles are uniformly covered with a Cr_2O_3 layer, whereas only very few smaller ones are embedded into a “matrix” of voluminous nickel-rich oxide. Therefore it is reasonable to normalize the weigh change data by the weight gain results measured for an alloy 625 sheet (see section 6.2) to the value measured after approximately 100h of oxidation in air, i.e. the mass change of a foam specimen is divided by an arbitrary number in order to equate it with the weight gain in $\text{mg} \cdot \text{cm}^{-2}$ of the sheet specimen at the same time and temperature. This procedure is equivalent to dividing the mass change of the foam specimen in mg by the overall specimen surface area in cm^2 . The weight gain curves of sheet specimens at lower temperatures, i.e. 700 and 800°C, were calculated using the Arrhenius equation and the values of k_p from chapter 6 (Figures 6.5 and 6.13). The activation energy of

chromia growth E_A was estimated to be 222 kJ mole^{-1} which is in good agreement with the value 232 kJ mole^{-1} quoted in reference [136].

8.2.2 Oxidation behavior of metal foams at 700°C

Irrespective of the mean particle size, all foams exhibit protective, near parabolic oxidation behavior at 700°C up to the maximum exposure time of 1000h (Figure 8.1). The experimental weight gain data shows no deviation from the parabolic fit curve, i.e. even the metal foam with the finest particles (LKW, $\bar{r} = 6.1 \pm 1.8 \mu\text{m}$) exhibited no indication for scale failure up to the maximum exposure time of 1000h.

A few local agglomerations of completely oxidized, very small particles are visible in the optical micrographs (Figure 8.2) of the foams but they do not contribute essentially to the overall weight change of the entire foam specimen and do not result in a substantial deviation of the overall observed near parabolic time dependence of the weight change curve.

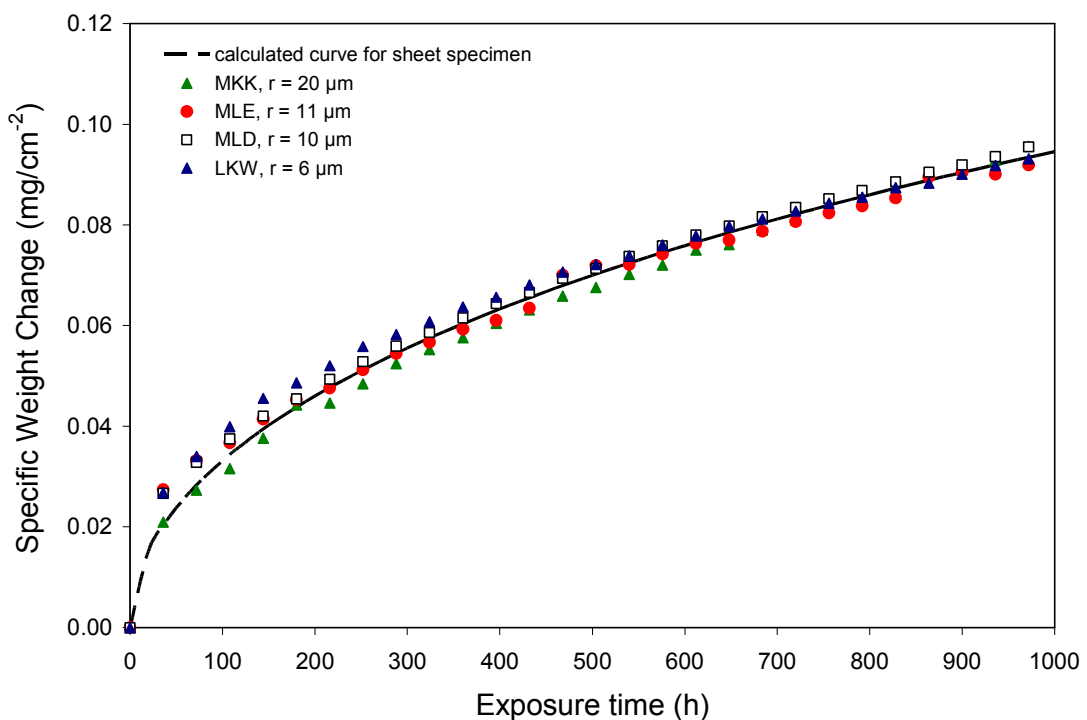


Figure 8.1: Specific weight gain data for various alloy 625 metal foams during cyclic oxidation in air at 700°C compared with calculated weight change data for sheet specimen

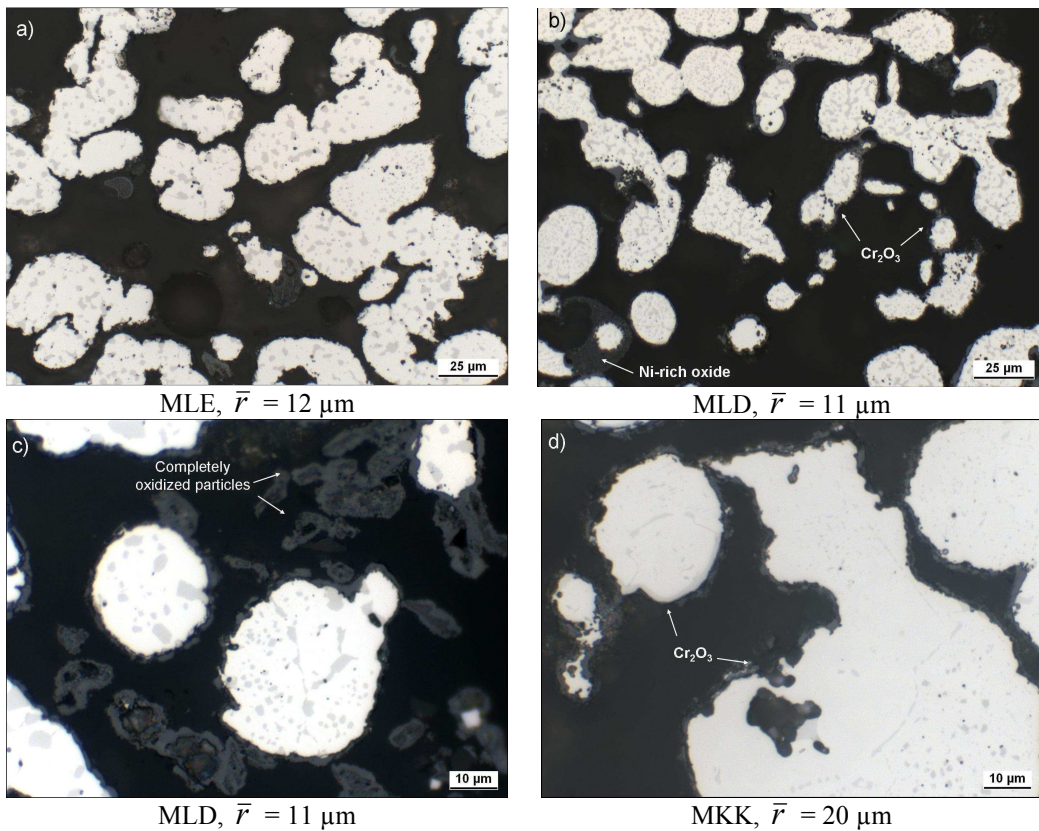


Figure 8.2: Optical micrographs of various INCONEL 625 metal foams after cyclic oxidation in air at 700°C: (a) MLE after 100h; (b) and (c) MLD after 1000h; (d) MKK after 1000 h

After 100h oxidation (Figure 8.2a) the light optical micrographs do not allow to distinguish clearly visible signs of the scale formation, i.e. the chromia scale is extremely thin. Figure 8.2b shows the relatively small foam particles after 1000h oxidation at 700°C in air indicating that virtually all particles are covered with a thin and continuous chromium oxide layer. The foam with larger foam particles (MKK) shows no indication of breakaway oxidation after 1000h oxidation (Figure 8.2d) whereas extremely small foam particles ($r \leq 3\mu\text{m}$) are completely oxidized as shown in Figure 8.2c.

8.2.3 Oxidation behavior of metal foams at 800°C

Figure 8.3 shows that the most fine-grained material (LKW) exhibits at 800°C accelerated oxidation after approximately 250h, subsequently showing a substantially different parabolic range with a higher value of the parabolic rate constant. The oxygen uptake calculated per 1 gram of the foam sample indicates that approximately 70% of the metal has been transformed

into oxide after the 830 h oxidation. This makes any further analysis of the oxidation parameters in the way mentioned above unsuitable because of unaccounted surface recession effect. The testing of the LKW specimen was therefore stopped after 830 h because of severe sample cracking (Figure 8.4) which eventually would lead to destruction of the foam sample.

The weight change curve of the foam with a twice larger mean particle size (MLD) starts to deflect from the parabolic behavior after approximately 500h. Deviation form the parabolic shape of the curve is attributed to breakaway oxidation of smaller particles constituting the foam (Figure 8.5). As chromium is continuously removed from the particle surface as a result of chromia scale growth, small foam particles are rapidly depleted in Cr due to their low chromium reservoir. After the Cr-concentration at the oxide/metal interface has decreased below C_B , formation of Cr_2O_3 can no longer be sustained and voluminous, rapidly growing Ni-rich oxides are formed. As the oxidation proceeds, larger particles undergo accelerated breakaway oxidation, which manifests itself in faster oxidation kinetics and results in mechanical breakdown of the foam specimens after a certain time. The time at which a normalized weight gain curve of a foam sample starts to deviate from the parabolic time dependence can in a first approximation be defined as a measure of the foam lifetime, i.e. the average time to breakaway.

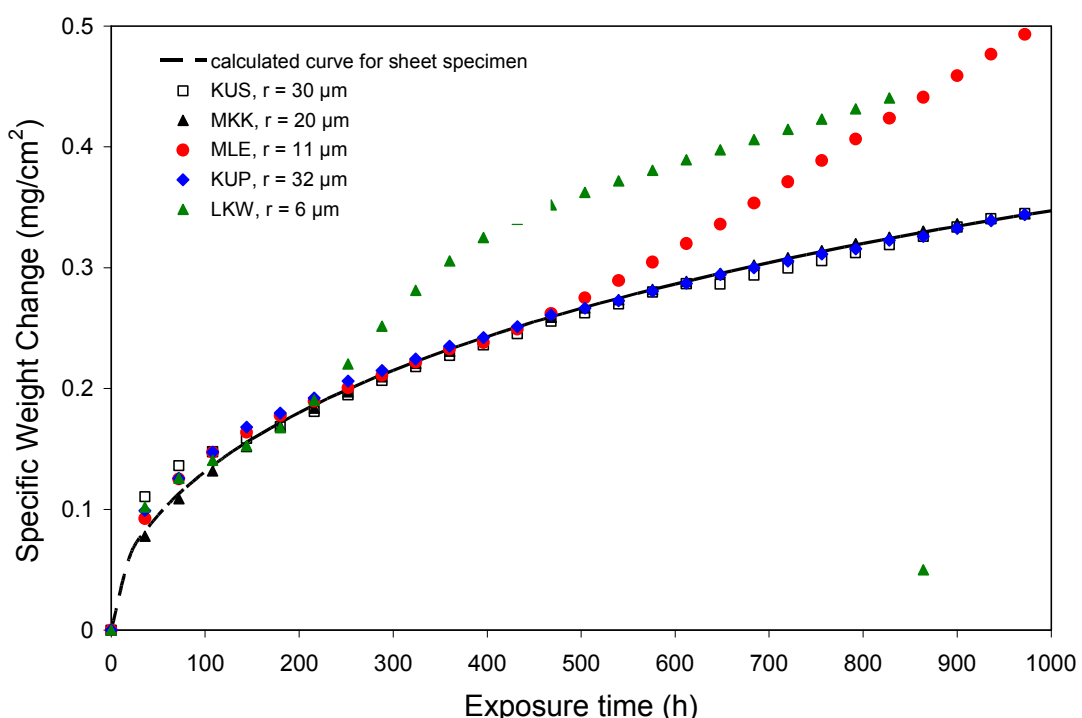


Figure 8.3: Specific weight gain data for INCONEL 625 metal foams during cyclic oxidation in laboratory air at 800°C

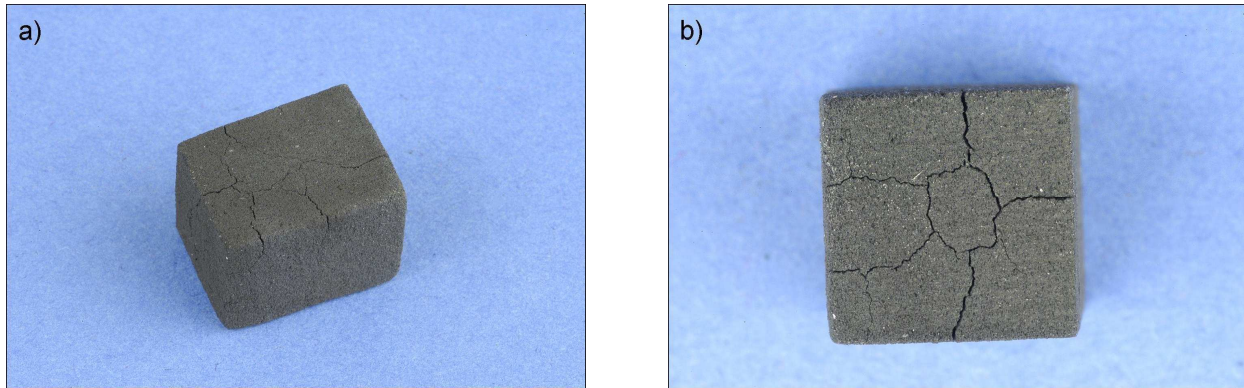


Figure 8.4: Macroimages of the LKW foam specimen after cyclic oxidation in air at 800°C for 830 h

Figure 8.5 shows the microstructures of the metal foams after oxidation in air at 800°C. The foam particles of the most fine-grained material LKW are covered with a thin layer of chromia after 100h exposure (Figure 8.5a). After 823h exposure, the foam specimen exhibits cracks (Figure 8.4) and weight loss (Figure 8.3) due to mechanical disintegration of the specimen. The metal foam particles thus change into poorly connected oxide spheres (Figure 8.5b).

The coarser foam MLD (11 µm) remains intact after 300h exposure (Figure 8.5c) but shows evident signs of breakaway oxidation after 1000h (Figure 8.5d) which correlates with the sudden increase in the oxidation kinetics of this foam (Figure 8.3) after approximately 500h. Based on the optical micrographs, particles smaller than approximately 10 µm underwent breakaway oxidation thus contributing to the accelerated oxidation, i.e. deviation from the overall near parabolic behavior, of the metal foam. As seen in Figures 8.5e and 8.5f, the coarse-grained metal foams MKK and KUS exhibited protective oxidation behavior at 800°C. The gravimetric curves exhibited a near parabolic time dependence up to 1000h exposure (Figure 8.3) while the microstructures of these foams show no signs of Ni-rich oxide particles formed even after 1000h exposure at 800°C. These foams retain near parabolic behavior because their respective times to breakaway have not yet been reached.

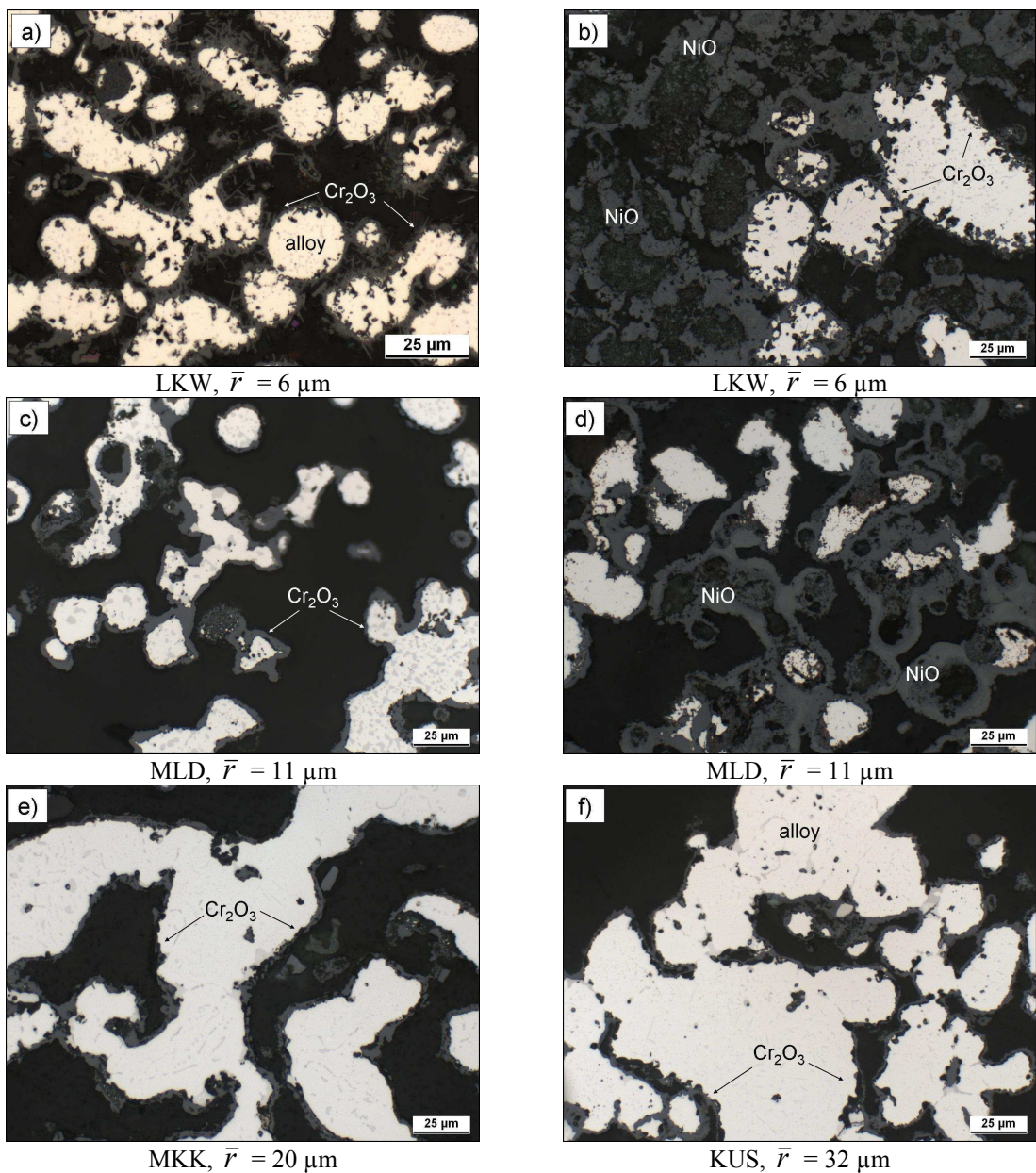


Figure 8.5: Optical micrographs of various INCONEL 625 metal foams after cyclic oxidation in air at 800°C: LKW after 100 (a) and 823h (b); MLD after 300 (c) and 1000h (d); MKK (e) and KUS(f) after 1000h

8.2.4 Oxidation behavior of metal foams at 900°C

At 900°C the lifetime for the foam MLD appears to be approximately 216h, i.e. 50% of that at 800°C (Figure 8.6), while the foam LKW is transformed completely into oxide powder during the first 36h of exposure at 900°C.

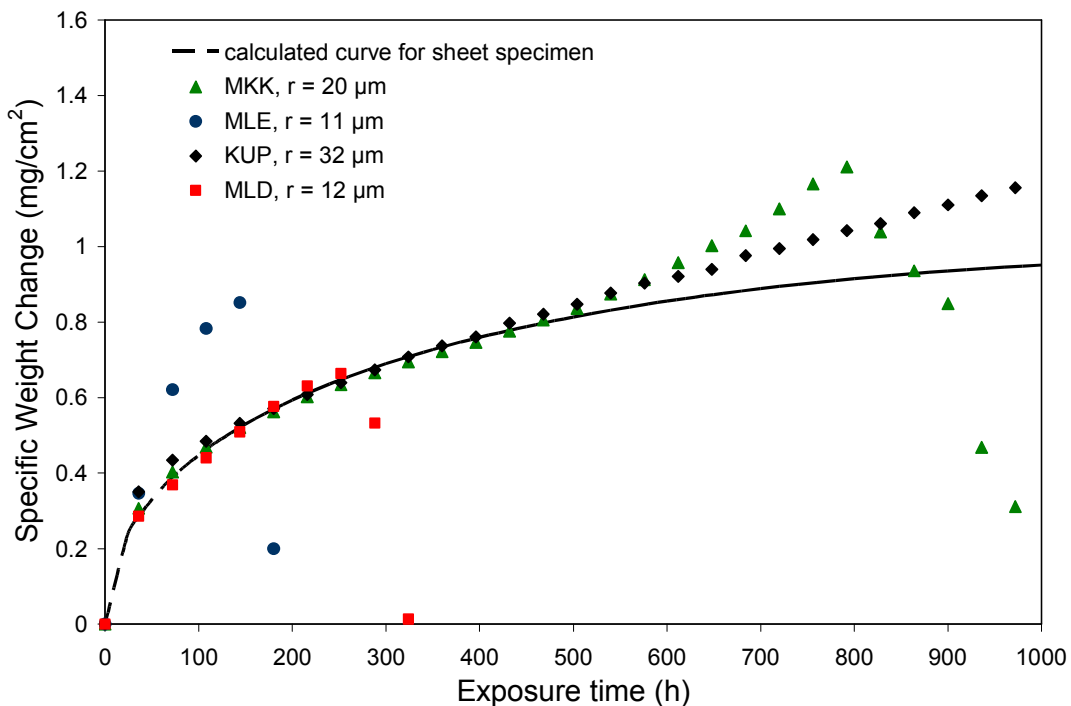


Figure 8.6: Specific weight gain data for INCONEL 625 metal foams during oxidation in laboratory air at 900°C

The optical images of the cross-sectioned foam MLD after 100 and 216h at 900°C in Figures 8.7a and 8.7b illustrate that most alloy particles are virtually completely transformed into oxide. The foam MKK ($\bar{r} = 20 \mu\text{m}$) started to show accelerated oxidation after 500h and considerable weight loss after 792h. As the time to breakaway for MKK is not reached after 100h, there are no indications of NiO formation in the foam microstructure (Figure 8.7c). After 1000h oxidation, the alloy particles of MKK are covered with a thick, multilayered oxide scale, the outer part containing Ni-rich oxides (Figure 8.7d).

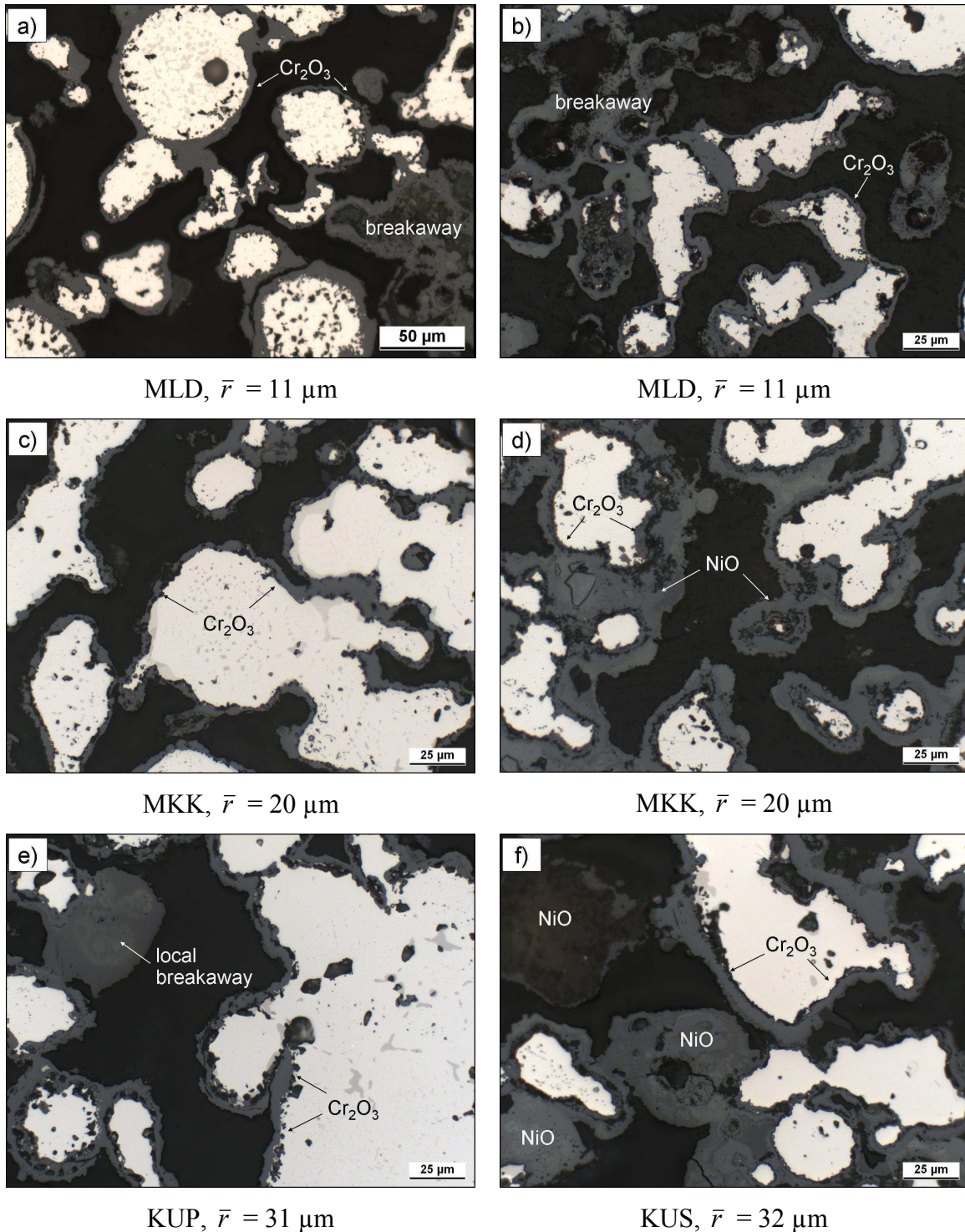


Figure 8.7: Optical micrographs of various INCONEL 625 metal foams after cyclic oxidation in air at 900°C: MLD after 100 (a) and 216h (b); MKK after 100 (c) and 1000h (d); KUP after 100h (e) and KUS (f) after 1000h

The most coarse-grained foams KUP and KUS ($\bar{r} = 30 \mu\text{m}$) started to exhibit breakaway oxidation at 900°C after approximately 600h. The optical micrographs of the foam KUP after 100h oxidation at 900°C (Figure 8.7e) show a few local breakaway spots on particles with $\bar{r} <$

10 μm , whereas the larger ones are covered with a uniform chromia layer. After 1000h exposure at 900°C, the coarse-grained foam KUS is beyond its time to breakaway. The smaller foam particles suffered from breakaway oxidation (Figure 8.7f) thus contributing to the accelerated oxide growth starting approximately after 500h reflected in the weight gain curves (Figure 8.6).

Since all metal foams suffer from breakaway oxidation during exposure up to 1000h at 900°C, additional cyclic oxidation tests in air were carried out on an additional number of foam specimens with different granularity to acquire a more extensive set of breakaway data as a function of foam microstructure for the validation of the lifetime model. The weight gain curves in Figure 8.8 show stronger deviations from the parabolic oxidation kinetics compared to the curves in Figure 8.6.

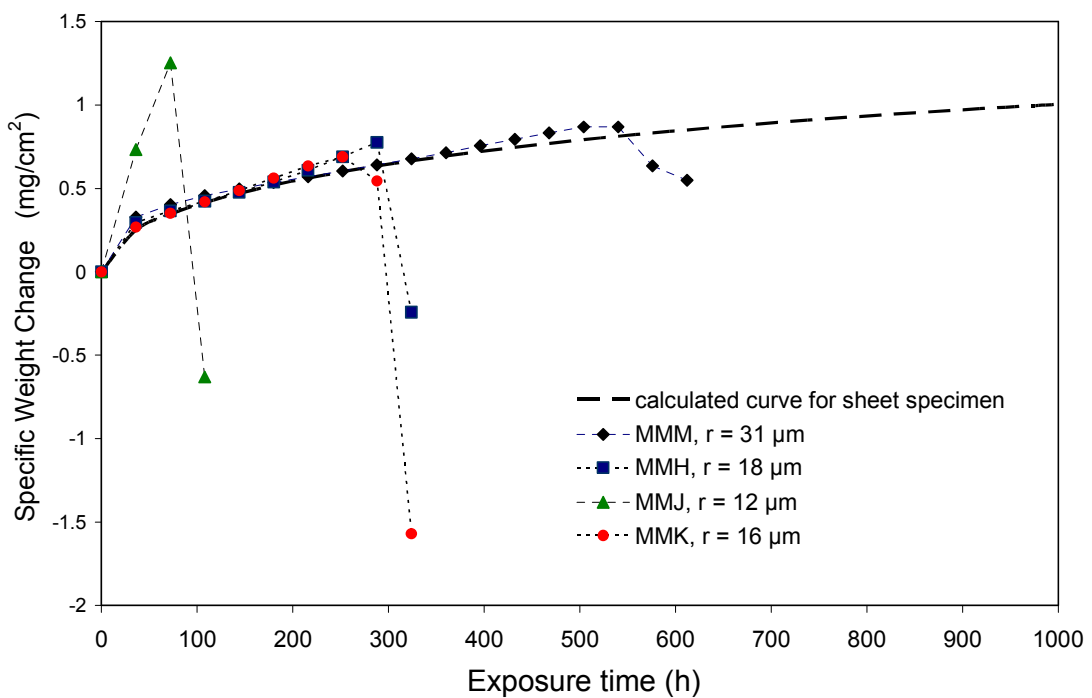


Figure 8.8: Specific weight gain data for INCONEL 625 metal foams during cyclic oxidation in laboratory air at 900°C

Even the most coarse-grained foam MMM ($\bar{r} \sim 31 \mu\text{m}$) revealed a shorter lifetime than the foams KUS and KUP. Although its mean particle radius is comparable with that of the foams KUS and KUP, the accelerated oxidation of the MMM specimen at 900°C begins approximately 250h earlier than for the foams KUS and KUP (600h compared to 350h). After

500h the foam MMM suffered severe weight loss and it readily mechanically disintegrated (Figure 8.9). The longer lifetimes of the foams KUS and KUP are explained by their network microstructure, whereas the MMM foam consisted of agglomerations of metal particles uniformly distributed in space.

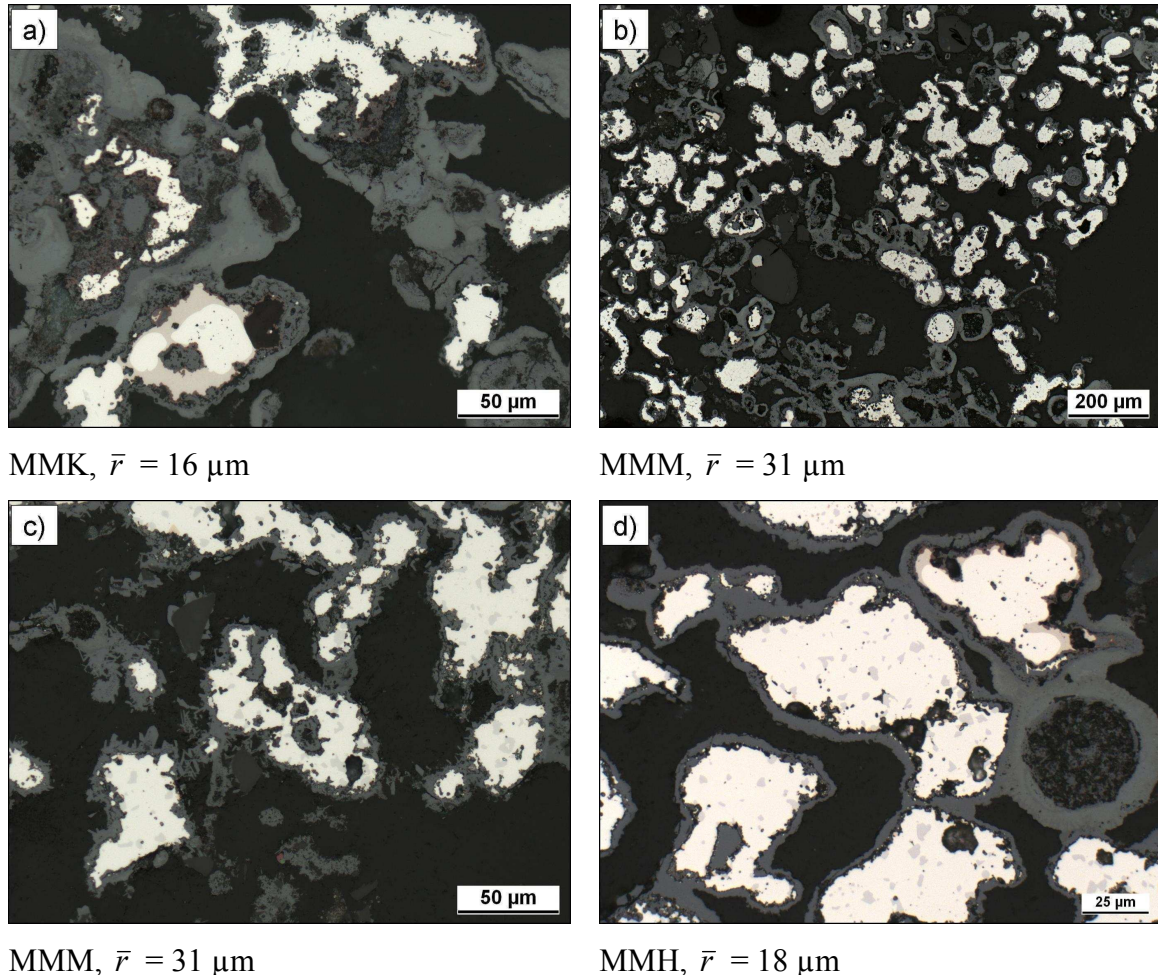


Figure 8.9: Optical micrographs of INCONEL 625 metal foams after oxidation in air at 900°C: (a) MMK after 324h; (b) and (c) MMM after 612h; (d) MMH after 312h

The presented results illustrate that the weight change data for the INCONEL 625 metal foams with respect to occurrence of breakaway oxidation is in qualitative agreement with the general understanding of the oxidation behavior of thin-walled components. The foam microstructure affects the lifetime in two ways: (i) lifetime increases with increasing particle size; (ii) a 3D network structure formed by properly sintered foam particles can increase the lifetime to some extent due to the higher mechanical stability of the foam.

8.3 Chromium depletion in alloy 625 foam particles

8.3.1 EDX spectra

In order to estimate the extent of chromium depletion in small foam particles, EDX spectra were taken on a particle of approximately 25 µm in diameter in the foam KUP oxidized in air at 900°C for 1000h. The particle shown in Figure 8.10 is not completely oxidized; however, it is covered with a thick multilayered oxide scale. The outer scale consists of a voluminous Ni-rich oxide underneath which a non-even Cr_2O_3 layer is present. The inner part of the scale is rich in nickel-chromium spinel and niobium oxide covering the metallic remnants of the foam particle. According to the EDX measurements, the chromium content in the particle dropped from the initial value of 21.5 to 2.1 wt %; the niobium content decreased from 3.5 to virtually zero, i.e. below the detection limit by EDX.

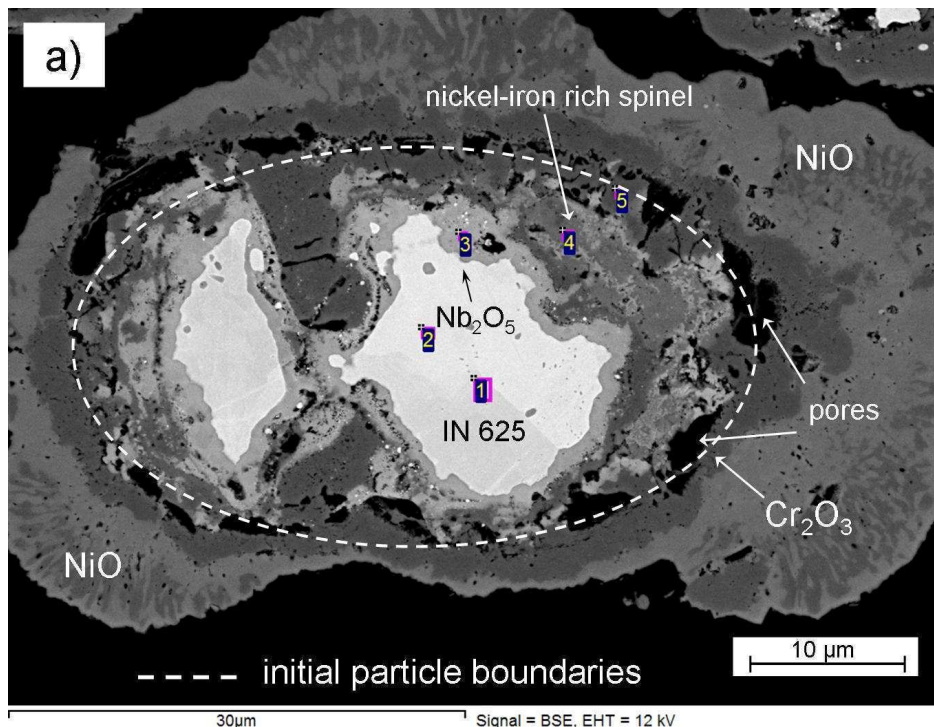
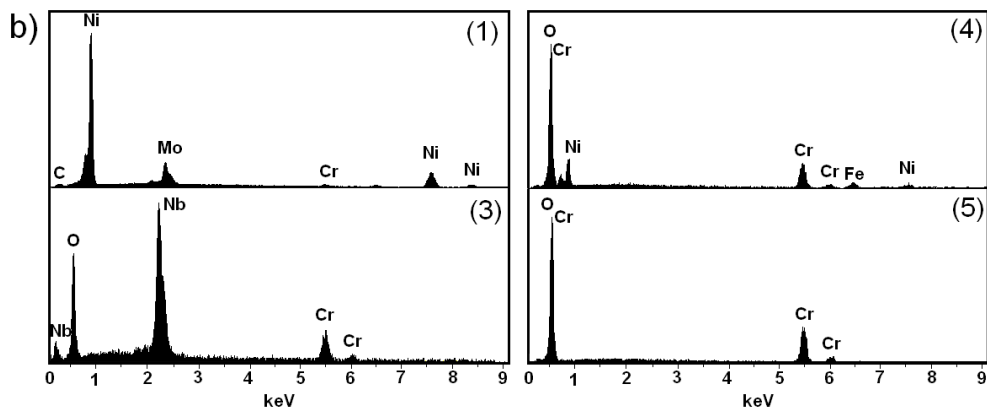


Figure 8.10: SEM/BSE-image of the cross-section of a particle in foam KUP after 1000h exposure at 900°C in air and EDX spectra (accelerating voltage 12 kV) of points marked in figure (a)



Continued Figure 8.10

Apparently, the particle underwent breakaway oxidation long before the exposure time of 1000h was reached. The Cr depletion model described in section 8.6 revealed that the Cr concentration in the middle of the finest particle with a radius of 12 µm decreased from 21.5 to 2.1 wt% after approximately 4 hours of oxidation, i.e. far less than the exposure time of 1000h. A number of EDX spectra were measured on a chromium depleted foam particle in the same foam specimen after 1000h exposure in air (Figure 8.11).

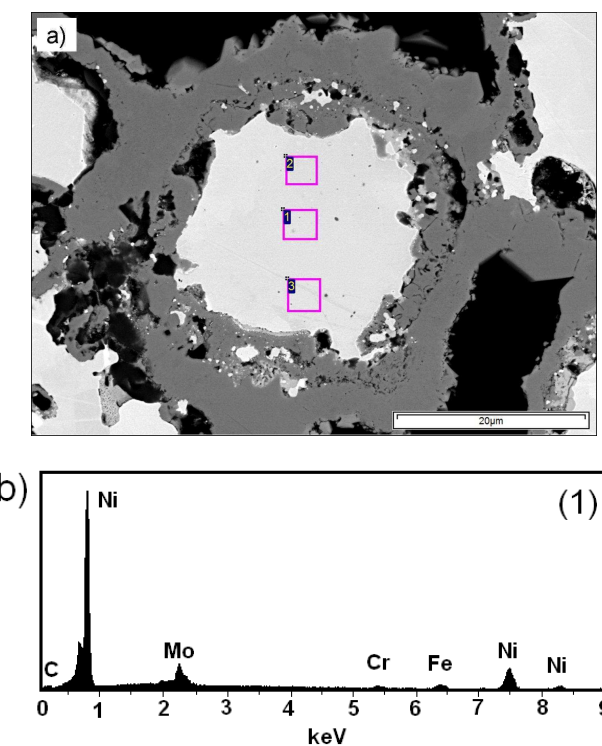


Figure 8.11: SEM/BSE-image of the cross-section of a particle in foam KUP after 1000h exposure at 900°C in air and EDX spectrum (accelerating voltage 12 kV) of the area marked 1 in figure (a)

The average chromium concentration in the failed foam particle was found to be approximately 1.7 wt%, as shown in Figure 8.11a, (see Table 8.1) irrespective of the analysis point in the particle cross-section.

Table 8.1: *Chemical composition of chromium depleted alloy particle shown in Figure 8.11 in wt% measured using EDX spectroscopy (accelerating voltage 12 kV)*

No.	Ni	Mo	Fe	Cr	Nb	Si
1	79.1	10.9	7.2	1.7	1.2	0.0
2	78.7	11.2	7.1	1.7	1.3	0.0
3	80.6	10.4	6.9	1.6	0.6	0.0

8.3.2 Chromium depletion profiles in foam particles

According to classical Wagner's oxidation theory [29], for a binary single-phase alloy, a constant chromium concentration would establish at the scale/alloy interface during the time period of protective chromia scale formation if certain conditions are fulfilled:

- The specimen is flat;
- The specimen is semi-infinite;
- The scale thickening rate is parabolic;
- Interface recession is ignored.

The interface concentration of the scale-forming element (here Cr) is mainly governed by the ratio between the oxidation rate constant k_p and the chromium alloy interdiffusion coefficient D (see Equation 2.14), i.e. the interface concentration will decrease with increasing ratio k_p/D .

At least two of the requirements listed above are not fulfilled for metal foam particles due to geometry effects. First, the foam particles are spherical and therefore have a larger surface to volume ratio than a flat specimen (see section 8.2.1). This means that, after a given time, the subsurface region of a spherical specimen would be more depleted in the scale-forming element than that beneath an oxide scale of a flat specimen [35]. In other words, the spherical

particles tend to become depleted faster than flat specimens of the same thickness/diameter, i.e. the metal particle would suffer earlier from breakaway oxidation than their flat counterparts.

Figure 8.12 shows the concentration profiles of chromium calculated using DICTRA for flat and spherical geometries of alloy 617. The input data for the oxidation rate were taken from [137] for a nickel-base alloy 617 containing 22 wt % of chromium after oxidation at 950°C.

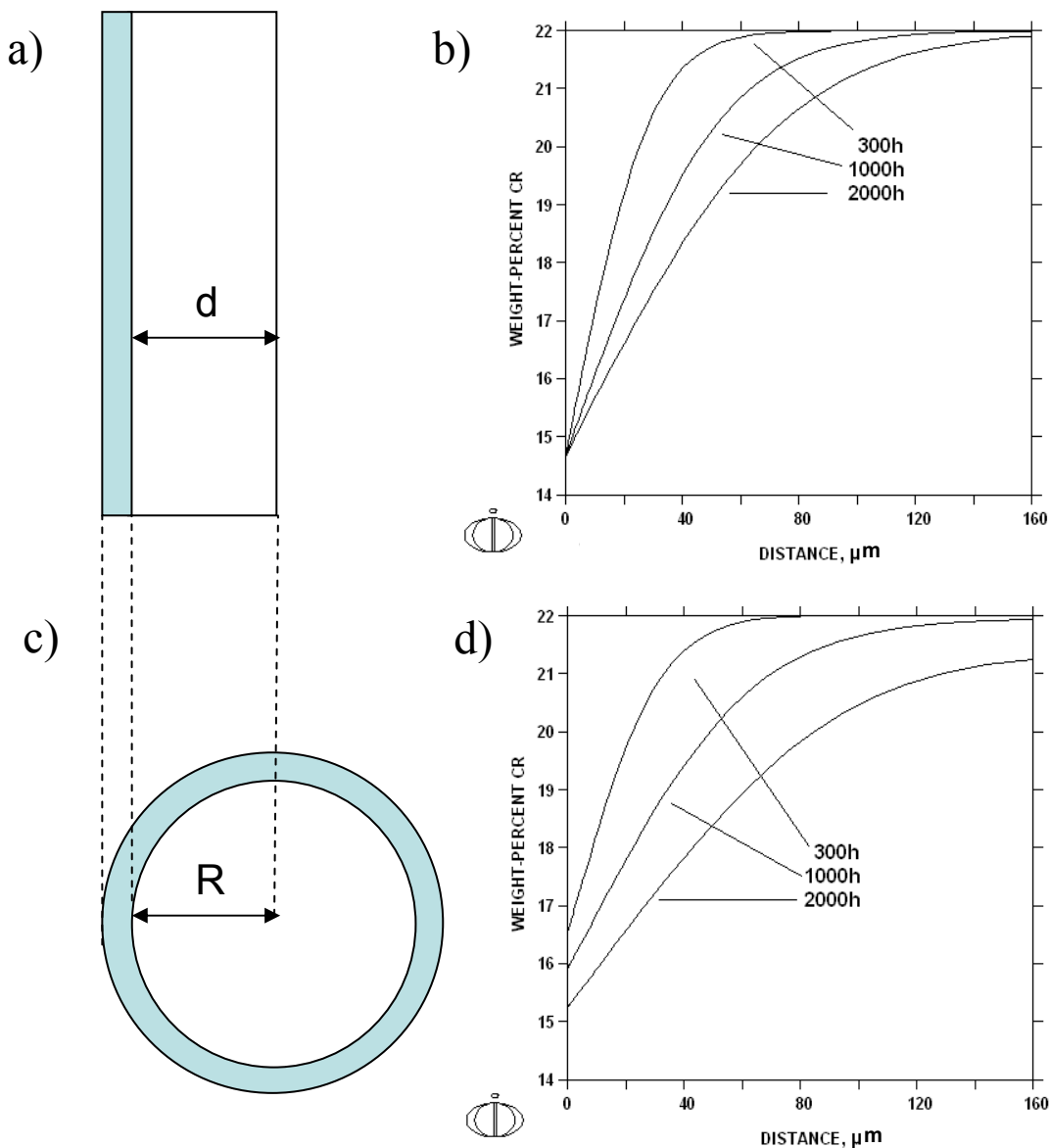


Figure 8.12: Schematic representation of depletion processes in a flat (a, b) and spherical (c, d) specimen of chromia-forming Ni-base alloy 617 of same thickness/diameter. The concentration profiles were calculated using oxidation data taken from reference [137]

Although a relatively thick specimen was considered (160 µm is half-thickness or radius, respectively) the geometry effect can be well recognized in the spherical specimen. The scale/alloy interface concentration of chromium in the sphere decreases with increasing oxidation time whereas it remains constant in the flat specimen. EDX line scans were conducted on several cross-sectioned foam particles of the coarse-grained foam KUS after 100h oxidation at 1000°C (Figure 8.13). Taking the oxidation rate measured for flat specimens at 1000°C (see section 6.4), the concentration profile of chromium was calculated using DICTRA (Figure 8.14). Although the foam particle in Figure 8.13 is larger than the average particle size (160 µm in diameter) in the foam, the chromium concentration is lower than 22 wt% throughout the entire particle, i.e. fast diffusion of chromium at 1000°C results in substantial chromium depletion also in the centre of the particle.

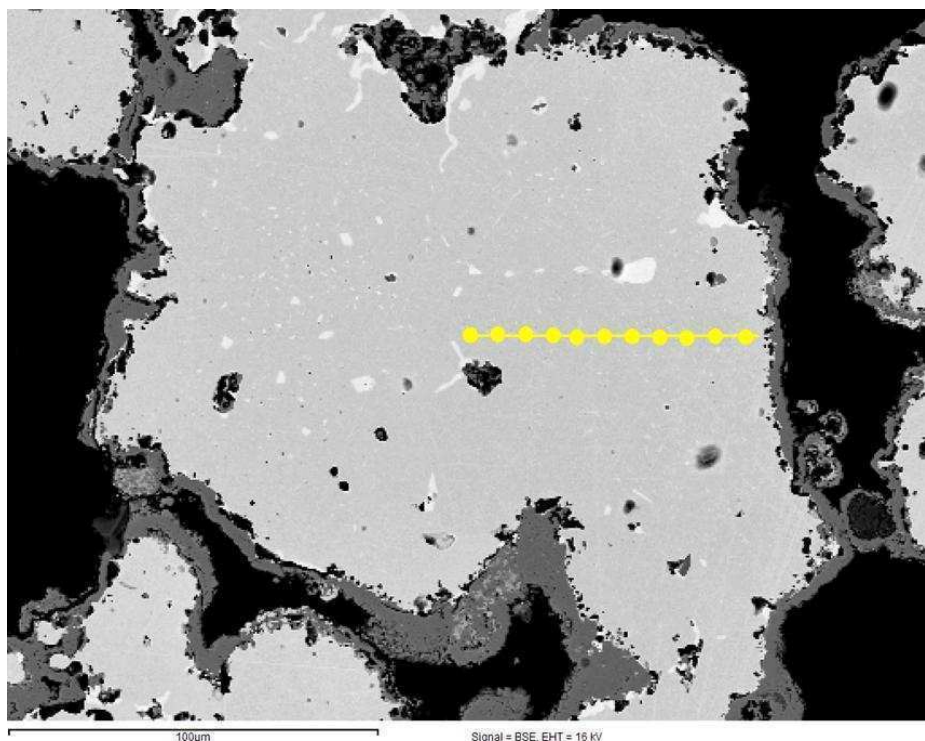


Figure 8.13: SEM/BSE image of a cross-sectioned particle in foam KUS after 100h oxidation at 1000°C; the yellow points indicate the area analyzed by EDX

An essentially steeper Cr concentration profile was measured in a smaller foam particle (100 µm in diameter) found in the same metallographic cross-section (Figure 8.15).

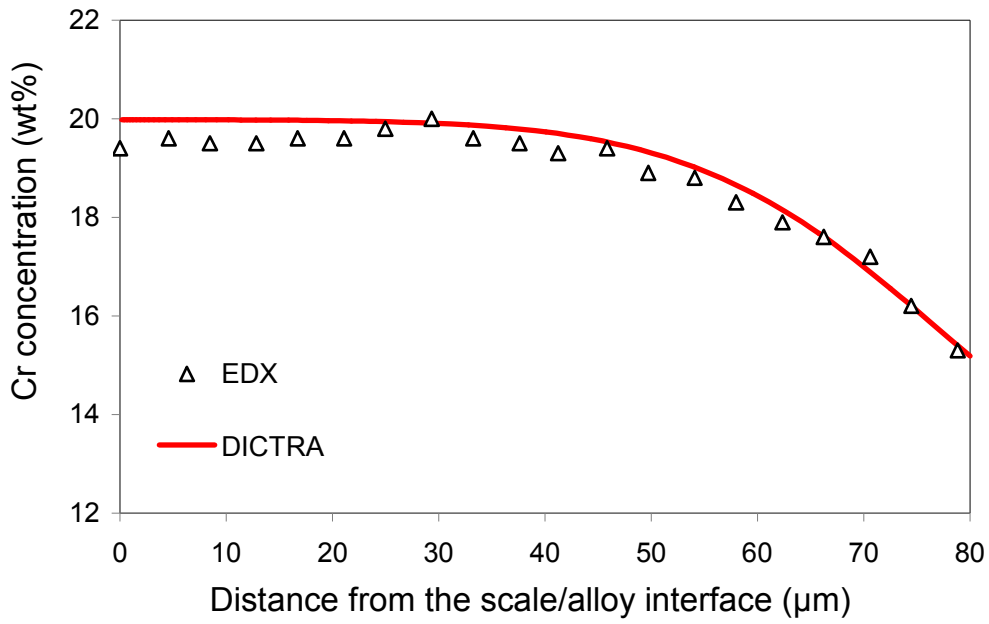


Figure 8.14: Chromium concentration profile calculated using DICTRA compared with EDX point measurements on the foam particle shown in Figure 8.13 (100h oxidation in air at 1000°C)

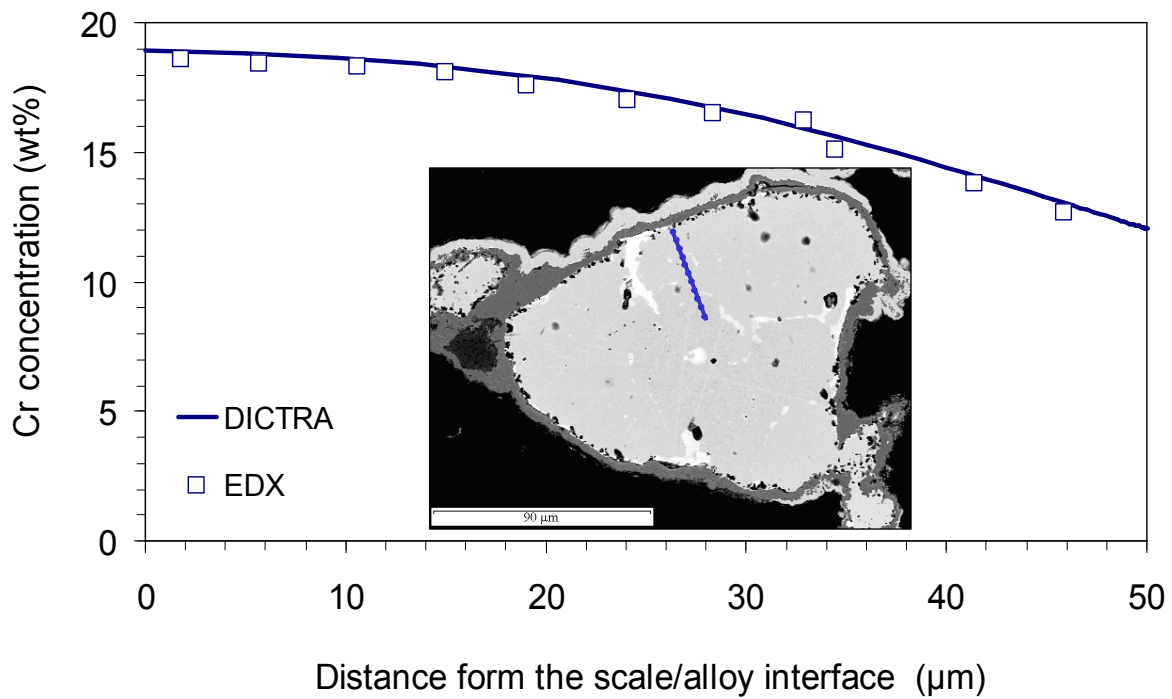


Figure 8.15: Chromium concentration profile calculated using DICTRA compared with the data measured using an EDX line scan in foam KUS (100h oxidation in air at 1000°C)

The highest chromium concentration in the middle of the particle cross-section is less than 19 wt% whereas the interface concentration of Cr is approximately 12 wt%. The chromium

concentration profiles suggest that the smaller foam particles will suffer from chemical breakaway earlier than the larger ones due to stronger chromium depletion as a result of a larger surface to volume ratio. The latter is experimentally observed in the gravimetrical studies (see section 8.2). The time to accelerated oxidation of the metal foam increases with increasing the foam granularity.

Thus, the EDX measurements conducted on the “failed” metal foam particles illustrate the mechanism of breakaway oxidation. The increase in oxidation rate which is observed experimentally on fine-grained metal foams at higher temperatures (800-900°C) is directly associated with the formation of a less protective, fast growing oxide scale (e.g. Ni-rich oxides) after occurrence of a critical chromium depletion. The model to predict the lifetime of the metal foams should therefore be based on a balance between chromium consumed by oxidation and remaining chromium reservoir in a spherical foam particle. The corresponding diffusion equation has to be solved with a boundary condition defined as chromium consumption kinetics which is governed by the growth rate of the chromia scale. For that purpose a separate set of oxidation tests on flat sheet specimens were carried out to acquire more accurate and reliable oxidation rates than can be determined from metallographic cross-sections of oxidized metal foams.

Meaningful oxidation rates (for instance expressed in oxygen uptake per surface area) can not be determined from the weight change data derived in the oxidation tests performed on metallic foams because it is virtually impossible to accurately define their specific surface area. Also a metallographic oxide thickness measurement is not an appropriate way to estimate oxidation kinetics correctly because the oxide layers presented in the metallographic cross-sections of an oxidized particle are for the most part not located normal to the grinding surface, i.e. the oxide thickness is systematically overestimated in virtually all cross-sections. None of these obstacles arise when metallic sheets are used to determine oxidation kinetics.

8.4 Oxidation kinetics of alloy 625 sheets

In the previous examples, the oxidation kinetics was determined using discontinuous weight change measurements (in combination with microstructural analysis). For a more accurate

estimate of the oxidation kinetics without a possible effect of thermal cycling on scale growth, a series of thermogravimetric (TG) studies on a selected number of alloy 625 specimens was carried out.

Figure 8.16 shows TG-curves for 1 mm thick alloy 625 sheet specimens during oxidation in air and in Ar-4%H₂-2%H₂O at 900 and 1000°C. The k_p values for lifetime modeling were determined from the weight gain curves of the specimens which were exposed in air. Figure 8.17 shows the microstructure of the oxide scales grown on the alloy 625 specimens during the corresponding TG-tests. The chromia scale grown in Ar-4%H₂-2%H₂O is smoother than that formed in Ar-20%O₂.

The oxidation rate of alloy 625 is higher in Ar-4%H₂-2%H₂O (low P_{O_2} environment) than that in air, which is consistent with previous results for chromium [138] and chromia-forming alloys [130]. As shown in the long term oxidation tests (Figure 6.5), the thinner sheets (0.3 mm) tend to oxidize slightly faster than the thick ones (1 mm) which is also in agreement with previous observations [31, 130].

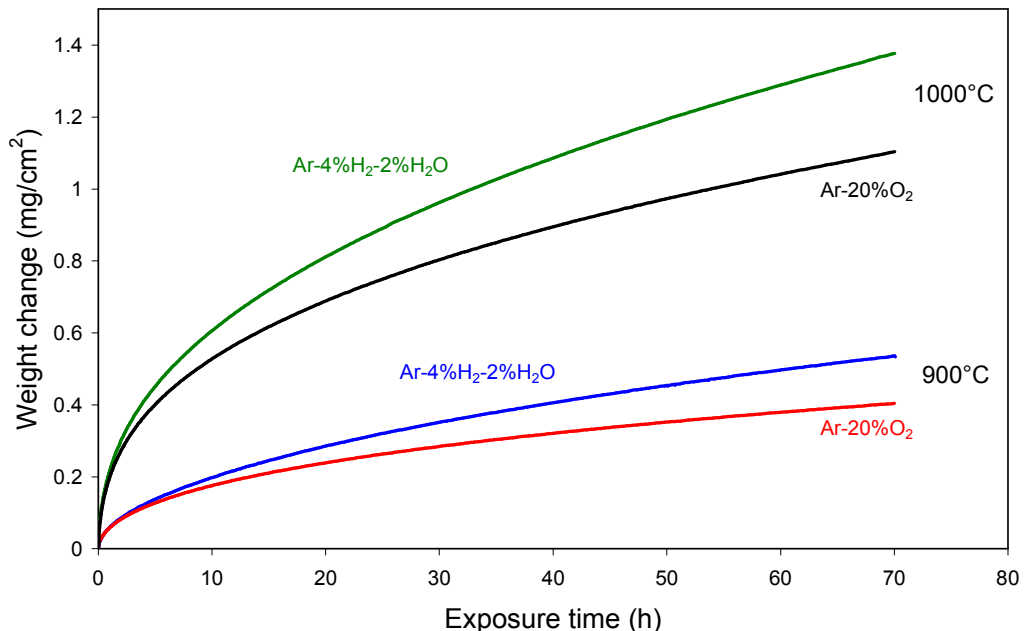


Figure 8.16: Weight change of 1mm thick alloy 625 specimens during isothermal oxidation at 900 and 1000°C in synthetic air and in Ar-4%H₂-2%H₂O

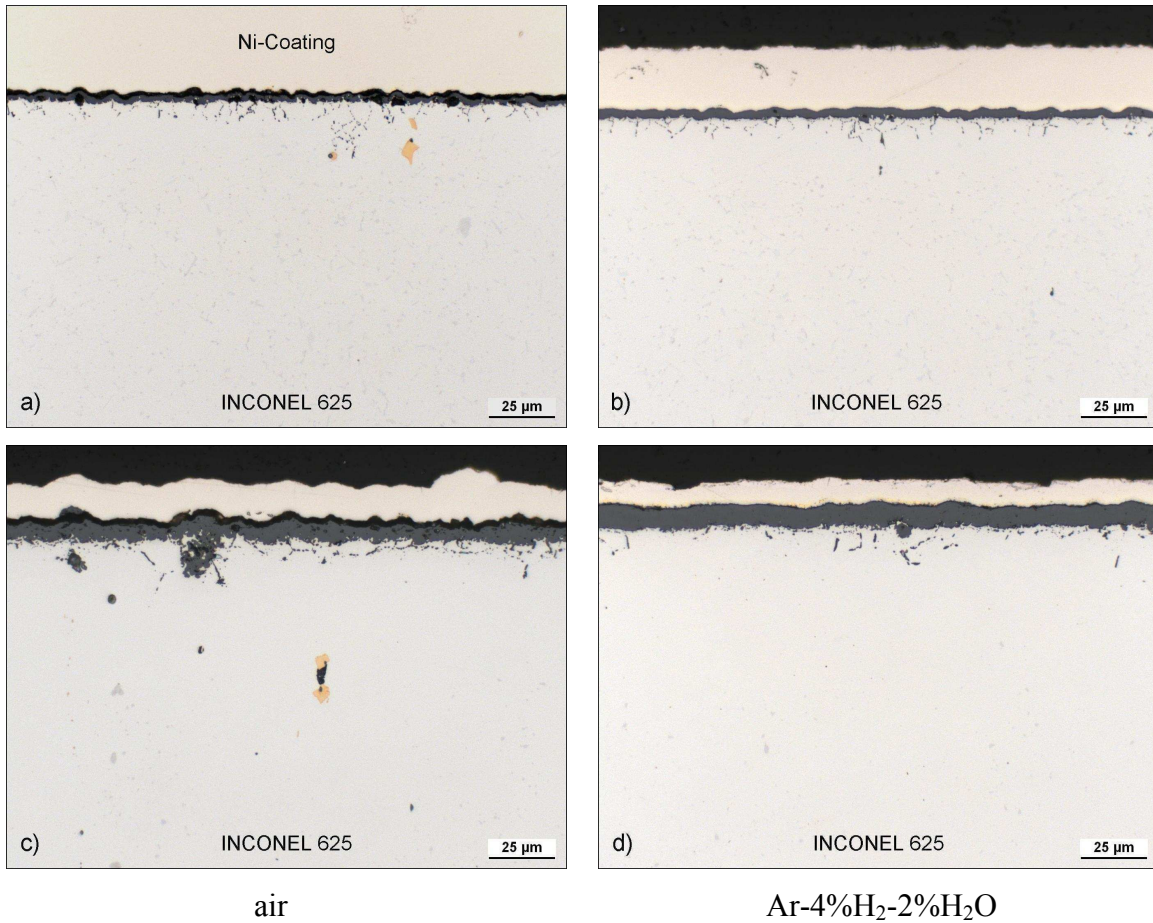


Figure 8.17: Optical micrographs of cross-sectioned 1mm thick alloy 625 specimens after 72h isothermal oxidation at 900 (a, b) and 1000°C (c, d) in air (a, c) and in Ar-4%H₂-2%H₂O (b, d)

However, the differences between the specimens of different thickness are small and do not substantially affect the considerations in the following sections. The oxide scale morphologies formed on alloy 625 after 1000h oxidation in both atmospheres shown in Figure 8.18 (see also Figure 6.6) confirm that the Cr₂O₃ layer formed in Ar-4%H₂-2%H₂O is slightly thicker and more uniform than that grown in air. It should be pointed out that the equilibrium oxygen partial pressure in Ar-4%H₂-2%H₂O at 900°C equals 1.5×10^{-17} bar which is far below the dissociation pressure of NiO at 900°C (8.5×10^{-13} bar). Thus, occurrence of breakaway oxidation of NiCr-base alloys as a result of formation of Ni-rich oxides is not possible in this low P_{O_2} atmosphere.

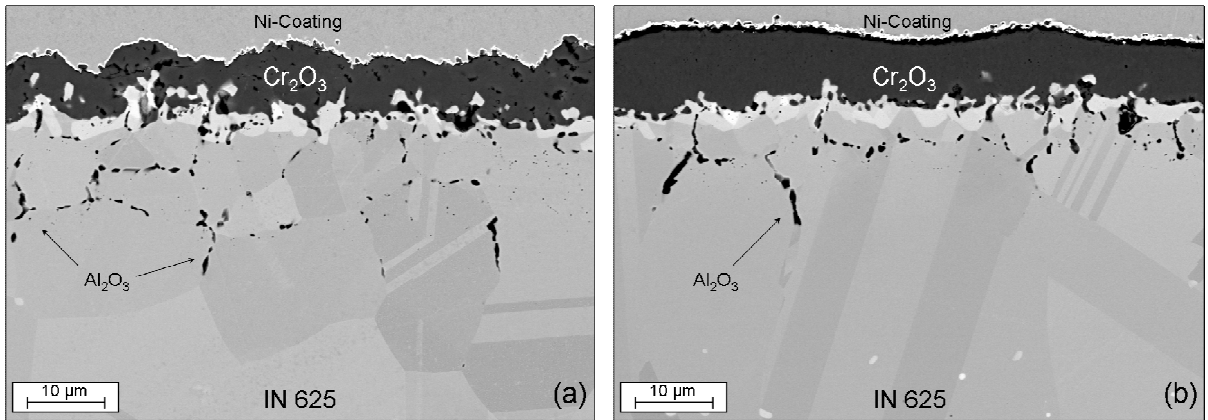


Figure 8.18: Cross-sections showing oxide scale morphologies of 1mm thick alloy 625 specimens after 1000 h discontinuous oxidation at 900°C in (a) air and in (b) $\text{Ar} - 4\% \text{H}_2 - 2\% \text{H}_2\text{O}$

The weight gain data of alloy 625 sheets oxidized in air at 900°C (Figure 8.16) was used to determine the parabolic rate constant as input parameter for the depletion modeling of the metallic foam particles. The value of k_p at 900°C found in the present study is $2.5 \times 10^{-12} \text{ g}^2 \cdot \text{cm}^{-4} \cdot \text{s}^{-1}$. Available literature data to compare the experimental k_p is that by Kumar et. al. [136] who studied the oxidation of INCONEL 625 in the range 1050 to 1250°C at P_{O_2} of 0.12kPa during the first 90 min of oxidation in pure oxygen. The obtained Arrhenius relation yields $3.9 \times 10^{-12} \text{ g}^2 \cdot \text{cm}^{-4} \cdot \text{s}^{-1}$ at 900°C. The activation energy for oxidation of the INCONEL 625 foams derived using the weight change data normalized by the initial sample weight (see section 6.1) was $222 \text{ kJ} \cdot \text{mole}^{-1}$ which is in good agreement with the value of $232 \pm 11 \text{ kJ} \cdot \text{mole}^{-1}$ in [136]. Thus, k_p was calculated for the oxidation of INCONEL 625 at 800°C to be $4.2 \times 10^{-13} \text{ g}^2 \cdot \text{cm}^{-4} \cdot \text{s}^{-1}$ and $2.9 \times 10^{-14} \text{ g}^2 \cdot \text{cm}^{-4} \cdot \text{s}^{-1}$ at 700°C, the latter values being used for lifetime calculation using the DICTRA-based Cr-depletion model for the INCONEL 625 foam particles during oxidation in air.

8.5 Oxidation behavior of alloy 625 foams in $\text{Ar} - 4\% \text{H}_2 - 20\% \text{H}_2\text{O}$

For a predictive modeling of the lifetime of the metallic foams it is of great importance to elucidate the main factor which is responsible for the eventually observed mechanical disintegration of the component after long oxidation times. In sections 8.2 and 8.3 it was assumed that this lifetime limit is related to occurrence of breakaway oxidation of the

individual powder particles because voluminous Ni-rich oxides were observed by microstructural analyses of failed foams after long term exposure.

However, these observations do not unequivocally exclude that the initiation of failure is caused by the growth of the protective chromia scale itself. Continuing growth of that scale during long-term exposure results in a volume increase and the stresses generated by this process in the inner of the foam could principally result in the component failure. In order to elucidate whether eventually the thickening of the chromia scale or the occurrence of breakaway of individual powder particles is responsible for deterioration of the mechanical stability of the metal foams, a series of oxidation tests at 900°C were performed in a low P_{O_2} atmosphere, Ar–4%H₂–20%H₂O. Since nickel oxide cannot be formed at $P_{O_2} < 10^{-12}$ bar at 900°C [12] (Figure 2.2), breakaway oxidation of the INCONEL 625 foams is impossible in Ar–4%H₂–20% H₂O in which the equilibrium oxygen partial pressure equals 1.5×10^{-15} bar at 900°C.

The weight change data shown in Figure 8.19 confirms that no accelerated oxidation occurs in Ar–4%H₂–20%H₂O for both foams KUS and MMH, while during air exposure at 900°C KUS suffered from breakaway oxidation after approximately 600h and MMH after 325h (Figure 8.8). The macroimages of the corresponding specimens as well as the optical micrographs of their cross-sections are shown in Figure 8.20.

The foam MMH retains its mechanical integrity during the 1000h exposure in Ar–4%H₂–20%H₂O, although severely oxidized, while it is almost completely destroyed after 325h when exposed in air (Figure 8.20a). Up to the maximum test times of 1000h in Ar–4%H₂–20%H₂O, none of the various foams exhibited mechanical degradation although the growth rate of chromia scale is higher than that in air. The presented results thus show that during air exposure, the breakaway oxidation of individual foam particles rather than the growth of the chromia scale is the main factor which is responsible for the loss of mechanical stability of metal foams after long term exposure.

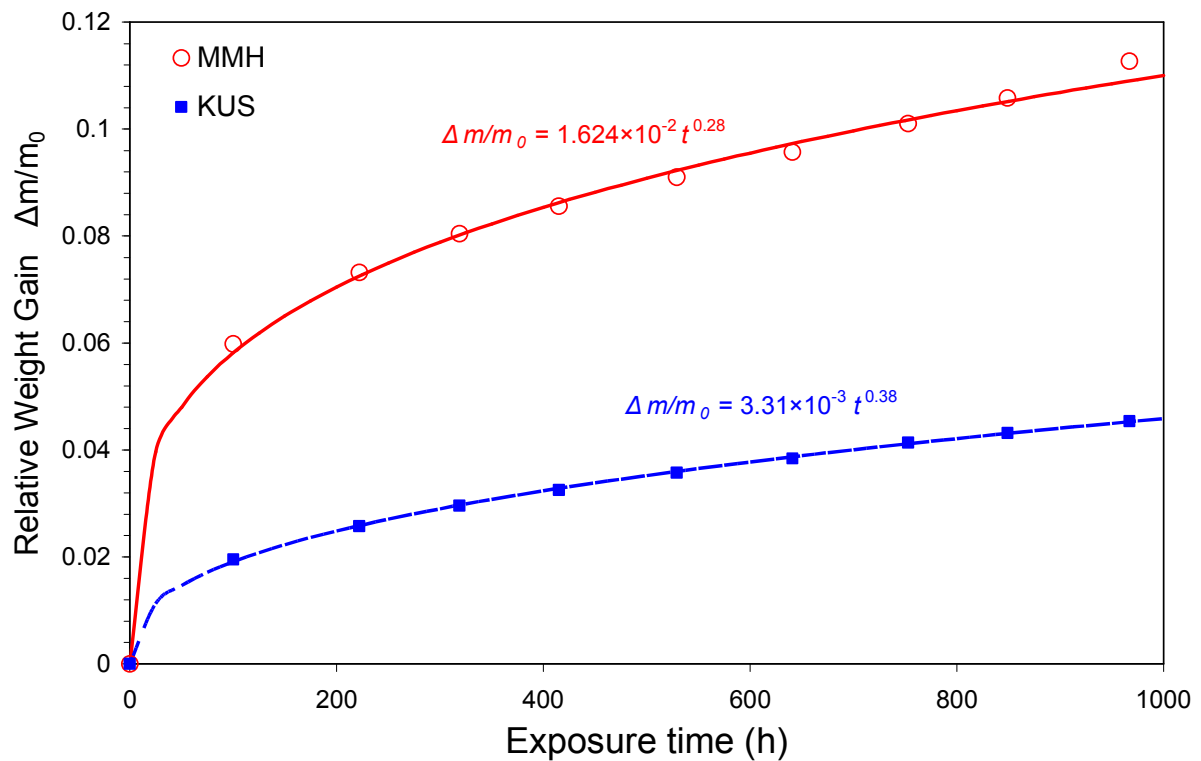


Figure 8.19: Weight change curves of two different INCONEL 625 foams during oxidation at 900°C in Ar - 4% H₂ - 20% H₂O

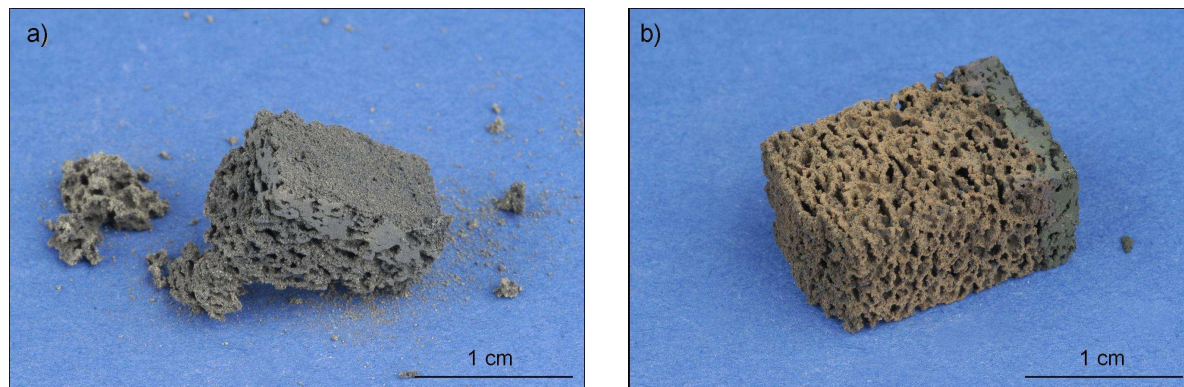


Figure 8.20: Macroimages of the MMH foam specimens after oxidation at 900°C for 325h in air (a) and for 1000h in Ar - 4% H₂ - 20% H₂O (b)

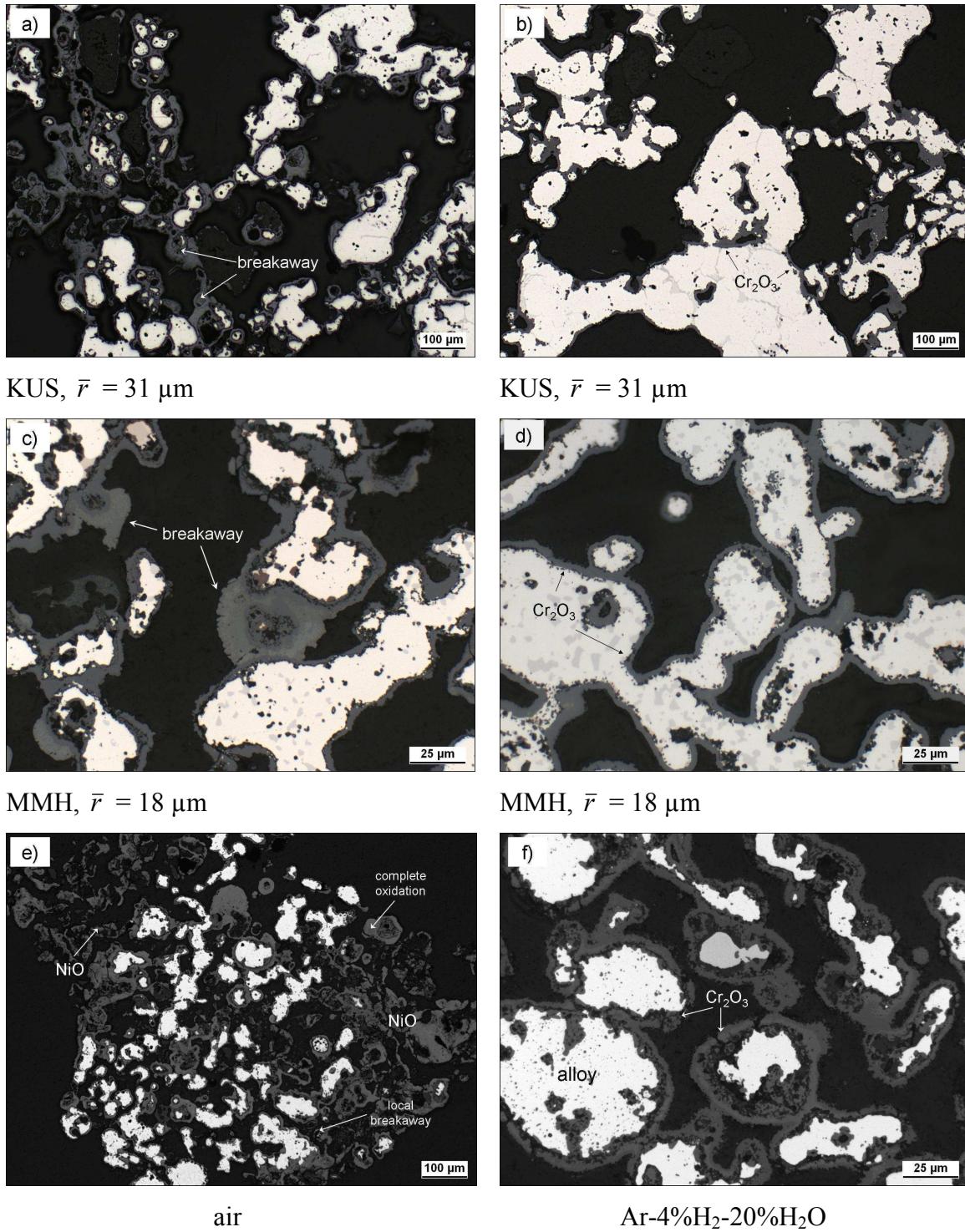


Figure 8.21: Optical micrographs of INCONEL 625 metal foams after oxidation at 900°C: KUS after 1000h in air (a) and Ar-4%H₂-20%H₂O (b); MMH after 325h in air (c) and (e); MMH in Ar-4%H₂-20%H₂O after 300h (d) and 1000h (f)

The coarse-grained foam KUS retained its mechanical integrity after 1000h exposure in air although numerous indications of breakaway oxidation on small foam particles are clearly visible in the microstructure (Figure 8.21a) of the oxidized foam specimen. In contrast to air

oxidation, no indications of chemical failure of the KUS foam particles after 1000h exposure at the same temperature in Ar-4%H₂-20%H₂O were found (Figure 8.21b).

The same applies to the MMH foam which suffered severe oxidizing attack in air at 900°C and eventually disintegrated due to voluminous and fast growing Ni-rich oxides after approximately 325h. The particles of the specimens oxidized in the low pO₂-environment were uniformly covered with a thick and adherent layer of chromia and revealed neither indications of breakaway oxidation in the microstructures (Figure 8.21) nor macroscopically observed deterioration of mechanical integrity.

8.6 Finite-difference lifetime model for metal foams

It was experimentally observed (see section 8.2) that the onset of breakaway oxidation of individual INCONEL 625 foam particles is accompanied by a clear deviation from the parabolic time dependence in the measured weight change curves. In order to compare the experimental values of t_B with those calculated using the DICTRA-based depletion model, the average times to breakaway are plotted as a function of the mean particle size of the foams in Figure 8.22. Most t_B values were determined at 900°C at which all metal foams exhibited the accelerated oxidation behavior within the maximum test time of 1000h. At 800°C only two experimental t_B values could be experimentally determined, i.e. for the most fine-grained foams.

In the present investigation the finite-difference software DICTRA [64] was used to simulate the chromium depletion in a spherical particle of a Ni-22%Cr alloy. The DICTRA software predicts the evolution of the chromium depletion profiles in the underlying alloy and as a result, the time at which the interface concentration of Cr reaches C_B can be evaluated. This treatment of chromium being removed from the alloy surface following a time dependent kinetic law using DICTRA is equivalent to Whittle's analytical model, i.e. Equation (2.28) [39], with the chromium flux being proportional to $t^{1/2}$. However, the DICTRA modeling is preferred because it can easily be applied to a spherical particle required to describe the breakaway behavior of the INCONEL 625 metal foams. In the present study the modeling was performed using the nickel-alloy mobility database MOBNi1 and the thermodynamic factors were calculated using the TTNI7 database. The geometrical factor was set 2 in order to

account for spherical symmetry. The region width (particle radius) was varied from 5 to 40 μm . The chromium flux was set in the form

$$J_{Cr} = \frac{dN_{Cr}^i(t)}{dt} = -(k_p^*)^{1/2} \cdot t^{-1/2} \quad (8.3)$$

where N_{Cr}^i is the number of moles of chromium transferred through the oxide/metal interface as a function of time (in $\text{mole}\cdot\text{cm}^{-2}$); k_p^* is the parabolic oxidation rate constant recalculated in $\text{mole}^2\cdot\text{cm}^{-4}\text{s}^{-1}$.

$$k_p^* = \frac{2k_p}{\bar{V}_{Cr_2O_3}^2} \quad (8.4)$$

Where k_p is the parabolic rate constant in $\text{cm}^2\cdot\text{s}^{-1}$, $\bar{V}_{Cr_2O_3}$ the molar volume of chromia in $\text{cm}^3\cdot\text{mole}^{-1}$. An experimentally observed value of C_B for the high-temperature oxidation of chromia-forming Ni-base alloys with composition close to Ni–22Cr within the oxidation temperature range 900–1000°C is approximately 10 wt% [27]. The value of k_p was established in a parallel isothermal oxidation test at 900°C in air on INCONEL 625 sheets (see sections 6.2 and 8.4). The lifetime of the INCONEL 625 foam under isothermal oxidation conditions, i.e. time to breakaway, is then defined by the time when the Cr interface concentration drops below the critical value $C_B = 10$ wt% and is calculated as a function of the foam particle radius.

As input data for the DICTRA calculation, the directly measured oxidation rate for alloy 625 sheet at 900°C and the activation energy derived from the Arrhenius plot of the weight change data normalized by the initial specimen weight (see section 8.1) was used. As shown in Figure 8.22, the experimental values of t_B at 800 and 900°C are in a reasonable agreement with the calculated lifetime curves (linear in a double logarithmic plot with slope 0.5). This numerically calculated curve can be precisely approximated by a parabola, in agreement with findings in [43] where the lifetime calculated for an austenitic steel of the type 1.4841, with a Cr content of 25 wt% at 1013°C using Equation (2.28) was found to be a parabolic function of sheet thickness as shown in Figure (9.2).

An important conclusion can be drawn from this finding: the specimen geometry (sphere compared to sheet) is important for the absolute lifetime but does not substantially affect the character of oxidation related lifetime dependence from specimen thickness or particle radius; it is defined exclusively by the prevailing oxidation kinetics of the actually used chromia-forming alloy.

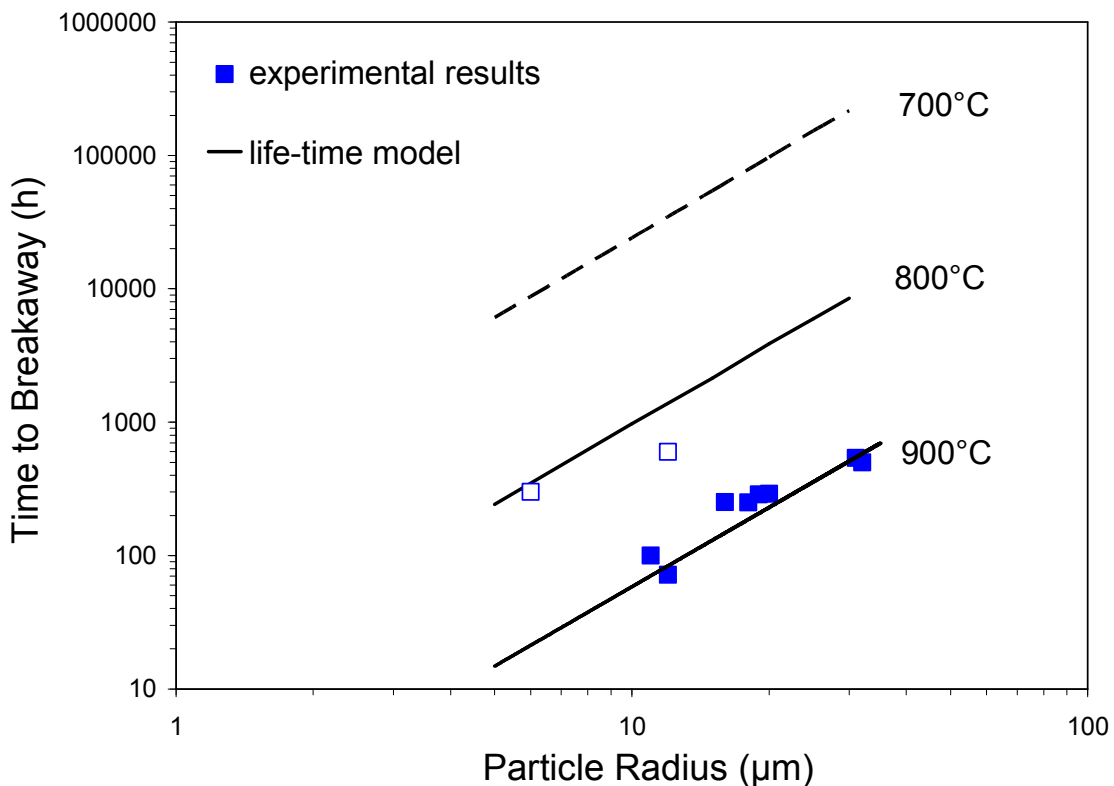


Figure 8.22: DICTRA calculation of lifetimes for various metals foams as a function of mean particle radius during exposure in air at different temperatures compared with experimental data at 800 and 900°C

In spite of the good agreement between measured and calculated lifetimes, it has to be considered that a number of simplifying assumptions were made in the modeling approach:

- ideal spherical particle
- parabolic oxidation
- no interface recession due to Cr consumption

The presented calculations thus provide a pragmatic method to estimate the oxidation limited lifetime of metallic foam as a function of foam microstructure and temperature. In this way, it allows design of a suitable foam microstructure if a certain lifetime at a given service temperature is required.

8.7 Summary of oxidation behavior of INCONEL 625 metal foams

During cyclic oxidation in air in the temperature range from 700 to 900°C highly porous INCONEL 625 foams exhibit after a certain time accelerated oxidation behavior which is determined by a rapid increase in mass gain, resulting in a destruction of the foam specimens. Chemically induced breakaway, i.e. formation of rapidly growing voluminous nickel-rich oxides, was shown to be responsible for the mechanical disintegration of the metal foams during long term exposure.

Although exhibiting a higher growth rate of the initially forming chromia scale in low P_{O_2} environments (Ar–4%H₂–20%H₂O) than in air, the Ni-base foams preserve their mechanical stability when oxidized in the first mentioned gas up to the longest test time of 1000h due to thermodynamic instability of nickel oxide in this atmosphere.

The time to breakaway oxidation of the INCONEL 625 foams was found to increase with increasing particle size of the foam and with decreasing oxidation temperature.

9. Lifetime prediction for alloys with large k_p/D ratio

9.1 General remarks

In heat-resistant austenitic steels and Ni-base alloys diffusion of Cr and/or Al is slower than in ferritic chromia- and alumina-forming alloys [16]. Therefore the concentration profiles of the scale-forming element in the FCC alloys are generally not flat (see e.g. Figure 9.1) because of the high ratio $\frac{k_p}{D}$ (see also section 2.2.1). Therefore Equation (2.28) should be used for lifetime calculation instead of Equations (2.21) and (2.24). Equation (2.28) is extremely robust and requires a computer assisted calculation algorithm which is much less convenient compared to the model for ferritic materials which is based on material balance in Equation (2.21):

$$t_B = \left[4.4 \cdot 10^{-3} (C_{Al}^0 - C_B) \frac{\rho \cdot d}{k} \right]^{\frac{1}{n}} \quad (2.21)$$

$$t_B = 4.4 \cdot 10^{-3} \frac{(C_{Al}^0 - C_B) \cdot \rho \cdot d}{k} \cdot (\Delta W_{Al}^*)^{\frac{1}{n}-1} \quad (2.23)$$

$$C(x, t) = C^0 - \frac{100M_{el}}{M_{alloy}} \frac{1}{2\phi} \left(\frac{\pi \cdot k_p}{D} \right)^{1/2} \sum_{n=0}^{\infty} \left(erfc \left[\frac{2nL + x}{(4Dt)^{1/2}} \right] + erfc \left[\frac{2(n+1)L - x}{(4Dt)^{1/2}} \right] \right) \quad (2.28)$$

9.2 Analytical lifetime model for alloys with large k_p/D ratio

It can be generally assumed that the time to breakaway is a function of (i) temperature, i.e. k_p and D_{Cr} ; (ii) alloy composition and (iii) specimen thickness:

$$t_B = f(k_p, D_{Cr}, C^0, C_B, L) \quad (9.1)$$

If a parabolic scaling rate prevails for a ferritic chromia-forming alloy, n in Equation (2.24) is equal to 0.5 and for a given temperature the lifetime is then a parabolic function of the specimen thickness $d = 2L$

$$t_B^{ferrite} = \alpha \cdot d^2 \quad (9.2)$$

where α is the factor which is for a given material constant at a given temperature, e.g. for a chromia-forming alloy

$$\alpha = \left[2.3 \cdot 10^{-3} (C^0 - C_B) \frac{\rho}{k} \right]^2. \quad (9.3)$$

Bauer et al. [43] used Equation (2.28) to calculate the lifetime (see Figure 9.2), i.e. the time at which the Cr concentration in the middle of the sheet specimen from austenitic steel dropped to 16 wt%, as a function of the alloy sheet thickness. The resulting calculated lifetime curve was found to be a parabolic function of the alloy sheet thickness as well

$$t_B^{austenite} = \beta \cdot d^2. \quad (9.4)$$

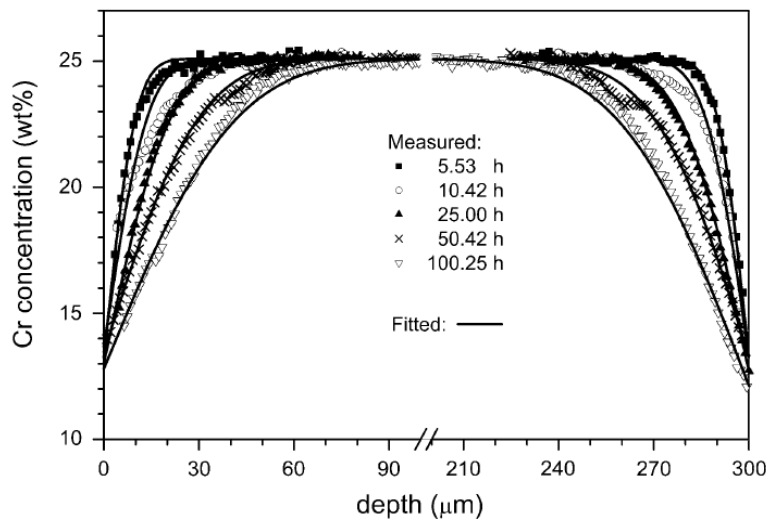


Figure 9.1: Measured and calculated concentration-depth profiles of Cr in alloy Fe-25Cr-20Ni-2.8Si (300 μm thick) after oxidation at 1,286 K for various times in the range of 5.53–100.25 h [43]

It is rather surprising that the calculation of the time to breakaway carried out using Equation (2.28) leads to essentially the same specimen thickness dependence of the lifetime as Equation (2.21). It seems therefore reasonable to assume that Equation (9.2) is a limiting case of Equation (9.4) for $k_p/D \ll 1$ (see Figure 2.8). The factor β would converge into α under the condition that k_p/D is very small.

In order to establish the relationship between Equations (9.2) and (9.4), a number of calculations were carried out with a systematic variation of the parameters C^θ , C_B , k_p , D_{Cr} , L , and t in Equation (2.28). For fixed C^θ , C_B , k_p , D_{Cr} values, Equation (2.28) was rewritten in the form

$$C(t) = f(L, t) . \quad (9.5)$$

For a fixed value of L , the oxidation time t was varied until $|C(t) - C_B| < \varepsilon$; the convergence parameter ε was defined as 0.01 wt%. The factor β was calculated as

$$\beta = \frac{t_B}{L^2} . \quad (9.6)$$

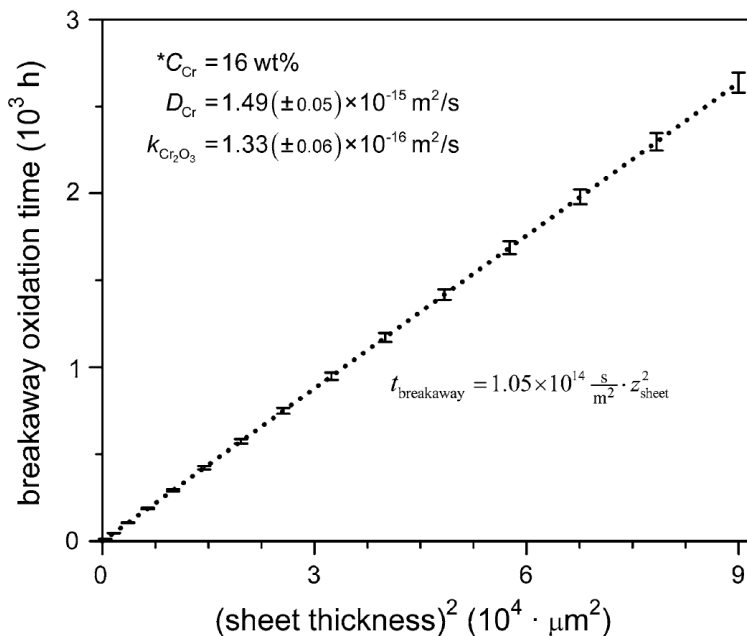


Figure 9.2: Predicted time to breakaway as a function of the alloy sheet thickness, as calculated for the isothermal oxidation of alloy Fe–25Cr–20Ni–2.8Si at 1,286 K in air [43]

The calculation was then re-iterated for the next L value thus creating an array of t_B values as a function of L .

The next step was a variation of k_p for fixed D_{Cr} values and vice versa. The data from [43] was used as an input for the calculation, i.e. $C^0 = 25 \text{ wt\%}$, $C_B = 11.4 \text{ wt\%}$, $k_p = 1.33 \times 10^{-16} \text{ m}^2 \text{s}^{-1}$, $D_{Cr} = 1.49 \times 10^{-15} \text{ m}^2 \text{s}^{-1}$.

Figure 9.3 shows the calculated lifetime of a sheet specimen for which the following computation parameters were used: $L = 100 \mu\text{m}$, $C^0 = 25 \text{ wt\%}$, $C_B = 10 \text{ wt\%}$, $k_p = 1.0 \times 10^{-16} \text{ m}^2 \text{s}^{-1}$. For a fixed k_p value of $1.0 \times 10^{-16} \text{ m}^2 \text{s}^{-1}$, the calculated time to breakaway appeared to be a linear function of the k_p/D_{Cr} ratio in the range 0 to 0.1. The upper limit of the linear range ($k_p/D_{Cr} = 0.1$) includes also the original input data ($k_p/D_{Cr} = 0.089$). It is apparent that the k_p/D_{Cr} values larger than 0.14 have no physical meaning because the time to breakaway becomes negative, i.e. $C^i < C_B$ at $t = 0$, which imposes explicit restrictions on varying the k_p/D_{Cr} ratio.

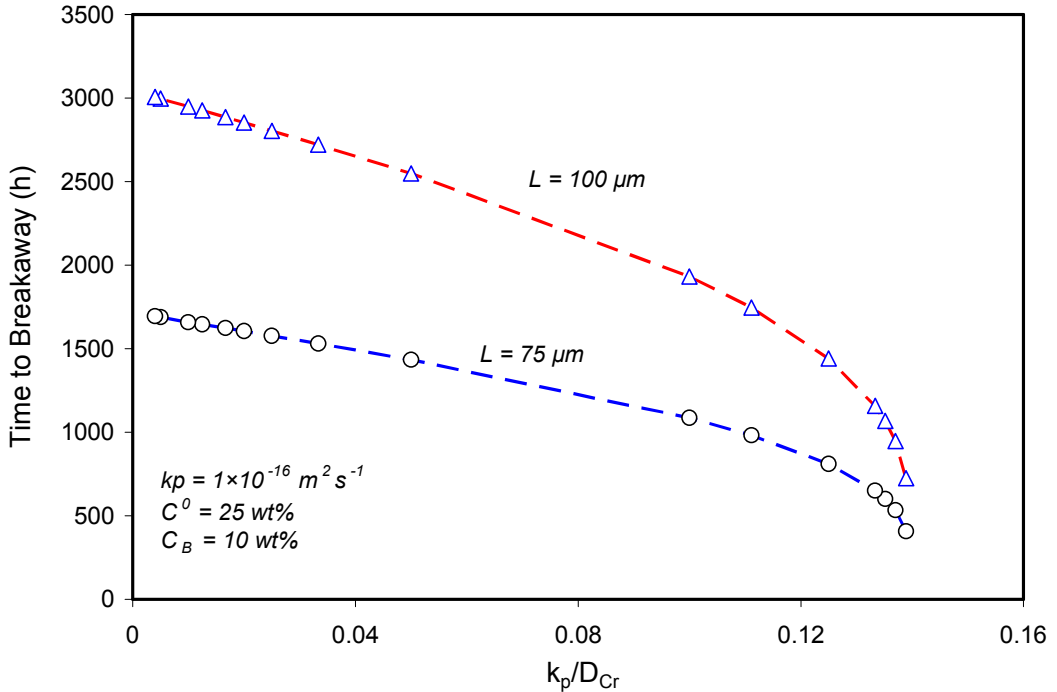


Figure 9.3: Calculated time to breakaway as a function of k_p/D_{Cr} ratio for varying D_{Cr} in Equation (2.28) for $L = 75$ and $100 \mu\text{m}$, $k_p = 1.0 \times 10^{-16} \text{ m}^2 \text{s}^{-1}$, $C^0 = 25 \text{ wt\%}$, and $C_B = 10 \text{ wt\%}$

The lower limit of the linear range ($k_p/D_{Cr} \rightarrow 0$) corresponds to the limiting case of Equation (9.4), i.e. ferritic materials exhibiting fast Cr diffusion. The value intercepted on the lifetime

axis at $k_p/D_{Cr} = 0$ thus should be equal to that calculated using Equation (2.24). The time to breakaway calculated for the 200 μm thick specimen using Equation (2.24) and the above data is approximately 3033 hours whereas the red line in Figure 9.3 crosses the ordinate axis at 3045h. For the 150 μm thick specimen ($L = 75 \mu\text{m}$) the lifetimes are 1701 and 1707 hours, respectively.

An interesting observation was made during the parametric analysis of Equation (2.28). If both k_p and D_{Cr} are simultaneously increased by an arbitrary factor f , the time to breakaway decreases exactly by the factor f . Increasing both k_p and D_{Cr} is qualitatively equivalent to increasing oxidation temperature which is known to reduce the lifetime.

The latter statement is only an approximate analogy because changing the temperature may affect not only k_p and D_{Cr} but also C_B . Depending on the activation energies for chromia growth and chromium diffusion in the alloy, the k_p/D_{Cr} ratio may upon temperature change increase as well as decrease thereby affecting the oxide/metal interface concentration of Cr (see Equation (2.17)). This, for instance, is the case for alloy 625 (see sections 6.2 and 6.4). The Cr interface concentration for thick specimens was for that alloy measured to be approximately 15 wt% at 900°C and 10 wt% at 1000°C, which shows that the activation energy for oxidation is higher than that for chromium diffusion in alloy 625.

As illustrated in Figure 9.3, the time to breakaway at constant k_p decreases with decreasing D_{Cr} starting from the limit value defined by Equations (2.24) and (9.3). It is reasonable to seek the general expression for the thickness dependent time to breakaway as a sum of the “kinetic” term t_B^{kin} and a negative “diffusion” term t_B^{dif} reducing the total time to breakaway

$$t_B = t_B^{kin} - t_B^{dif}. \quad (9.7)$$

The following findings should be considered:

- Both terms were shown to be parabolic functions of L :
- t_B^{kin} is proportional to $\frac{1}{k_p}$ (Equation 9.3)

- t_B^{dif} is proportional to $\frac{1}{D_{Cr}}$ (Figure 9.3)

The generalized solution for t_B should thus be sought in the form

$$t_B = [A^{kin} - A^{dif}] \times L^2 \quad (9.8)$$

where A^{kin} and A^{dif} for given C^0 and C_B are constants (in $s \cdot m^{-2}$), i.e. proportional to $\frac{1}{k_p}$ and $\frac{1}{D_{Cr}}$, respectively. Rearranging Equation (9.8)

$$t_B = \left[\frac{A_1}{k_p} - \frac{A_2}{D_{Cr}} \right] \times L^2 = \frac{1}{k_p} \left[A_1 - A_2 \frac{k_p}{D_{Cr}} \right] \times L^2 . \quad (9.9)$$

Combining Equation (9.2) with Equation (9.9) and assuming that k_p/D_{Cr} is small, as is e.g. the case for fast chromium diffusion in a ferritic steel, it is clear that $A_1 = \alpha$ or for k_p expressed in terms of oxide scale thickness

$$A_1 = \left[\frac{C^0 - C_B}{100} \frac{M_{all}}{M_{Cr}} \phi \right]^2 . \quad (9.10)$$

For $k_p/D_{Cr} \ll 1$, Equation (9.9) converges into Equation (2.24).

The second constant A_2 in Equation (9.9) cannot be defined as explicitly as A_1 because k_p in Equation (2.28) cannot be varied arbitrarily. According to Equation (2.17), the interface concentration of chromium C^i decreases with increasing k_p . Meaningful solutions for Equation (2.28) obviously exist only for $C^i \geq C_B$. Otherwise breakaway oxidation would occur at $t = 0$.

From Equation (2.17) it is apparent that for $C^i \geq C_B$, k_p should not exceed

$$k_p \leq \left[\frac{C^0 - C_B}{100} \frac{M_{all}}{M_{Cr}} \phi \right]^2 \times \frac{4D}{\pi} \quad (9.11)$$

or, combining with Equation (9.10),

$$k_p \leq A_1 \times \frac{4D}{\pi} \quad (9.12)$$

A number of lifetime calculations were carried out for $k_p = 1.0 \times 10^{-16} \text{ m}^2 \text{s}^{-1}$ and $2.0 \times 10^{-16} \text{ m}^2 \text{s}^{-1}$ respectively, with $C^0 = 25 \text{ wt\%}$, and $C_B = 10 \text{ wt\%}$ and variation of L between 25 and 150 μm . It appears that, irrespective of the sheet thickness, the parameter β defined by Equation (9.6) is a straight line when plotted versus $1/D_{Cr}$ (Figure 9.4). The slope of the lines in Figure 9.4, i.e. the parameter A_2 , varies from 35.7 (for $k_p = 1.0 \times 10^{-16} \text{ m}^2 \text{s}^{-1}$) to 37.4 (for $k_p = 2.0 \times 10^{-16} \text{ m}^2 \text{s}^{-1}$). This means that the dimensionless parameter A_2 in Equation (9.9) is approximately 0.37.

The calculations solving Equation (2.28) with varying k_p (up to the value defined by Equation 9.11) showed that for small values of k_p the time to breakaway plotted versus D_{Cr}/k_p is a straight line with a negative intercept which is consistent with Equation (9.9).

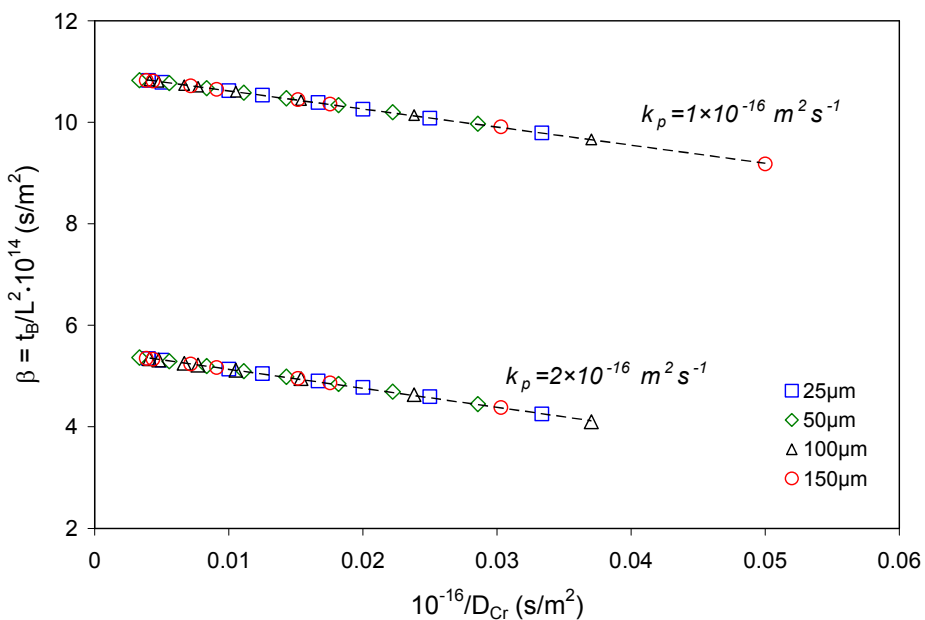


Figure 9.4: Parameter β from Equation (9.5) as a function of $1/D_{Cr}$ calculated varying D_{Cr} in Equation (2.28) for $k_p = 1.0 \times 10^{-16} \text{ m}^2 \text{s}^{-1}$ and $2.0 \times 10^{-16} \text{ m}^2 \text{s}^{-1}$, $C^0 = 25 \text{ wt\%}$, $C_B = 10 \text{ wt\%}$ and L varying from 25 to 150 μm

Figure 9.5 summarizes the calculated time to breakaway for a thin foil specimen plotted as a function of $1/k_p$ and $1/D_{Cr}$. The linear parts of the lifetime curves correspond to two limiting cases: (a) $k_p / D_{Cr} \gg 1$; the intercept defines the constant A_2 from t_B^{dif} , and the limiting case (b) for $k_p / D_{Cr} \ll 1$, i.e. ferritic steel, which allows estimation of A_1 from the intercept t_B^{kin} .

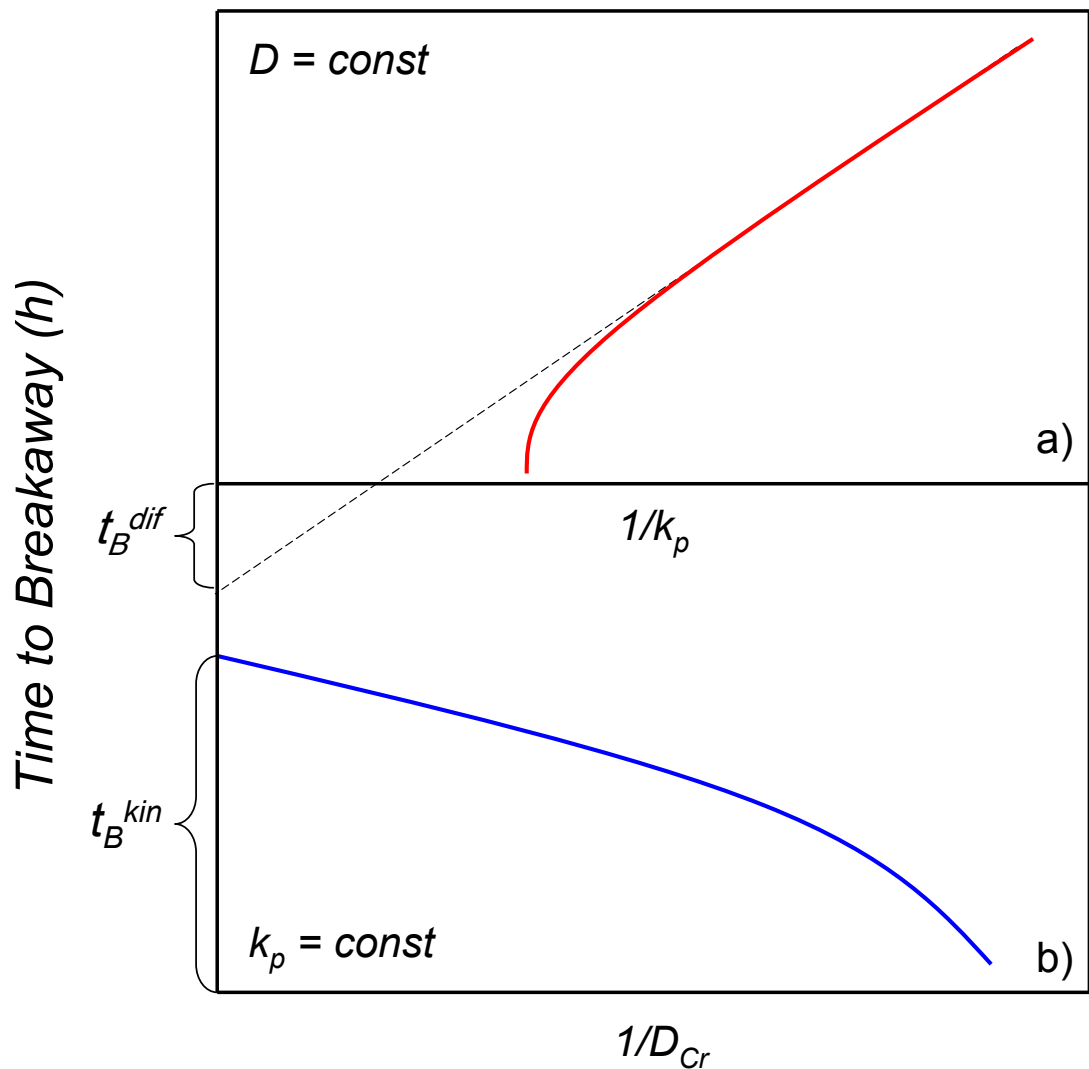


Figure 9.5: Schematic representation of time to breakaway on a thin foil specimen calculated using Equation (2.28) and plotted versus $1/k_p$ and $1/D_{Cr}$. The lifetime t_B is the difference between t_B^{kin} and t_B^{dif}

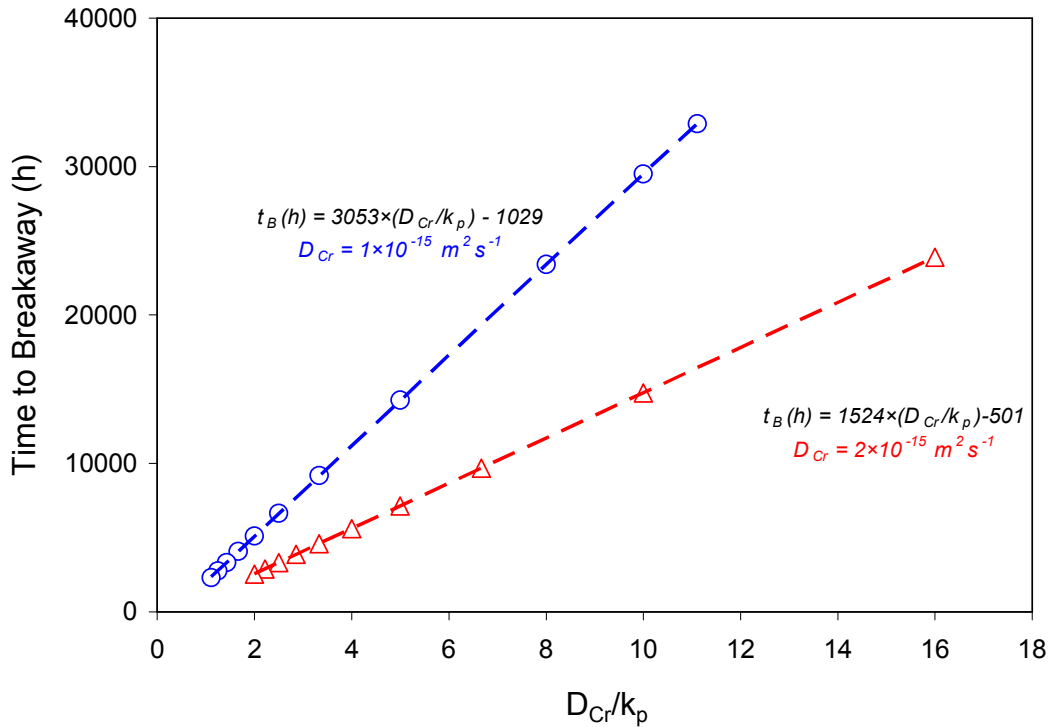


Figure 9.6: Calculated time to breakaway as a function of the ratio D_{Cr}/k_p calculated varying D_{Cr} and k_p in Equation (2.28) for $L = 100 \mu\text{m}$, $C^0 = 25 \text{ wt\%}$, and $C_B = 10 \text{ wt\%}$

Additional calculations revealed that variation of C^0 and C_B affects A_1 , as predicted by Equation (9.10), but not A_2 . Thus, A_2 is a general dimensionless constant which can be taken equal to approximately $\chi = 0.37$ irrespective of the alloy system. Finally, combining Equations (9.9) and (9.10) the general expression for the time to breakaway for a thin sheet of a chromia-forming material can be written in the form:

$$t_B = \left[\left(\frac{C^0 - C_B}{100} \frac{M_{all}}{M_{Cr}} \phi \right)^2 \times \frac{1}{k_p} - \frac{\chi}{D_{Cr}} \right] \times L^2. \quad (9.13)$$

For the alloy Fe–25Cr–20Ni–2.8Si at 1013°C, as calculated using the data from reference [43], the dimensionless constant A_1 equals 0.090 whereas for alloy 625 at 900°C (data from chapter 6) A_1 is 0.075.

Equation (9.13) can be a useful and simple tool to predict the time to breakaway on FCC-type materials with slow chromium diffusion, e.g. austenitic steels or Ni-base alloys with reasonable accuracy. Application of more precise expressions such as Equation (2.28) and/or

numerical solutions of the diffusion equation (see section 8.6) requires in most cases a sophisticated computation procedure. As apparent from Table 9.1, a relative error in the calculation of lifetimes using Equation (9.3) for arbitrarily chosen C^0 , C_B , k_p , D_{Cr} values does not exceed 3% compared to the calculation Equation (2.28). This can be considered as a reasonable agreement for most practical applications.

Table 9.1: Comparison of lifetimes calculated for a sheet specimen using Equations (2.28) and (9.13). The input parameters were $k_p = 1.0 \times 10^{-16} \text{ m}^2\text{s}^{-1}$, $C^0 = 25 \text{ wt\%}$, $C_B = 10 \text{ wt\%}$, L varying from 25 to 150 μm

$L (\mu\text{m})$	$D_{Cr} = 1.0 \times 10^{-16} \text{ m}^2\text{s}^{-1}$		$D_{Cr} = 3.0 \times 10^{-16} \text{ m}^2\text{s}^{-1}$	
	Time to breakaway (h)			
	Equation 9.13	Equation 2.28	Equation 9.13	Equation 2.28
150	4482.3	4345.3	6086.4	6125.1
100	1992.1	1931.2	2705.1	2722.3
75	1120.6	1086.3	1521.6	1531.3
50	498.0	482.8	676.3	680.6
25	126.2	120.7	169.1	170.1

An important conclusion can be drawn from Equations (9.9) and/or (9.13): considering a given oxidation rate, the lifetime of a thin foil manufactured from a material with slow diffusion of chromium, e.g. austenitic steels or Ni-base alloys, is reduced approximately by one third compared to that of the identical component produced from materials with rapid Cr diffusion, such as ferritic steel.

9.3 Oxidation-induced lifetime limits of alloy 625 at 900°C

Equation (9.13) can be used to calculate the oxidation-induced lifetime limits of alloy 625 sheets taking as input parameters the values of k_p and D_{Cr} determined in chapter 6. At 900°C during air oxidation k_p was found to be $9 \times 10^{-18} \text{ m}^2\cdot\text{s}^{-1}$ whereas the value of D_{Cr} calculated from the chromium depletion profiles is $2.5 \times 10^{-16} \text{ m}^2\cdot\text{s}^{-1}$. The initial chromium concentration in alloy 625, C^0 , is 22 wt%, the breakaway concentration C_B can be taken as 7 wt%. As apparent from Equations (2.24) and (9.13) and illustrated in Figure 9.6, the time to breakaway

is a parabolic function of the specimen thickness d or half-thickness L ($d = 2L$). The lifetimes calculated using Equation (2.24) by Quadakkers et al. [30] assuming rapid chromium diffusion are slightly higher than those calculated using Equations (2.28) and (9.13), which is expected taking the respective formulations into account. It should be also noted that the lifetime values calculated using the depletion model by Whittle et al. [39] (red dots in Figure 9.7) are in very good agreement with those predicted by Equation (9.13) derived in the present study (red line in Figure 9.7). The so called oxidation diagram [32] plotted in Figure 9.7 suggests the service time for e.g. a 100 μm thick foil of alloy 625 at 900°C to be approximately 10,000h (approximately one year) if no spallation of the oxide scale occurs during the exposure.

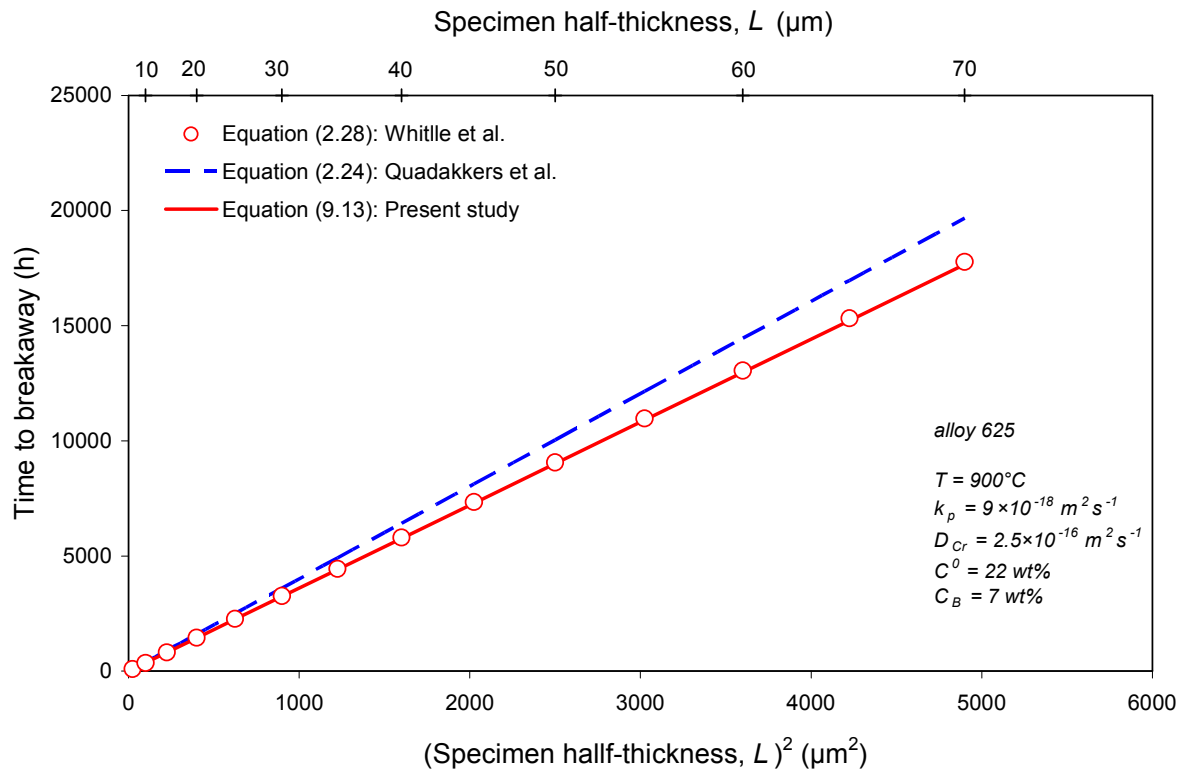


Figure 9.7: Time to breakaway as function of specimen half-thickness for alloy 625 at 900°C in air calculated using different analytical lifetime models

In order to validate the lifetime model developed in the present study, a number of calculations were carried out using the input data from literature [43] with further comparison of the calculated lifetime value with the literature data. The corresponding values of k_p , D_{Cr} , C^0 and C_B were taken from reference [43]. The lifetimes were calculated using Equations (2.24), (2.28) and (9.13) and compared with the lifetimes of alloy 625 at 900°C in Figure 9.8.

When plotted in double logarithmic scale, the lifetime curves calculated using Equations (2.24) and (9.13) become parallel lines. Their slope are identical and defined by the term containing k_p , i.e. A_1 in Equation (9.9), whereas the absolute values (the intercepts) are corrected (generally decreased) by subtracting the term A_2/D_{Cr} .

As is apparent from Figure 9.8, the difference between the lifetimes calculated using Equations (2.24) and (9.13) is smaller for alloy 625 at 900°C than that for the alloy Fe-25Cr-20Ni-2.8Si from reference [43] which is obviously related to the smaller k_p/D_{Cr} ratio for alloy 625 (0.036) compared to that for alloy Fe-25Cr-20Ni-2.8Si (0.089). In other words, alloy 625 at 900°C represents an intermediate situation between purely BCC materials and austenitic steels (like Fe-25Cr-20Ni-2.8Si) while the concentration profiles in alloy 625 at 900°C (Figure 6.9) are rather steep than flat like in ferritic steels.

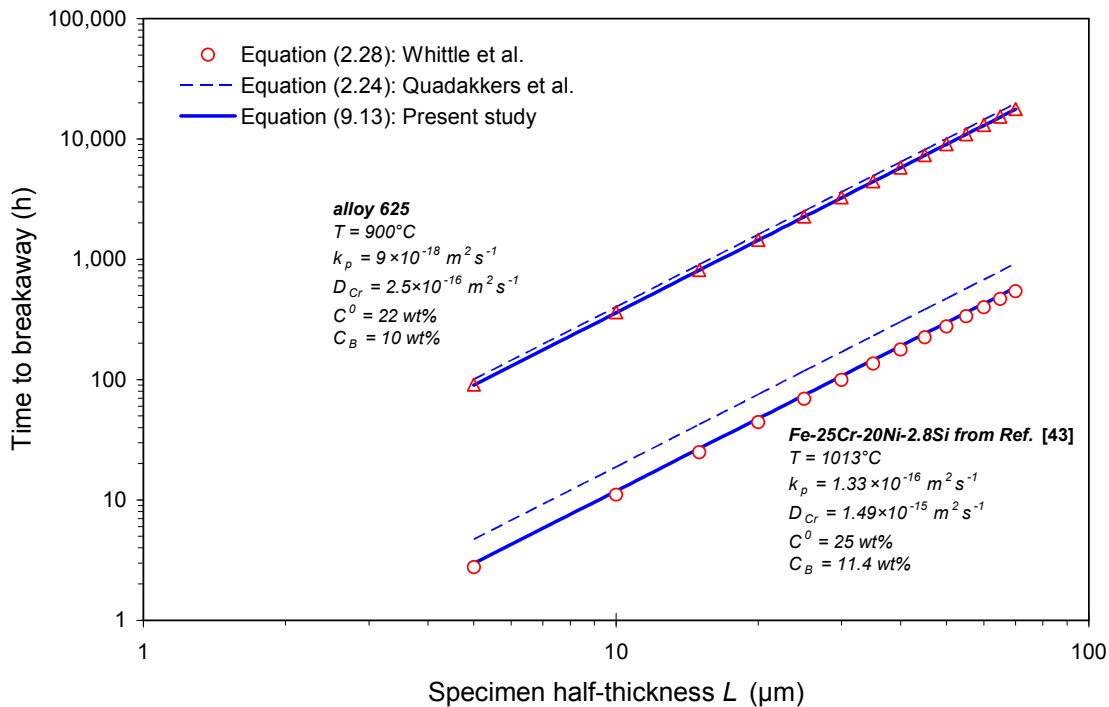


Figure 9.8: Calculated lifetimes of alloy 625 at 900°C and model alloy Fe-25Ni-25Cr-2.8S at 1013°C from Ref. [43]

As can be generally expected, the lifetimes calculated for alloy Fe-25Cr-20Ni-2.8Si at 1013°C are by more than one order of magnitude shorter than those for alloy 625 at 900°C because of the higher exposure temperature for the former alloy. Again, good agreement is found between the lifetimes calculated using both Equations (2.24) and (9.13) for the alloy Fe-25Cr-20Ni-2.8Si. This illustrates that the lifetime model developed in the previous section may with reasonable accuracy be used to calculate time to breakaway fro FCC materials.

Equation (9.13) can also be applied to predict the lifetime limits for alloy 625 metal foams. If a spherical foam particle is considered (see section 8.6), the specimen half-thickness L in Equation (9.13) should be replaced by the geometry factor f introduced by Gurrappa et al. [35] as

$$f_{geo} = \frac{\text{Volume}}{\text{Surface area}} \quad (9.14)$$

The factor f_{geo} is a substitution for the specimen half-thickness L for pure geometrical reasons. From Equation (9.14), the geometry factor for a sphere of radius r is

$$f_{geo} = \frac{r}{3} \quad (9.15)$$

where r is the particle radius. The experimental times to breakaway measured in chapter 8 (from Figure 8.22) should thus be plotted in Figure 9.8 versus the f_{geo} values calculated using Equation (9.15). This is illustrated in Figure 9.9.

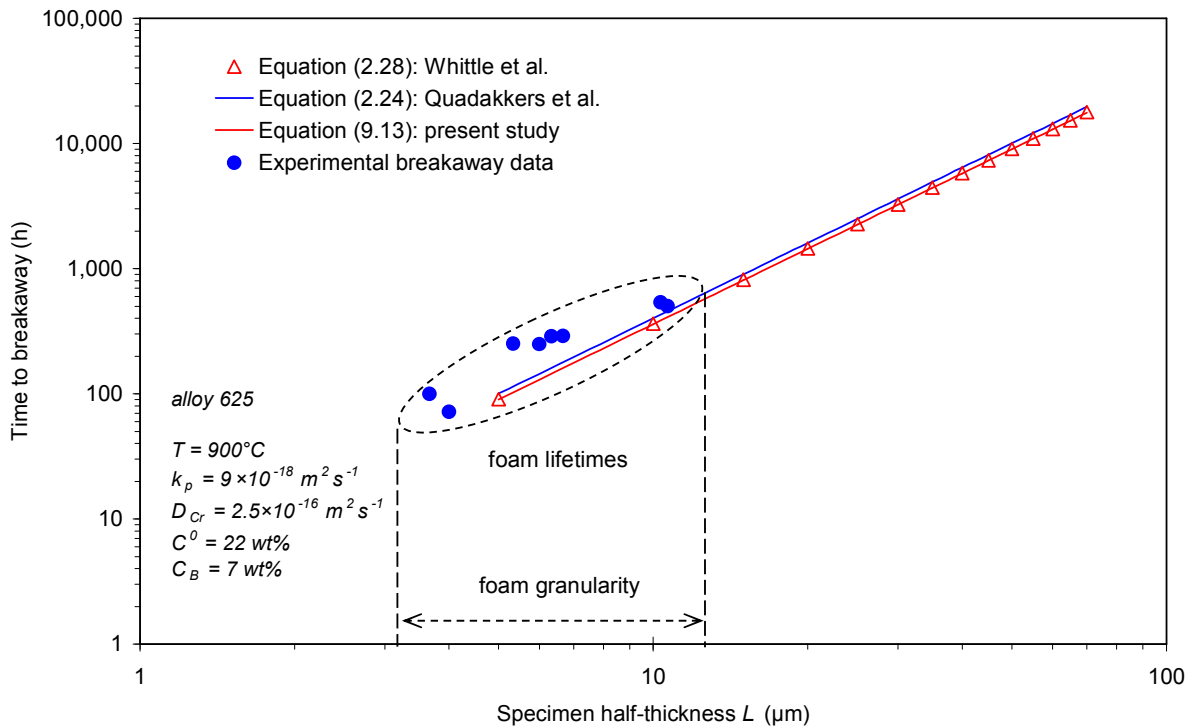


Figure 9.9: Calculated and measured lifetimes of alloy 625 sheets at 900°C in air. The experimental breakaway data points for alloy 625 metal foams are plotted taking effect of specimen geometry into account

As shown in Figure 9.9, the experimental breakaway data for alloy 625 metal foams is in relatively good agreement with the predicted lifetime curve for alloy 625 sheet at 900°C.

Finally, the lifetimes for alloy 625 sheets at 1000°C can be calculated using the kinetic parameters from Figure 6.17: $k_p = 4 \times 10^{-17} \text{ m}^2 \cdot \text{s}^{-1}$ and $D_{Cr} = 7.2 \times 10^{-16} \text{ m}^2 \cdot \text{s}^{-1}$. The C_B value is also taken 7 wt% as the steady-state interface chromium concentration in alloy 625 at 1000°C is approximately 10 wt% (Figure 6.17). Since no available C_B values for alloy 625 at 1000°C could be found in the literature, it was arbitrary set at 7 wt%, just to demonstrate the applicability of Equation (9.13). The calculated lifetimes for alloy 625 at 1000°C in air are compared with those at 900°C in Figure 9.10,

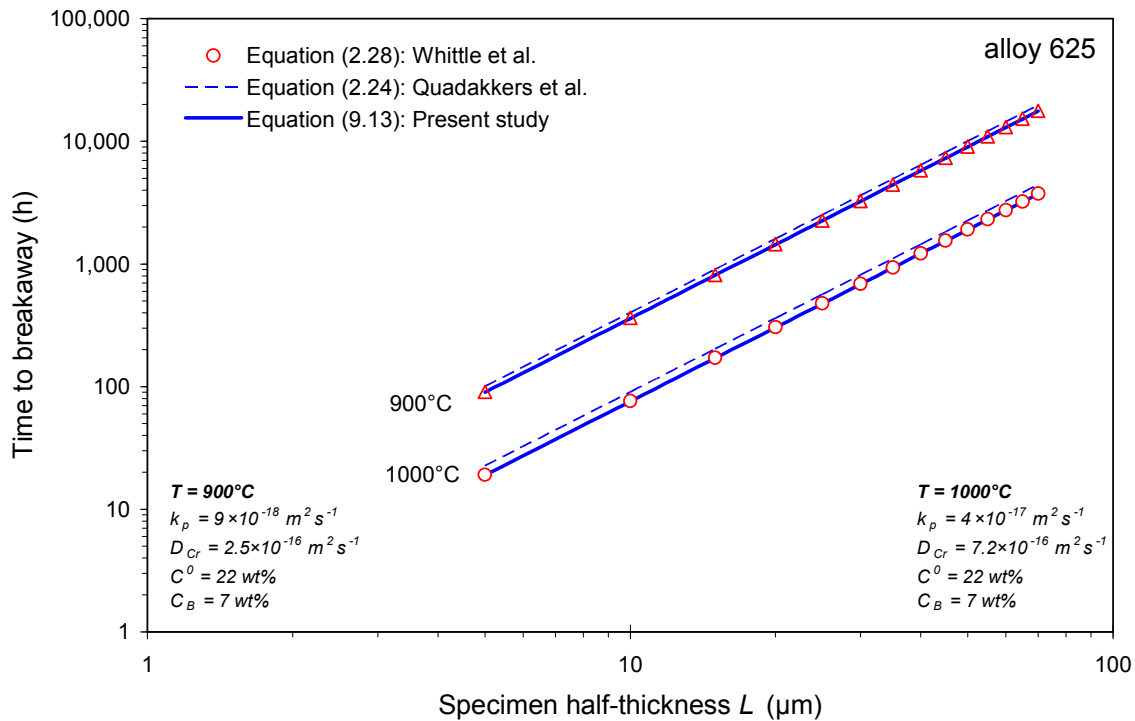


Figure 9.10: Calculated lifetimes of alloy 625 at 900 and 1000°C comparing various lifetime models

Like for 900°C, the difference between lifetime values calculated using Equations (2.24) and (9.13) is also slight for alloy 625 at 1000°C. Good agreement is also observed between the calculation results for 1000°C using Equations (2.28) and (9.13).

9.4 Summary of lifetime modeling

The above results illustrate that a new lifetime model was derived in this chapter based on two lifetime treatments available up to date: the depletion model by Whittle et al. [39] as the

general solution given by Equation (2.28) and the mass-balance model by Quadakkers et al. [32] as a limiting case of the Whittle model applicable for alloys with a small k_p/D_{Cr} ratio (see Equation (2.24)).

The new simplified lifetime treatment was developed for alloys in which the ratio k_p/D is not small enough to use the mass balance model derived by Quadakkers et al. [32] for alumina-forming ferritic steels. The parametric analysis of the general lifetime model derived by Whittle [39] revealed that the Quadakkers model is a limiting case for alloys with fast diffusion of the selectively oxidizing solute in the alloy, i.e. when the ratio k_p/D_{Cr} is considered extremely small. The mass balance model can be extended by introducing an additional negative term, inversely proportional to D_{Cr} , which would account for slow Cr diffusion of the solute in the alloy. The modified lifetime expression, which takes slow diffusion into account, shows very good agreement with the numerical solutions of the Whittle model.

The lifetime model derived was used to calculate the time to breakaway in a spherical particle of alloy 625 thus simulating the breakaway oxidation of alloy 625 metal foams. The calculation lifetime curve for 900°C showed reasonable agreement with the experimental breakaway data.

10. Conclusions

The nickel-base chromia-forming alloy INCONEL® 625 contains two types of strengthening precipitate phases at 900°C, i.e. $(\text{Ni},\text{Mo})_6\text{C}$ carbide and the niobium-rich intermetallic phase $\delta\text{-Ni}_3\text{Nb}$. At temperatures as high as 1000°C only M_6C carbide is present in the alloy microstructure.

The formation of a protective chromia scale at the alloy surface during high-temperature exposure is associated with continuous consumption of chromium from the bulk alloy and results in chromium depletion in the subsurface zone. The formation of a subscale chromium depletion zone has two important consequences for alloy microstructure:

- The chemical activity of niobium in the chromium-depleted subsurface zone of alloy 625, i.e. the area in the immediate vicinity of the scale/alloy interface, is two orders of magnitude lower than in the bulk alloy at 900°C. This results in uphill-diffusion of niobium towards the scale/alloy interface with the consequence that a Nb-enrichment and precipitation of the $\delta\text{-Ni}_3\text{Nb}$ phase occurs beneath the chromia scale. In parallel, Nb-depletion accompanied by dissolution of the δ -phase is observed along the chromium depletion profile in the subsurface zone.
- On the other hand, the carbon activity was found to be higher in the subscale zone than that in the bulk alloy. This resulted in back diffusion of carbon towards the middle of the specimen and consequently to a dissolution of the M_6C particles in the subscale zone.

The formation of the $\delta\text{-Ni}_3\text{Nb}$ layer was also shown to occur at 1000°C although this phase is not stable in the original alloy microstructure above 930°C. The precipitation of the $\delta\text{-Ni}_3\text{Nb}$ phase beneath the chromia scale was illustrated to be a natural consequence of the uphill-diffusion of Nb towards the chromium depleted scale/alloy interface, i.e. of the effect of chromium concentration on the chemical activities of the alloying elements in alloy 625. Both effects, i.e. M_6C dissolution and enrichment/depletion of the δ -phase, were modeled using Thermo-Calc/DICTRA software package and shown to be the natural consequence of high temperature oxidation process of alloy 625.

The phase transformation effects in alloy 625 (SPE) were found to be substantially less pronounced for thin than for thick specimen. The thin foils (approximately 100 μm thick) are characterized by limited reservoirs of alloying elements. They are therefore inclined to exhibit a more rapid depletion of chromium and a less intensive enrichment of niobium at the scale/alloy interface. Decreasing the specimen thickness suppresses the enrichment/depletion process of the δ - Ni_3Nb phase and results in complete dissolution of the M_6C carbide after longer exposure times. In extremely thin specimens, e.g. metal foam particles, the δ - Ni_3Nb phase enrichment/depletion effect is not observed during high-temperature oxidation due to the reservoir considerations and thus can be ignored when modeling the oxidation-induced lifetime of alloy 625 metal foams.

During cyclic oxidation in air in the temperature range from 700 to 900°C highly porous alloy 625 foams exhibit after a certain time accelerated oxidation behavior which is correlated with a rapid increase in mass gain, resulting in a destruction of the foam specimens. Chemically induced breakaway, i.e. formation of rapidly growing voluminous nickel-rich oxides, was shown to be responsible for the mechanical disintegration of the metal foams during long-term exposure. The latter could be proven by exposure in the low-pO₂ gas Ar–4%H₂–20%H₂O.

Although exhibiting a higher growth rate of the initially forming chromia scale in this environment than in air, the Ni-base foams preserved their mechanical stability when oxidized in this gas up to the largest test time of 1000 h due to thermodynamic instability of nickel oxide in this atmosphere. The lifetime prediction based on the finite-element calculation of the time dependent chromium concentration at the metal/oxide interface assuming a binary Ni-22Cr alloy as a model for alloy 625 showed a parabolic dependence of the time to breakaway from the foam particle radius. The calculated lifetimes were shown to increase with increasing particle radius and decreasing oxidation temperature. The predicted lifetimes for metal foams were found to be in good agreement with the experimental breakaway data.

A new simplified lifetime treatment was developed for FCC materials in which the ratio k_p/D is not small enough to use the mass balance model previously derived by Quadakkers et al [32] for alumina forming ferritic materials. The parametric analysis of the general lifetime model derived by Whittle revealed that the Quadakkers model is a limiting case for alloys with fast diffusion of the selectively oxidizing solute in the alloy, i.e. when the ratio k_p/D is

extremely small. The mass balance model can be extended by introducing an additional negative term, inversely proportional to D_{Cr} , which accounts for slow diffusion of the solute. The modified lifetime expression, which takes slow diffusion into account, shows very good agreement with the numerical solutions of the Whittle model.

The lifetime model derived was used to calculate the time to breakaway in a spherical particle of alloy 625 thus simulating the breakaway oxidation of alloy 625 metal foams. The calculation lifetime curve for 900°C showed reasonable agreement with the experimental breakaway data.

11. References

1. D.P. WHITTLE, D.J. EVANS, D.B. SCULLY, and G.C. WOOD: Compositional changes in underlying alloy during protective oxidation of alloys, *Acta Metallurgica*, **15**, 1421 (1967).
2. T. SOURMAIL: Precipitation in creep resistant austenitic stainless steels, *Materials Science and Technology*, **17**, 1 (2001).
3. S. KIHARA, J.B. NEWKIRK, A. OHTOMO, and Y. SAIGA: Morphological changes of carbides during creep and their effects on the creep properties of Inconel 617 at 1000°C, *Metallurgical Transactions A*, **11**, 1019 (1980).
4. D. NAUMENKO, V. SHEMET, L. SINGHEISER, and W.J. QUADAKKERS: Failure mechanisms of thermal barrier coatings on MCrAlY-type bondcoats associated with the formation of the thermally grown oxide, *Journal of Materials Science*, **44**, 1687 (2009).
5. W.G. SLOOF and T.J. NIJDAM: On the high-temperature oxidation of MCrAlY coatings, *International Journal of Materials Research*, **100**, 1318 (2009).
6. R. COZAR and A. PINEAU: Morphology of γ' and γ'' precipitates and thermal stability of Inconel 718 type alloys, *Metallurgical Transactions*, **4**, 47 (1973).
7. M.D. MATHEW, P. PARAMESWARAN, and K.B.S. RAO: Microstructural changes in alloy 625 during high temperature creep, *Materials Characterization*, **59**, 508 (2008).
8. J. FROITZHEIM, G.H. MEIER, L. NIEWOLAK, P. ENNIS, H. HATTENDORF, L. SINGHEISER, and W.J. QUADAKKERS: Development of high strength ferritic steel for interconnect application in SOFCs, *Journal of Power Sources*, **178**, 163 (2008).
9. P.D. JABLONSKI, C.J. COWEN, and J.S. SEARS: Exploration of alloy 441 chemistry for solid oxide fuel cell interconnect application, *Journal of Power Sources*, **195**, 813 (2010).
10. Z.G. YANG, G.G. XIA, C.M. WANG, Z.M. NIE, J. TEMPLETON, J.W. STEVENSON, and P. SINGH: Investigation of iron-chromium-niobium-titanium ferritic stainless steel for solid oxide fuel cell interconnect applications, *Journal of Power Sources*, **183**, 660 (2008).
11. V. KOCHUBEY, D. NAUMENKO, E. WESSEL, J. LE COZE, L. SINGHEISER, H. AL-BADAIRY, G.J. TATLOCK, and W.J. QUADAKKERS: Evidence for Cr-carbide formation at the scale/metal interface during oxidation of FeCrAl alloys, *Materials Letters*, **60**, 1654 (2006).
12. P. KOFSTAD: *High temperature oxidation* (Elsevier Applied Science, London and New York, 1988).
13. N. BIRKS, G.H. MEIER, and F.S. PETTIT: *Introduction into the high temperature oxidation of metals* (Cambridge University Press, Cambridge, 2006).
14. K.T. JACOB, C. SHEKHAR, M. VINAY, and Y. WASEDA: Thermodynamic properties of niobium oxides, *Journal of Chemical and Engineering Data*, **55**, 4854 (2010).

15. H.P. TRIPP and B.W. KING: Thermodynamic data on oxides at elevated temperatures, *Journal of the American Ceramic Society*, **38**, 432 (1955).
16. D.J. YOUNG: *High temperature oxidation and corrosion of metals* (Elsevier, Oxford, 2008).
17. C. WAGNER: Beitrag zur Theorie des Anlaufvorgangs, *Zeitschrift für physikalische Chemie*, **21**, 25 (1933).
18. D.P. WHITTLE: Spalling of protective oxide scales, *Oxidation of Metals*, **4**, 171 (1972).
19. D.J. YOUNG and B.A. PINT: Chromium volatilization rates from Cr₂O₃ scales into flowing gases containing water vapor, *Oxidation of Metals*, **66**, 137 (2006).
20. W.J. QUADAKKERS, D. NAUMENKO, E. WESSEL, V. KOCHUBEY, and L. SINGHEISER: Growth rates of alumina scales on Fe-Cr-Al alloys, *Oxidation of Metals*, **61**, 17 (2004).
21. G.R. WALLWORK: The oxidation of alloys, *Reports on Progress in Physics*, **39**, 401 (1976).
22. G.C. WOOD, I.G. WRIGHT, T. HODGKIESS, and D.P. WHITTLE: A comparison of the oxidation of Fe-Cr, Ni-Cr and Co-Cr alloys in oxygen and water vapour, *Werkstoffe und Korrosion*, **21**, 900 (1970).
23. A.D. DALVI and D.E. COATES: Review of diffusion path concept and its application to high-temperature oxidation of binary-alloys, *Oxidation of Metals*, **5**, 113 (1972).
24. C. WAGNER: Theoretical analysis of the diffusion processes determining the oxidation rate of alloys, *Journal of the Electrochemical Society*, **99**, 369 (1952).
25. R.A. RAPP: The transition from internal to external oxidation and the formation of interruption bands in silver-indium alloys, *Acta Metallurgica*, **9**, 730 (1961).
26. C. WAGNER: Reaktionstypen bei der Oxydation von Legierungen, *Zeitschrift für Elektrochemie*, **63**, 772 (1959).
27. E. ESSUMAN, G.H. MEIER, J. ZUREK, M. HÄNSEL, T. NORBY, L. SINGHEISER, and W.J. QUADAKKERS: Protective and non-protective scale formation of NiCr alloys in water vapour containing high- and low-pO₂ gases, *Corrosion Science*, **50**, 1753 (2008).
28. B.D. BASTOW, D.P. WHITTLE, and G.C. WOOD: Alloy depletion profiles resulting from preferential removal of less noble-metal during alloy oxidation, *Oxidation of Metals*, **12**, 413 (1978).
29. C. WAGNER: Oxidation of alloys involving noble metals, *Journal of the Electrochemical Society*, **103**, 571 (1956).

30. P. HUCZKOWSKI, N. CHRISTIANSEN, V. SHEMET, J. PIROŃ-ABELLAN, L. SINGHEISER, and W.J. QUADAKKERS: Oxidation limited life times of chromia forming ferritic steels, *Materials and Corrosion*, **55**, 825 (2004).
31. P. HUCZKOWSKI, N. CHRISTIANSEN, V. SHEMET, J. PIROŃ-ABELLAN, L. SINGHEISER, and W.J. QUADAKKERS: Oxidation-induced lifetime limits of chromia forming ferritic interconnector steels, *Journal of Fuel Cell Science and Technology*, **1**, 30 (2004).
32. W.J. QUADAKKERS and M.J. BENNETT: Oxidation-induced lifetime limits of thin-walled, iron-based, alumina forming, oxide dispersion-strengthened alloy components, *Materials Science and Technology*, **10**, 126 (1994).
33. W.J. QUADAKKERS and K. BONGARTZ: The prediction of breakaway oxidation for alumina forming ODS alloys using oxidation diagrams, *Werkstoffe und Korrosion*, **45**, 232 (1994).
34. W.J. QUADAKKERS: Growth mechanisms of oxide scales on ODS alloys in the temperature range 1000-1100°C, *Werkstoffe und Korrosion*, **41**, 659 (1990).
35. I. GURRAPPA, S. WEINBRUCH, D. NAUMENKO, and W.J. QUADAKKERS: Factors governing breakaway oxidation of FeCrAl-based alloys, *Materials and Corrosion*, **51**, 224 (2000).
36. L. MARECHAL, B. LESAGE, A.M. HUNTZ, and R. MOLINS: Oxidation behavior of ods Fe-Cr-Al alloys: Aluminum depletion and lifetime, *Oxidation of Metals*, **60**, 1 (2003).
37. J. CRANK: *The mathematics of diffusion* (Clarendon Press, Oxford, 1956).
38. H.S. CARSLAW and J.C. JAEGER: *Conduction of heat in solids* (Clarendon Press, Oxford, 1959).
39. D.P. WHITTLE: Oxidation of finite samples of heat-resistant alloys, *Corrosion Science*, **12**, 869 (1972).
40. H.C. COWEN and S.J. WEBSTER: Chromium depletion during oxidation of stainless steel foils, in *Corrosion of steels in CO₂* (London, 1974) p. 349.
41. H.E. EVANS and A.T. DONALDSON: Silicon and chromium depletion during the long-term oxidation of thin-sectioned austenitic steel, *Oxidation of Metals*, **50**, 457 (1998).
42. A.J. STRUTT and K.S. VECCHIO: Simultaneous oxidation and sigma-phase formation in a stainless steel, *Metallurgical and Materials Transactions A*, **30**, 355 (1999).
43. R. BAUER, M. BACCALARO, L.P.H. JEURGENS, M. POHL, and E.J. MITTEMEIJER: Oxidation behavior of Fe-25Cr-20Ni-2.8Si during isothermal oxidation at 1,286 K; life-time prediction, *Oxidation of Metals*, **69**, 265 (2008).

44. H.E. EVANS, A.T. DONALDSON, and T.C. GILMOUR: Mechanisms of breakaway oxidation and application to a chromia-forming steel, *Oxidation of Metals*, **52**, 379 (1999).
45. R. HALES: Compositional changes due to removal of one constituent in an alloy by a surface-reaction, *Oxidation of Metals*, **10**, 29 (1976).
46. T. HODGKIESS, G.C. WOOD, D.P. WHITTLE, and B.D. BASTOW: Compositional changes in underlying alloy produced by oxidation of Ni-Cr alloys, *Oxidation of Metals*, **12**, 439 (1978).
47. G.R. HOLCOMB: Calculation of reactive-evaporation rates of chromia, *Oxidation of Metals*, **69**, 163 (2008).
48. J.A. NESBITT: Predicting minimum Al concentrations for protective scale formation on Ni-base alloys: 1. Isothermal oxidation, *Journal of the Electrochemical Society*, **136**, 1511 (1989).
49. J.A. NESBITT: Numerical modeling of high-temperature corrosion processes, *Oxidation of Metals*, **44**, 309 (1995).
50. J.A. NESBITT: COSIM - a finite-difference computer model to predict ternary concentration profiles associated with oxidation and interdiffusion of overlay-coated substrates, *Lifetime Modelling of High Temperature Corrosion Processes*, 359 (2001).
51. J.A. NESBITT and R.W. HECKEL: Modeling degradation and failure of Ni-Cr-Al overlay coatings, *Thin Solid Films*, **119**, 281 (1984).
52. M. DANIELEWSKI, R. FILIPEK, and B. KUCHARSKA: Prediction of the depletion zone due to selective oxidation of P91 steel, *Diffusion in Materials: DIMAT 2004, Pts 1 and 2*, **237-240**, 965 (2005).
53. M. DANIELEWSKI, R. FILIPEK, M. PAWELKIEWICZ, D. KLASSEK, and K. KURZYDLOWSKI: Modelling of oxidation of Fe-Ni-Cr alloys, in *Diffusion in materials: DIMAT 2004, pts 1 and 2* (2005) p. 958.
54. M. DANIELEWSKI and B. WIERZBA: Diffusion processes determining the oxidation rate of multicomponent alloys, *Corrosion Science*, **50**, 1161 (2008).
55. W.M. PRAGNELL and H.E. EVANS: Chromium depletion at 2-dimensional features during the selective oxidation of a 20Cr-25Ni austenitic steel, *Oxidation of Metals*, **66**, 209 (2006).
56. W.M. PRAGNELL, H.E. EVANS, D. NAUMENKO, and W.J. QUADAKERS: Aluminium depletion in FeCrAlY steel during transitional alumina formation, *Materials at high temperatures*, **22**, 561 (2005).
57. A.N. HANSSON, J.H. HATTEL, K.V. DAHL, and M.A.J. SOMERS: Modelling Cr depletion under a growing Cr_2O_3 layer on austenitic stainless steel: The influence of grain boundary diffusion, *Modelling and Simulation in Materials Science and Engineering*, **17**, 1 (2009).

58. E.Y. LEE, D.M. CHARTIER, R.R. BIEDERMAN, and R.D. SISSON: Modeling the microstructural evolution and degradation of MCrAlY coatings during high-temperature oxidation, *Surface and Coatings Technology*, **32**, 19 (1987).
59. K. BONGARTZ, W.J. QUADAKKERS, J.P. PFEIFER, and J.S. BECKER: Mathematical-modeling of oxide-growth mechanisms measured by O¹⁸ tracer experiments, *Surface Science*, **292**, 196 (1993).
60. K. BONGARTZ, W.J. QUADAKKERS, R. SCHULTEN, and H. NICKEL: A mathematical-model describing carburization in multielement alloy systems, *Metallurgical Transactions A*, **20**, 1021 (1989).
61. K. BONGARTZ, R. SCHULTEN, W.J. QUADAKKERS, and H. NICKEL: A finite-difference model describing carburization in high-temperature alloys, *Corrosion*, **42**, 390 (1986).
62. T. TURPIN, J. DULCY, and M. GANTOIS: Prediction of phase distribution and chemical composition during gas carburizing of stainless steels, *Journal de Physique IV*, **120**, 249 (2004).
63. T. TURPIN, J. DULCY, and M. GANTOIS: Carbon diffusion and phase transformations during gas carburizing of high-alloyed stainless steels: Experimental study and theoretical modeling, *Metallurgical and Materials Transactions A*, **36A**, 2751 (2005).
64. A. BORGENSTAM, A. ENGSTROM, L. HOGLUND, and J. AGRENN: DICTRA, a tool for simulation of diffusional transformations in alloys, *Journal of Phase Equilibria*, **21**, 269 (2000).
65. K.V. DAHL, J. HALD, and A. HORSEWELL: Interdiffusion between Ni-based superalloy and MCrAlY coating, in *Diffusion in solids and liquids - mass diffusion* (Trans Tech Publications Ltd, Stafa-Zürich, 2006) p. 73.
66. T. GOMEZ-ACEBO, B. NAVARCORENA, and F. CASTRO: Interdiffusion in multiphase, Al-Co-Cr-Ni-Ti diffusion couples, *Journal of Phase Equilibria and Diffusion*, **25**, 237 (2004).
67. B. SUNDMAN, S. FORD, X.G. LU, T. NARITA, and D. MONCEAU: Experimental and simulation study of uphill diffusion of Al in a Pt-coated gamma-Ni-Al model alloy, *Journal of Phase Equilibria and Diffusion*, **30**, 602 (2009).
68. T.J. NIJDAM, L.P.H. JEURGENS, and W.G. SLOOF: Modelling the thermal oxidation of ternary alloys - compositional changes in the alloy and the development of oxide phases, *Acta Materialia*, **51**, 5295 (2003).
69. T.J. NIJDAM and W.G. SLOOF: Modelling of composition and phase changes in multiphase alloys due to growth of an oxide layer, *Acta Materialia*, **56**, 4972 (2008).
70. D.J. YOUNG and B. GLEESON: Alloy phase transformations driven by high temperature corrosion processes, *Corrosion Science*, **44**, 345 (2002).

71. K.S. CHAN, N.S. CHERUVU, and G.R. LEVERANT: Coating life prediction under cyclic oxidation conditions, *Journal of Engineering for Gas Turbines and Power-Transactions of the ASME*, **120**, 609 (1998).
72. F. GESMUNDO and B. GLEESON: Oxidation of multicomponent 2-phase alloys, *Oxidation of Metals*, **44**, 211 (1995).
73. M. LEVY, P. FARRELL, and F. PETTIT: Oxidation of some advanced single-crystal nickel-base superalloys in air at 2000°F (1093°C), *Corrosion*, **42**, 708 (1986).
74. R. OROSZ, U. KRUPP, H.J. CHRIST, and D. MONCEAU: The influence of specimen thickness on the high temperature corrosion behavior of CMSX-4 during thermal cycling exposure, *Oxidation of Metals*, **68**, 165 (2007).
75. R. OROSZ, U. KRUPP, and H.J. CHRIST: Study of the oxide scale integrity on Ni-base alloy CMSX-4 during isothermal and thermal-cycling exposure, *Materials and Corrosion*, **57**, 154 (2006).
76. R. DURHAM, B. GLEESON, and D.J. YOUNG: Silicon contamination effects in the oxidation of carbide-containing cobalt-chromium alloys, *Materials and Corrosion*, **49**, 855 (1998).
77. R.N. DURHAM, B. GLEESON, and D.J. YOUNG: Factors affecting chromium carbide precipitate dissolution during alloy oxidation, *Oxidation of Metals*, **50**, 139 (1998).
78. P.J. ENNIS, W.J. QUADAKKERS, and H. SCHUSTER: The effect of selective oxidation of chromium on the creep strength of alloy 617, *Journal de Physique IV*, **3**, 979 (1993).
79. R. PETKOVIC-LUTON and T.A. RAMANARAYANAN: Mixed-oxidant attack of high-temperature alloys in carbon-containing and oxygen-containing environments, *Oxidation of Metals*, **34**, 381 (1990).
80. P. CARTER, B. GLEESON, and D.J. YOUNG: Calculation of precipitate dissolution zone kinetics in oxidising binary two-phase alloys, *Acta Materialia*, **44**, 4033 (1996).
81. B. JANSSON, M. SCHALIN, M. SELLEBY, and B. SUNDMAN: The Thermo-Calc database system, in *Computer software in chemical and extractive metallurgy* (Canadian Inst Mining, Metallurgy and Petroleum, Montreal, 1993) p. 57.
82. F.H. STOTT, G.J. GABRIEL, F.I. WEI, and G.C. WOOD: The development of silicon-containing oxides during the oxidation of iron-chromium-base alloys, *Werkstoffe und Korrosion*, **38**, 521 (1987).
83. G.C. WOOD, RICHARDS.JA, M.G. HOBBY, and J. BOUSTEAD: Identification of thin healing layers at base of oxide scales on Fe-Cr base alloys, *Corrosion Science*, **9**, 659 (1969).
84. M.J. BENNETT, J.A. DESPORT, and P.A. LABUN: Analytical electron-microscopy of a selective oxide scale formed on 20%Cr-25%Ni-Nb stainless-steel, *Oxidation of Metals*, **22**, 291 (1984).

85. A. KUMAR and D.L. DOUGLASS: Modification of oxidation behavior of high-purity austenitic Fe14Cr14Ni by addition of silicon, *Oxidation of Metals*, **10**, 1 (1976).
86. Y.Q. LIU, G. SHAO, and P. TSAKIROPOULOS: On the oxidation behaviour of MoSi₂, *Intermetallics*, **9**, 125 (2001).
87. G.R. BLAIR, H. LEVIN, and R.E. OBRIEN: Evaporation of silicon from molybdenum silicides at high temperature and in hard vacuum, *Journal of the American Ceramic Society*, **48**, 430 (1965).
88. G.B. CHERNIACK and A.G. ELLIOT: High-temperature behavior of MoSi₂ and Mo₅Si₃, *Journal of the American Ceramic Society*, **47**, 136 (1964).
89. A.W. SEARCY: Predicting the thermodynamic stabilities and oxidation resistances of silicide cermets, *Journal of the American Ceramic Society*, **40**, 431 (1957).
90. C.D. WIRKUS and D.R. WILDER: High-temperature oxidation of molybdenum disilicide, *Journal of the American Ceramic Society*, **49**, 173 (1966).
91. H.S. KIM, J.K. YOON, G.H. KIM, J.M. DOH, S.I. KWUN, and K.T. HONG: Growth behavior and microstructure of oxide scales grown on WSi₂ coating, *Intermetallics*, **16**, 360 (2008).
92. E. FITZER: Diffusionskontrollierte Reaktionen an Siliziden Hochschmelzender Metalle, *Planseeberichte für Pulvermetallurgie*, **17**, 36 (1969).
93. P.C. TORTORICI and M.A. DAYANANDA: Growth of silicides and interdiffusion in the Mo-Si system, *Metallurgical and Materials Transactions A*, **30**, 545 (1999).
94. Binary Alloy Phase Diagrams, ASM International: Materials Park, OH.
95. E.H. COPLAND, B. GLEESON, and D.J. YOUNG: Formation of Z-Ti₅₀Al₃₀O₂₀ in the sub-oxide zones of γ -TiAl-based alloys during oxidation at 1000°C, *Acta Materialia*, **47**, 2937 (1999).
96. N. ZHENG, W. FISCHER, H. GRUBMEIER, V. SHEMET, and W.J. QUADAKKERS: The significance of subsurface depletion layer composition for the oxidation behavior of γ -titanium aluminides, *Scripta Metallurgica et Materialia*, **33**, 47 (1995).
97. V. SHEMET, A.K. TYAGI, J.S. BECKER, P. LERSCH, L. SINGHEISER, and W.J. QUADAKKERS: The formation of protective alumina-based scales during high-temperature air oxidation of γ -TiAl alloys, *Oxidation of Metals*, **54**, 211 (2000).
98. U. MOHR, W. BLECK, and P.F. SCHOLZ: Metallic foams produced by slipcasting, *Advanced Engineering Materials*, **4**, 28 (2002).
99. P. HUCZKOWSKI, S. ERTL, J. PIRON-ABELLAN, N. CHRISTIANSEN, T. HOFLER, V. SHEMET, L. SINGHEISER, and W.J. QUADAKKERS: Effect of component thickness

on lifetime and oxidation rate of chromia forming ferritic steels in low and high pO₂ environments, *Materials at high temperatures*, **22**, 253 (2005).

100. J. TOSCANO, D. NAUMENKO, A. GIL, L. SINGHEISER, and W.J. QUADAKKERS: Parameters affecting TGO growth rate and the lifetime of TBC systems with MCrAlY-bondcoats, *Materials and Corrosion*, **59**, 501 (2008).
101. G.R. HOLCOMB: Steam oxidation and chromia evaporation in ultrasupercritical steam boilers and turbines, *Journal of the Electrochemical Society*, **156**, C292 (2009).
102. Olympus: Image analysis software.
103. W.J. QUADAKKERS, A. ELSCHNER, W. SPEIER, and H. NICKEL: Composition and growth mechanisms of alumina scales on FeCrAl-based alloys determined by SNMS, *Applied Surface Science*, **52**, 271 (1991).
104. W.J. QUADAKKERS and H. VIEFHaus: The application of surface analysis techniques in high temperature corrosion research, in *EFC-Workshop "Methods and Testing in High Temperature Corrosion"*, H.J. Grabke and D.B. Meadowcroft, ed. (Frankfurt, FRG, 1995) p. 189.
105. Y.M. MUGGIANU, M. GAMBINO, and J.P. BROS: Enthalpies of formation of liquid alloys bismuth-gallium-tin at 723K - choice of an analytical representation of integral and partial thermodynamic functions of mixing for this ternary system, *Journal de Chimie Physique et Physico-Chimie Biologique*, **72**, 83 (1975) (in French).
106. N. SAUNDERS and A.P. MIODOWNIK: *CALPHAD (calculation of phase diagrams): A comprehensive guide* (Pergamon Materials Series, Oxford, 1998).
107. L. ONSAGER: Reciprocal relations in irreversible processes. II, *Physical Review*, **38**, 2265 (1931).
108. J. AGREn: Numerical treatment of diffusional reactions in multicomponent alloys, *Journal of Physics and Chemistry of Solids*, **43**, 385 (1982).
109. A. ENGSTRÖM, L. HOGLUND, and J. AGREn: Computer-simulation of diffusion in multiphase systems, *Metallurgical and Materials Transactions A*, **25**, 1127 (1994).
110. A. ENGSTRÖM, J.E. MORRAL, and J. AGREn: Computer simulations of Ni-Cr-Al multiphase diffusion couples, *Acta Materialia*, **45**, 1189 (1997).
111. A. TAYLOR and K. SACHS: A new complex eta-carbide, *Nature*, **169**, 411 (1952).
112. M.J. GODDEN and J. BEECH: Effect of silicon on M₆C in molybdenum steels, *Journal of Metals*, **21**, A43 (1969).
113. T.M. WILLIAMS and J.M. TITCHMARSH: Occurrence of a silicon-rich phase of the M₆C type in neutron-irradiated Fv548 steel, *Journal of Nuclear Materials*, **87**, 398 (1979).

114. X.M. GUAN and H.Q. YE: Intergranular embrittlement caused by the precipitation of M₆C carbide containing silicon, *Journal of Materials Science*, **15**, 2935 (1980).
115. S. HAMAR-THIBAULT, N. VALIGNAT, and S. LEBAILI: Composition of M₆C carbides formed in nickel-based hardfacing alloys, in *X-Ray Optics and Microanalysis* P.B. Kenway, ed. (Manchester, 1992) p. 189.
116. S. LEBAILI, J. AJAO, and S. HAMARTHIBAULT: Preparation and characterization of melt-spun nickel-based alloys containing heavy metals, *Journal of Alloys and Compounds*, **188**, 87 (1992).
117. M. SUNDARAMAN, L. KUMAR, G.E. PRASAD, P. MUKHOPADHYAY, and S. BANERJEE: Precipitation of an intermetallic phase with Pt₂Mo-type structure in alloy 625, *Metallurgical and Materials Transactions A*, **30**, 41 (1999).
118. H.M. TAWANCY, I.M. ALLAM, and N.M. ABBAS: Effect of Ni₃Nb precipitation on the corrosion-resistance of Inconel alloy 625, *Journal of Materials Science Letters*, **9**, 343 (1990).
119. W.E. MODDEMAN, S.M. CRAVEN, and D.P. KRAMER: Ni₃Nb alloy species in oxide surfaces of Inconel 718, *Metallurgical Transactions A*, **17**, 351 (1986).
120. F. DELAUNAY, C. BERTHIER, M. LENGLLET, and J.M. LAMEILLE: SEM-EDS and XPS studies of the high temperature oxidation behaviour of Inconel 718, *Mikrochimica Acta*, **132**, 337 (2000).
121. E. N'DAH, M.P. HIERRO, K. BORRERO, and F.J. PEREZ: Study of the cyclic oxidation resistance of superalloy IN-625: Lifetime predicted by COSP-modelling program, *Oxidation of Metals*, **68**, 9 (2007).
122. L.S. DARKEN: Diffusion of carbon in austenite with a discontinuity in composition, *Transactions of the American Institute of Mining and Metallurgical Engineers*, **180**, 430 (1949).
123. H. STRANDLUND and H. LARSSON: Diffusion process simulations, in *Defects and diffusion in metals - an annual retrospective VII* (Trans Tech Publications Ltd, Zürich-Uetikon, 2004) p. 97.
124. P. HUCZKOWSKI, private communication, Forschungszentrum Jülich, Germany Jülich, 2010.
125. M. MICHALIK, M. HÄNSEL, J. ZUREK, L. SINGHEISER, and W.J. QUADAKKERS: Effect of water vapour on growth and adherence of chromia scales formed on Cr in high and low pO₂-environments at 1000 and 1050°C, *Materials at High Temperatures*, **22**, 213 (2005).
126. V.B. TRINADE, U. KRUPP, P.E.G. WAGENHUBER, and H.J. CHRIST: Oxidation mechanisms of Cr-containing steels and Ni-base alloys at high-temperatures - part I: The different role of alloy grain boundaries, *Materials and Corrosion*, **56**, 785 (2005).

127. C. WAGNER: Formation of composite scales consisting of oxides of different metals, *Journal of the Electrochemical Society*, **103**, 627 (1956).
128. E. WESSEL, V. KOCHUBEY, D. NAUMENKO, L. NIEWOLAK, L. SINGHEISER, and W.J. QUADAKKERS: Effect of Zr addition on the microstructure of the alumina scales on FeCrAlY-alloys, *Scripta Materialia*, **51**, 987 (2004).
129. J. TOSCANO, R. VASSEN, A. GIL, M. SUBANOVIC, D. NAUMENKO, L. SINGHELSE, and W. QUADAKKERS: Parameters affecting TGO growth and adherence on MCrAlY-bond coats for TBC's, *Surface & Coatings Technology*, **201**, 3906 (2006).
130. J. ZUREK, G.H. MEIER, E. ESSUMAN, M. HÄNSEL, L. SINGHEISER, and W.J. QUADAKKERS: Effect of specimen thickness on the growth rate of chromia scales on Ni-base alloys in high- and low-pO₂ gases, *Journal of Alloys and Compounds*, **467**, 450 (2009).
131. I.E. ANDERSON, B.K. LOGRASSO, R. TERPSTRA, and B. GLEESON: Development of advanced metallic filters for hot gas cleaning, in *Power metallurgy alloys and particulate materials for industrial applications* (TMS, Warrandale, 2000) p. 11.
132. M.F. ASHBY, T. EVANS, N.A. FLECK, J.W. HUTCHINSON, H.N.G. WADLEY, and L.J. GIBSON: *Metal foams: A design guide* (Butterworth-Heinemann, Boston, 2000).
134. H. CHOE and D.C. DUNAND: Mechanical properties of oxidation-resistant Ni-Cr foams, *Materials Science and Engineering A*, **384**, 184 (2004).
135. A. LEONOV and A. ROMASHKO: Laminar Ni-Ni_xAl- α Al₂O₃ foam material with high oxidation resistance, in *Cellular Metals: Manufacture, Properties, Applications*, ed. (Berlin, 2003) p. 271.
136. L. KUMAR, R. VENKATARAMANI, M. SUNDARARAMAN, P. MUKHOPADHYAY, and S.P. GARG: Studies on the oxidation behavior of Inconel 625 between 873 and 1523 K, *Oxidation of Metals*, **45**, 221 (1996).
137. W.J. QUADAKKERS: Corrosion of high-temperature alloys in the primary circuit helium of high-temperature gas-cooled reactors; 2. Experimental results, *Werkstoffe und Korrosion*, **36**, 335 (1985).
138. M. HÄNSEL, W.J. QUADAKKERS, and D.J. YOUNG: Role of water vapor in chromia-scale growth at low oxygen partial pressure, *Oxidation of Metals*, **59**, 285 (2003).

Acknowledgements

I would like to express my gratitude to Prof. L. Singheiser and Prof. W.J. Quadakkers for their supervising of my studies in IEK-2, very stimulating discussions, and all the time they dedicated to my work.

Special thanks to Prof. D.J. Young (The University of New South Wales, Sidney, Australia) for critical reading of the last chapter of this work and very valuable comments on it.

Dr. S.L. Schulze and Prof. W. Bleck (IEHK, RWTH Aachen) are kindly acknowledged for cooperation and supplying metal foams.

Further I would like to thank Dr. E. Wessel for SEM studies, Ms. A. Kick and Mr. H. Cosler for carrying out the high-temperature exposures, Mr. J. Bartsch and Mr. V. Gutzeit for the optical microscopy and assistance in metallographic preparation, Dr. V. Shemet for measuring the GDOES profiles and Dr. W. Fischer for the XRD patterns.

Many thanks to all the colleagues of the high-temperature corrosion group: Javier, Dmitri, Pawel, Joanna, Leszek, Cristina, Laura, Peng, Tomasz, Alexandra as well as many other colleagues at the Institute for Energy and Climate Research (IEK-2).